

¹

Doctoral Dissertation

² **Estimating intervention-induced air pollution**
³ **changes and tracking carbon neutrality progress**
⁴ **employing the Digital Earth Systems Approach:**
⁵ **Applications and Policy Implications**

⁶

Phan Anh

⁷

February 1, 2024

⁸

Graduate School of Engineering
Chubu University

⁹

¹⁰ A Doctoral Dissertation
¹¹ submitted to Graduate School of Engineering,
¹² Chubu University
¹³ in partial fulfillment of the requirements for the degree of
¹⁴ Doctor of ENGINEERING

¹⁵ Phan Anh

¹⁶ Thesis Committee:

Professor Hiromichi Fukui (Supervisor)
Professor Kiyoshi Honda (Chubu University)
Professor Jun Izutsu (Chubu University)
Professor Masao Takano (Nagoya University)

¹⁷ **Estimating intervention-induced air pollution**
¹⁸ **changes and tracking carbon neutrality progress**
¹⁹ **employing the Digital Earth Systems Approach:**
²⁰ **Applications and Policy Implications***

²¹ Phan Anh

²² **Abstract**

²³ Simultaneously reducing air pollution and greenhouse gases (GHGs) is crucial
²⁴ for combating climate change. Due to their intricate characteristics and interre-
²⁵ lation, a comprehensive understanding, along with significant efforts, is necessary
²⁶ to address and diminish these pollutants and gases for future sustainable devel-
²⁷ opment on a regional to global scale. This thesis concentrates on three main
²⁸ topics to enhance understanding of regional air pollution characteristics and ap-
²⁹ proaches to monitor carbon neutrality progress at various scales. Initially, this
³⁰ thesis furnishes evidence and recommendations for regional air pollution miti-
³¹ gation policies. It accomplishes this by utilizing multisource data to evaluate
³² extreme intervention events on air quality, which are regarded as real-world prac-
³³ tices for reducing anthropogenic activities, as demonstrated by two case studies in
³⁴ Japan and Ukraine. Next, the thesis tackles the gap in estimating seasonal pat-
³⁵ terns and long-term trends in global terrestrial carbon fluxes, the largest carbon
³⁶ sink that requires accurate quantification to achieve carbon neutrality at both
³⁷ regional and global scales. Finally, the thesis introduces the development of a
³⁸ digital earth platform. This platform incorporates carbon neutrality roadmaps
³⁹ and the monitoring of fossil fuel GHG emissions and forest sinks at a local scale,
⁴⁰ using Japan's municipalities as a case study. This is assumed to be essential for

*Doctoral Dissertation, Graduate School of Engineering
Chubu University, February 1, 2024.

41 local policymakers to monitor progress toward achieving carbon neutrality and
42 develop appropriate local roadmaps to facilitate this goal.

43 Based on the experiments conducted in this thesis, the key findings are as
44 follows:

- 45 • I conducted an analysis of tropospheric NO₂ levels in Ukraine during two
46 significant periods. To isolate the meteorological effects, I utilized a business-
47 as-usual NO₂ time series. My findings provide evidence that the reduction
48 in road transportation in Ukraine did not significantly result in a decrease in
49 NO₂ levels during the Covid-19 lockdown in 2020. This is likely attributed
50 to limited reductions in the operation of Coal Power Plants (CPPs), in con-
51 trast to Europe, where road transport is identified as the primary contrib-
52 utor to NO₂ emissions, even after accounting for weather effects. However,
53 during the armed conflict with Russia in 2022, numerous CPPs in Ukraine
54 incurred damage, leading to a noticeable decline in NO₂ emissions in densely
55 populated cities. Based on these findings and evidence, it is suggested that
56 future policies aimed at reducing NO₂ from road transportation may not
57 achieve comparable effectiveness in Ukraine's populous cities.
- 58 • I examined the impact of NO₂ reduction on O₃ and CH₄ variations in 14
59 metropolitan areas (MAs) of Japan in 2020. This analysis utilized air qual-
60 ity time series generated by machine learning models under business-as-
61 usual conditions. My findings present evidence of an increase in O₃ levels
62 after the Covid-19 lockdown in most MAs in 2020, ranging from Okayama
63 to the northeast. This phenomenon may be attributed to these MAs being
64 VOC-limited areas, suggesting that future reductions in NO₂ could poten-
65 tially lead to elevated O₃ levels under favorable sunny conditions. How-
66 ever, in MAs from Hiroshima to the southwest, instances of NO_x limitation
67 were observed during the summer, indicating that future reductions in an-
68 thropogenic non-methane volatile organic compounds may have minimal
69 effectiveness in lowering O₃ levels. Therefore, based on these findings and
70 evidence, I recommend simultaneous reduction of air pollutants, as well as
71 anthropogenic and biogenic volatile organic compounds, in future policies
72 to effectively mitigate adverse effects on both O₃ and CH₄.

- By employing the recently updated dataset of plant functional types (PFTs) in conjunction with a multivariate time series Transformer-based model, I have generated a monthly global dataset of gross primary production (GPP) and ecosystem respiration (RECO) spanning from 1990 to 2019 at a spatial resolution of $0.25^\circ \times 0.25^\circ$ named FluxFormer. This dataset demonstrates superior performance compared to FLUXCOM, NIES, and MetaFlux datasets when assessing correlations at the site level and seasonal patterns with FLUXNET 2015, particularly in tropical regions. Moreover, FluxFormer exhibits the highest positive trend in GPP from 2001 to 2019, aligning with trends derived from dynamic global vegetation models that account for the CO₂ fertilization effect. Notably, it captures positive long-term trends that FLUXCOM and MetaFlux fail to replicate. Finally, I compare the interannual variations in FluxFormer with those in other datasets, observing reduced variations in deserts and semi-arid regions compared to the NIES data, despite utilizing the same remote sensing resources. This observation appears more reasonable, considering the extremely low GPP in these areas, which should not result in high interannual variations. The FluxFormer GPP and RECO products are available at <https://zenodo.org/records/10258644>.
- I have developed a digital earth platform with a specific emphasis on creating roadmaps for achieving carbon neutrality at the municipal level in Japan. The platform also serves the purpose of monitoring local greenhouse gas emissions from fossil fuels and assessing the capacity of local forest sinks. It incorporates energy-related data, including information on energy consumption and electricity statistics sourced from major domestic power companies. This data encompasses details on electricity usage, forecasts, supply, and the distribution of electricity power plants throughout the country. Through the consolidation of this information, my aim is for the platform to provide a comprehensive overview of the current progress toward attaining a zero-carbon status at the municipal level in Japan. The platform is accessible at <http://de14.digitalasia.chubu.ac.jp/>.

Building upon the findings and experiments conducted in this thesis, my future works involve researching the utilization of high-frequency temporal data from

106 satellite-derived NO₂ observations for predicting fossil fuel CO₂, given its recent
107 prominence. In conjunction with the globally upscaled terrestrial carbon fluxes
108 (FluxFormer), my objective is to incorporate monthly predictions of fossil fuel
109 CO₂ into the digital earth platform. This integration will enhance the continuous
110 monitoring of progress toward achieving zero carbon at both the local and regional
111 levels, offering a higher frequency of assessment.

112 **Keywords:**

113 air pollution, greenhouse gas, terrestrial carbon fluxes, carbon neutrality, digital
114 earth

¹¹⁵ Acknowledgements

¹¹⁶ First and foremost, I would like to express my deepest thanks to my principal
¹¹⁷ supervisor Professor Hiromichi Fukui for his patient guidance and constant sup-
¹¹⁸ port throughout my three years of studies. His broad vision has significantly
¹¹⁹ influenced my journey during my Ph.D. His mentorship goes beyond academic
¹²⁰ matters, assisting me in navigating life in Japan. I am sincerely thankful for his
¹²¹ encouragement and constructive feedback on my research, paper writing, and the
¹²² draft of this thesis. I feel incredibly fortunate to have been his student and to
¹²³ have had the opportunity to work with him.

¹²⁴ I would like to express my deep appreciation to Mr. Kyoshi Takejima for his
¹²⁵ kind support and guidance. He has taught me the basics and fundamentals of
¹²⁶ local forest remote sensing characteristics. The field trip to Ena for a forest thin-
¹²⁷ ning operation with him and Professor Hiromichi Fukui was a valuable learning
¹²⁸ experience. I would like to greatly thank Dr. Satoru Sugita for his kind and
¹²⁹ instant support with server deployment and addressing other technical issues in
¹³⁰ the laboratory. I would like to express my gratitude to Dr. Tsubasa Hirakawa
¹³¹ for the discussion and feedback regarding my research on mapping local forest
¹³² attributes. I would like to extend my sincere gratitude to Dr. Shinya Yasumoto
¹³³ for his generous assistance in preparing various documents, including scholarship
¹³⁴ applications and housing arrangements. His kind support has been crucial for
¹³⁵ me in various aspects both before and after my arrival in Japan. I would like to
¹³⁶ thank the officers and staffs of the International Digital Earth Applied Science
¹³⁷ Research Center (IDEAS) and Chubu Institute for Advanced Study for their kind
¹³⁸ support with paperwork and technical assistance during my study.

¹³⁹ I would like to thank the officers and staffs of the Division of Student Support
¹⁴⁰ and the Department of Engineering at Chubu University for their considerate
¹⁴¹ care and immediate support throughout my student life. I wish to thank the

¹⁴² teachers from the Center for International Affairs for providing a very helpful
¹⁴³ and necessary Japanese course for international students, aiding me in acquiring
¹⁴⁴ essential basic Japanese language skills for daily life.

¹⁴⁵ My appreciation extends to my colleagues and friends at Chubu University,
¹⁴⁶ including Man Duc Chuc, Rie Kanai, Titipakorn Prakayapan, and Hasnat Lalon,
¹⁴⁷ for their generous support during my studies. I cherished the enjoyable times and
¹⁴⁸ discussions we shared over lunches, dinners, and trips.

¹⁴⁹ I would like to give special thanks to Dr. Bui Quang Hung and Dr. Nguyen
¹⁵⁰ Thi Nhat Thanh, my former supervisors at Vietnam National University, who
¹⁵¹ taught me foundational knowledge in this field and kindly introduced me to my
¹⁵² current supervisor, Professor Hiromichi Fukui.

¹⁵³ I acknowledge the funding received for my Ph.D. candidacy from the Japanese
¹⁵⁴ Government through the Ministry of Education, Culture, Sports, Science, and
¹⁵⁵ Technology (MEXT) scholarship and the funding for Ph.D. students from Chubu
¹⁵⁶ University.

¹⁵⁷ For this study, all the equipment and tools I used were provided and purchased
¹⁵⁸ by the IDEAS center and Chubu University.

¹⁵⁹ Finally, I express my gratitude to my family for their unconditional love and
¹⁶⁰ support over the years. This thesis is also their accomplishment, and I dedicate
¹⁶¹ it to them.

Contents

¹⁶²	List of Figures	^x
¹⁶⁴	List of Tables	^{xii}
¹⁶⁵	1 Introduction	1
¹⁶⁶	1.1 Context	1
¹⁶⁷	1.2 Problem statement	3
¹⁶⁸	1.3 Research questions	5
¹⁶⁹	1.4 Outline of the thesis and scope	5
¹⁷⁰	2 Background	7
¹⁷¹	2.1 Air pollution	7
¹⁷²	2.1.1 Introduction	7
¹⁷³	2.1.2 Impact of weather variations on air pollution changes	9
¹⁷⁴	2.2 Greenhouse gases (GHGs)	10
¹⁷⁵	2.2.1 Fossil fuel GHGs	10
¹⁷⁶	2.2.2 Terrestrial carbon fluxes	11
¹⁷⁷	2.3 Relationship between air pollution and fossil fuel CO ₂	13
¹⁷⁸	2.4 Air pollution, GHGs and SDGs	16
¹⁷⁹	2.4.1 Air pollution and SDGs	16
¹⁸⁰	2.4.2 Greenhouse gases and SDGs	20
¹⁸¹	2.4.3 Digital Earth approach and perspective	22
¹⁸²	3 Impact of interventions on air quality	25
¹⁸³	3.1 Case Study in Ukraine	25
¹⁸⁴	3.1.1 Introduction	25
¹⁸⁵	3.1.2 Data	28
¹⁸⁶	3.1.3 Business-as-usual (BAU) modelling	34

187	3.1.4	COVID-19 induced NO ₂ changes	37
188	3.1.5	NO ₂ changes induced by the armed conflict	44
189	3.1.6	Conclusion	53
190	3.2	Case Study in Japan	55
191	3.2.1	Introduction	55
192	3.2.2	Data	59
193	3.2.3	Method	62
194	3.2.4	Results	66
195	3.2.5	Discussion	76
196	3.2.6	Conclusion	78
197	4	Terrestrial carbon fluxes estimation	80
198	4.1	Local plant functional types mapping	80
199	4.1.1	Introduction	81
200	4.1.2	Data	82
201	4.1.3	Methodology	85
202	4.1.4	Experimental results	89
203	4.1.5	Conclusion	94
204	4.2	Global terrestrial carbon fluxes estimates	95
205	4.2.1	Introduction	95
206	4.2.2	Methods	97
207	4.2.3	Data records	102
208	4.2.4	Technical validation	102
209	4.2.5	Conclusion	111
210	5	Carbon neutrality roadmaps platform	114
211	5.1	Introduction	114
212	5.2	Method	116
213	5.2.1	Data collection	117
214	5.2.2	API development	118
215	5.2.3	Web application	121
216	5.3	Result and discussion	122
217	5.3.1	Result	122
218	5.3.2	Discussion	125

²¹⁹	6 Conclusions and future prospects	127
²²⁰	6.1 Key finding and contributions	127
²²¹	6.2 Future prospects	131
²²²	Bibliography	132

List of Figures

224 1.1	Resident time in atmosphere and the area of dispersion	2
225 1.2	Outline of this thesis	6
226 2.1	Terrestrial carbon cycle (Xiao et al., 2019a)	12
227 2.2	Fossil fuel CO ₂ prediction from top-down NO _x	15
228 2.3	How air pollution relates to the SDGs (Ortiz et al., 2017)	17
229 2.4	Relation of SDGs to air pollution drivers and impacts (Elder, 2016)	18
230 2.5	Impacts of climate change on the achievement of the SDGs (Fuso Nerini et al., 2019)	20
231 2.6	Synergies and trade-offs of climate action to other SDGs	21
232 2.7	An example of abstract architecture of a digital earth system (Fukui et al., 2021)	23
235 3.1	Monthly map of S5P NO ₂ in Ukraine	30
236 3.2	Monthly number of qualitfied S5P NO ₂ observations in Ukraine .	31
237 3.3	Feature importance estimated using LightGBM split method.	36
238 3.4	Model performance evaluation	37
239 3.5	Examples of OBS and BAU data in 2022	38
240 3.6	Meteorological variations during pre-lockdown and lockdown . . .	40
241 3.7	S5P NO ₂ level changes for most populous cities	42
242 3.8	Analyzed conflict hotspots using satellite and ACLED data	46
243 3.9	NO ₂ level changes estimates for conflict events	48
244 3.10	OBS and BAU S5P NO ₂ trends (2020-2022) in populous cities .	50
245 3.11	OBS and BAU S5P NO ₂ trends (2020-2022) for selected CPPs .	52
246 3.12	Mobility changes for six prefectures in Japan	58
247 3.13	Study area	60
248 3.14	Model performance evaluation	64

249	3.15 NO ₂ reduction trends in 2020	67
250	3.16 NO ₂ , O ₃ , SR, T2M, FNR, and HCHO variations in 2020	70
251	3.17 2020 O ₃ mean trends (4 MAs)	71
252	3.18 NO ₂ , CO and CH ₄ , and HCHO variations in 2020	74
253	3.19 2020 CO and CH ₄ mean trends (4 MAs)	75
254	4.1 National forest in Ena city	82
255	4.2 Study area and annotated data	84
256	4.3 Workflow and the proposed CNN architecture	86
257	4.4 Inferred forest map in Ena City	90
258	4.5 Study area and annotated data	91
259	4.6 Inferred forest age map in Ena City	93
260	4.7 Inferred PFTs map in Ena City	94
261	4.8 PFTs mapping in other regions	95
262	4.9 Schematic workflow of our FluxFormer methodology	97
263	4.10 Mean estimate of GPP and RECO in 2017	103
264	4.11 Latitudinal distribution of mean annual GPP and RECO from 2001 to 2019	104
265	4.12 Estimated uncertainty for the year 2017 of GPP and RECO . . .	105
266	4.13 Validation with FLUXNET 2015	106
267	4.14 Seasonality validation with FLUXNET 2015	107
268	4.15 Validation with SIF products	109
269	4.16 Long term trend and latitudinal distribution of GPP and RECO .	111
270	4.17 Interannual variations from 2001 to 2019 of GPP (a), and RECO (b)	112
273	5.1 Platform architecture	116
274	5.2 APIs interfaces Emission Tracker APIs (a) Zero Emission APIs (b)	121
275	5.3 Emission Tracker interfaces	122
276	5.4 Drawdown tab interfaces	124
277	5.5 Additional platform interfaces	124
278	5.6 Comparison with other platforms	125

List of Tables

280	3.1	Model performance evaluation	35
281	3.2	The hyperparameters used to develop the LightGBM model	39
282	3.3	S5P NO ₂ level changes estimates for most populous cities	43
283	3.4	Comparison of NO ₂ changes during 2020 and 2022 lockdown period	49
284	3.5	S5P NO ₂ variations in populous cities from February to July 2022	51
285	3.6	Model performance evaluation	63
286	3.7	OBS-BAU estimates for NO ₂	66
287	3.8	OBS-BAU estimates for O ₃	69
288	3.9	OBS-BAU estimates for NO ₂ and CO and CH ₄	76
289	4.1	Samples, weights for cross-entropy loss training	88
290	4.2	The experimental results of UNET and our model.	92
291	4.3	Number of samples for training and validation	100
292	4.4	Pearson correlation of seasonal trend with FLUXNET 2015	108
293	5.1	The dataset used for the GIS platform development	117
294	5.2	APIs specifications	118

²⁹⁵ 1 Introduction

²⁹⁶ 1.1 Context

²⁹⁷ Air pollutants, including nitrogen oxides, carbon monoxide, ozone, and green-
²⁹⁸ house gases (GHGs) such as carbon dioxide and methane, are chemical elements
²⁹⁹ present in the atmosphere. These elements have a substantial impact on human
³⁰⁰ health (Kampa and Castanas, 2008) and play a significant role in global warming-
³⁰¹ ing and climate change (Haines et al., 2006). Furthermore, these elements are
³⁰² essential components that need to be reduced to foster sustainable development.

³⁰³ Effectively mitigating the impact of climate change requires a simultaneous re-
³⁰⁴ duction in both air pollution and GHGs emissions through the implementation
³⁰⁵ of future policies. The development of impactful strategies to address air pollu-
³⁰⁶ tion is intricately tied to the specific circumstances of each locality, emphasizing
³⁰⁷ the necessity for context-specific approaches. Conversely, the success of GHGs
³⁰⁸ reduction policies relies on a concerted global effort (Keohane and Victor, 2011).
³⁰⁹ This is due to the unique characteristics of air pollution and GHGs concerning
³¹⁰ their residence time in the atmosphere and area of dispersion, as illustrated in
³¹¹ Figure 1.1.

³¹² In the field of air pollution research, the COVID-19 lockdown is viewed as
³¹³ a valuable intervention for shaping future air pollution policies. While the pri-
³¹⁴ mary objective of the lockdown was not explicitly to address air pollution and
³¹⁵ GHGs emissions, the adoption of these measures provides valuable insights for
³¹⁶ atmospheric modeling. This experience imparts practical knowledge and first-
³¹⁷ hand lessons that can contribute to the development of more efficient strategies
³¹⁸ for mitigating air pollution and curbing GHGs emissions in the future (Grange
³¹⁹ et al., 2021).

³²⁰ For zero-carbon emission modeling research, the most critical measure for mit-

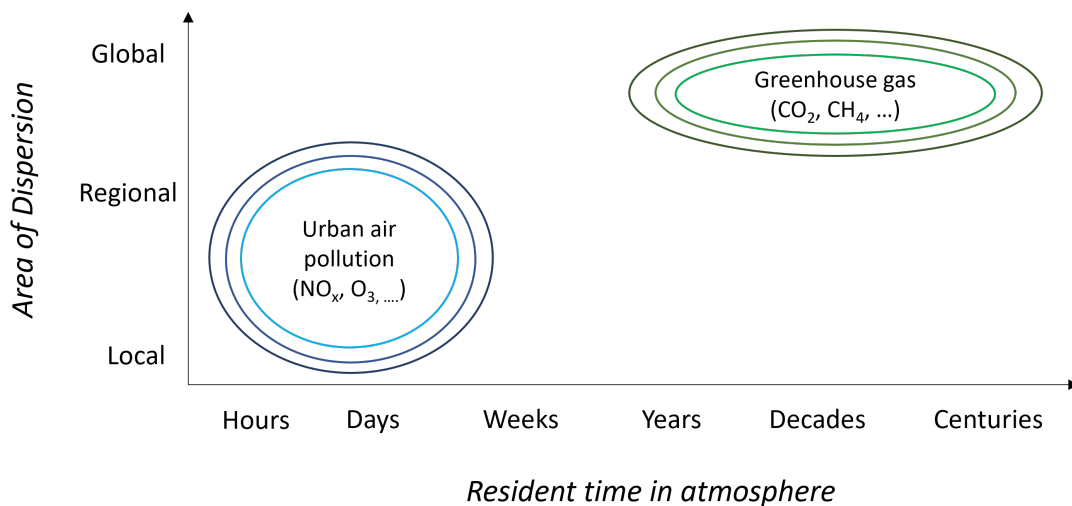


Figure 1.1. Resident time in atmosphere and the area of dispersion of air pollution and GHGs

321 mitigating the impact of climate change involves a significant reduction in GHGs
 322 emissions. One highly effective avenue to achieve this reduction is by enhancing
 323 the capacity of terrestrial carbon sequestration, primarily through the preserva-
 324 tion and restoration of forests. Notably, the terrestrial CO₂ sink is estimated to
 325 offset fossil CO₂ emissions by 35% during the 2010-2019 period (Friedlingstein
 326 et al., 2020; Wang et al., 2022), by 29% during the 2012-2021 period (Friedling-
 327 stein et al., 2022), surpassing the ocean, which is projected to remove 26% of
 328 fossil-fuel-derived CO₂ (Friedlingstein et al., 2022). The substantial global ter-
 329 restrial carbon flux, known as terrestrial gross primary production (GPP), plays
 330 a substantial role in diminishing anthropogenic CO₂ emissions (Beer et al., 2010).
 331 This comprehensive approach not only aids in reducing GHGs levels but also fos-
 332 ters biodiversity and fortifies ecosystem resilience in the face of climate change.

333 While addressing air pollution and GHGs may involve varying levels of col-
 334 laboration from regional to global scale, the responsibility for monitoring these
 335 chemical pollutants is evidently at the local government level. Hence, the neces-
 336 sity of an integrated digital earth platform for air pollution and GHGs monitoring
 337 and carbon neutrality roadmaps modelling, as discussed by (Fukui et al., 2021),
 338 is evident for local policymakers to formulate appropriate future policies.

339 1.2 Problem statement

340 Based on the context of the study described above, this research focuses on three
341 primary themes. The first one directly relates to regional lessons learned from
342 the impact of intervention events, such as the effects of the COVID-19 lockdown
343 on future air pollution policies. The second issue pertains to existing challenges
344 in accurately quantifying the global and local capacity of terrestrial ecosystem
345 carbon flux variables, such as GPP. Lastly, the study concentrates on developing
346 a digital earth platform capable of integrating GHGs emissions monitoring
347 and carbon neutrality roadmaps modelling at the local level, aiming to aid local
348 policymakers in formulating future policies.

349 Concerning the first topic, spanning the period from 2019 to 2022, the world
350 has witnessed two significant intervention events that have profoundly influenced
351 human anthropogenic activities both at local and, to some extent, global levels.
352 The initial event was the COVID-19 lockdown in 2020, followed by the ongoing
353 armed conflict between Russia and Ukraine. These occurrences have led to ex-
354 pected alterations in local and regional air quality, environmental factors, and
355 GHGs emissions. Despite numerous prior studies exploring the impact of the
356 COVID-19 lockdown in many countries, there is considerable variability in re-
357 sults across study areas, as well as in the adopted analytical approaches (Shi
358 et al., 2021; Grange et al., 2021). At the time of our research, to the best of our
359 knowledge, there were limited studies that had thoroughly and comprehensively
360 examined the impact of the COVID-19 lockdown on air pollution in metropoli-
361 tan areas of Japan. Additionally, there was a scarcity of studies investigating
362 the combined impact of the COVID-19 lockdown and the armed conflict on air
363 pollution in Ukraine, along with the valuable lessons learned for future policy
364 considerations.

365 Regarding the second topic, the estimation of GPP involves a range of meth-
366 ods, including the utilization of dynamic global vegetation models (DGVMs)
367 such as those applied in the TRENDY project (Sitch et al., 2015; Le Quéré et al.,
368 2018), as well as upscaling from measurements acquired through eddy covariance
369 (EC) flux towers and satellite observations (Jung et al., 2019; Zeng et al., 2020).
370 However, all these approaches rely on categorizations known as plant functional
371 types (PFTs) to gauge ecosystem productivity (Poulter et al., 2011, 2015; Lin

et al., 2021; Guo et al., 2023; Yan et al., 2023). Discrepancies in PFT maps can introduce significant uncertainties into GPP estimations, as well as other climate-relevant variables, at both regional and global scales (Poulter et al., 2011). In the tropical region, specifically, challenges arise due to the sparse distribution of EC sites, the high species richness of trees, and the complex vertical structure of tropical rainforests (Montgomery and Chazdon, 2001), making it challenging to accurately quantify the seasonality of carbon fluxes (Xu et al., 2015). Recently, there has been a growing adoption of timeseries (TS) foundation models that employ a transformer-inspired architecture for addressing timeseries problems and representation learning. Noteworthy examples include the MVTS Transformer (Zerveas et al., 2021), Informer (Zhou et al., 2021), Autoformer (Wu et al., 2021), and Fedformer (Zhou et al., 2022). The integration of the Transformer architecture is expected to enhance the modeling of seasonality based on the timeseries representation. However, as far as our knowledge extends, its application in the task of upscaling global terrestrial carbon fluxes remains limited.

The widely recognition of climate change's significance (Primack et al., 2009; Watanabe and Kume, 2009; Ogawa-Onishi and Berry, 2013; Shibuya and Croxford, 2016) is driving an accelerated momentum toward achieving Carbon Neutrality (CN) in local Japanese governments (Nakazawa et al., 2023). Amidst a growing demand for GHGs emissions measurement in corporations (Kauffmann et al., 2012), 991 local governments, including Tokyo, Kyoto, and Yokohama, commit to net-zero carbon emissions by 2050 (Ministry of the Environment, 2023). Achieving this requires comprehensive sector-specific risk analysis and emissions calculation. While local governments integrate map information through Geographic Information Systems (GIS) (Nikkei, 2023), separate GIS systems for national energy consumption and power generation as well as forest sinks (local terrestrial carbon fluxes) pose challenges for policymakers (Tohoku University, 2023; Asanobu, 2023; Planning and Regional Policy Bureau, 2023). An integrated WebGIS platform facilitates monitoring and modelling, enabling better understanding and implementation of renewable energy and emission reduction measures.

403 1.3 Research questions

404 Based the prior problem statements, I am seeking answers to the following ques-
405 tions:

406 **Evaluation of intervention events on regional air quality and policy
407 implications**

- 408 • 1. What was the influence of the COVID-19 lockdown and the armed con-
409 flict on air quality in Ukraine, and how can this information offer evidence
410 and recommendations for future policies?
- 411 • 2. In what ways did the COVID-19 lockdown influence air quality in Japan,
412 and how can this information serve as evidence and provide suggestions for
413 future policies?

414 **Improved quantification of global terrestrial carbon fluxes**

- 415 • 3. What methodologies can be employed to improve PFTs mapping perfor-
416 mance in data-sparse regions?
- 417 • 4. Can the utilization of updated PFT maps and Transformer-based models
418 enhance the accuracy of global terrestrial carbon flux estimates?

419 **Tracking carbon neutrality progress at local level**

- 420 • 5. How can we efficiently monitor fossil fuels GHGs emissions as well as
421 the capacity of terrestrial forest carbon fluxes, enabling the development
422 of efficient carbon neutrality roadmaps as well as tracking progress at the
423 local level?

424 1.4 Outline of the thesis and scope

425 The thesis is structured into six chapters, as depicted in Figure 1.2. Chapter 2
426 provides the background on air pollution, GHGs, as well as the interrelationship
427 between these factors themselves and with Sustainable Development Goals (SDGs).
428 This chapter also details how this thesis utilizes the digital earth systems approach
429 in each experiment.

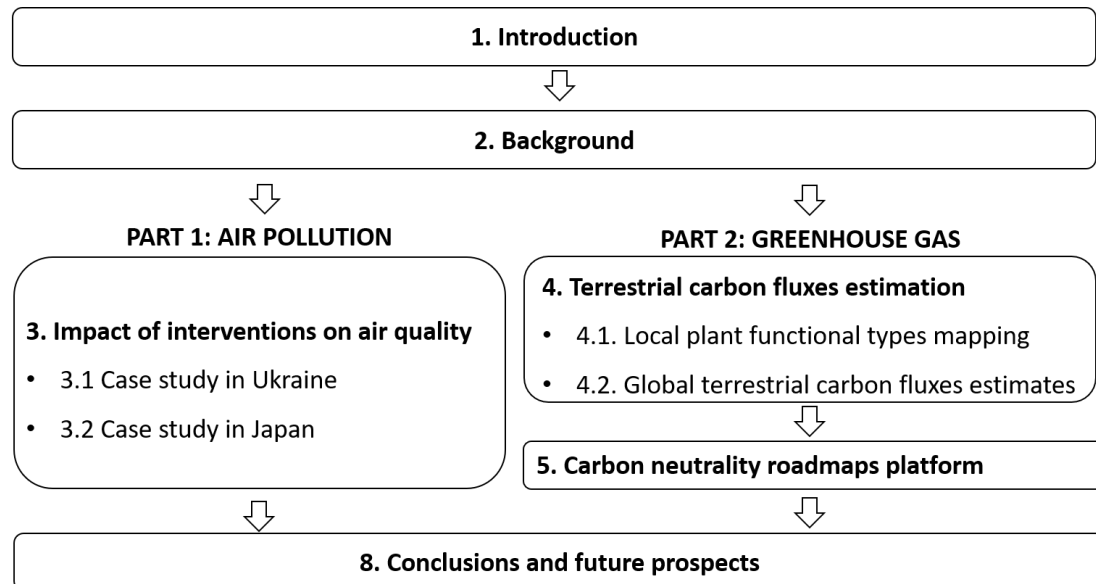


Figure 1.2. Outline of this thesis

430 In Chapter 3, section 3.1, I discuss the examination of fluctuations in nitrogen
 431 dioxide (NO_2) levels in Ukraine during two noteworthy periods: the COVID-
 432 19 pandemic lockdown in 2020 and the armed conflict with Russia in 2022. In
 433 Chapter 3, section 3.2, I provide an assessment of the impact of alterations in
 434 anthropogenic activities during the COVID-19 pandemic (spanning from April 7
 435 to December 31) on NO_2 , O_3 , CO , and CH_4 levels in metropolitan areas of Japan
 436 in 2020.

437 In Chapter 4, section 4.1, I introduced an approach to monitor local forest
 438 utilization towards SDGs, focusing on aspects such as PFTs and forest age in
 439 data-scarce regions of Japan. In Chapter 4, section 4.2, I assess the effectiveness
 440 of utilizing timeseries representation, particularly leveraging recently updated
 441 PFTs and a model based on Transformer architecture, to more accurately quantify
 442 seasonal patterns and long-term trends in global terrestrial carbon fluxes.

443 In Chapter 5, I designed a prototype of digital earth platform that facilitates the
 444 visualization and support of CO_2 monitoring and the carbon neutrality roadmaps
 445 modelling at the municipality level in Japan.

446 Finally, in Chapter 6, I summarize the key findings and contributions of the
 447 study and discuss future prospects.

⁴⁴⁸ 2 Background

⁴⁴⁹ 2.1 Air pollution

⁴⁵⁰ 2.1.1 Introduction

⁴⁵¹ Air pollution stands as a critical environmental issue, significantly impacting hu-
⁴⁵² man health, ecosystems, and climate patterns. According to the World Health
⁴⁵³ Organization (WHO) in 2020, approximately seven million deaths worldwide were
⁴⁵⁴ attributed to air pollution (WHO, 2020). Air pollutants such as nitrogen oxides
⁴⁵⁵ ($\text{NO}_x = \text{NO} + \text{NO}_2$), carbon monoxide (CO), ground-level ozone (O_3), sulfur
⁴⁵⁶ dioxide (SO_2) and particulate matter (PM), are directly emitted from natural or
⁴⁵⁷ anthropogenic activities or through atmospheric photochemical reactions. Some
⁴⁵⁸ pollutants are emitted alongside carbon dioxide (CO_2) during combustion pro-
⁴⁵⁹ cesses, while others act as short-lived climate forcers, directly or indirectly in-
⁴⁶⁰ fluencing climate change by affecting the global radiation budget (Chen et al.,
⁴⁶¹ 2021b). Moreover, ozone can negatively affect crop yield, presenting potential
⁴⁶² challenges to future food security (Avnery et al., 2011a,b; Chuwah et al., 2015;
⁴⁶³ Tai and Martin, 2017).

⁴⁶⁴ Nitrogen dioxide (NO_2) is a particularly worrisome pollutant due to its adverse
⁴⁶⁵ effects on human health (Hamra et al., 2015). Short-term exposure to elevated
⁴⁶⁶ NO_2 concentrations can induce airway inflammation, increase susceptibility to
⁴⁶⁷ respiratory infections and allergies, and worsen pre-existing lung or heart con-
⁴⁶⁸ ditions (Bono et al., 2016; Kelly and Fussell, 2011). Furthermore, NO_x induces
⁴⁶⁹ environmental changes by altering soil chemistry and biodiversity through nitro-
⁴⁷⁰ gen deposition via dry and wet processes (Bobbink et al., 2010). Additionally,
⁴⁷¹ NO_x plays a crucial role as a precursor to tropospheric ozone (O_3), alongside
⁴⁷² volatile organic compounds (VOCs) (Akimoto and Tanimoto, 2022). NO_x , CO,
⁴⁷³ and non-methane volatile organic compounds (NMVOCs) influence the lifetime

474 of methane (CH_4) by affecting the atmospheric mixing ratio of hydroxyl rad-
475 icals (OH) (Akimoto and Tanimoto, 2022), which serve as a primary sink for
476 CH_4 (Turner et al., 2019). Both O_3 and CH_4 are short-lived climate pollutants
477 (SLCPs) that contribute to positive radiative forcing, thereby exacerbating global
478 warming (Akimoto and Tanimoto, 2022).

479 Global NO_x emissions primarily result from fossil fuel combustion in the en-
480 ergy, industry, and transportation sectors. In 2017, the energy generation (22%),
481 industry (15%), and on-road transportation (23%) sectors collectively accounted
482 for nearly 60% of global NO_x emissions. Notably, these sectors significantly con-
483 tributed to emissions from coal combustion, with the energy and industry sectors
484 alone contributing over 46% of the total emissions. Furthermore, the combined
485 combustion of liquid fuels (oil) and natural gas constituted 100% of on-road NO_x
486 emissions (McDuffie et al., 2020). Examining historical emissions from 1970 to
487 2017 documented in the CEDS database (McDuffie et al., 2020), global NO_x
488 emissions peaked between 2011 and 2013, followed by a subsequent 7% decrease
489 by 2017. This decline was primarily attributed to more stringent emission stan-
490 dards implemented in North America and Europe since 1992 and in China since
491 2013 (McDuffie et al., 2020; Zheng et al., 2018). Nevertheless, within the same
492 timeframe, global NO_x emissions from the energy and industry sectors experi-
493 enced a substantial increase, nearly multiplying six-fold between 1970 and 2011.
494 This upsurge was predominantly fueled by regional increments in China, India,
495 the Other Asia/Pacific region, and several African countries. The subsequent
496 reduction in emissions between 2011 and 2017 was mainly a result of stringent
497 emission control policies in China, specifically aimed at coal-fired power plants
498 and industrial coal use (Zheng et al., 2018; Liu et al., 2015).

499 In Japan, measures have been in place since the 1950s to control air pollutant
500 emissions from various stationary and mobile sources (Ito et al., 2021). An anal-
501 ysis of air pollution trends in Japan from 1970 to 2018 (Ito et al., 2021; Kannari
502 and Kokuryo, 2013; Wakamatsu et al., 2013) demonstrates a consistent decline
503 in the concentrations of $\text{PM}_{2.5}$, NO_2 , and SO_2 , indicating the direct effectiveness
504 of human-induced emission control strategies in mitigating pollution levels. The
505 decline in pollutant concentrations corresponds with specific measures taken to
506 address emissions. For instance, the decrease in NO_x levels may be attributed

507 to the implementation of more stringent regulations governing vehicle emissions.
508 Likewise, the decrease in SO₂ levels may be associated with the widespread adop-
509 tion of marine fuels with lower sulfur content, highlighting the direct impact of
510 focused interventions on reducing pollution. However, there has been a persistent
511 year-on-year rise in ozone concentrations across broad areas in Japan, including
512 rural zones unaffected by direct anthropogenic sources of air pollutants (Ito et al.,
513 2021).

514 **2.1.2 Impact of weather variations on air pollution
515 changes**

516 Air pollution levels are influenced not only by emissions themselves but also by
517 meteorological conditions. The lifetime of NO₂ is strongly influenced by meteo-
518 rological parameters and photochemical reactions (Barré et al., 2021) and varies
519 seasonally (Dragomir et al., 2015; Kendrick et al., 2015). During winter, photo-
520 chemical reaction activity is reduced, resulting in a longer lifetime of the NO₂.
521 Additionally, seasonal variations in NO₂ concentration are controlled by disper-
522 sion processes which are significantly affected by changes in boundary layer height
523 (BLH), wind speed and direction patterns due to temperature inversions in sum-
524 mer and winter (Barré et al., 2021; Kendrick et al., 2015). Changes in seasonal
525 meteorological patterns, such as temperature and radiation, have also been doc-
526 umented as factors influencing local variations in ozone in China (Yang et al.,
527 2019; Yu et al., 2021).

528 Earlier research underscored the substantial impact of meteorological fluctua-
529 tions on ozone levels in Japan. Specifically, (Kurokawa et al., 2009) emphasized
530 the sensitivity of springtime ozone variation in Japan to outflows from continental
531 Asia. They identified a correlation between springtime ozone and the El Niño-
532 Southern Oscillation, suggesting a relationship where higher and lower springtime
533 ozone levels are associated with La Niña and El Niño, respectively. The summer
534 of 2019 saw widespread instances of elevated ozone concentrations across Japan,
535 as reported by (Fukunaga et al., 2021; Ito et al., 2021). According to (Fukunaga
536 et al., 2021), the favorable conditions for increased ozone levels during this pe-
537 riod were linked to clear skies and higher temperatures. They proposed that a

538 migrating anticyclone might have transported ozone and its precursors eastward,
539 contributing to this phenomenon. This underscores the significance of not only
540 examining the direct impact of air pollution control measures but also under-
541 standing the role of meteorological conditions in shaping air pollution dynamics.
542 Investigating these interdependencies could significantly improve our ability to
543 formulate more effective measures for mitigating air pollution.

544 2.2 Greenhouse gases (GHGs)

545 2.2.1 Fossil fuel GHGs

546 GHGs are atmospheric gases that trap heat and contribute to warming the Earth.
547 The major ones include carbon dioxide (CO_2), methane (CH_4), nitrous oxide
548 (N_2O) and Fluorinated gases (F-gases) like hydrofluorocarbons (HFCs), perfluoro-
549 rocarbons (PFCs), and sulfur hexafluoride (SF_6). These gases persist in the at-
550 mosphere for various durations, ranging from a few years to thousands of years.
551 They reach a well-mixed state, meaning their concentrations worldwide remain
552 relatively consistent regardless of their sources. These gases differ significantly in
553 their impact on atmospheric warming.

554 GHGs originate from diverse sources, encompassing both natural processes and
555 human activities. Carbon dioxide is naturally present in the atmosphere as part
556 of the Earth's carbon cycle, which is consistently exchanged carbon among the
557 atmosphere, oceans, soil, plants, and animals. Human activities are altering the
558 carbon cycle—both by adding more carbon dioxide to the atmosphere and by influ-
559 encing the ability of natural sinks, like forests and soils, to remove and store car-
560 bon dioxide from the atmosphere. While carbon dioxide emissions originate from
561 various natural sources, human-induced emissions have been primarily responsi-
562 ble for the substantial increase in GHGs in the atmosphere since the Industrial
563 Revolution commenced around 1750 (Chen et al., 2021b). In 2019, emissions in-
564 cluded approximately $45 \pm 5.5 \text{ GtCO}_2$ emissions, $11 \pm 3.2 \text{ GtCO}_2\text{-eq}$ of methane
565 (CH_4), $2.7 \pm 1.6 \text{ GtCO}_2\text{-eq}$ of nitrous oxide (N_2O) and $1.4 \pm 0.41 \text{ GtCO}_2\text{-eq}$ of
566 fluorinated gases (F-gases) (Dhakal et al., 2022). The primary source of carbon
567 dioxide stems from the combustion of fossil fuels within energy conversion systems

like boilers in electric power plants, engines in aircraft and automobiles, and in cooking and heating within homes and businesses, accounting for approximately 64% of emissions (Dhakal et al., 2022). Fossil fuels also play a significant role in methane emissions, the second-largest contributor to global warming. While most GHGs originate from fossil fuel combustion, about one quarter comes from land-related activities like agriculture (mainly methane and nitrous oxide) and deforestation (mainly carbon dioxide). Additional emissions come from industrial processes (primarily carbon dioxide, nitrous oxide, and F-gases), as well as municipal waste and wastewater (mainly CH₄) (Dhakal et al., 2022). The estimated global net anthropogenic GHGs emissions for the year 2019 reached approximately 59 ± 6.6 GtCO₂-eq, marking a 12% increase compared to the levels seen in 2010 and a significant 54% surge compared to the figures from 1990 (Dhakal et al., 2022). Among these emissions, the dominant share and escalating growth came from CO₂ emissions originating from fossil fuels combustion and industrial processes, followed closely by methane emissions. Notably, the highest relative growth occurred in F-gases, albeit starting from minimal levels in 1990. During 2010–2019 period, the average annual GHGs emissions surpassed those of any preceding decade on record. However, the rate of growth between 2010 and 2019 ($1.3\% \text{ yr}^{-1}$) was comparatively lower than that observed between 2000 and 2009 ($2.1\% \text{ yr}^{-1}$). In 2019, a substantial 78% of global GHGs emissions stemmed from energy, industry, transport, and building sectors combined, while 22% originated from agriculture, forestry, and other land use (Dhakal et al., 2022).

2.2.2 Terrestrial carbon fluxes

Terrestrial ecosystems play a crucial role in mitigating global warming by serving as a persistent carbon sink, actively absorbing and storing excess carbon dioxide from the atmosphere (Pan et al., 2011). Over the period from 2010 to 2019, the terrestrial CO₂ sink is estimated to offset fossil CO₂ emissions by 35%, surpassing the ocean, which is projected to remove 26% of fossil-fuel-derived CO₂ (Friedlingstein et al., 2020; Wang et al., 2022). The substantial global carbon flux, known as terrestrial gross primary production (GPP), significantly contributes to the reduction of anthropogenic CO₂ emissions (Beer et al., 2010).

As presented in Figure 2.1, we illustrate that gross primary production (GPP)

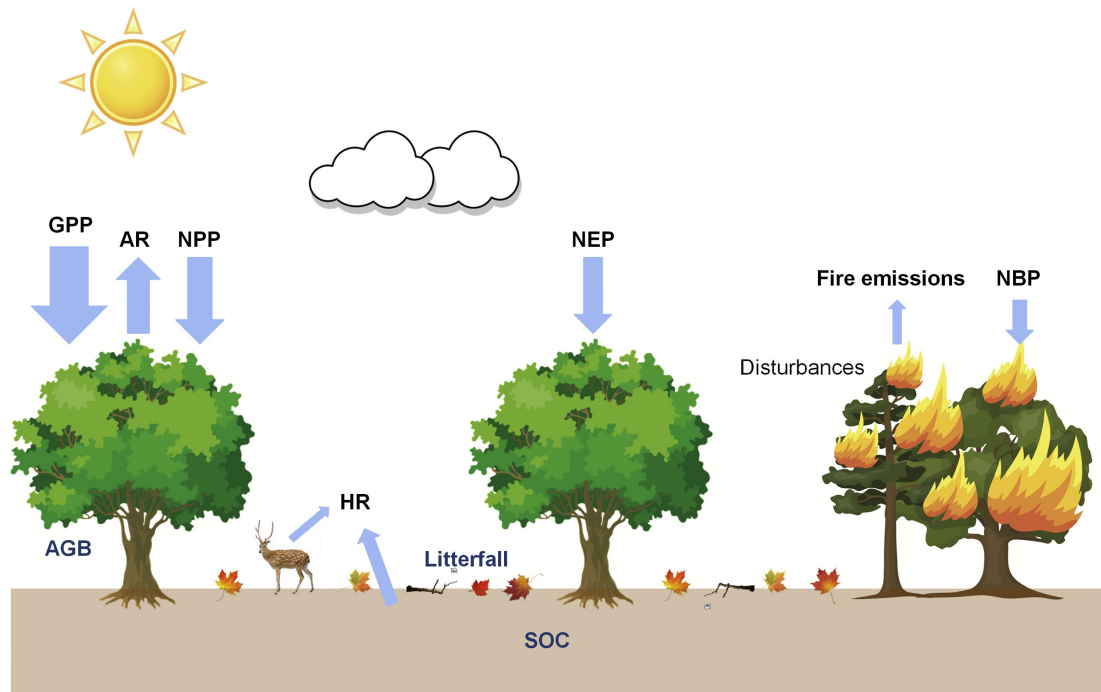


Figure 2.1. Terrestrial carbon cycle (Xiao et al., 2019a)

represents the total carbon sequestered by terrestrial ecosystems, serving as the foundation for food, wood, and fiber production and thereby holding significant implications for human well-being (Xiao et al., 2019a). A portion of the absorbed carbon is released back into the atmosphere through plant autotrophic respiration (AR). The disparity between GPP and AR is Net Primary Production (NPP). Soil organic carbon (SOC) accumulates from plant materials, such as leaves and branches, that fall to the ground, also known as litterfall. The size of the SOC pool is impacted by carbon inputs from litterfall and root mortality/exudation, as well as carbon release from decomposition, referred to as heterotrophic respiration (HR) (Liu et al., 2011). AR and HR collectively constitute ecosystem respiration (RECO). Net Ecosystem Production (NEP) is the difference between GPP and RECO.

Processes like deforestation, harvesting, and fires can result in carbon loss, with the net ecosystem carbon balance referred to as Net Biome Production (NBP). Disturbances, crucial ecosystem processes, impact carbon cycle dynamics. Wildfires, for example, lead to immediate carbon transfer from ecosystems to the

atmosphere. Fires, along with other disturbances such as insect and disease outbreaks, droughts, severe storms, and harvesting, can cause substantial effects on GPP and respiration, with these impacts persisting for decades as ecosystems recover (Xiao et al., 2019a).

Estimating GPP and RECO encompasses diverse methods, including the simulation of DGVMs similar to those utilized in the TRENDY project (Sitch et al., 2015; Le Quéré et al., 2018), as well as the upscaling from measurements acquired through eddy covariance (EC) flux tower and satellite observations (Jung et al., 2019; Zeng et al., 2020). Nevertheless, these methods depend on the use of plant functional types (PFTs) to estimate ecosystem productivity (Poulter et al., 2011, 2015; Lin et al., 2021; Guo et al., 2023; Yan et al., 2023). Discrepancies in PFTs data can introduce notable uncertainties into fluxes estimations both regionally and globally (Poulter et al., 2011). Specifically, in tropical regions, challenges arise due to the sparse distribution of ground stations, the high species richness of trees, and the intricate vertical structure of tropical rainforests (Montgomery and Chazdon, 2001). These factors make it challenging to precisely quantify the seasonality of carbon fluxes (Xu et al., 2015).

2.3 Relationship between air pollution and fossil fuel CO₂

CO₂ is considered one of the most important GHGs, which has played a significant role in the current and future global climate change. Meanwhile, NO₂ emerges as a particularly concerning pollutant due to its adverse effects on human health and ecosystem. Their atmospheric concentration has considerably increased since the Industrial Revolution and is attributed mostly to anthropogenic sources, especially fossil-fuel combustion. While CO₂ emission reduction has become a goal of international agreements such as the Kyoto Protocol (Protocol, 1997) and the Paris Agreement on Climate Change (<https://unfccc.int/process-and-meetings/the-paris-agreement>), the air pollution control measures reducing NO₂ emission have been implemented in Northern America, Europe and China to improve local air quality. Therefore, accurate knowledge of fossil fuel CO₂ and NO₂ emissions as well as their trends pose an

importance both for climate prediction and mitigation policy purposes.

Fossil fuel combustion is mainly contributor of CO₂ and co-emitter NO₂ emission. These emissions are driven by activity such as fuel consumption, but differ by their relative proportion (i.e., emission factor)(Miyazaki and Bowman, 2023). Global fossil fuel CO₂ emission inventories (e.g. CDIAC (Andres et al., 2012), ODIAC (Oda and Maksyutov, 2011; Oda et al., 2018), EDGAR (Crippa et al., 2020), FFDAS (Asefi-Najafabady et al., 2014), and CEDS (Hoesly et al., 2018)) are compiled from available national emission inventory. Fossil CO₂ emissions are estimated by combining economic activity data and emissions factors, with different levels of methodological complexity (tiers) or approaches (e.g., IPCC Guidelines for National Greenhouse Gas Inventories). Various organizations or groups offer estimations of fossil CO₂ emissions, with each dataset having slightly different settings in system boundaries, methods, activity data, and emissions factors (Andrew, 2020). This “bottom-up” approach based on available statistical information regarding economic activities and corresponding technologies. Such error and bias information can cause the an uncertainty that is generally within ±10% among these inventories at global scale, however, the uncertainty in emission estimates significantly varied in different countries, from 10% in developed countries (Friedlingstein et al., 2019), but larger uncertainty in rapidly developing countries such as 8% to 24% for China (Han et al., 2020; Marland, 2008), to more than 50% for least developed countries (Andres et al., 2016; Friedlingstein et al., 2019; Oda et al., 2018). For the case in China, large variations between nine emission inventories were largely due to the different emission factors related to coal quality and activity data (Han et al., 2020; Miyazaki and Bowman, 2023). Variations in these approaches, combined with errors in spatial allocation utilizing remote sensing source, can result in significant discrepancies in local estimates for a city or municipality (Oda et al., 2019; Hutchins et al., 2017). Furthermore, these emissions data are mostly self-reported by national governments, which can take several years to produce (Marland, 2008). Air quality emission inventories, like fossil fuel CO₂ emission, use similar methods to determine fuel consumption and sector-based emission factors, and consequently incur substantial latency in their reporting (Miyazaki and Bowman, 2023).

Recently, the "top-down" method has emerged as an additional approach for

estimating fossil fuel CO₂ emissions, driven by advancements in satellite observations and data assimilation frameworks. This method utilizes direct CO₂ observations obtained from satellite imagery to estimate CO₂ emissions. However, existing satellites, such as the Greenhouse gases Observing SATellite (GOSAT) and Orbiting Carbon Observatory-2 (OCO-2), were designed to focus on the spatiotemporal distribution of natural carbon fluxes on regional scales rather than to quantify anthropogenic emissions (Nassar et al., 2017; Yang et al., 2023). Consequently, the limitations in the spatial and temporal resolution of these CO₂ observations hinder their capacity to estimate CO₂ emissions at urban or city levels.

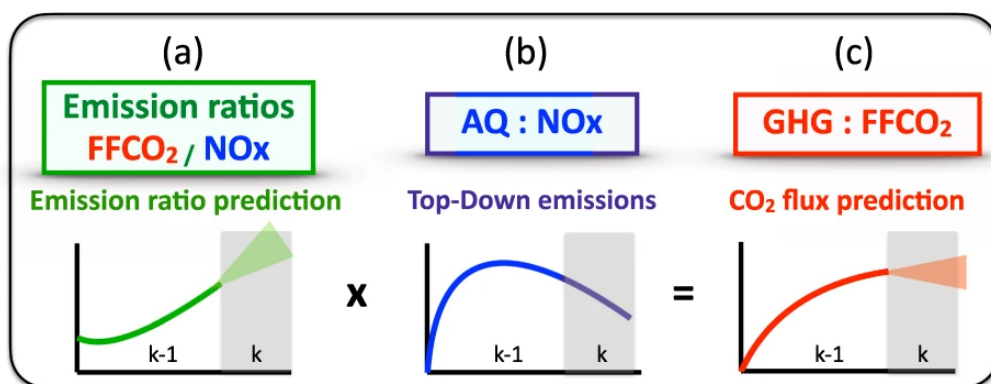


Figure 2.2. Changes in CO₂/NO_x emission ratio for the past ($t=k-1$) are estimated using top-down NO_x emissions and bottom-up fossil fuel CO₂ (FFCO₂) inventories (a and b). The recent ($t=k$) CO₂/NO_x level is predicted using time-series forecasting model based on data in the past ($t=k-1$) to predict (c) the CO₂ at the recent time ($t=k$) (Miyazaki and Bowman, 2023).

In contrast, currently available satellite-derived NO₂ observations, like OMI or TROPOMI, demonstrate more advanced capabilities with higher resolutions in spatiotemporal aspects. They have the potential to function as instruments in deducing fossil fuel CO₂ emissions at the local level. Hence, an indirect "top-down" approach utilizes proxies such as NO₂ observations, leveraging their co-emission with fossil fuel CO₂ combustion. This indirect method proves advantageous in predicting fossil fuel CO₂ emissions, monitoring their temporal fluctuations while distinguishing them from biogenic sources of CO₂ emissions itself (Ciais et al.,

698 2014; Goldberg et al., 2019). Satellite-based NO₂ observations, combined with
699 NO_x:CO₂ inventory ratios, have been instrumental in estimating CO₂ emissions
700 indirectly (see Figure 2.2). These approaches have been applied at national scales
701 in countries such as the US, Europe, China, and India (Konovalov et al., 2016;
702 Zheng et al., 2020; Miyazaki and Bowman, 2023) and at city levels, such as in
703 Wuhan (Zhang et al., 2023a) Buenos Aires, Melbourne, and Mexico City (Yang
704 et al., 2023). However, such analyses have not yet been conducted either at
705 the national or municipal levels in Japan. Conducting studies employing these
706 methodologies both at national and cities levels in Japan could provide supple-
707 mental independent datasets. These datasets would serve to refine and evalu-
708 ate "bottom-up" inventories and to assess the efficacy of current climate change
709 mitigation strategies related to reducing fossil fuel CO₂ emissions, contributing
710 insights from local to global scales. Therefore, such investigations are necessary
711 and could offer valuable information to refine our understanding of CO₂ emissions
712 and strategies for mitigating climate change.

713 2.4 Air pollution, GHGs and SDGs

714 2.4.1 Air pollution and SDGs

715 While air pollution is intricately linked to almost all other SDGs, encompassing
716 areas such as health, water, energy, economic growth, employment, infrastructure,
717 cities, sustainable consumption and production, climate, water, and land, its
718 significance is not clearly emphasized in the structure of the SDGs, as noted by
719 (Elder, 2016). To be specific, air pollution is explicitly addressed in three goals,
720 with one target assigned to each:

- 721 • **3.9 (Health):** By 2030, substantially reduce the number of deaths and
722 illnesses from hazardous chemicals andair, water and soil pollution and
723 contamination.
- 724 • **11.6 (Cities):** By 2030, reduce the adverse per capita environmental im-
725 pact of cities, including by payingspecial attention to air quality and mu-
726 nicipal and other waste Management.

- 727 • **12.4 (Responsible consumption and production):** By 2020, achieve
 728 the environmentally sound management of chemicals and all wastes through-
 729 out their lifecycle, in accordance with agreed international frameworks, and
 730 significantly reduce their release to air, water and soil in order to minimize
 731 their adverse impacts on human health and the environment.

	Reducing air pollution can help families become healthier, save on medical expenses, and improve productivity.		Power generation, industry and transportation are large contributors to air pollution. A new focus on decreasing energy consumption and on improving sustainable and public transportation could progressively reduce pollution.
	Air pollution can cause crop damage and affect food quality and security.		Urban areas significantly contribute to air pollution. Making cities sustainable could progressively improve the air quality.
	Air pollution poses a major threat to human health. It is linked to respiratory infection and cardiovascular disease. It causes increases in population morbidity and mortality.		Chemicals released into the air increase air pollution and contribute to harmful effects on human health. Responsible production and consumption could help to reduce these harmful chemicals.
	Pollutants such as sulfur dioxide (SO_2) and nitrogen oxides (NO_x) from open fires and the combustion of fossil fuels mix with precipitation causing harmful acid rain that can compromise water quality.		Combustion of fossil fuels plays a key role in the process of climate change, which places food, air and water supplies at risk, and poses a major threat to human health.
	Electricity from renewable energy rather than fossil fuels offers significant public health benefits through a reduction in air pollution.		Deposition of air pollutants on water may negatively affect its quality and life under water. It can lead to eutrophication and acidification of fresh water bodies, and accumulation of toxic metals and Persistent Organic Pollutants (POPs) in fresh and marine waters.
	Air pollution impacts on health, crop and forest yields, ecosystems, the climate and the built environment, with consequences for productivity and economic growth. Ambient and indoor air pollution also has negative effects on the working environment and its safety.		Emissions from combustion of fossil fuels mixed with precipitation cause acid rains that pose a major threat to forests and ecosystems.

Figure 2.3. How air pollution relates to the SDGs (Ortiz et al., 2017)

732 In Figures 2.3 and 2.4, I illustrate the connection between air pollution and
 733 the Sustainable Development Goals (SDGs) using insights from the earlier study
 734 by (Ortiz et al., 2017). Additionally, I depict the relation between SDGs and the
 735 drivers and impacts of air pollution, as highlighted in the work by (Elder, 2016).

- 736 • Goal 1 - No Poverty: Individuals and families experiencing poverty are more

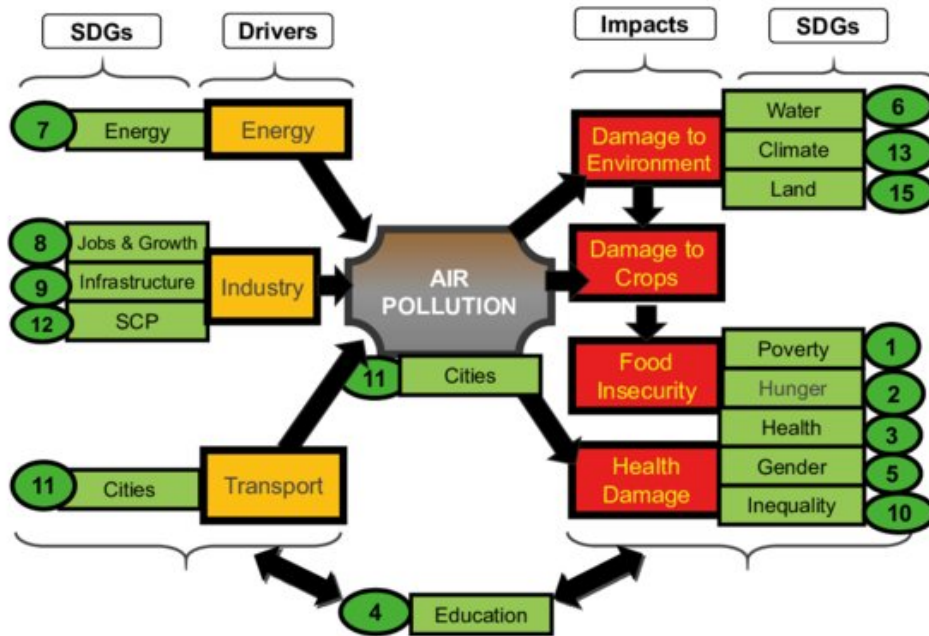


Figure 2.4. Relation of SDGs to air pollution drivers and impacts (Elder, 2016)

737 susceptible to the adverse effects of air pollution, particularly those reliant
 738 on outdoor labor, such as sulphur mining in active volcanoes.

- 739 • Goal 2 - Zero Hunger: Air pollution has the potential to diminish crop
 740 yields and agricultural productivity, as evidenced by studies like (Avnery
 741 et al., 2011a).
- 742 • Goal 3 - Health and Well-being: Air pollution poses a significant threat to
 743 human health (WHO, 2020), leading to heightened morbidity and mortality
 744 rates.
- 745 • Goal 4 - Education: There is an expectation that educating the population
 746 will contribute to the reduction of air pollution and its future impacts.
- 747 • Goal 5 - Gender equality: In certain countries, women, especially those
 748 exposed to indoor air pollution from cook stoves, are more likely to bear
 749 the brunt of air pollution.
- 750 • Goal 6 - Water and sanitation: Pollutants like SO₂ and NO₂, originating

751 from open fires and fossil fuel combustion, can mix with precipitation, re-
752 sulting in harmful acid rain that compromises water quality.

- 753 • Goal 7 - Energy: The anticipated adoption of renewable energy is expected
754 to significantly mitigate air pollution.
- 755 • Goal 8 - Economic growth: Air pollution affects health, agricultural pro-
756 duction, and ecosystems, with repercussions for productivity and economic
757 growth. Improving resource efficiency and decoupling economic growth from
758 environmental degradation should contribute to reducing air pollution.
- 759 • Goal 9 - Infrastructure, industrialization: Power generation, industry, and
760 transportation are major contributors to air pollution. Calls for sustainable
761 industrialization and infrastructure, with increased resource use efficiency
762 and the adoption of clean technologies, are expected to reduce air pollution.
- 763 • Goal 11 - Cities: Urban areas are significant contributors to air pollution.
764 Making cities sustainable could progressively enhance air quality.
- 765 • Goal 12 - Sustainable consumption and production: Sustainable produc-
766 tion, coupled with the removal of fossil fuel subsidies, would contribute to
767 reducing air pollution.
- 768 • Goal 13 - Climate action: Simultaneously reducing greenhouse gases and
769 air pollution requires a reduction in the combustion of fossil fuels, a key
770 contributor to climate change.
- 771 • Goal 14 - Oceans: Air pollution deposition on water may affect its quality
772 and marine life, leading to eutrophication and acidification of freshwater.
- 773 • Goal 15 - Biodiversity, Forest: Emissions from the combustion of fossil
774 fuels mixed with precipitation can cause acid rain, threatening forests and
775 ecosystems.
- 776 • Goal 16 - Peace: Recent armed conflicts in Ukraine and Russia, and Israel
777 and Palestine contribute to an increase in military vehicles and weapons,
778 causing air pollution and producing toxic dust.

779 2.4.2 Greenhouse gases and SDGs

780 GHGs are atmospheric gases that trap heat and contribute to warming the Earth
 781 causing climate change which pose a significant threat to SDGs, impacting vul-
 782 nerable populations in developing and less-developed countries with intensified
 783 extreme weather events such as drought and flood, resulting in inequalities and
 784 hindering progress toward many SDGs (as shown in Figure 2.5).

785 Effective action to combat climate change is articulated as the goal 13 (Climate
 786 Action), emphasizing mitigation, adaptation measures and building resilience to
 787 climate-related hazards. Actions to reduce climate risk can interact with other
 788 sustainable development objectives in positive ways (synergies) and negative ways
 789 (trade-offs) (Lee et al., 2023).

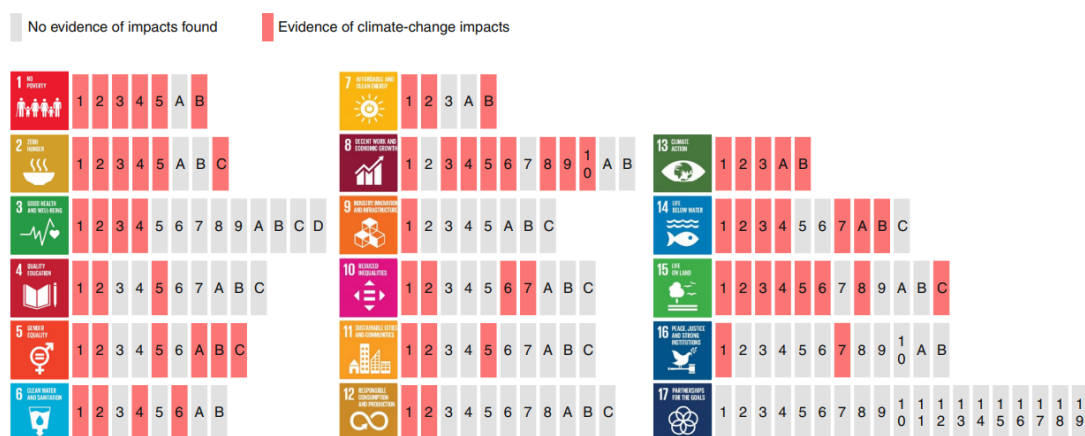


Figure 2.5. Impacts of climate change on the achievement of the SDGs
 (Fuso Nerini et al., 2019)

790 Figure 2.6 illustrate the potential synergies and trade-offs between the portfolio
 791 of climate change mitigation and adaptation options and the SDGs based on the
 792 IPCC report (Lee et al., 2023). An example of synergy can be observed in sustain-
 793 able forest management, which prevents deforestation emissions and sequesters
 794 carbon at a reasonable cost, aligning with various dimensions of sustainable de-
 795 velopment. For instance, it supports food security (SDG 2), clean water (SDG
 796 6), and ecosystem protection (SDG 15). Another instance of synergy arises when
 797 climate adaptation measures, such as coastal or agricultural projects, empower

Near-term adaptation and mitigation actions have more synergies than trade-offs with Sustainable Development Goals (SDGs)

Synergies and trade-offs depend on context and scale

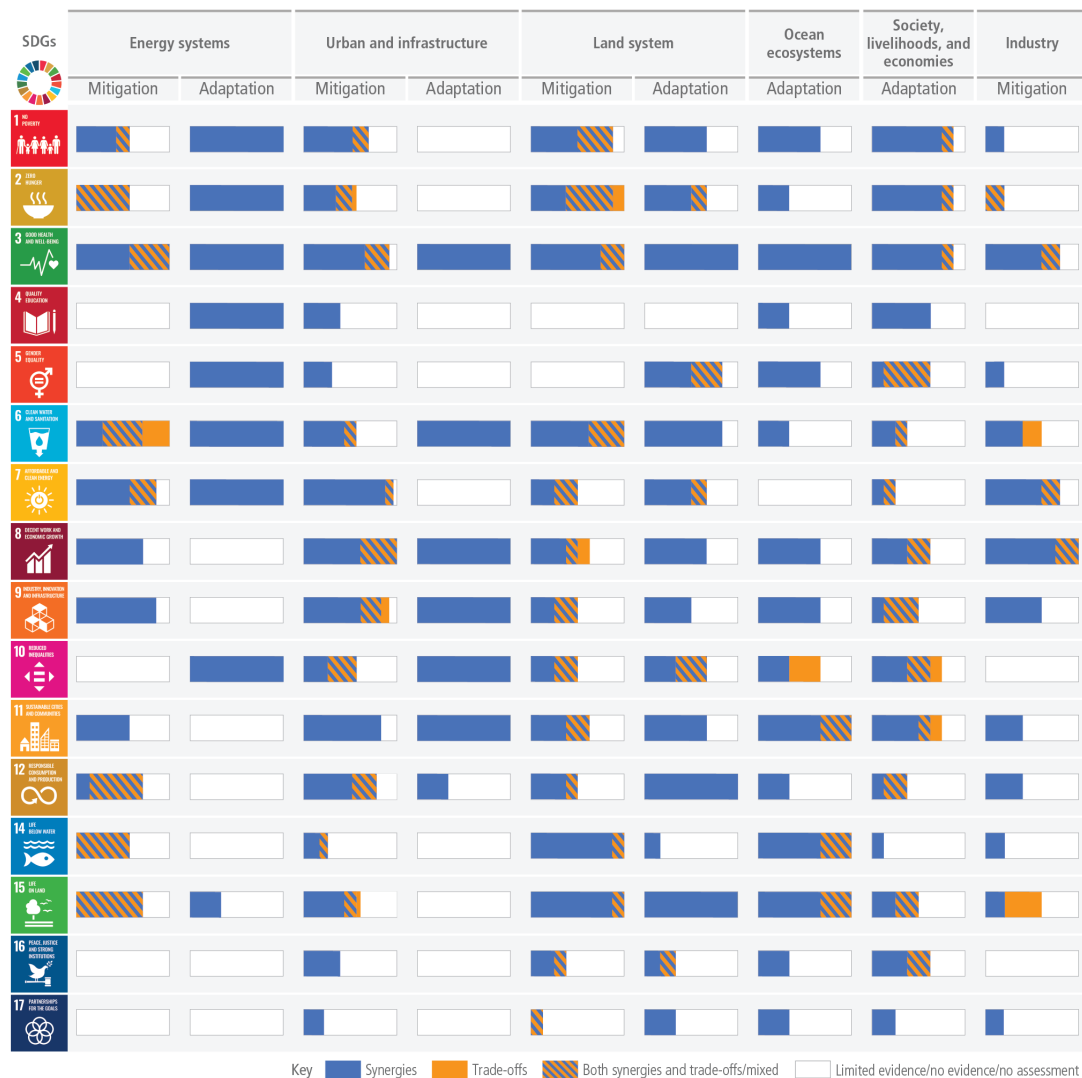


Figure 2.6. Synergies and trade-offs between the portfolio of climate change mitigation and adaptation options and the SDGs (Lee et al., 2023)

798 women, leading to improvements in local incomes, health, and ecosystems (IPCC,
799 2018).

800 Conversely, trade-offs might arise if ambitious climate change mitigation, aligned
801 with a 1.5°C target, alters land use in ways that are detrimental to sustainable
802 development. For instance, the conversion of natural forests, agricultural areas,
803 or lands under indigenous or local ownership into plantations for bioenergy pro-
804 duction could pose threats to food and water security, result in conflicts over land
805 rights, and contribute to biodiversity loss. Additionally, trade-offs may manifest
806 in certain regions if the transition from fossil fuels to alternative energy sources
807 lacks careful planning, affecting existing assets, workers, and infrastructure. Ef-
808 fective management strategies can mitigate these trade-offs, such as enhancing
809 bioenergy crop yields to reduce harmful land-use changes or providing retraining
810 opportunities for workers transitioning to lower carbon sectors (IPCC, 2018).

811 **2.4.3 Digital Earth approach and perspective**

812 The Digital Earth Systems approach is an approach that uses a bird's-eye view
813 of information infrastructure to reveal the overall picture. In this context, Digital
814 Earth has been introduced as a proposed platform for advancing the SDGs and
815 facilitating green transformations both globally and locally, incorporating crucial
816 SDGs variables (Fukui et al., 2021) with an illustration of the abstract architec-
817 ture of a digital earth system approach is shown in Figure 2.7. Essentially, we
818 have devised various methods to effectively and accurately monitor data from
819 diverse sources. Based on the monitored data from these sources, we formulate
820 future policies and roadmaps, which are considered as interventions. Once an
821 intervention is implemented, we monitor its performance and continually adjust
822 it to align with the trajectory of sustainable development through simulations.

823 In alignment with the core concept of the digital earth system, each experi-
824 ment in this study corresponds to a step in the digital earth system approach.
825 Firstly, we employed diverse data sources, including ground-based sensor network
826 measurements and space-based satellite observations, to analyze and quantify
827 the primary factors contributing to changes in air pollution during intervention
828 events. This phase can be likened to the monitoring stage in the digital earth
829 system approach, occurring subsequent to the adoption of interventions. Based

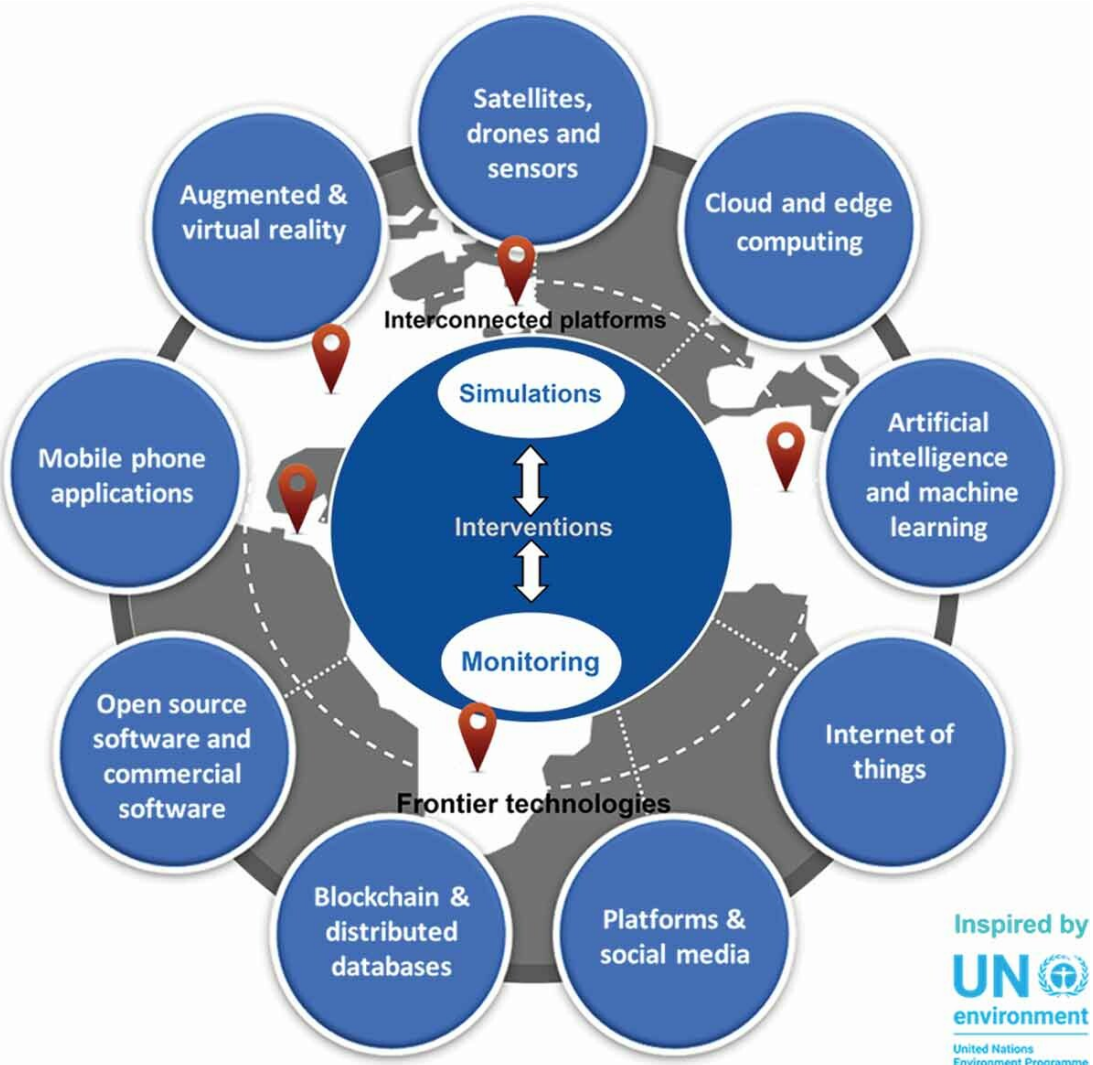


Figure 2.7. An example of abstract architecture of a digital earth system (Fukui et al., 2021)

830 on insights from these findings, we provide evidence and recommendations for
 831 future policies.

832 In the second experiment, we also utilized multisource data to enhance the es-
 833 timation of terrestrial carbon fluxes, which constitute the largest source of carbon
 834 sink on the planet. Precisely quantifying these fluxes is crucial for a thorough
 835 grasp of advancements toward carbon neutrality at both regional and global lev-

836 els, thereby furnishing reliable input for the simulation phase.

837 Lastly, in the third experiment, we developed a prototype for a digital earth
838 system dedicated to the carbon neutrality roadmap and progress tracking. This
839 platform involved integrating multisource data for both monitoring and roadmaps
840 purposes at the local scale.

⁸⁴¹ **3 Impact of interventions on air ⁸⁴² quality**

⁸⁴³ This chapter is based on my papers (Phan and Fukui, 2023a) and (Phan and
⁸⁴⁴ Fukui, 2024):

- ⁸⁴⁵ • Anh Phan, Hiromichi Fukui (2023), Quantifying the impacts of the COVID-
⁸⁴⁶ 19 pandemic lockdown and the armed conflict with Russia on Sentinel 5P
⁸⁴⁷ TROPOMI NO₂ changes in Ukraine, Big Earth Data, doi: <https://doi.org/10.1080/20964471.2023.2265105>.
- ⁸⁴⁹ • Anh Phan, Hiromichi Fukui (2024), Unusual response of O₃ and CH₄ to NO₂
⁸⁵⁰ emissions reduction in Japan during the COVID-19 pandemic, International
⁸⁵¹ Journal of Digital Earth, 17:1, doi: <https://doi.org/10.1080/17538947.2023.2297844>.

⁸⁵³ **3.1 Case Study in Ukraine**

⁸⁵⁴ **3.1.1 Introduction**

⁸⁵⁵ Nitrogen dioxide (NO₂) is a key air pollutant that can have harmful effects on
⁸⁵⁶ human health. An increase in nitrogen oxide (NO_x = NO + NO₂) concentrations
⁸⁵⁷ contributes to global warming through a chemical reaction that leads to the
⁸⁵⁸ formation of ozone (O₃), a short- lived climate pollutant with a potent warm-
⁸⁵⁹ ing effect (Stocker et al., 2013). The lifetime of NO₂ is strongly influenced by
⁸⁶⁰ photochemical reactions and meteorological parameters (Barré et al., 2021) and
⁸⁶¹ varies seasonally (Dragomir et al., 2015; Kendrick et al., 2015). During winter,
⁸⁶² photochemical reaction activity is reduced, resulting in a longer lifetime of the

863 NO₂. Additionally, seasonal variations in NO₂ concentration are controlled by
864 dispersion processes which are significantly affected by changes in boundary layer
865 height (BLH), wind speed and direction patterns due to temperature inversions in
866 summer and winter (Barré et al., 2021; Kendrick et al., 2015). NO₂ concentration
867 levels have been widely used to evaluate decreases in emissions associated with
868 intervention events such as the COVID-19 pandemic lockdown and impacts on
869 the air quality due to the short lifetime of NO₂ in the atmosphere (Barré et al.,
870 2021; Cooper et al., 2022).

871 In Europe, anthropogenic NO_x emissions are mainly attributed to combustion
872 processes in transportation, as well as energy production and distribution.
873 In Ukraine, coal-fired power plants (CPPs) dominantly account for 80% of total SO₂ and 25% of total NO_x emissions, and some have been identified as the
874 highest-emitting CPPs in the region and in the world (Lauri and Rosa, 2021).
875 Since the pandemic started in March 2020, and now with the ongoing armed
876 conflict with Russia, Ukraine has faced a series of threats to the economy, hu-
877 man security and the environment, as well as geopolitical tensions (Pereira et al.,
878 2022). During the pandemic response starting in 2020, many national and local
879 lockdown restrictions were issued to prevent the spread of the virus, causing a
880 sharp decrease in gross domestic product growth rate, as well as industrial and
881 energy production (Danylyshyn, 2020). In 2021, Ukraine's economy started to
882 recover from the pandemic but the recovery was eventually upended by an armed
883 conflict with Russia that started on February 24, 2022. The conflict has been
884 causing a multi-pronged crisis not only in Ukraine but also in Europe, with in-
885 creased prices and exacerbated inflation among the many impacts. Many facilities
886 and extensive areas of housing and other infrastructure, including some CPPs,
887 have been reported destroyed or damaged in Ukraine. These impacts have con-
888 sequently triggered an unprecedented refugee crisis in Ukraine, clogging border
889 crossings between Ukraine and bordering European countries (Júlia et al., 2022).
890 The many socio-economic changes that have occurred during the pandemic and
891 the conflict could be expected to contribute to major variability in air quality in
892 Ukraine, including NO₂ pollution levels, during the 2020–2022 period.

894 A report by the United Nations Development Programme (UNDP) (Dumitru
895 et al., 2020), estimated the impacts of the pandemic lockdown on NO₂ levels in

Ukraine by using Sentinel 5P (S5P) NO₂ column concentrations and Copernicus Atmosphere Monitoring Service (CAMS) surface NO₂ data (Marécal et al., 2015). However, meteorological variables were not acknowledged, although ignoring weather factors could strongly affect final estimates of changes in pollution concentration levels induced by the lockdown (Schiermeier, 2020). A more recent study (Zalakeviciute et al., 2022) utilized direct satellite observation from 2019 and early 2020 as business-as-usual data to evaluate the impact of the Russia-Ukraine conflict in 2022 on air quality, but again, without acknowledging weather effects. These two studies utilized estimates of year-to-year differences. However, such estimates can easily be affected and dominated by changes in meteorological parameters rather than emission sources (Grange et al., 2021; Shi et al., 2021). Therefore, a more sophisticated method is needed to measure the impacts of intervention events through better quantification of actual air quality.

In order to normalize the meteorological effects to accurately and reliably quantify the impact of intervention events, the use of machine learning is increasingly being adopted, but mostly applied for ground-based measurements following the original idea proposed by (Grange et al., 2018) and (Grange and Carslaw, 2019). The objective of this approach is to construct a business-as-usual (BAU) model for predicting air pollution levels independently of the impacts of any intervention events. This is achieved by integrating meteorological, spatial, and temporal features into the model during the BAU period to accurately represent air pollution levels. An intervention event, in this context, refers to an occurrence that has caused changes in air quality. Recently, (Barré et al., 2021) have introduced their weather normalization approach to improve estimates of lockdown impacts not only on NO₂ levels from ground-based observations and CAMS simulations, but also in satellite measurements from S5P. The original method in (Grange et al., 2018; Grange and Carslaw, 2019) has been altered in order to work with satellite retrieval column NO₂ concentration levels from S5P by adopting a new feature, the forecast surface NO₂ level from CAMS data. Alternatively, gradient boosting machines (GBMs) (Friedman, 2001) have been also utilized instead of random forests (Grange et al., 2018) to develop weather-normalization models under the BAU conditions. (Barré et al., 2021) reported an overall reduction (ranging from 23% to 32%) in major European cities using the three datasets. Their study

929 showed an average difference of 14% between satellite-based and ground-based
930 estimates, and 11% between simulations from the CAMS regional ensemble of
931 air quality models and ground-based estimates. These findings suggest that esti-
932 mates of the impacts of the lockdown on NO₂ levels can vary depending on the
933 source of the data.

934 This study aims to investigate the actual satellite-derived column NO₂ pollution
935 levels induced by pandemic lockdown restrictions and the armed conflict with
936 Russia, which have been two major changes in human activities in Ukraine since
937 2019. In order to do so, we developed a weather-normalization model under
938 BAU scenarios for S5P column NO₂ levels to decouple the meteorological effects
939 from the intervention effects. The BAU simulation NO₂ levels are then used to
940 quantify changes in S5P column NO₂ concentrations during the lockdown and the
941 armed conflict. We describe the data used in the study in section 3.1.2 and the
942 methodology in section 3.1.3. The results and discussion on NO₂ level changes
943 are summarized in section 3.1.4 for the lockdown, and section 3.1.5 for the armed
944 conflict. Finally, we conclude the results of the study in section 3.1.6.

945 3.1.2 Data

946 3.1.2.1 Selection of analysis periods

947 In this study, we consider the three years 2019, 2020, and 2022 for our analysis.
948 We assumed that in 2019, before the lockdown in 2020 and the armed conflict with
949 Russia in 2022, there were no other significant factors impacting socio-economic
950 activities. Hence, we used 2019 NO₂ pollution levels as the reference data for
951 development of the BAU model.

952 Ukraine reported its first active case of COVID-19 on March 3, 2020, and began
953 closing its borders to foreign citizens from March 15 onwards. Around the same
954 time, the country also witnessed its first COVID-19 related death. On April 6,
955 the government introduced a strict lockdown, imposing significant restrictions
956 on movement and requiring the public to wear masks in public spaces. This
957 lockdown was eventually extended until June, although certain restrictions were
958 already lifted starting from May 11. For the lockdown component of our study,
959 we focused on two specific periods: the pre-lockdown period, which ran from

960 March 1 to 15, 2020, and the strict lockdown period, spanning from April 6 to
961 May 10, 2020. The decision to count the pre-lockdown period from March 1
962 was based on the lack of qualified S5P data available for analysis before March,
963 as indicated in Figure 3.2. In 2021, even though COVID-19 vaccines had been
964 developed and distributed to citizens of Ukraine (vaccinations started on February
965 24, 2021), many local lockdowns and restrictions continued to be issued to cope
966 with growing numbers of daily COVID-19 active cases, while trying to keep socio-
967 economic activities on track for recovery.

968 The Russia-Ukraine conflict began on February 24, 2022. We employed data for
969 the period February 1 to July 31 each year from 2019 to 2022 for NO₂ variability
970 analysis. This time frame covers the pre-lockdown and lockdown periods in 2020
971 and extends beyond the first five months (February 24 to July 31) of the armed
972 conflict in 2022.

973 3.1.2.2 TROPOMI NO₂ from Sentinel 5P

974 Most previous studies assessing the impacts of intervention involved ground ob-
975 servations in their analysis. However, reliable ground measurement data was
976 only available in Kyiv (capital of Ukraine) as other sites had been damaged or
977 destroyed in the armed conflict and taken out of service (Savenets, 2021). Thus,
978 open satellite data is considered the most efficient way to monitor air quality for
979 all parts of Ukrainian territory (Shelestov et al., 2021).

980 The S5P data has been distributed from 2018 to the present with two available
981 options. The first is original data (ORG) processed with either of two versions of
982 processor, v1.x (5/2018–6/2021) or v2.x (7/2021 onwards). The second is repro-
983 cessed datasets (RPRO) with the processor (v2.x) for the full mission. According
984 to (Van Geffen et al., 2022), the S5P NO₂ v2.2 data has larger vertical column
985 density (VCDs) than v1.x data, ranging from 10% to 40%, mostly found at mid
986 and high latitudes in winter. Therefore, bias between S5P v1.x and v2.x could
987 lead to overestimation and underestimation when comparing air pollution data in
988 2022 versus 2019, thereby affecting evaluations of the conflict’s impacts on S5P
989 NO₂ levels.

990 In this study, we conducted experiments using two versions of S5P NO₂ data.
991 The first dataset is ORG data which was collected through level 3 (L3) offline

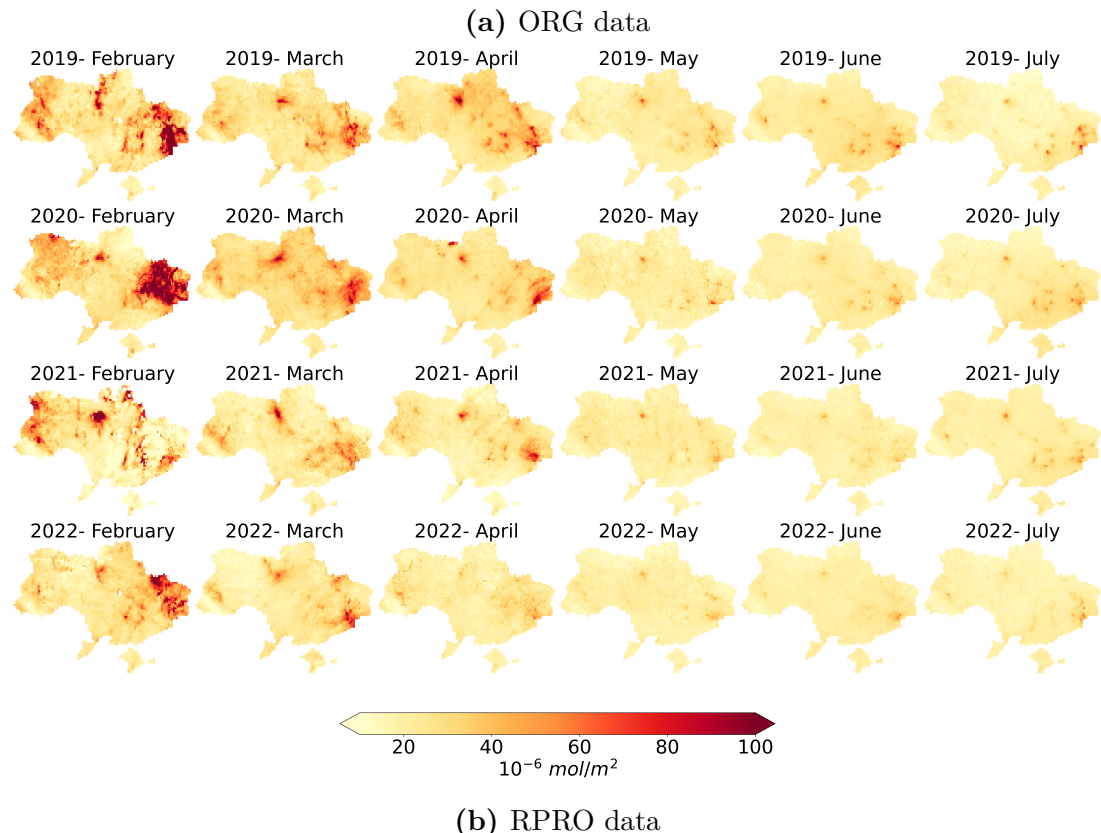
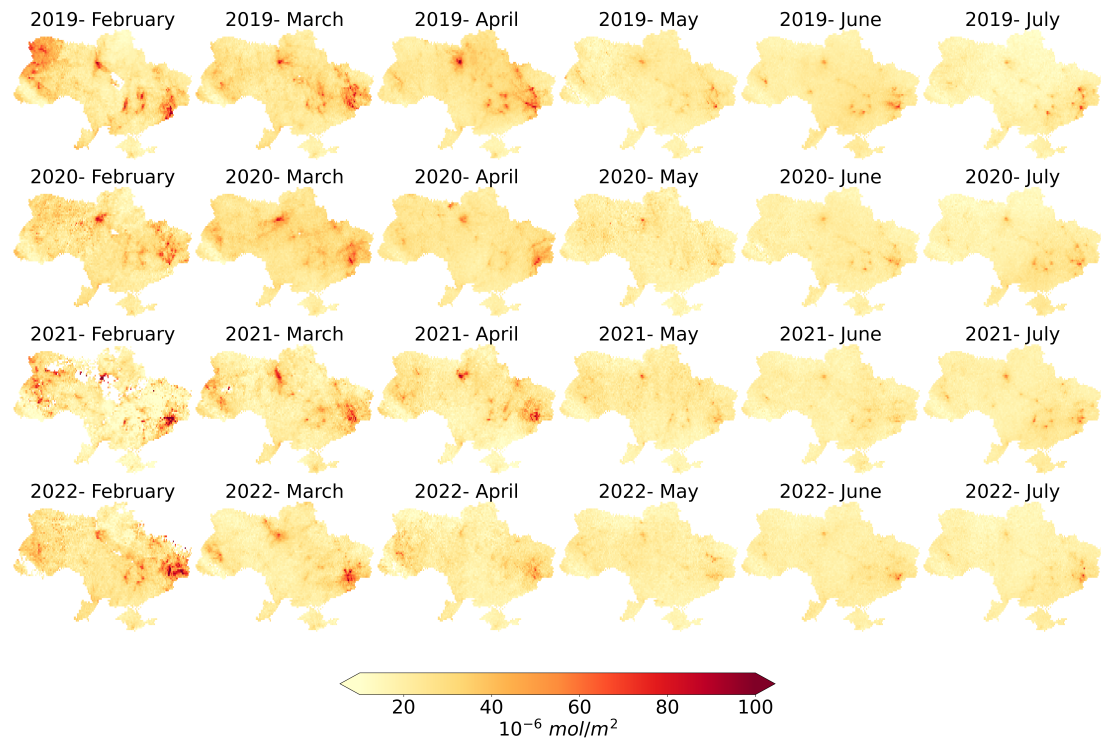


Figure 3.1. Monthly (February to July) average map of TROPOMI S5P NO₂ tropospheric columns for Ukraine from 2019 to 2022

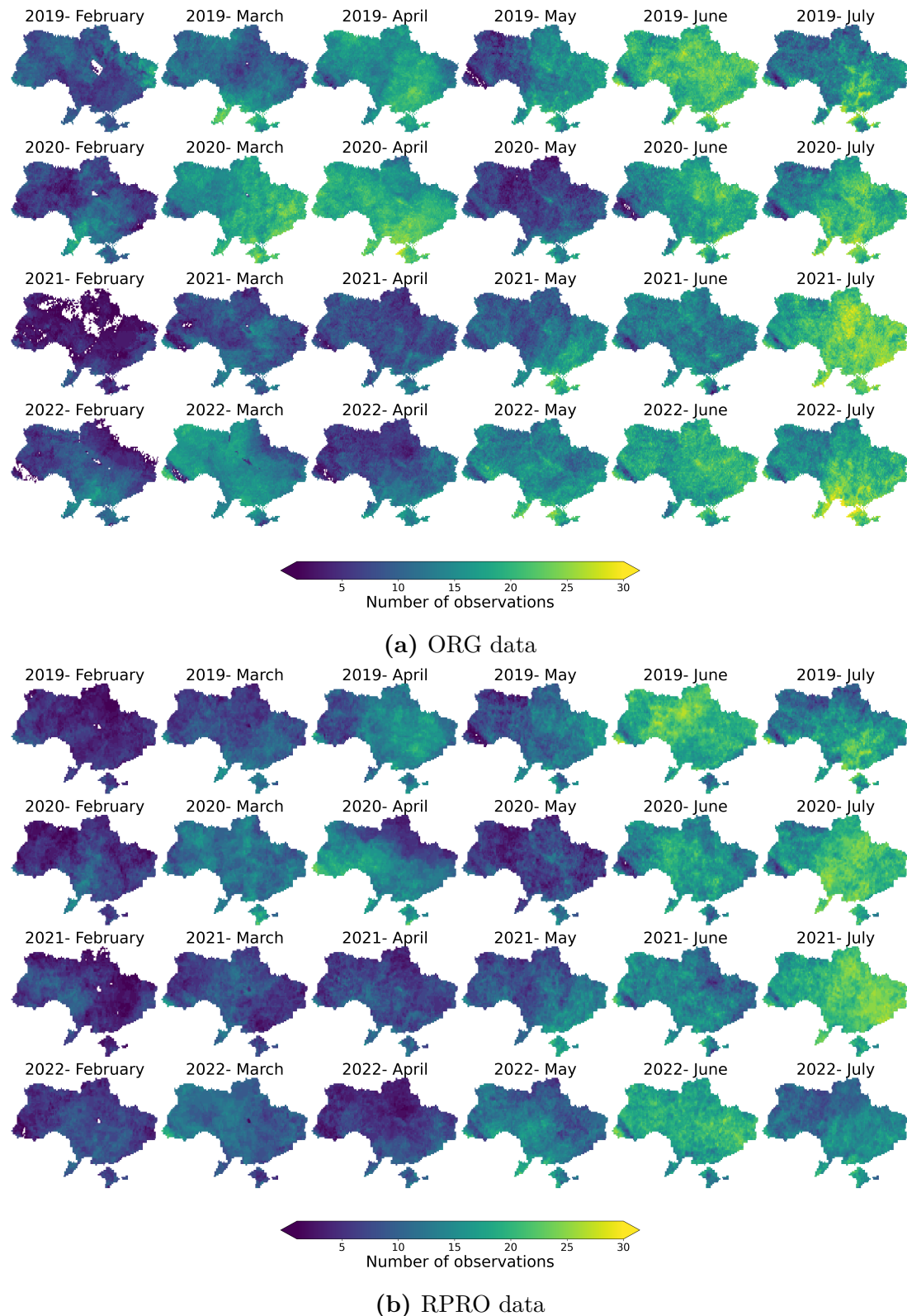


Figure 3.2. Monthly (from February to July) number of TROPOMI S5P NO₂ tropospheric columns observations for Ukraine from 2019 to 2022

992 processing (OFF) of the S5P product available on Google Earth Engine (Gorelick
993 et al., 2017). This dataset comprises processed data from different processor
994 versions for each year from 2019 to 2022 (v1.3.1 in 2019, v1.3.2 in 2020, and
995 v2.3.1 in 2022). The second dataset, denoted as the RPRO product, employs
996 processor version v2.4.0 for the full mission duration. This dataset was acquired
997 from the Sentinel-5P Pre-Operations Data Hub (s5phub.copernicus.eu) using the
998 Sentinel API.

999 Regarding the RPRO data, we began by downloading the level 2 (L2) dataset.
1000 In order to generate the L3 NO₂ dataset, each operational L2 product underwent
1001 mosaicking and filtering of low-quality pixels, which involved removing items with
1002 quality assurance (QA) values less than 75% for the tropospheric NO₂ column
1003 number density band. The harpconvert tool was utilized to perform the conver-
1004 sion from L2 to L3 product. Subsequently, both datasets were linearly interpo-
1005 lated to a spatial resolution of 0.1×0.1 degree. At the time of the experiment,
1006 the RPRO data was only accessible until July 2022.

1007 Plots presented in Figure 3.1 display the average monthly TROPOMI NO₂
1008 tropospheric column over Ukraine from 2019 to 2022 (February to July) using
1009 the ORG data (Figure 3.1a) and RPRO data (Figure 3.1b), respectively. In
1010 2020, a reduction of 4.8% (ORG data) and 8.3% (RPRO data) in mean NO₂
1011 levels over the Ukrainian territory was observed from April to May, compared
1012 to levels recorded in 2019. In 2022, a reduction of 2.4% (ORG data) and 2.9%
1013 (RPRO data) was seen from March to July, compared to levels recorded in 2021.
1014 Additionally, during the same period, a reduction of 10.3% (ORG data) and 15%
1015 (RPRO data) was observed, compared to the NO₂ levels recorded in 2019. We
1016 observed that the reduction in NO₂ levels was more significant in the RPRO data
1017 compared to the ORG data, both during the lockdown in 2020 and the first five
1018 months (March–July) of the conflict in 2022 in Ukraine.

1019 We summarize the number of qualified observations available for each month
1020 from 2019 to 2022 (February to July) in Ukraine using the ORG data (Figure
1021 3.2a) and RPRO data (Figure 3.2b). The quantification of seasonal NO₂ levels
1022 can be challenging, particularly during the selected months in winter (February)
1023 and spring (March, April) of 2021 and 2022, due to the limited availability of
1024 qualified observations. This is further complicated when attempting to estimate

1025 changes before and after intervention events such as the lockdown and the armed
1026 conflict in Ukraine, as the before period falls within the winter months when
1027 observations are scarce.

1028 **3.1.2.3 Meteorological and surface NO₂ data**

1029 In this study, the meteorological and surface NO₂ data are utilized as the pre-
1030 dictors for the estimation of NO₂ under BAU conditions as suggested by (Barré
1031 et al., 2021). The meteorological data is ERA5 reanalysis data which is collected
1032 from the Climate Data Store of the Copernicus Climate Change Service (Hersbach
1033 et al., 2018). We use the following weather variables: 10 m wind speed (u and v
1034 component, m/s) and direction (degrees), 2m air temperature (K), 2m dewpoint
1035 temperature (K), relative humidity (%), geopotential (m^2/s^2), and BLH (m). All
1036 the variables are downloaded at the original resolution of 0.25×0.25 degree and
1037 then linearly interpolated to 0.1×0.1 degree (about $10\text{km} \times 10\text{km}$) resolution. The
1038 utilized surface NO₂ data is collected from CAMS European air quality forecast
1039 and reanalyses and forecast (Marécal et al., 2015) by using the Atmosphere Data
1040 Store of the CAMS (<https://ads.atmosphere.copernicus.eu/>). Since the forecast
1041 data is a 3-year rolling archive from the present, we utilized the analysis data
1042 for 2019. The surface NO₂ forecast data served as the predictors under the BAU
1043 scenario for 2020 to 2022. As forecast predictions do not involve an assimilation
1044 process (Barré et al., 2021), we expect no effect of the pandemic lockdown, and
1045 the impact of the armed conflict related events on air pollution was included in the
1046 surface NO₂ pollution level. Both forecast and analysis data are available at the
1047 resolution of 0.1×0.1 degree. We calculated the mean values based on data from
1048 13:00 and 14:00hours local time to represent the surface NO₂ and meteorology
1049 value at the time the satellite S5P overpassed Ukraine.

1050 **3.1.2.4 Fire spots database and Ukraine crisis hub**

1051 In order to draw a detailed picture of the battle spots, we utilized data from Fire
1052 Information for Resource Management System (FIRMS) provided by National
1053 Aeronautics and Space Administration (NASA) and Ukraine Crisis Hub data
1054 from the Armed Conflict Location and Event Data Project (ACLED) (Raleigh
1055 et al., 2010). The NASA FIRMS portal provides active fire data at three-hour

1056 intervals based on satellite observations from products of the Moderate Resolution
1057 Imaging Spectroradiometer (MODIS) and Visible Infrared Imaging Radiometer
1058 Suite (VIIRS). For the study, data from the VIIRS product was employed to
1059 access the active fire spots due to its superior fire detection capabilities compared
1060 to the MODIS products (Csiszar et al., 2014; Schroeder et al., 2014).

1061 Detailed data on conflict hotspot locations are extracted from the Ukraine
1062 Crisis Hub which is distributed by ACLED (Raleigh et al., 2010). Information
1063 regarding the conflict events is updated weekly and disaggregated to event type
1064 with time and location (latitude and longitude) in Ukraine and the Black Sea
1065 region available from 2018 until the present. As a result of the conflict, we expect
1066 to see and identify corresponding patterns between locations of active fire spots
1067 and the locations of conflict events.

1068 **3.1.2.5 Population data**

1069 As NO₂ pollution levels are closely related to human socio-economic activities and
1070 frequently high in populous urban areas, we downloaded 2020 population data
1071 for Ukraine from the WorldPop Global Project (www.worldpop.org), available
1072 annually at the spatial resolution of 100m×100m as one of the features for the
1073 BAU NO₂ model. The population data was collected, clipped to the Ukrainian
1074 territory, and linearly interpolated to 0.1×0.1 degree (about 10km×10km).

1075 **3.1.3 Business-as-usual (BAU) modelling**

1076 When considering changes induced by the pandemic lockdown and the armed con-
1077 flict, especially for before-after analysis, an important factor is the meteorology
1078 variations. In this study, we use a suggested list of predictors by (Barré et al.,
1079 2021), which consists of meteorological, spatial, and temporal features, popu-
1080 lation counts from WorldPop Global Project, and surface NO₂ pollution levels
1081 from CAMS European analysis data for 2019 and forecast data for 2020 to 2022
1082 for BAU model development. The spatial and temporal features contain lati-
1083 tude, longitude, Julian date (number of the day from January 1), and day of the
1084 week, respectively. However, unlike the study cited (Barré et al., 2021), for ma-
1085 chine learning model selection, instead of GBM we utilized LightGBM (Ke et al.,

1086 2017), which is a gradient boosting decision tree, to build the BAU model. During
 1087 the training process, other than in studies that used the grid search with an n-
 1088 fold cross-validation approach to tune the model's hyperparameters (Barré et al.,
 1089 2021; Petetin et al., 2020), we employed the Fast Library for Automated Machine
 1090 Learning (FLAML) (Wang et al., 2021), which is a new lightweight library for
 1091 quickly determining the accurate model, to find the optimum hyperparameters
 1092 for the LightGBM model in our case.

Table 3.1. The performance of the BAU model on the validation set described using the following metrics: mean bias (MB), normalized mean bias (nMB), root mean square error (RMSE), normalized root mean square error (nRMSE) and Pearson correlation coefficient (R). N represents the number of points in both the training set and validation set, where each point is associated with unique latitude and longitude values. There are no duplicate points shared between the training and validation sets.

	MB	nMB	RMSE	nRMSE	R	n
Performance with S5P data version 1.x–ORG data						
Training set	3.68×10^{-5}	1.53×10^{-4}	7.80	7.40	0.87	5022
Validation set	0.03	0.10	9.53	10.98	0.80	1269
Performance with S5P data version 2.4–RPRO data						
Training set	2.67×10^{-4}	1.04×10^{-3}	6.97	5.12	0.91	5051
Validation set	0.07	0.26	8.47	7.75	0.86	1242

1093 In order to assess the performance of the BAU simulation model, we randomly
 1094 selected and used 80% of the data for the training set and 20% for the vali-
 1095 dation set. We used the following metrics: mean bias (MB), normalized mean
 1096 bias (nMB), root mean square error (RMSE), normalized root mean square er-
 1097 rror (nRMSE) and Pearson correlation coefficient (R). As shown in the detailed
 1098 results presented in Table 3.1, the model achieved high R on the validation set
 1099 (0.8 for ORG data, 0.86 for RPRO data), with low MB and RMSE indicating
 1100 that the column NO₂ levels are well represented by the input features. Based on
 1101 the feature importance measure as shown in Figure 3.3, we found that the most
 1102 important predictors are wind speed and direction, and BLH, which is also con-

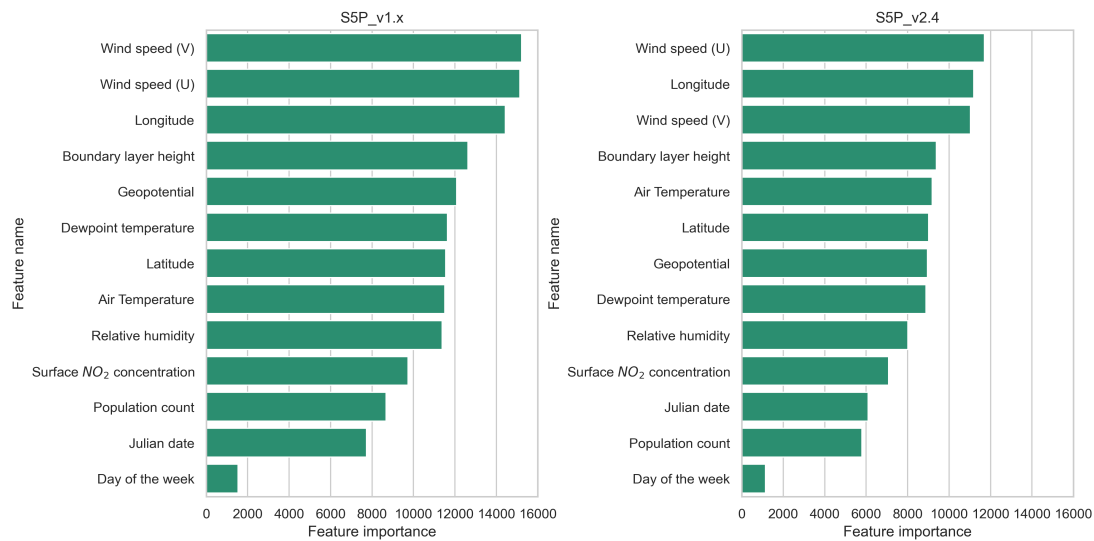


Figure 3.3. Feature importance estimated using LightGBM split method.

sistent with our hypothesis about the impact of the meteorological parameters on column NO₂ levels mentioned above. In Figure 3.4, we present the performance of the BAU model on the validation set using trend lines and scatter plots to compare the predictions with the actual ground truth data. Furthermore, Figure 3.5 displays the OBS data, BAU model's predictions during the lockdown period in 2020, and more than five months of the conflict (February 24–July 31) in 2022. This data is accompanied by the reference NO₂ levels from 2019 which were utilized to train the BAU for corresponding periods. The hyperparameters used to develop the LightGBM model are listed in Table 3.2 for S5P data version 1.x and version 2.4.

The main shortcoming of this method is the lack of qualified reference data to develop the weather normalization model under BAU conditions, as the S5P TROPOMI data has been only available since mid-2018. Only one year of training data in 2019 is considered relatively small, thus resulting in large errors in BAU simulations in winter months as during this time, limited qualified S5P observations are available and NO₂ pollution levels are quite unpredictable due to the inconsistency in heating activities and NO₂ intake from Poland.

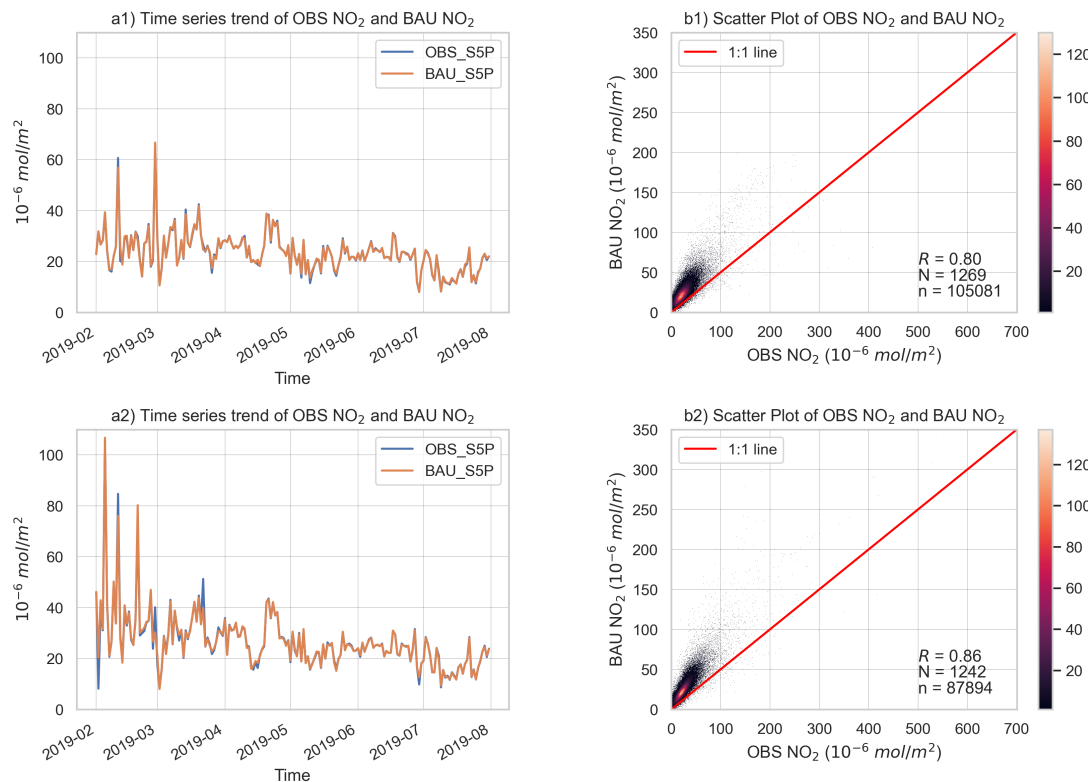
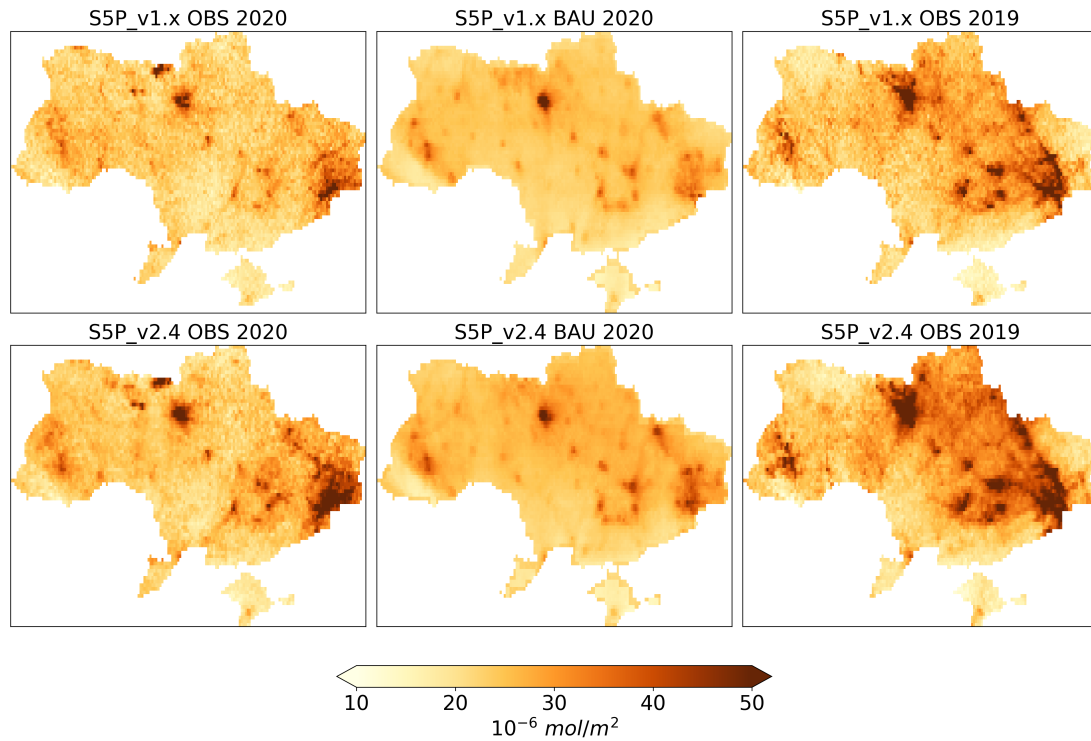


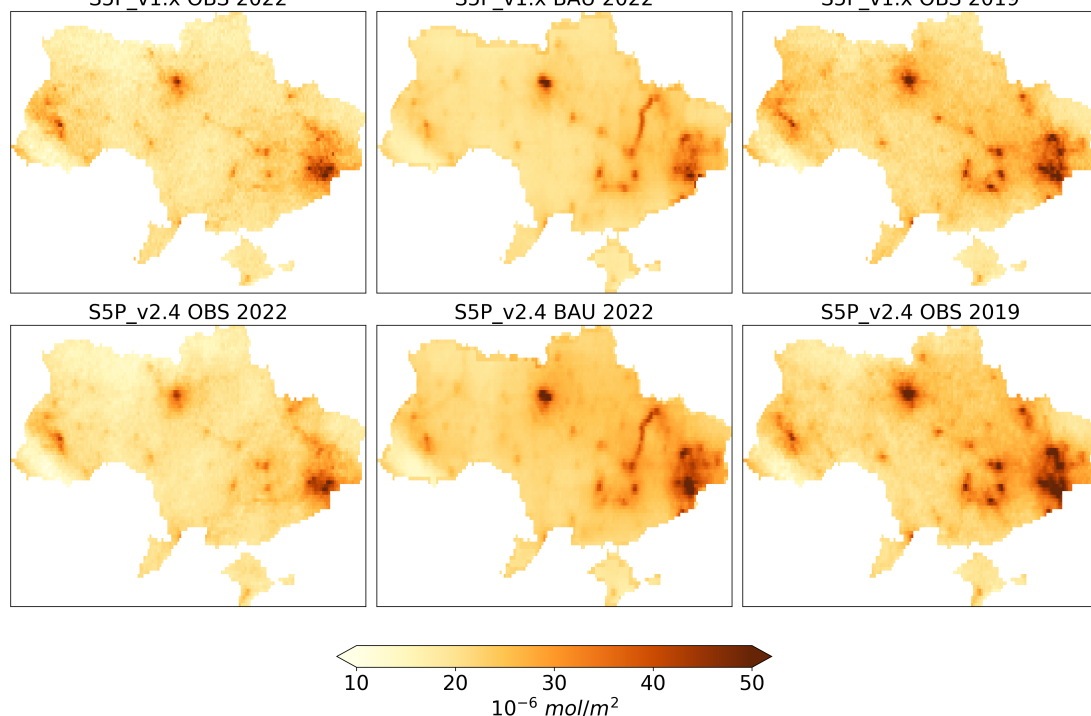
Figure 3.4. The timeseries trend lines (a1) and (a2) and scatter plots (b1) and (b2) depict the OBS NO_2 and BAU NO_2 on the validation set in 2019. Sub-figures (a1) and (b1) correspond to the S5P version 1.x data, while sub-figures (a2) and (b2) represent the S5P version 2.4 data. In the scatter plot, we showed the 1:1 line, Pearson correlation coefficient (R), N represents the number of points in both the training set and validation set, where each point is associated with unique latitude and longitude values. At each point, we used the available daily data from February 1 to July 31, 2019, to make the training and validation set with total number samples is denoted as n . There are no duplicate points and samples shared between the training and validation sets.

1120 3.1.4 COVID-19 induced NO_2 changes

1121 The purpose of this section is to examine the effect of the lockdown on changes in
 1122 NO_2 column levels in populous urban areas, namely the nine cities Kyiv, Kharkiv,
 1123 Odessa, Dnipro, Donetsk, Zaporizhzhia, Lviv, Kryvyi Rih, and Mykolaiv (listed in



(a) The OBS, BAU data in 2020 (April 6 to May 10) with reference data in 2019



(b) The OBS, BAU data in 2022 (February 24 to July 31) with reference data in 2019

Figure 3.5. The OBS (1st column), BAU (2nd column) data from April 6 to May 10, 2020 (a) and from February 24 to July 31, 2022 (b) with the corresponding reference data in 2019 (3rd column)

Table 3.2. The hyperparameters used to develop the LightGBM model with S5P data version 1.x and version 2.4. We used FLAML library (Wang et al., 2021) for tuning these following parameters: shrinkage rate (learning_rate), minimal number of data in one leaf (min_data_in_leaf), minimal sum hessian in one leaf (min_sum_hessian_in_leaf), number of boosting iterations (num_iterations), max number of leaves in one tree (num_leaves).

Parameter	S5P v1.x	S5P v2.4
learning_rate	0.30775042929674906	0.3858774543125185
min_data_in_leaf	11	5
min_sum_hessian_in_leaf	0.001	0.001
num_iterations	907	3451
num_leaves	8604	4342

1124 declining order of population). To begin, we analyse the meteorological patterns
 1125 during the pre-lockdown and lockdown periods and discuss how these might in-
 1126 fluence the NO₂ levels, apart from the impacts of the lockdown measures. Next,
 1127 we utilize two methods to estimate changes in NO₂ levels. The first method,
 1128 known as the year-to-year approach suggested by (Barré et al., 2021), involves
 1129 calculating the median value of the actual S5P observation data in 2020 and sub-
 1130 tracting the observation data from 2019. The second method, OBS-BAU, utilizes
 1131 the median value of the actual observation data (OBS) in 2020 and subtracts the
 1132 simulated NO₂ levels that represent the BAU scenario, which are predicted by
 1133 the S5P tropospheric NO₂ column levels without any lockdown measures. The
 1134 BAU simulations are based on the representation of meteorological, spatial, and
 1135 temporal parameters.

1136 3.1.4.1 Lockdown and pre-lockdown meteorological patterns

1137 Figures 3.6a and 3.6b display the probability density functions of the BLH, and
 1138 Figures 3.6c and 3.6d display wind speed and direction during the pre-lockdown
 1139 and lockdown periods of 2019 and 2020 based on data from the nine selected
 1140 cities. In 2020, the BLH exhibited a similar distribution to that of 2019 during
 1141 the pre-lockdown period, but with lower values. This decrease in BLH would have

resulted in an increase in NO_2 levels in 2020 compared to 2019, as the reduced BLH restricts the dispersion of NO_2 emissions, leading to an increase in NO_2 concentration levels (see Figure 3.6a).

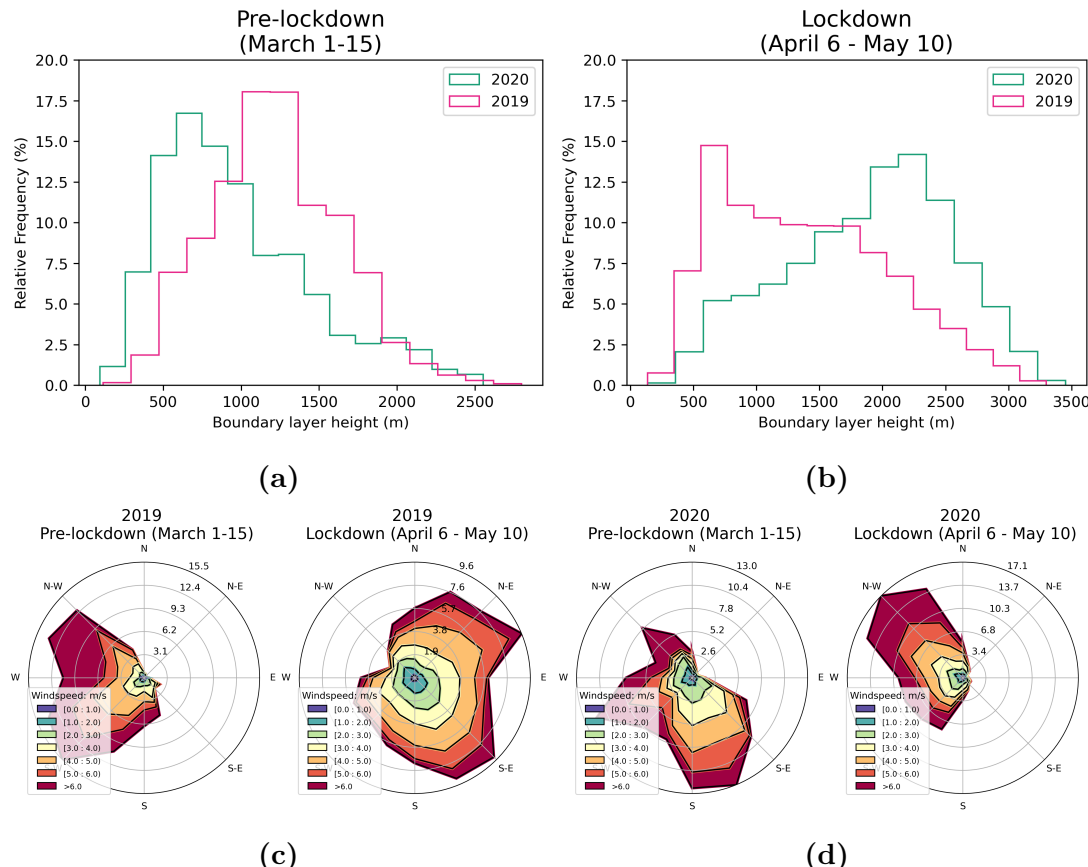


Figure 3.6. Probability density functions of BLH during (a) the pre-lockdown (March 1–15) and (b) the lockdown period (April 6–May 10) between 2019 and 2020 based on data from the nine most populous cities of Ukraine. Wind rose plots for wind speed and direction for pre-lockdown (March 1–15) and lockdown (April 6–May 10) periods in (c) 2019 and (d) 2020 based on data from the nine most populous cities of Ukraine

Conversely, during the lockdown period (see Figure 3.6b), we observed higher values of BLH in 2020 compared to 2019. This increase in BLH could have contributed to the dispersion of NO_2 concentration, resulting in a reduction of NO_2 levels during the lockdown in 2020. This phenomenon, in addition to the

1149 effects of the lockdown restrictions, may have also contributed to minimizing the
1150 NO₂ levels over major cities in Ukraine. Therefore, it is essential to consider the
1151 impacts of meteorological variables on NO₂ level variability analysis.

1152 3.1.4.2 NO₂ changes in populous Ukrainian cities

1153 In Figures (3.7a, 3.7b), and Table 3.3, we present the result of the year-to-year
1154 approach. We assumed that there would be a minimal change in NO₂ pollution
1155 levels during the pre-lockdown period, but a significant reduction during the
1156 lockdown when comparing the same time frame in 2019 and 2020 due to the
1157 implemented lockdown measures and social distancing practices. In Figure 3.7,
1158 two different methods, namely the OBS-BAU and year-to-year approaches, were
1159 used for the analysis. The circle size in the figures corresponds to the population
1160 of each city. For each sub-figure (a) and (b), the first row (a1, a2, b1, b2) contains
1161 two plots showing the results based on the ORG data (S5P v1.x), while the second
1162 row (a3, a4, b3, b4) includes two plots presenting the results based on the RPRO
1163 data (S5P v2.4). The left column plots (a1, a3, b1, b3) of Figures (3.7a, 3.7b)
1164 display the year-to-year estimates, while the right column plots (a2, a4, b2, b4)
1165 display the OBS-BAU estimates. Figure 3.7a illustrates that the prevailing trend
1166 in the nine selected cities during the pre-lockdown period showed an increase, with
1167 an average of 5.2% (ORG data) and 13.9% (RPRO data) in NO₂ levels, while
1168 during the lockdown period (Figure 3.7b), a general reduction was observed in
1169 most cities with an average of 15.6% (ORG data) and 11.1% (RPRO data). This
1170 confirms that the lockdown measures reduced the NO₂ column concentrations in
1171 major urban areas of Ukraine, as we anticipated. It is worth noting that the year-
1172 to-year approach using the original satellite observations has been widely used in
1173 many studies and online resources. However, as mentioned in (Barré et al., 2021;
1174 Grange et al., 2021), it is heavily influenced by meteorological variables such as
1175 wind speed and direction, and BLH (Wallace and Kanaroglou, 2009).

1176 In order to quantify the true improvement in air quality with respect to column
1177 NO₂ levels due to the lockdown restrictions, we calculated the difference between
1178 the actual observation data and the simulated data under BAU conditions with
1179 the meteorological effects decoupled. Like the year-to-year approach, we antic-
1180 ipate a slight variation between the OBS NO₂ levels and the BAU NO₂ levels

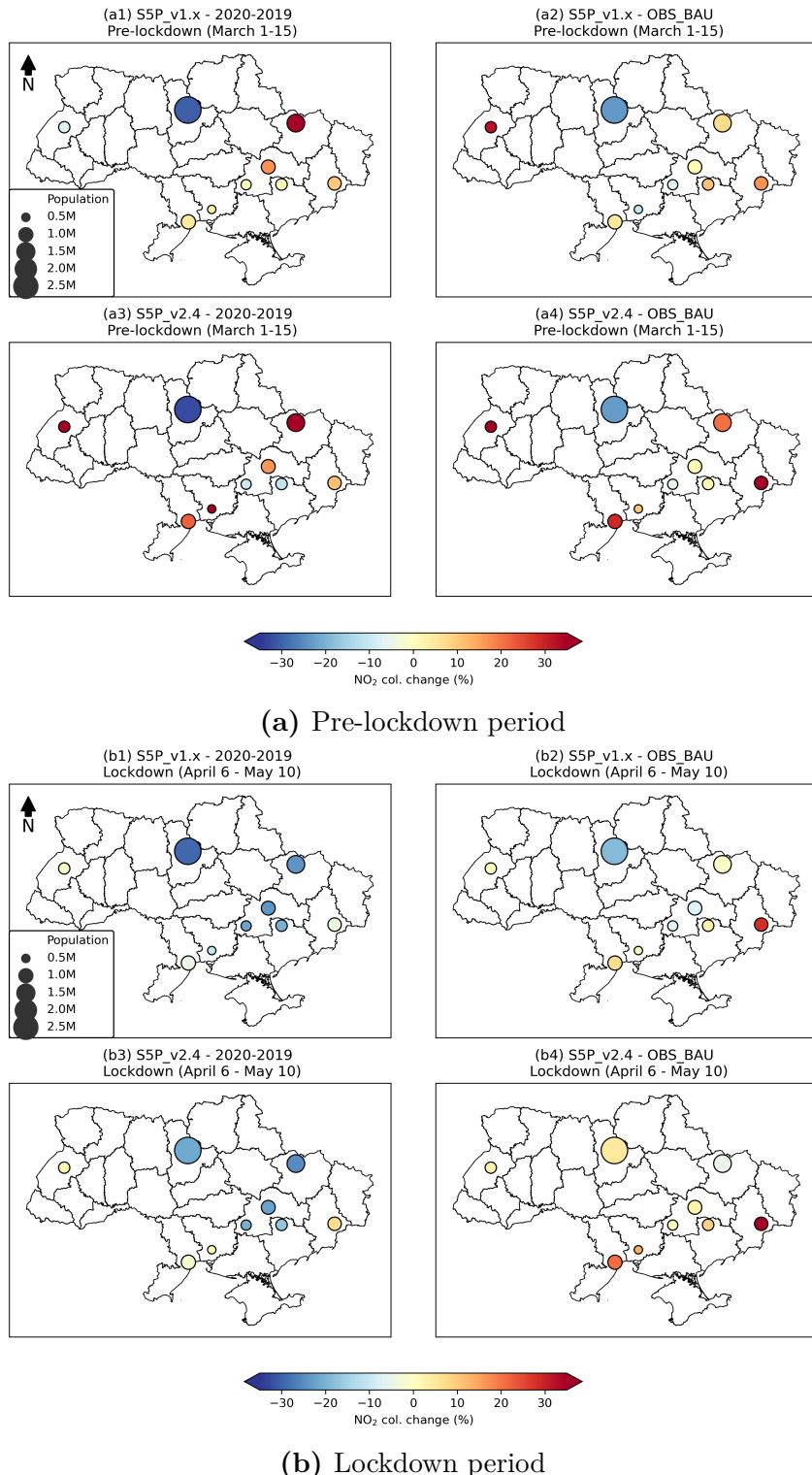


Figure 3.7. Estimates of S5P NO₂ column changes for the nine most populous cities in Ukraine during the (a) pre-lockdown and (b) lockdown periods.

Table 3.3. The OBS-BAU and year-to-year (2020–2019) estimates (in percentage) during pre-lockdown and lockdown periods in the nine most populous cities in Ukraine. The values are represented as mean, while standard deviation is not presented here due to lack of space.

City	Pre-lockdown (March 1 – 15)				Lockdown (April 6 – May 10)			
	OBS-BAU		2020–2019		OBS-BAU		2020–2019	
	ORG	RPRO	ORG	RPRO	ORG	RPRO	ORG	RPRO
Kyiv	−23.7	−23.1	−30.6	−32.8	−18.8	4.9	−29.4	−21.4
Kharkiv	7.6	20.8	47.9	49.1	−0.9	−4.9	−24.1	−24.9
Odessa	5.1	29.0	4.8	22.4	6.9	21.0	−4.4	−1.9
Dnipro	1.3	1.5	17.0	16.7	−6.6	2.8	−23.9	−22.3
Donetsk	16.8	41.9	10.3	11.2	28.2	42.0	−4.0	7.2
Zaporizhzhia	11.5	1.9	0.6	−11.1	2.5	9.1	−20.1	−17.2
Lviv	32.2	35.7	−7.3	37.7	0.0	3.0	−1.2	1.4
Kryvyi Rih	−7.3	−5.3	1.2	−9.8	−6.4	0.1	−21.9	−20.5
Mykolaiv	−10.2	10.1	3.3	41.5	−0.6	13.8	−11.1	−0.4
Mean	3.7	12.5	5.2	13.9	0.5	10.2	−15.6	−11.1

1181 during the pre-lockdown period. Furthermore, we expect to observe an overall
 1182 reduction in the OBS data compared to the BAU data, or at least, a lesser increase
 1183 during the lockdown when compared to the pre-lockdown levels, due to the impact
 1184 of the lockdown measures. Figure 3.7((a2, a4) and (b2, b4)) shows the OBS-BAU
 1185 estimates for pre-lockdown and lockdown in 2020. During the pre-lockdown (Fig-
 1186 ure 3.7(a2, a4)), we observed an average increase of 3.7% (ORG data) and 12.5%
 1187 (RPRO data), which is smaller than the year-to-year estimate. However, during
 1188 the lockdown period (Figure 3.7(b2, b4)) a smaller increase trend was observed,
 1189 with an average of 0.5% (ORG data) and 10.2% (RPRO data). This indicates
 1190 that while the OBS NO₂ levels in 2020 were higher than those predicted under the
 1191 BAU scenario during the lockdown period, the measures implemented during the
 1192 lockdown effectively curbed the increase in NO₂ column concentrations in major
 1193 urban areas of Ukraine when compared to the pre-lockdown levels, aligning with
 1194 our initial expectations. By using the OBS-BAU estimate based on the ORG
 1195 data, the most significant reduction was observed in Kyiv (18.8%), with Dnipro

and Kryvyi Rih experiencing smaller reductions of 6.6% and 6.4%, respectively. However, when using RPRO data, a reduction was only seen in Kharkiv (4.9%).

In comparison with the year-to-year approach with respect to the pre-lockdown (see Table 3.3), the OBS-BAU estimates (3.7% for ORG data, 12.5% for RPRO data) show a smaller change than in year-to-year estimates (5.2% for ORG data, 13.9% for RPRO data). We consider the OBS-BAU estimate to be more reasonable as mentioned above, and the lower values in BLH in 2020 could result in higher year-to-year estimates during the pre-lockdown period between 2020 and 2019. Therefore, we anticipate a lower estimate, which is a smaller increase, after the weather effects are decoupled. Similar findings are seen during the lockdown for OBS-BAU and year-to-year estimates. The contribution from the lower BLH in 2019 could overestimate the reduction of NO₂ concentrations by 15.6% (ORG data) and 11.1% (RPRO data) in the year-to-year lockdown estimates. By normalizing the weather effects, a lower reduction in the increase is anticipated and estimated from the OBS-BAU approach (0.5% for ORG data, 10.2% for RPRO data). Additionally, the year-to-year approaches mostly present a larger standard deviation than the OBS-BAU approach, which could be attributed to local biases caused by meteorological variabilities (Barré et al., 2021). Using weather-normalization techniques, we observed that much of the reduction in NO₂ levels between 2020 and 2019 can be attributed to weather variability. This suggests that stricter measures may need to be considered in the future to achieve significant NO₂ reductions in densely populated areas of Ukraine.

3.1.5 NO₂ changes induced by the armed conflict

In the previous section, we discussed the influence of meteorological factors on the concentration of NO₂ and how using OBS-BAU estimates can mitigate overestimation or underestimation in the year-to-year approach. In this section, we shift our focus solely to the OBS-BAU estimates to explore the impacts of the armed conflict on NO₂ column concentration. The year-to-year estimates are displayed together for the purpose of comparison.

During the lockdown, one might reasonably assume that pollution levels were likely to decrease as the result of an anticipated reduction in socio-economic activities in major urban areas. However, trends in NO₂ levels during the conflict

are likely to be unpredictable in the chaos of armed conflict actions and regionally attributed to various type of emissions at multiple locations, especially at the beginning of the conflict. On one hand, the NO₂ levels should be expected to decline as anthropogenic emissions would be expected to decline due to minimized activities in transportation, industry and other socio-economic activities. On the other hand, surges in conflict activities – such as attacks with missiles, artillery shelling, bomb and mine explosions, etc., as well as the constant usage of military vehicles and the transportation of civilian populations from conflict zones in such a short time – could result in a rise in air pollution levels. Therefore, we extend our study beyond the most populous cities and include other territories in Ukraine affected by the conflict. To accomplish this, we begin by locating the conflict hotspots where military actions and battles took place, and then analyse the changes in NO₂ concentrations in the hotspots, which are highly contested zones. We estimated the changes in pollution levels from individual conflict points, and the results are presented in Section 5.1. In Section 5.2, we analyse the impacts of the conflict on NO₂ levels in other affected regions, such as major cities with populations exceeding 0.5 million, and the areas surrounding CPPs.

3.1.5.1 S5P NO₂ level changes in conflict hotspots

Satellite-captured fire spots and statistics in conflict hotspots

To understand the distribution of conflict hotspots, we utilized both the satellite-capture fire data from the NASA FIRMS portal, and in particular, the locations of battles provided by ACLED (Raleigh et al., 2010). First, we inspect the fire data from the VIIRS fire product for two consecutive years (2021 and 2022), searching for patterns representing the appearance of conflict hotspots. Then, we visually compare the pattern of fire spots captured by satellite with the reported battle locations.

Figure 3.8 displays the satellite-captured fire spots for 2021 (1st column), 2022 (2nd column) and locations of conflict hotspots (3rd column). We only show the similar patterns captured from the monthly NASA FIRMS product and the reported conflict hotspot locations from Ukraine Crisis Hub, to avoid the overwhelming plots of 12 months. We observe that from February 24 until the end of March, the distribution of the detected fire spots forms no certain pattern and is

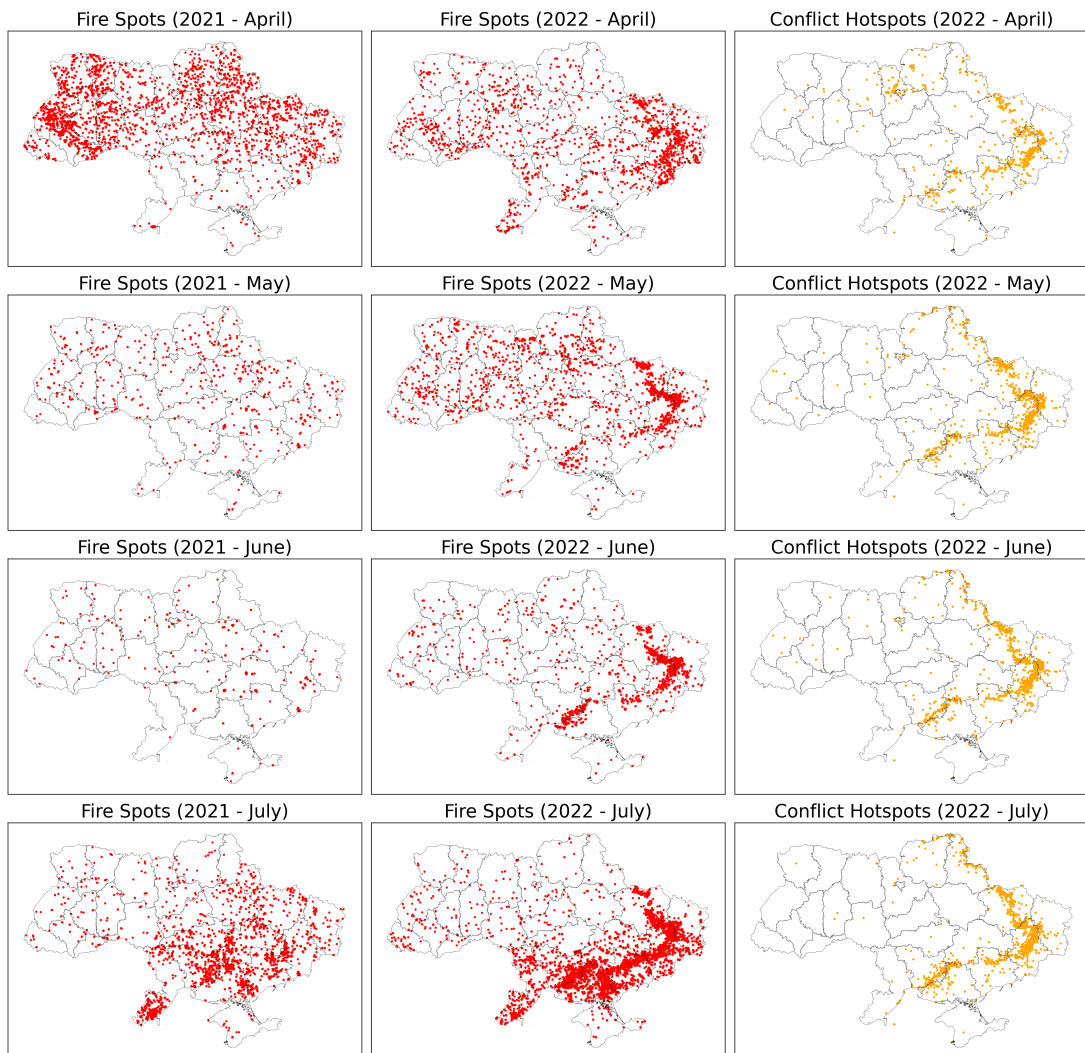


Figure 3.8. Satellite-captured fire spots for 2021 (1st column), 2022 (2nd column) and conflict hotspots (3rd column) in April, May, June and July. The patterns of conflict hotspots are clearly recognizable in the satellite-capture fire product from NASA FIRMS

1260 scattered over the Ukrainian territory. From April to July 2022 the fire pattern
 1261 starts to form and gradually be identifiable as similar to the conflict spots in the
 1262 eastern part of the Ukrainian territory, while no special pattern is found in the
 1263 2021 figures for the corresponding periods. It is notable that the eastern region
 1264 comprising of five oblasts (typically translated as regions or provinces, namely

Dnipropetrovsk, Donetsk, Kharkiv, Luhansk, and Zaporizhzhia) has been at the frontline of the armed conflict and subject to intense conflict hotspots since the conflict began. Given our understanding that the ongoing armed conflict is the source of explosions and smoke, it is reasonable to assume that the conflict has resulted in a significant increase in air pollution (Pereira et al., 2022), particularly in the areas directly affected by the conflict events that are detectable via VIIRS satellite products, so we would expect that S5P observations have the capability to show the resulting impacts on both overall air quality and concentrations of NO₂ in the affected areas.

Changes of S5P NO₂ column levels

Until March 2023, as reported by (Nichita and Ana, 2023), nearly 40,000 events related to the conflict were recorded across the Ukrainian territory by the ACLED project (Raleigh et al., 2010). The five oblasts Dnipropetrovsk, Donetsk, Kharkiv, Luhansk and Zaporizhzhia have been on the frontline of the Russia-Ukraine armed conflict since February 24, 2022. In these areas, shelling, artillery, and missile attacks accounted for 71% of conflict events recorded between February 24 and July 31, 2022 (Nichita and Ana, 2023). In order to evaluate the impacts of conflict events at the smallest level, we quantify changes in NO₂ column levels directly at the reported event location using OBS-BAU and year-to-year estimates for the corresponding pixel from S5P data, which is equivalent a 10 km²-area containing the event location (Figure 3.9).

The OBS-BAU estimates based on ORG data indicate an average increase of 0.3%, while the year-to-year estimates show a more substantial increase of 13.2%. However, when using RPRO data, we observed an 11% reduction in the OBS-BAU estimate and a 1.35% increase in the year-to-year estimate. Although there is a high level of uncertainty in estimating changes at the event location-pixel level, and the inconsistent timing between the reported conflict related events and S5P overpass may lead to an underestimation of changes in air pollution levels, the information gathered can still be useful in identifying changes in the NO₂ columns associated with conflict related event locations in the five oblasts.

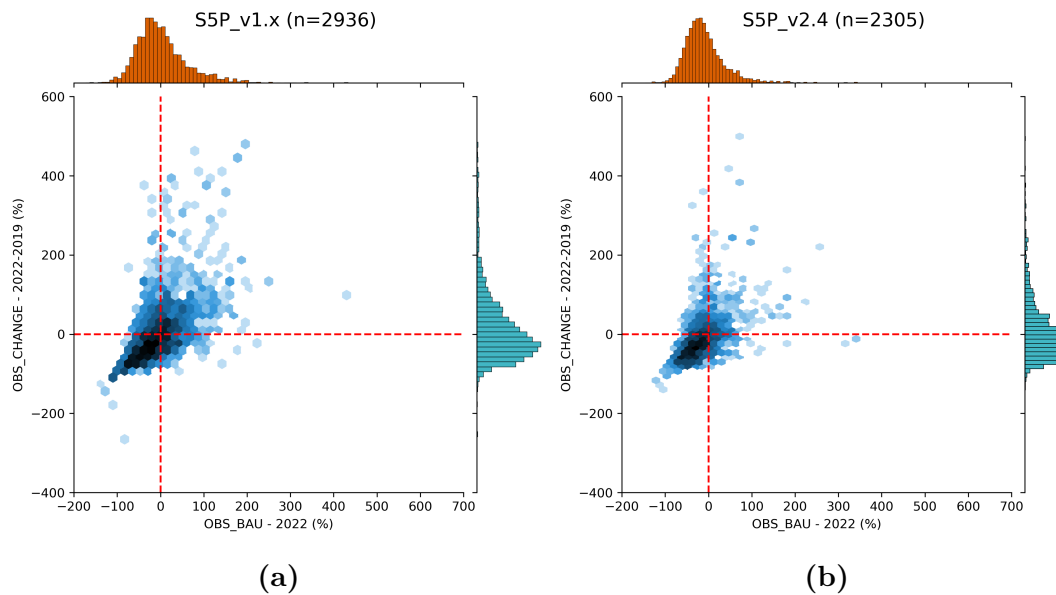


Figure 3.9. OBS-BAU and year-to-year estimates for the individual conflict events including air/drone strikes, armed clashes, remote explosive/landmine occurrences, shelling/artillery/missile attacks, and other forms of attacks that occurred between February 24 and July 31, 2022, for five frontline oblasts, Dnipropetrovsk, Donetsk, Kharkiv, Luhansk and Zaporizhzhia. The number of data points is denoted by (n).

1295 3.1.5.2 Changes of S5P NO₂ levels in other affected areas

1296 Most populous cities of Ukraine

1297 In the nine most populous cities in Ukraine, both the lockdown and the conflict
 1298 have led to a reduction in daily anthropogenic activities. Although this reduction
 1299 was expected to lower the NO₂ levels, as discussed in Section 4, the lockdown
 1300 measures did not result in a significant reduction in NO₂ column levels in 2020. To
 1301 quantify the changes caused by the conflict and compare them with the effects
 1302 of the lockdown measures, we analysed the OBS-BAU estimate for the most
 1303 populous cities in Ukraine during the strict lockdown period from April 6 to
 1304 May 10 in 2020 and 2022 (Table 3.4). To avoid overwhelming plots, Figure
 1305 3.10 displays the NO₂ column trend lines for OBS data and BAU predictions
 1306 from February to July in 2020 and 2022 for five cities (Kyiv, Kharkiv, Dnipro,

¹³⁰⁷ Zaporizhzhia, and Kryvyi Rih) only.

Table 3.4. The OBS-BAU estimate (in percentage) of ORG data and RPRO data for the strict lockdown period (April 6 to May 10) in 2020 and in 2022 for the nine most populous cities in Ukraine. The values are represented as mean (with standard deviation in parentheses). The mean and standard deviation in the last row were calculated across the nine cities.

City	2020 (April 6 –May 10)		2022 (April 6 –May 10)	
	ORG	RPRO	ORG	RPRO
Kyiv	-18.8 (6.5)	4.9 (17.4)	-29.3 (9.5)	-34.6 (7.6)
Kharkiv	-0.9 (10.3)	-4.9 (15.9)	-24.9 (17.9)	-29.7 (20.8)
Odessa	6.9 (12.4)	21.0 (16.4)	-7.6 (14.3)	-14.5 (9.7)
Dnipro	-6.6 (9.2)	2.8 (10.9)	-17.4 (10.0)	-19.5 (8.6)
Donetsk	28.2 (35.2)	42.0 (29.8)	3.5 (19.9)	3.2 (18.7)
Zaporizhzhia	2.5 (9.1)	9.1 (12.7)	-12.6 (13.7)	-18.4 (11.6)
Lviv	0.0 (10.9)	3.0 (8.5)	14.9 (17.9)	-3.3 (9.9)
Kryvyi Rih	-6.4 (8.7)	0.1 (9.9)	-20.8 (9.8)	-27.7 (8.1)
Mykolaiv	-0.6 (9.8)	13.8 (17.6)	-14.6 (10.1)	-18.0 (6.8)
Mean	0.5 (11.9)	10.2 (13.3)	-12.1 (13.2)	-18.1 (11.5)

¹³⁰⁸ Table 3.4 presents the OBS-BAU estimates corresponding to the strict lock-
¹³⁰⁹ down period (April 6 to May 10) in 2020 and 2022 for the nine most populous
¹³¹⁰ cities in Ukraine. Our findings indicate that the conflict has caused more signifi-
¹³¹¹ cant reductions in NO₂ levels, compared to the lockdown measures. While minor
¹³¹² reductions to increases were observed during the 2020 lockdown, a consistent and
¹³¹³ continuous reduction has been noticed in most cities, during the same lockdown
¹³¹⁴ period (April 6 to May 10) in 2022. The average reduction across all the cities of
¹³¹⁵ interest, as shown in Table 3.4, is about 12.1% (based on ORG data) and 18.1%
¹³¹⁶ (based on RPRO data). The largest reduction was observed in Kyiv, while the
¹³¹⁷ increase occurred in Lviv (14.9% based on ORG data) and in Donetsk (3.5%
¹³¹⁸ based on ORG data, 3.2% based on RPRO data).

¹³¹⁹ In more than the first five months after the conflict began until the end of July
¹³²⁰ 2022, an overall reduction is observed across the nine cities (see Table 3.5) with

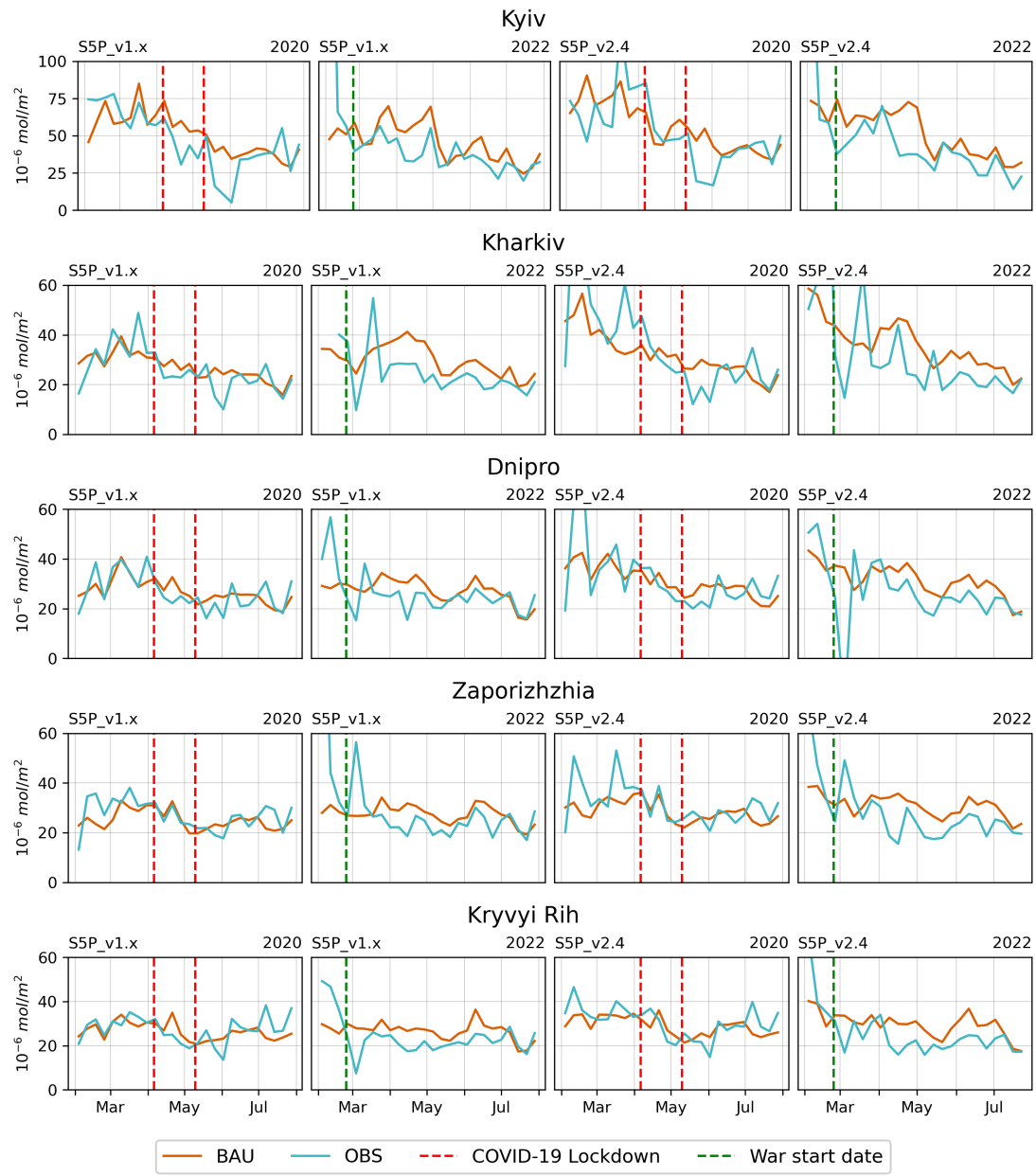


Figure 3.10. The trend lines of OBS and BAU S5P NO₂ column levels from February to July in 2020 and 2022 for five cities in Ukraine. Each row displays plots for a different city. The first and second column plots represent the ORG data (S5P version 1.x), while the third and last column plots show the RPRO data (S5P version 2.4). The first and third column plots pertain to 2020, while the second and last column plots pertain to 2022.

Table 3.5. Average OBS-BAU and year-to-year estimate (in percentage) of ORG data and RPRO data from February 24 to July 31, 2022, for the nine most populous cities in Ukraine. The values are represented as mean (with standard deviation in parentheses). The mean and standard deviation in the last row were calculated across the nine cities.

City	ORG		RPRO	
	OBS-BAU	year-to-year	OBS-BAU	year-to-year
Kyiv	-14.9 (17.3)	-30.5 (14.7)	-27.6 (12.1)	-37.3 (11.3)
Kharkiv	-3.2 (28.5)	20.7 (39.8)	-3.0 (33.3)	2.4 (23.6)
Odessa	-6.8 (15.4)	-13.6 (16.4)	-5.4 (13.0)	4.5 (61.0)
Dnipro	-12.4 (16.6)	-15.0 (21.3)	-17.6 (13.8)	-17.0 (20.5)
Donetsk	19.4 (26.6)	4.2 (21.5)	17.0 (22.8)	-9.4 (15.8)
Zaporizhzhia	-10.5 (16.4)	-15.7 (27.3)	-13.7 (14.4)	-19.1 (18.6)
Lviv	20.8 (21.9)	-9.0 (24.1)	2.2 (16.8)	-9.8 (17.3)
Kryvyi Rih	-15.5 (15.7)	-22.4 (21.7)	-17.4 (15.0)	-26.2 (42.7)
Mykolaiv	-4.8 (13.1)	-7.8 (23.5)	2.1 (14.8)	12.9 (21.9)
Mean	-3.1 (13)	-9.9 (14.1)	-7 (12.7)	-11 (15)

an average of 3.1% (ORG data) and 7% (RPRO data). The largest reductions in NO₂ levels were observed in Kyiv, with an average of 14.9% (ORG data) and 27.6% (RPRO data). Conversely, Donetsk and Lviv experienced increases in NO₂ levels, with both ORG and RPRO data, while in Mykolaiv only RPRO data showed the increases. The rise in Donetsk can be attributed to it being where major armed conflicts occurred during this period.

Coal power plants

Besides anthropogenic activities in major cities, the contribution of CPPs to NO₂ concentration levels is considered to be significant in Ukraine (Lauri and Rosa, 2021). The Zaporizhzhia CPP is one of the largest emitters among CPPs in Ukraine, emitting 21,830 tonnes of NO_x in 2019. Many power plants have been targeted in the conflict, and their damage or destruction has resulted in power blackouts affecting millions of people.

According to Draft Ukraine Recovery Plan, Materials of the “Energy Security”

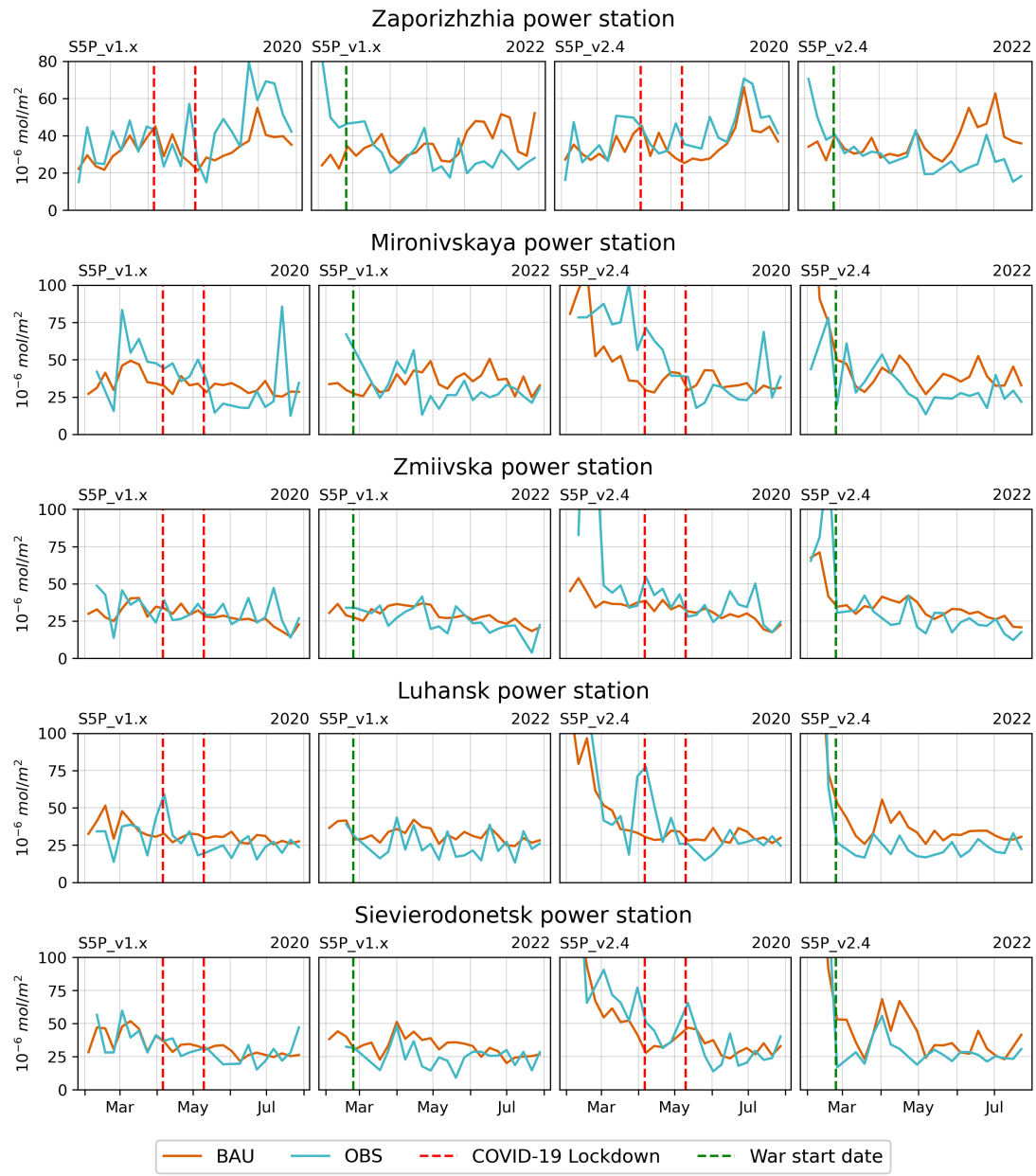


Figure 3.11. The trend lines for the OBS and BAU S5P NO₂ column levels from February to July in 2020 and 2022 are presented for selected CPPs. Each row displays plots for a different CPP. The first and second column plots represent ORG data (S5P version 1.x), while the third and last column plots show RPRO data (S5P version 2.4). The first and third column plots pertain to 2020, while the second and last column plots pertain to 2022.

1335 Working Group covering the period to the end of June 2022, significant damage
1336 has been reported at the Zaporizhzhia, Luhansk, and Sievierodonetsk power sta-
1337 tions, as well as other CPPs. This damage could be expected to affect NO₂ levels
1338 in the areas surrounding the damaged power plants. To investigate such changes,
1339 we also compare trends in the NO₂ column levels between OBS data and BAU
1340 simulations for 2020 and 2022, utilizing both ORG and RPRO data as presented
1341 in Figure 3.11. Examining an area of 10 km² around each CPP, we find that,
1342 similar to previous discussions on lockdown effects, little changes are observed
1343 around most CPPs during the pandemic lockdown in 2020. However, a clear
1344 reduction is evident between the time when the conflict began and July 2022 at
1345 the Zaporizhzhia, Mironivskaya, Zmiivska, Luhansk, and Sievierodonetsk power
1346 stations. At areas surrounding other power stations, no noticeable reduction is
1347 observed.

1348 3.1.6 Conclusion

1349 In this study, we performed a comprehensive assessment of variations in the
1350 S5P column NO₂ levels in Ukraine during the COVID-19 pandemic lockdown in
1351 2020 and the armed conflict with Russia in 2022. For this purpose, we utilized
1352 two S5P products, namely, original and reprocessing data. We first developed
1353 a weather normalization model under business-as-usual conditions, using mete-
1354 orological parameters from ERA5 reanalysis, ensembled surface forecasts, and
1355 analysis NO₂ data from 11 CAMS models, along with other spatial and temporal
1356 features. Next, we applied the BAU prediction to estimate the change in NO₂
1357 levels during the lockdown period in 2020 for the nine most populous cities in
1358 Ukraine (Kyiv, Kharkiv, Odessa, Dnipro, Donetsk, Zaporizhzhia, Lviv, Kryvyi
1359 Rih, and Mykolaiv). We extended the analysis using BAU predictions to estimate
1360 the impact of the armed conflict from February 24 to July 31, 2022, in conflict
1361 hotspot locations, the nine most populous cities, and areas surrounding selected
1362 CPPs (Zaporizhzhia, Mironivskaya, Zmiivska, Luhansk, and Sievierodonetsk) in
1363 Ukraine.

1364 The main outcomes of the study can be summarized as follows:

- 1365 • In 2020, meteorological parameters also heavily influenced the NO₂ tropo-

spheric column levels, contributing to decreases in levels during the lock-down period.

- After normalizing the meteorological parameters, we found that the lock-down did not lead to lower NO₂ levels than the BAU prediction in 2020, although it did manage to mitigate the increase in NO₂ compared to the pre-lockdown period. Our study indicates that stricter measures may need to be considered in the future to achieve a significant reduction in NO₂ levels in densely populated areas of Ukraine.
- We observed that satellite-capture fire data from the VIIRS product can capture the spatial patterns of the conflict related events on the ground. From this product, conflict location patterns are clearly represented during the April–July 2022 period.
- Upon examining changes in NO₂ levels at conflict hotspots at the location-pixel level, we observed changes ranging from an 11% reduction to a slight increase of 0.3% when comparing the OBS to BAU predictions using RPRO and ORG data, respectively.
- During the strict lockdown period from April 6 to May 10, 2022, the reduction in NO₂ levels in the nine most populous cities was more significant compared to 2020. Across most cities, an average reduction of 12.1% (ORG data) and 18.1% (RPRO data) was observed. However, it is worth noting that Lviv and Donetsk showed an increase in NO₂ levels during this period.
- From February 24 to July 31, 2022, the nine most populous cities in Ukraine experienced an overall reduction of 3.1% (ORG data) and 7% (RPRO data) in NO₂ levels. The most significant reduction was observed in Kyiv, with an average decrease of 14.9% (ORG data) and 27.6% (RPRO data). However, in contrast, NO₂ levels increased in Lviv, Donetsk and Mykolaiv during this period.
- The conflict has resulted in damage to several CPPs, which are considered as major sources of NO₂ emissions in the country. Our analysis indicates a clear reduction in NO₂ levels in the areas closely surrounding Zaporizhzhia, Mironivskaya, Zmiivska, Luhansk, Sievierodonetsk CPPs.

- 1397 • By utilizing the OBS-BAU estimate for both ORG data and RPRO data to
1398 analyse NO₂ variations during the 2022 conflict, we found that discrepancies
1399 resulting from changes in the processor during the S5P lifetime in ORG data
1400 might lead to a slight underestimation of NO₂ reductions. Specifically, we
1401 observed a smaller decrease using ORG data (3.1%) than with RPRO data
1402 (7%) in the most populous cities of Ukraine.

1403 The consideration of meteorological effects is crucial in regulating pollution
1404 levels. Neglecting these effects could introduce errors in quantifying actual air
1405 quality changes attributed to an intervention event. For future studies assessing
1406 the impacts of conflict in Ukraine on air quality, it will be essential to account
1407 for meteorological variability to achieve genuine and quantitative estimates.

1408 NO₂ is a significant precursor to tropospheric O₃ and also affects the lifetime of
1409 methane (CH₄) (Akimoto and Tanimoto, 2022). Additionally, it has the potential
1410 to serve as an indicator for monitoring CO₂ emissions (Miyazaki and Bowman,
1411 2023). In future studies, it would be valuable to explore how changes in NO₂
1412 levels during conflict could impact O₃ and CH₄ concentrations in Ukraine as both
1413 are important short-lived climate pollutants that contribute to positive radiative
1414 forcing, thereby exacerbating global warming.

1415 3.2 Case Study in Japan

1416 3.2.1 Introduction

1417 Nitrogen dioxide (NO₂) is an important air pollutant that raises significant con-
1418 cerns due to its negative effects on human health (Hamra et al., 2015). Addi-
1419 tionally, it serves as a crucial precursor to tropospheric ozone (O₃), along with
1420 volatile organic compounds (VOCs) (Akimoto and Tanimoto, 2022). Nitrogen
1421 oxides (NO_x = NO + NO₂), carbon monoxide (CO) and non-methane volatile
1422 organic compounds (NMVOCs) have an influence on the methane (CH₄) lifetime
1423 by affecting the atmospheric mixing ratio of hydroxyl radicals (OH) (Akimoto
1424 and Tanimoto, 2022), which act as a primary sink for CH₄ (Turner et al., 2019).
1425 Both O₃ and CH₄ are short-lived climate pollutants (SLCPs) that contribute
1426 to positive radiative forcing, thereby intensifying global warming (Akimoto and

1427 Tanimoto, 2022). Moreover, owing to its short lifetime in the atmosphere and significant signal compared to carbon dioxide (CO_2), NO_2 possesses the potential to
1428 serve as an indicator for monitoring localized fossil fuel CO_2 emissions (Miyazaki
1429 and Bowman, 2023).

1430 In 2020, the implementation of COVID-19 social distancing policies in multiple
1431 countries led to a significant decrease in human activities worldwide (de Palma
1432 et al., 2022). While the general anticipation was for a reduction in NO_2 emissions
1433 in many cities due to the decline in anthropogenic activities (Bauwens et al., 2020;
1434 Barré et al., 2021; Cooper et al., 2022), the response of O_3 and CH_4 has been
1435 unexpected.

1436 Increased levels of O_3 have been observed in northern Europe, China, and
1437 South Africa as a consequence of the COVID-19 lockdown, according to sensitivity
1438 simulations conducted using the MIROC-CHASER global chemical transport
1439 model (Miyazaki et al., 2021). This rise in O_3 can be attributed to the general
1440 reduction in NO_x , which enhances O_3 production by reducing NO titration in
1441 areas with high levels of NO_x pollution or VOC-limited areas (Akimoto and Tan-
1442 imoto, 2022). Furthermore, meteorological effects have played a significant role in
1443 the changes observed in O_3 levels between 2020 and the reference year (Ordóñez
1444 et al., 2020; Liu et al., 2021). Despite accounting for the influence of weather
1445 conditions, significant variations in O_3 level estimates have been reported across
1446 studies, particularly in European countries (Ordóñez et al., 2020; Grange et al.,
1447 2021), and China (Liu et al., 2021; Shi et al., 2021). The presence of sunlight
1448 is essential for the O_3 generation in response to the decrease in NO_x during the
1449 lockdown period. As a result, the lack of sunny conditions in specific urban areas
1450 at the time of the atmospheric response to NO_2 reduction may have led to dif-
1451 fering time delays before observable changes in O_3 levels occurred (Grange et al.,
1452 2021).

1453 In 2020, during the COVID-19 pandemic, global CH_4 emissions experienced a
1454 significant growth rate, which was contrary to the expected decrease in anthro-
1455 pogenic CH_4 emissions due to the implementation of lockdown measures (Peng
1456 et al., 2022). In 2020, anthropogenic CH_4 emissions only slightly decreased com-
1457 pared to 2019, while wetland emissions rose sharply. This increase in wetland
1458 emissions was likely influenced by unusually warm and wet weather in the North-

ern Hemisphere (Peng et al., 2022), which could be connected to the impact of climate change (Zhang et al., 2023b). Apart from the variation in CH₄ emission itself, it was found that the decrease in hydroxyl radical (OH) concentration due to changes in air pollutants like NO_x, CO, and NMVOCs during the COVID-19 pandemic mainly accounted for approximately half (53 ± 10%) of the observed global CH₄ level growth in 2020 (Peng et al., 2022). A similar finding regarding the effect of NO_x, CO, and NMVOC emission changes on the 2020 methane levels is reported by (Stevenson et al., 2022). However, other studies using Greenhouse gases Observing SATellite (GOSAT) observations indicated that most of observed increase in atmospheric CH₄ during 2020 and 2021 can be attributed to increased CH₄ emissions (Qu et al., 2022; Feng et al., 2023). Although CH₄ has a long estimated lifetime of 8-10 years and has mostly been discussed at the global level, it is important to note that policies and approaches to address CH₄ emissions may vary locally.

In 2020, Japan also experienced the impact of the COVID-19 pandemic, and in response to prevent the virus's spread, a state of emergency was declared from April 7 to May 25. This measure resulted in the suspension of various economic activities and imposed restrictions on people's mobility. As a consequence, there was a significant decline in mobility trends (Figure 3.12a). The reduction was more pronounced during the weekend compared to the weekday (Damiani et al., 2022), as illustrated in Figure 3.12b.

Although the primary aim of the lockdown was not specifically to address air pollution and greenhouse gas emissions, the implementation of these measures offers valuable insights for atmospheric modelling. It provides practical knowledge and first-hand experience to develop more efficient strategies for mitigating air pollution and reducing greenhouse gas emissions in the future (Grange et al., 2021). It is important to note that the changes in air pollutant concentrations during this period varied across regions and were strongly influenced by meteorological conditions. A regional analysis of these changes could provide evidence to support the formulation of appropriate regional policies in the future. In this study, our objective is to evaluate the impact of changes in anthropogenic activities during the COVID-19 pandemic (from April 7 to December 31) on NO₂, O₃, CO and CH₄ concentrations in metropolitan areas (MAs) of Japan in 2020,

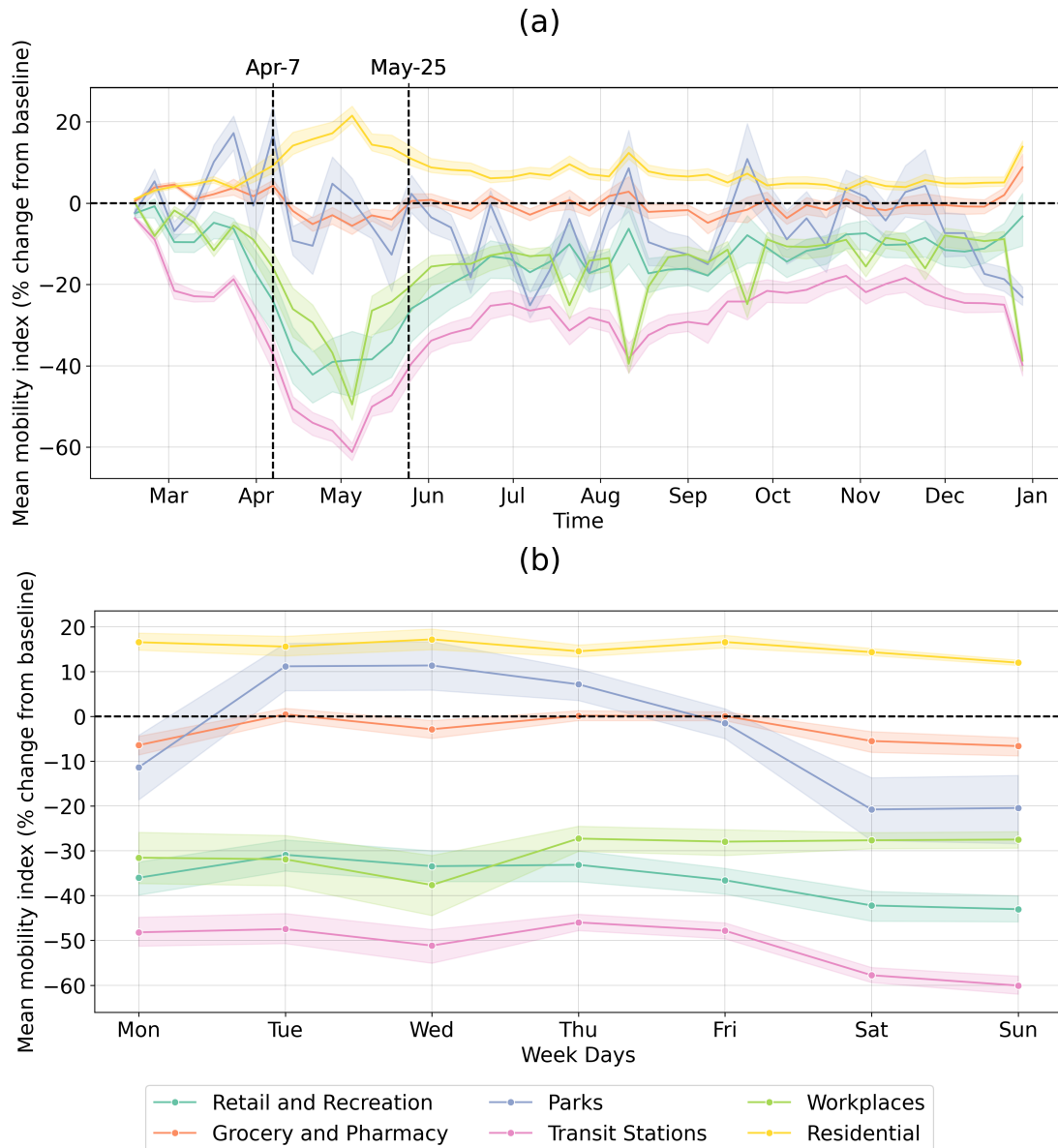


Figure 3.12. Mobility changes for six prefectures in Japan (Aichi, Fukuoka, Tokyo, Osaka, Kyoto, and Hyogo) in 2020 based on Google’s mobility indices for time series (a) and for days of the week (b)

¹⁴⁹³ a topic which has not yet been thoroughly investigated.

¹⁴⁹⁴ In the first phase (Section 3.2.2), we gather data from ground observations, satellite sources, and biogeochemical model simulations. Subsequently, we con-

¹⁴⁹⁵

1496 struct a weather normalization model under business-as-usual (BAU) conditions
1497 utilizing machine learning techniques, incorporating meteorological, spatial, and
1498 temporal predictors (Section 3.2.3). We investigate variations in air pollution lev-
1499 els by analysing the BAU predictions alongside additional data in Section 3.2.4.
1500 Lastly, we provided discussions in Section 3.2.5, while in Section 3.2.6, we present
1501 our findings, conclusions, and recommendations for future policy considerations.

1502 **3.2.2 Data**

1503 **3.2.2.1 Study area**

1504 Prior research primarily focused on assessing the impact of pandemic lockdown
1505 measures on air quality within the Greater Tokyo Area, being the most densely
1506 populated metropolitan area globally (Damiani et al., 2022; Zoran et al., 2023).
1507 Nevertheless, there is a notable absence of similar analyses for other MAs. Our
1508 study covers 14 MAs in Japan, extending from Sapporo in the north to Kagoshima
1509 in the south (Figure 3.13). We focus on these metropolitan areas as they house
1510 Japan’s most highly populated and vibrant cities, where we can observe the in-
1511 tricate connections between human activities and air pollution in Japan.

1512 **3.2.2.2 Ground observation**

1513 To acquire air quality data, we gathered ground observations for NO₂, O₃, CO,
1514 and CH₄ concentrations from the air quality monitoring data archive published
1515 by the National Institute for Environmental Studies (NIES). These observations
1516 spanned a ten-year period from 2010 to 2020 and were collected from 1,180 sta-
1517 tions for NO₂, 835 stations for O₃, 383 stations for CH₄, and 237 stations for
1518 CO. The study utilized two types of stations: roadside air monitoring stations
1519 (RsAMS), which are placed in areas prone to air pollution from vehicle exhaust
1520 caused by traffic congestion, like intersections, roads, and near road edges, and
1521 ambient air monitoring stations (AAMS), which are established to assess air pol-
1522 lution in general living spaces such as residential areas. These station types have
1523 been categorized by NIES, and the data can be readily acquired from the original
1524 downloadable dataset.

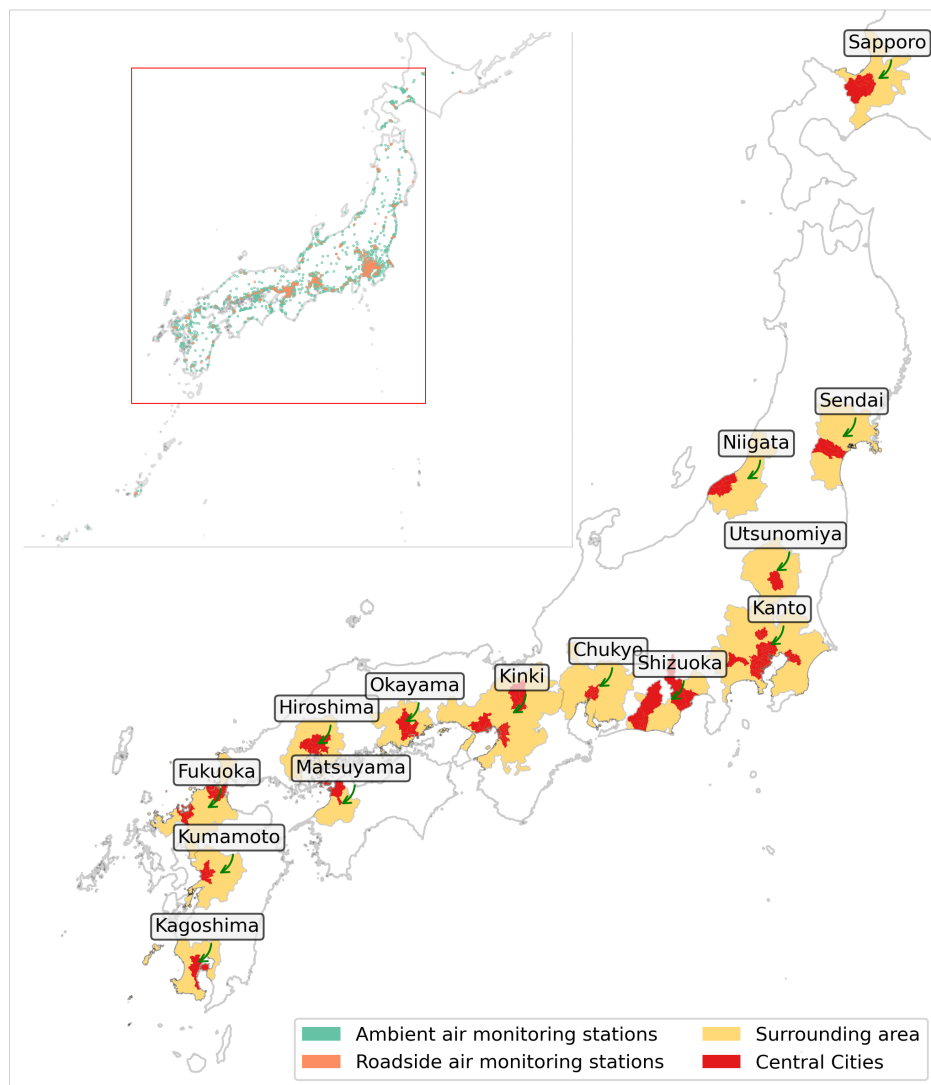


Figure 3.13. The locations of 14 metropolitan areas and the distribution of ground observations for air quality monitoring in Japan

Apart from air quality data, we incorporated ground observations of meteorological data from Japan Meteorological Agency (JMA) as input features for the BAU models used in the study. Specifically, we obtained daily records from 52 weather stations located within the same 14 MAs. At each weather station, we gathered temperature, wind direction and speed, local atmospheric pressure, and relative humidity, as suggested by (Grange et al., 2021). The corresponding meteorological parameters were extracted from the nearest weather observation site for each air quality station.

3.2.2.3 ERA5 reanalysis dataset

Alongside the weather data collected from the ground stations in the NIES database, for the features of the BAU models, we incorporated additional daily data pertaining to boundary layer height, total cloud cover, downward solar radiation (SR), and total precipitation, as recommended by (Shi et al., 2021). This supplementary information was sourced from the ERA5 reanalysis dataset (ERA5 hourly data on single levels from 1940 to the present) obtained from the Climate Data Store of the Copernicus Climate Change Service. Additionally, the ERA5 2m temperature variable (T2M) and SR will be utilized to assess the variation of sunny conditions during both the lockdown and post-lockdown periods within the study area. The original ERA5 data possesses a spatial resolution of $0.25^\circ \times 0.25^\circ$.

3.2.2.4 Sentinel 5P TROPOMI

In this study, we utilized the Sentinel 5P (S5P) Tropospheric Monitoring Instrument (TROPOMI) data to evaluate the tropospheric formaldehyde-to- NO_2 ratio (FNR) specifically for the year 2020. This ratio serves as a key indicator for the sensitivity of tropospheric ozone production. The tropospheric NO_2 and formaldehyde (HCHO –as a proxy for NMVOCs) data was obtained from the S5P L3 product “OFFL/L3_ NO_2 ” (based on processor version 1.2.x and 1.3.x) and “OFFL/L3_HCHO” (based on processor version 1.1.x) collections from Google Earth Engine, respectively. To generate the comprehensive L3 S5P product, each operational level (L2) product underwent preprocessing and mosaicking using the harpconvert tool. The low-quality pixels was filtered out in L3 NO_2 product by

excluding those with QA values below 75% for the band tropospheric NO₂ column number density. The resulting data, ready for download, is available with a spatial resolution of about 1×1 km².

3.2.2.5 Biogeochemical modelled CH₄ budget

In our assessment of CH₄ emission variations, with a specific focus on emissions from natural sources such as wetlands, we utilized CH₄ budget data obtained from the Vegetation Integrative SImulator for Trace gases (VISIT) (Ito et al., 2019). VISIT is a biogeochemical model that takes into account historical land use and climatic conditions to estimate CH₄ emissions (Ito et al., 2019). The CH₄ budgets generated by the VISIT model are now available and accessible through the Global Environmental Database provided by NIES, Japan (Ito et al., 2019). We utilized the global data versions “Ver.2021.1_CH₄Wetl_Cao” (Ito, 2021a), and “Ver.2021.1_CH₄Wetl_WH” (Ito, 2021b), which incorporate Cao scheme (Cao et al., 1996), and Walter and Heimann scheme (WH scheme) (Walter and Heimann, 2000), to estimate CH₄ emission for each MA, which offers CH₄ emission information at a spatial resolution of 0.5° × 0.5°.

3.2.3 Method

3.2.3.1 Business-as-usual (BAU) modelling

To accurately quantify the actual change in the levels of the four pollutants, we developed a weather normalization model under BAU conditions using machine learning. This model was specifically designed to simulate pollutant levels without the influence of COVID-19 restriction measures, using meteorological, spatial, and temporal features as inputs. The meteorological predictors utilized in our model include ground observation data such as temperature, wind direction and speed, local atmospheric pressure, and relative humidity. Additionally, we incorporated data from the ERA5 reanalysis dataset, which comprises boundary layer height, total cloud cover, downward solar radiation, and total precipitation. Temporal predictors included the Julian date (the number of days since January 1) and the day of the week. Furthermore, latitude and longitude coordinates of each station were utilized as spatial predictors. To develop the weather normalization

models for each pollutant at both AAMS and RsAMS, we utilized data from the years 2016 to 2019, which offers a comprehensive timeframe to account for the diverse air pollution concentration fluctuations experienced across various meteorological conditions. Extending the period, such as from 2010 to 2019, would not accurately represent recent air quality trends due to the impact of past air pollution reduction policies. Conversely, a shorter timeframe, such as the pre-lockdown period months would not adequately capture the full range of meteorological variations. Overall, four separate weather normalization models were developed for each pollutant (NO_2 , O_3 , CO, and CH_4), taking into account the specific station type (RsAMS and AAMS).

Table 3.6. The performance of BAU model on the test set (30% station data) with the following metrics: Pearson correlation coefficient (R), root mean square error (RMSE), normalized root mean square error (NormRMSE) and mean bias error (MBE), normalized mean bias error (NormMBE). For the normalized MBE and RMSE, we normalize values for each station and then compute the mean

Pollutants	Station type	R	RMSE	NormRMSE	MBE	NormMBE
NO_2	AAMS	0.89	3.13	0.15	-0.12	-0.07
	RsAMS	0.88	4.84	0.10	0.30	-0.03
O_3	AAMS	0.96	3.75	0.02	-0.37	-0.02
	RsAMS	0.96	4.92	0.06	-3.18	-0.16
CO	AAMS	0.73	0.84	0.17	0.00	-0.07
	RsAMS	0.77	1.23	0.13	0.39	0.04
CH_4	AAMS	0.82	3.75	0.00	-0.29	0.00
	RsAMS	0.80	3.82	0.00	-0.26	0.00

We employed the LightGBM machine learning model (Ke et al., 2017), a gradient boosting decision tree algorithm, to construct the BAU model using the aforementioned predictors. To fine-tune the model's hyperparameters, we utilized Fast and Lightweight AutoML Library (FLAML) (Wang et al., 2021), a lightweight library specifically designed for accurately identifying optimal hyperparameters for models. During the training process, we utilized 70% of the station data within each metropolitan area (MA), while the remaining 30% was reserved

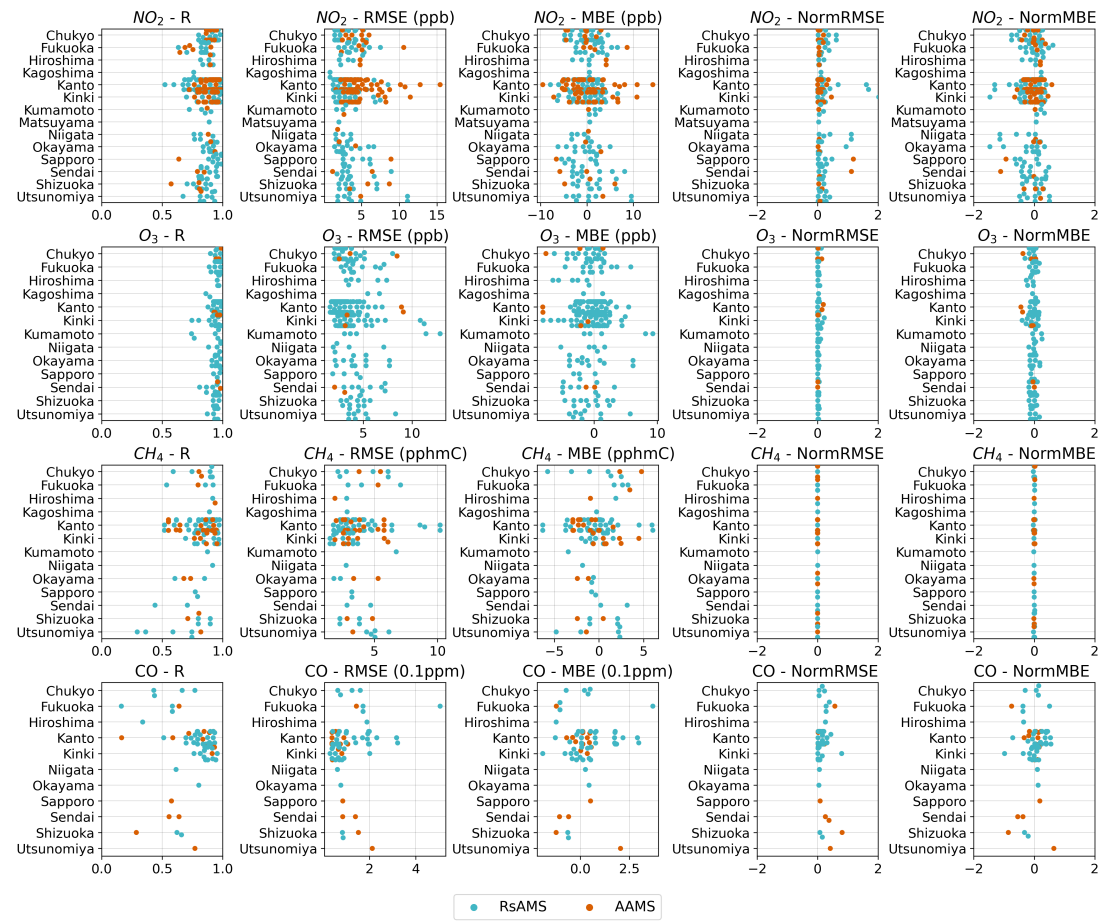


Figure 3.14. The details score of each station in the test set. For each station in the test set, we calculated the following scores and display it in this figure: Pearson correlation coefficient (r), root mean square error (RMSE), normalized root mean square error (NormRMSE) and mean bias error (MBE), normalized mean bias error (NormMBE)

for validating the model's performance. Both the training and test data sets were randomly selected for each MA, ensuring unbiased representation across the dataset.

In order to evaluate the performance of the BAU model we utilized the following metrics mean bias error (MBE), normalized mean bias error (NormMBE), root mean square error (RMSE), normalized root mean square error (NormRMSE) and Pearson correlation coefficient (R) as suggested by (Grange et al., 2021).

1610 The detailed results are presented in Figure 3.14 for each pollutant and station,
1611 average scores are shown in Table 3.6. In general, the model demonstrated strong
1612 performance with high R values (mostly $R > 0.8$) and low MBE and RMSE scores
1613 when applied to the test set for NO_2 , O_3 , and CH_4 . Regarding CO, the model
1614 achieved a satisfactory R value ($R > 0.73$).

1615 **3.2.3.2 Experiments design**

1616 Our aim is to assess the alterations in NO_2 levels within 14 MAs during both
1617 the lockdown and post-lockdown periods in 2020. We also intend to explore how
1618 changes in NO_2 may influence the shifts in O_3 and CH_4 levels in each of these
1619 timeframes. Notably, we were motivated to undertake this investigation based on
1620 an observation of an unusual O_3 response to NO_2 reduction in the Greater Tokyo
1621 Area (Damiani et al., 2022), prompting me to study the response of O_3 and CH_4
1622 in all 14 MAs across Japan.

1623 We conducted three experiments to assess the impacts of NO_2 changes on O_3
1624 and CH_4 levels. In the first experiment, we focused solely on quantifying the
1625 change in NO_2 levels using the time series observations and OBS-BAU estimate
1626 which involved subtracting the BAU prediction from the observed data (OBS).
1627 In the second experiment, we expanded the analysis to include O_3 , incorporating
1628 additional variables from the ERA5 (temperature –T2M and SR) and S5P
1629 datasets (FNR and HCHO). The last experiment included CH_4 , incorporating
1630 the OBS-BAU estimate for CH_4 and NO_2 , as well as the OBS-BAU estimate for
1631 CO and simulated CH_4 emissions from wetlands using the VISIT model.

1632 For the experiments, we selected April 7 to May 25 as the lockdown period,
1633 August 1–31 as the post-lockdown period for O_3 analysis, and June 1 to December
1634 31 for CH_4 analysis. We selected these timeframes to better understand how the
1635 four air pollutants changed in response to the unforeseen COVID-19 lockdown
1636 measures and the period after the lockdown.

1637 **3.2.4 Results**

1638 **3.2.4.1 NO₂ level changes**

1639 We initially examined the monthly trend of observed NO₂ concentration levels
1640 across 1,180 stations in the 14 MAs from 2010 to 2019, and we compared these
1641 trends with the NO₂ levels observed during the lockdown in 2020 as depicted
1642 in Figure 3.15a. The results indicate that the actual reduction in NO₂ levels
1643 during the lockdown in 2020 were lower than the trend observed during 2010–
1644 2019, specifically 2.7 ppb for RsAMS and 2.2 ppb for AAMS. This implies that
1645 the NO₂ levels observed during the lockdown were equivalent to those in 2023 for
1646 RsAMS and 2025 for AAMS, based on the trend observed during 2010–2019.

1647 Prior studies have indicated the importance of considering meteorological fac-
1648 tors when evaluating the effects of intervention measures (Ordóñez et al., 2020;
1649 Grange et al., 2021; Shi et al., 2021). In order to accurately assess the impact of
1650 the lockdown while isolating the effects of weather conditions, we computed the
1651 OBS-BAU estimates for all MAs as depicted in Figure 3.15b. Additionally, Figure
1652 3.15c presents the complete time series of NO₂ levels in 2020 (OBS), the expected
1653 levels without the lockdown (BAU), and the average data from 2016–2019 for four
1654 MAs (Kanto, Kinki, Chukyo, Fukuoka). We only show the figures for four MAs to
1655 avoid overwhelming complexity and to provide a more manageable representation
1656 of the figures.

Table 3.7. OBS-BAU estimates for NO₂ during the lockdown (April 7 to May 25) and post-lockdown (August 1 to 31). For timeseries estimate, we considered all days of the week. However, when considering weekday, we only included Monday to Friday, while for weekends, we only accounted for Sunday and Saturday. The values are represented as mean (standard deviation)

Station type	Lockdown (April 7 –May 25)			Post-lockdown (August 1–31)		
	Timeseries (%)	Weekday (%)	Weekend (%)	Timeseries (%)	Weekday (%)	Weekend (%)
AAMS	-14.5 (12.1)	-12.9 (14.3)	-18.4 (8.6)	-10.2 (7.3)	-6.8 (7.8)	-17.2 (8.3)
RsAMS	-19.1 (13.5)	-18.0 (14.2)	-21.9 (13.9)	-18.1 (11.2)	-13.6 (12.3)	-27.4 (10.0)

1657 Overall, NO₂ levels exhibited a decline across most MAs. The decline in emis-

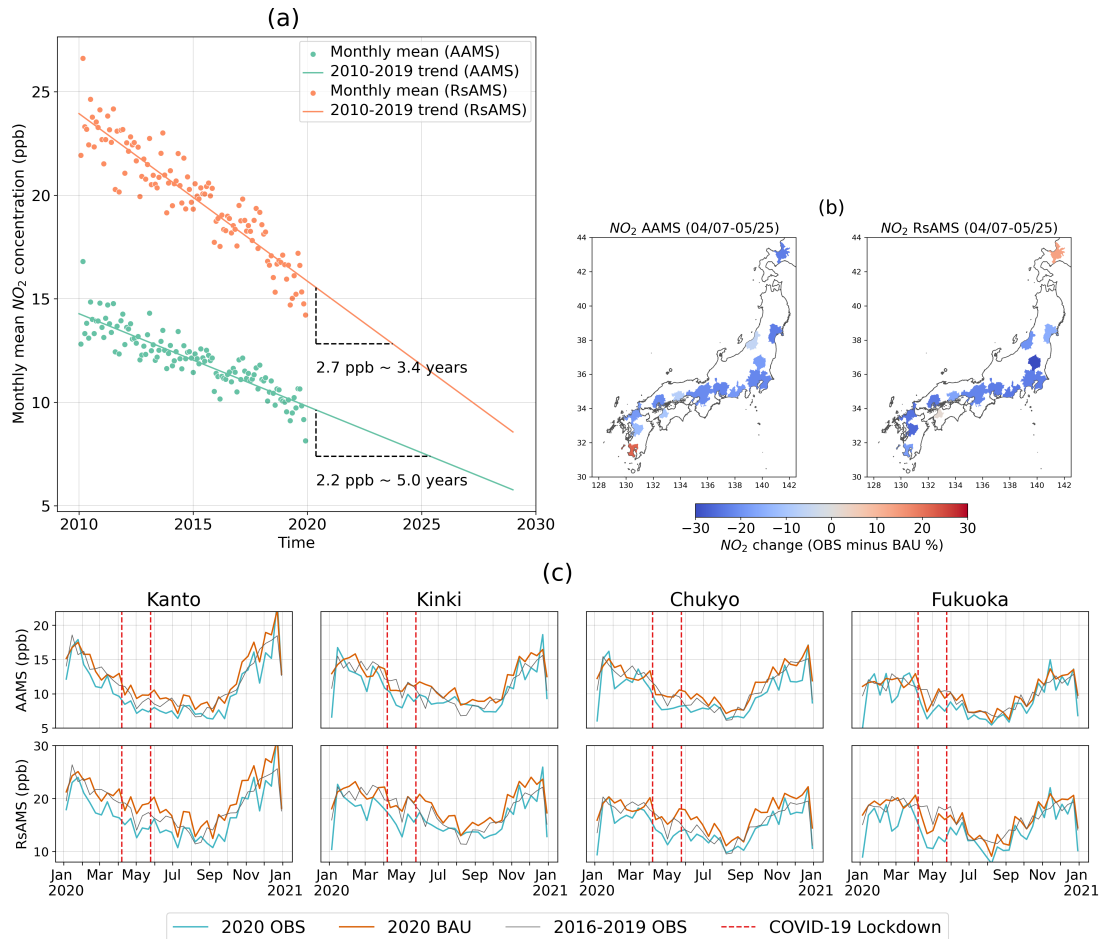


Figure 3.15. (a) Mean ground observation trend with the reduction in NO_2 due to the lockdown in 2020 for AAMS and RsAMS, (b) map visualization of the OBS-BAU estimate for NO_2 during the lockdown period, (c) seven-day rolling mean of 2020 observation (OBS), BAU prediction (BAU), and mean level of NO_2 from 2016 to 2019 for four MAs

sions was particularly significant in RsAMS compared to AAMS in most MAs, with an average reduction of 19.1% and 14.5% respectively. However, these reductions were smaller compared to those observed in European cities (Barré et al., 2021; Grange et al., 2021). Additionally, we observed that the reduction in NO_2 levels during weekends was more significant than on weekdays, primarily due to a substantial decrease in mobility during weekends compared to weekdays (refer

to Figure 3.12b). During the lockdown the average reduction in NO₂ levels for AAMS was 12.9% on weekdays and 18.4% on weekends. As for RsAMS, the average reduction stood at 18% on weekdays and 21.9% on weekends. For most MAs, even though the lockdown was lifted at the end of May 2020, the NO₂ levels continued to decline until the end of December 2020. This continued decrease may be attributed to the sustained reduction in mobility from the start of the lockdown through the end of 2020 (Figure 3.12a). These findings are summarized in Table 3.7 and Table 3.9.

3.2.4.2 O₃ level changes

In this experiment, we investigated various parameters to gain a better understanding of the changes in O₃ in response to the reduction of NO₂ caused by COVID-19 social distancing policies. Alongside the OBS-BAU estimates, we examined standardized anomalies of T2M and SR between 2020 and 2016-2019 period, S5P FNR in 2020, and changes in S5P HCHO between 2020 and 2019. These parameters were analyzed for two distinct periods: the lockdown period and the post-lockdown (August 1 –31), 2020.

Changes during the lockdown period

During the lockdown period (April 7 to May 25), we observed a slight change in O₃ levels across most MAs (Figure 3.16 second row and Figure 3.17). On average, there was a reduction of 2.3% in AAMS and 0.6% in RsAMS, as indicated in Table 3.8. Although the overall trend showed a decrease, we did find instances of increased O₃ levels in certain MAs, particularly in RsAMS such as Kanto (1.6%), Kinki (2.2 %), and Fukuoka (3.5 %), as depicted in Figure 3.16 (second row). Moreover, we observed the existence of an ozone weekend effect in the changes of O₃ levels, indicating higher increase in O₃ mixing ratios during weekends in comparison to weekdays (Akimoto and Tanimoto, 2022). This effect was observed in the OBS-BAU estimates for RsAMS in Fukuoka (increased 8.8% - weekends, 1.3% - weekdays) and Kinki (increased 4.9% - weekends, 1.2% - weekdays). The observed slight decrease in O₃ levels across most MAs in Japan contrasts with the trends observed in many other major cities worldwide (Shi et al., 2021; Grange et al., 2021), where significant increases in O₃ levels have been observed. For in-

stance, after accounting for weather effects, notable increases have been reported in Beijing (28.9 %), Wuhan (44.5 %), Milan (66.8 %) Rome (55.8 %), New York (17.4 %), Los Angeles (14.8 %), and Delhi (26.2 %) by (Shi et al., 2021).

To explore this variation further, we analyzed the disparity in T2M and SR between the corresponding period of 2020 and the reference period 2016-2019 as shown in Figure 3.16 (3rd row). We observed small positive SR anomalies in the southeast region of Japan and negative SR anomalies in the northeast region. Additionally, across the entire country, negative T2M anomalies were observed. The presence of negative T2M anomalies and fluctuating SR levels suggests that the prevailing weather conditions during this period impeded the production of O_3 .

Table 3.8. OBS-BAU estimates for O_3 during the lockdown (April 7 to May 25) and post-lockdown (August 1 to 31). For timeseries estimate, we considered all days of the week. However, when considering weekday, we only included Monday to Friday, while for weekends, we only accounted for Sunday and Saturday. The values are represented as mean (standard deviation)

Station type	Lockdown (April 7 –May 25)			Post-lockdown (August 1–31)		
	Timeseries	Weekday	Weekend	Timeseries	Weekday	Weekend
	(%)	(%)	(%)	(%)	(%)	(%)
AAMS	-2.3 (2.7)	-2.7 (3.2)	-1.2 (2.7)	2.2 (15.6)	3.2 (15.3)	0.0 (18.8)
RsAMS	-0.6 (2.7)	-1.4 (2.7)	1.4 (3.7)	8.9 (10.7)	8.9 (12.3)	8.6 (12.7)

Changes during the August, 2020

In August 2020, the NO_2 levels continued to decline in all MAs, albeit at a slower rate compared to the lockdown period, as shown in Table 3.8. However, during this period, we observed a more noticeable increase in O_3 levels across most MAs compared to the lockdown. On average, there was a 8.9% increase for RsAMS and a 2.2% increase for AAMS. Notably, the increase in O_3 levels during weekends was more significant than on weekdays in Niigata, Okayama, Kinki and Sendai. Specifically, For AAMS of Niigata, O_3 levels experienced a 9.4% increase on weekends and a 5.8% increase on weekdays. In RsAMS of Okayama, O_3 levels saw a 13% increase on weekends, exceeding the 10.6% increase observed on

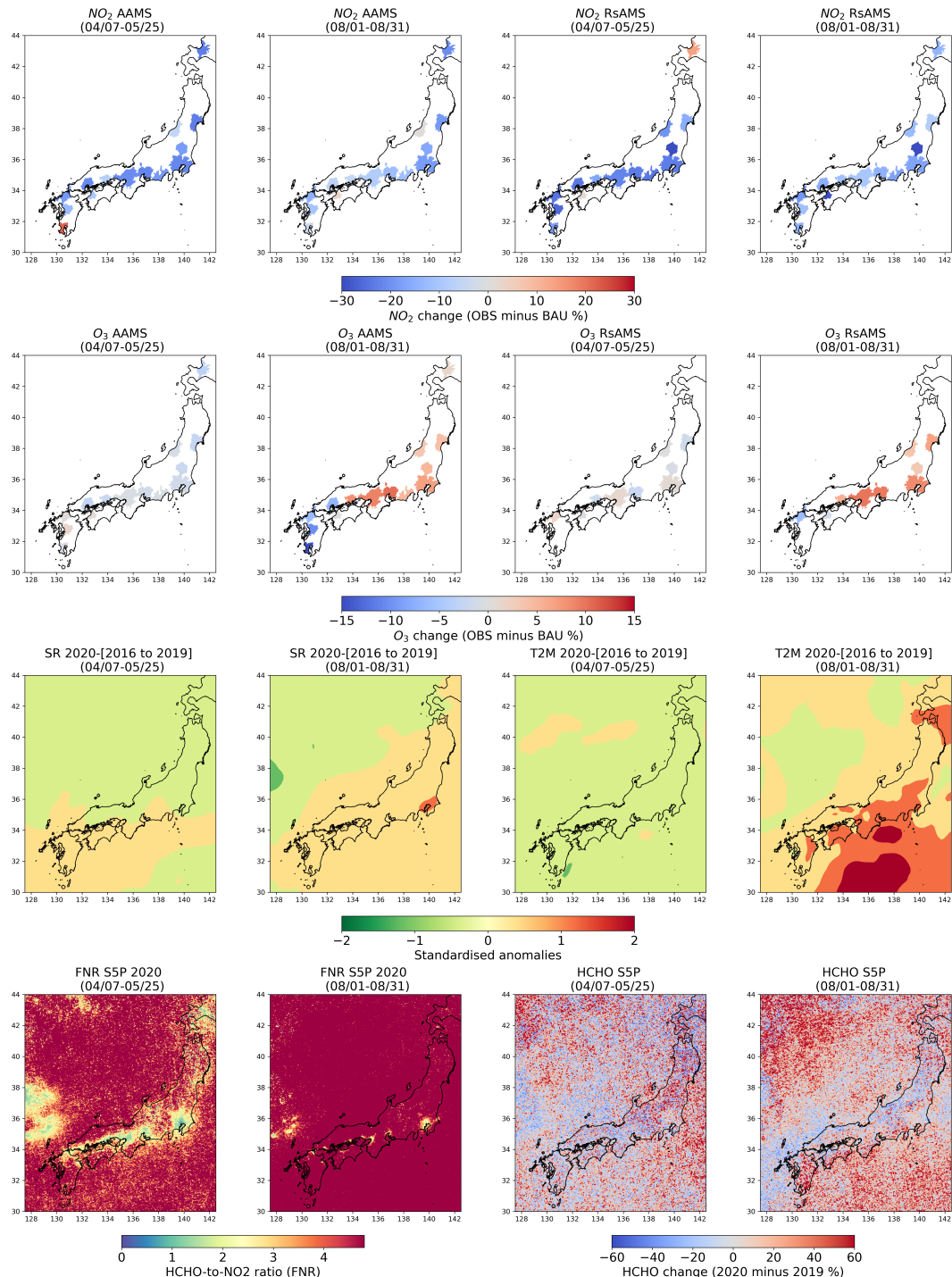


Figure 3.16. The first and third columns show the plots for the lockdown (April 7 to May 25). The second and last columns show the plots for August 1 – 31. First row: The OBS-BAU estimates of NO_2 for AAMS and RsAMS. Second row: The OBS-BAU estimates of O_3 for AAMS and RsAMS. Third row: The standardised anomalies of downward solar radiation (SR) and temperature (T2M) from ERA5 dataset. Last row: The formamide-to- NO_2 (FNR) ratio in 2020 and the HCHO change between 2020 and 2019 from Sentinel 5P data.

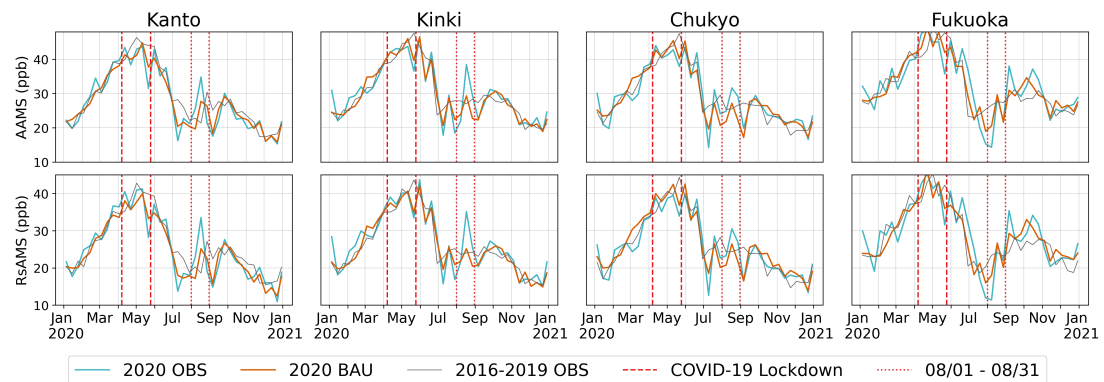


Figure 3.17. Seven-day rolling mean of 2020 observation (OBS), BAU prediction (BAU), and mean level of O₃ from 2016 to 2019 for 4 MAs (Kanto, Kinki, Chukyo, and Fukuoka)

1716 weekdays. Similarly, in AAMS in the Kinki region, O₃ levels exhibited a weekend
 1717 increase of 19.8%, surpassing the 17.4% increase observed on weekdays. In Sendai,
 1718 the increase during weekends was even more pronounced, with a 15.6% increase
 1719 for AAMS and a 22% increase for RsAMS, whereas on weekdays the increase
 1720 was 5.1% for AAMS and 9.8% for RsAMS. This observation could be attributed
 1721 to the greater reduction in movement during weekends compared to weekdays in
 1722 these MAs (Figure 3.12b).

1723 In order to investigate the differences in O₃ levels between August and the
 1724 lockdown period, we examined the standard anomalies of SR and T2M in August
 1725 2020, comparing them to the 2016-2019 period. Our analysis revealed positive
 1726 anomalies in both SR and T2M across all MAs, as shown in Figure 3.16 (3rd
 1727 row). These favorable weather conditions, combined with the reduced levels of
 1728 NO₂, likely facilitated increased O₃ production.

1729 Although there was an overall trend of increasing O₃ levels during this period,
 1730 we did observe a reduction in O₃ levels in five MAs which is located in the
 1731 southern region: Hiroshima (AAMS: 13.7%), Matsuyama (AAMS: 1%, RsAMS:
 1732 3%), Fukuoka (AAMS: 12.5%, RsAMS: 12.3%), Kumamoto (AAMS: 20.7%), and
 1733 Kagoshima (AAMS: 29.9%). To understand the decrease in O₃ levels observed
 1734 in these five MAs, we utilized the S5P FNR for 2020, as well as the changes in
 1735 HCHO as a proxy for NMVOCs between 2020 and 2019. The FNR is commonly

used to assess the sensitivity of near-surface O₃ levels (Martin et al., 2004). As suggested by (Duncan et al., 2010), when the FNR is below 1, the O₃ production regime is considered VOC-limited, and when it exceeds 2, it is considered NO_x-limited. When the FNR values fall within the range of 1–2, O₃ is expected to be in the transition regime (Duncan et al., 2010). However, it has been observed that the FNR can vary by region (Jin et al., 2020; Irie et al., 2021; Souri et al., 2023; Ren et al., 2022), and the assumption that it lies within the 1–2 range may not hold true at the global level (Schroeder et al., 2017). Hence, it might be essential to calculate this ratio on a regional scale (Damiani et al., 2022; Schroeder et al., 2017). Despite the FNR showing high variability in the region, it still provides information about the trend of O₃ production regimes in our study.

Figure 3.16 (last row) presents the FNR across all MAs indicating a shift in the O₃ production regime from VOC-limited during the initial lockdown to NO_x-limited in August. This transition is evident as the FNR changes from $0 < \text{FNR} < 2$ during the lockdown to $\text{FNR} > 4$ in August. During the VOC-limited regime, a decrease in NO_x typically leads to an increase in O₃ levels (Duncan et al., 2010). However, in the NO_x-limited regime, a reduction in NO_x can also result in a decrease in O₃ levels (Duncan et al., 2010). In Figure 3.16 (last row), we can observe that the NO_x-limited regime dominates the five MAs of Hiroshima, Matsuyama, Fukuoka, Kumamoto, and Kagoshima. Despite NO₂ levels continuing to decline during this period, the HCHO levels exhibited a more significant increase in these MAs compared to the lockdown period. This could explain the reduction in O₃ levels observed in these five southern MAs.

We elucidated the difference in O₃ levels between major MAs in Japan and other large urban areas worldwide by examining meteorological changes (T2M, SR), and variations in O₃ precursors levels by utilizing S5P FNR derived from S5P NO₂ and HCHO measurements. The difference can be attributed to the absence of sunny conditions during the lockdown period. However, in August, when sunny conditions became more prevalent, we observed an increase in O₃ levels in response to the sustained reduction in NO₂ levels across most MAs, which are likely VOC-limited areas. Based on the analysis of S5P data, it appears that the southern metropolitan areas (MAs) exhibited a predominant NO_x-limited trend during August 2020, potentially due to the increased presence of biogenic VOCs

(BVOCS). However, the monitoring of BVOCS emissions remains challenging due to limited observations (Tani and Mochizuki, 2021; Ito and Ichii, 2021). Therefore, it is also important to pay attention to those NO_x-limited areas, as future reductions in anthropogenic NMVOCs may have minimal effectiveness in reducing O₃ levels (Akimoto and Tanimoto, 2022).

3.2.4.3 CH₄ level changes

In this experiment, we analyze the OBS-BAU estimates for NO₂, CO, and CH₄, and incorporate the VISIT model's simulated CH₄ emissions from wetlands to investigate the changes in CH₄ levels during the 2020 lockdown and post-lockdown period. Our focus is on understanding the relationship between the reduction in NO₂ and its potential impact on OH (hydroxyl radicals), as well as the contrasting effect of CO. The decrease in NO₂ levels is expected to result in a reduction in OH, while reductions in CO can increase OH levels and shorten the lifetime of CH₄ (Akimoto and Tanimoto, 2022).

During the lockdown period, we observed a marginal rise in CH₄ levels across most MAs (Figure 3.18 third row and Figure 3.19b), with an average increase of 0.6% for AAMS and 0.8% for RsAMS (Table 3.9). While NO₂ levels decreased in most MAs (Figure 3.18 first row), the trend for CO varied (Figure 3.18 second row and Figure 3.19a). AAMS showed an average decrease of 10.9% in CO levels, while RsAMS saw a slightly smaller reduction 8.8%. Notably, CO levels significantly increased in RsAMS of Kagoshima (60.6%), while slight increases were observed in Kanto AAMS, and in Matsuyama for both RsAMS and AAMS. It is worth noting that although the increases in CO levels in Kagoshima were significant, this region have among the lowest natural CH₄ emissions in Japan as Figure 3.18 (last row), which explains the slight increase in CH₄ observed in this MA.

During the post-lockdown period from June to December 2020, NO₂ levels continued to decrease, showing an average reduction of 12.8% for AAMS and 18.3% for RsAMS (Table 3.9) which is smaller than during the lockdown period. In contrast, CO levels started to recover as the COVID-19 lockdown was lifted, with a smaller reduction of 5.7% for AAMS and 5.5% for RsAMS. Notably, significant increases in CO levels were still evident at RsAMS in Kagoshima (62.2%). In

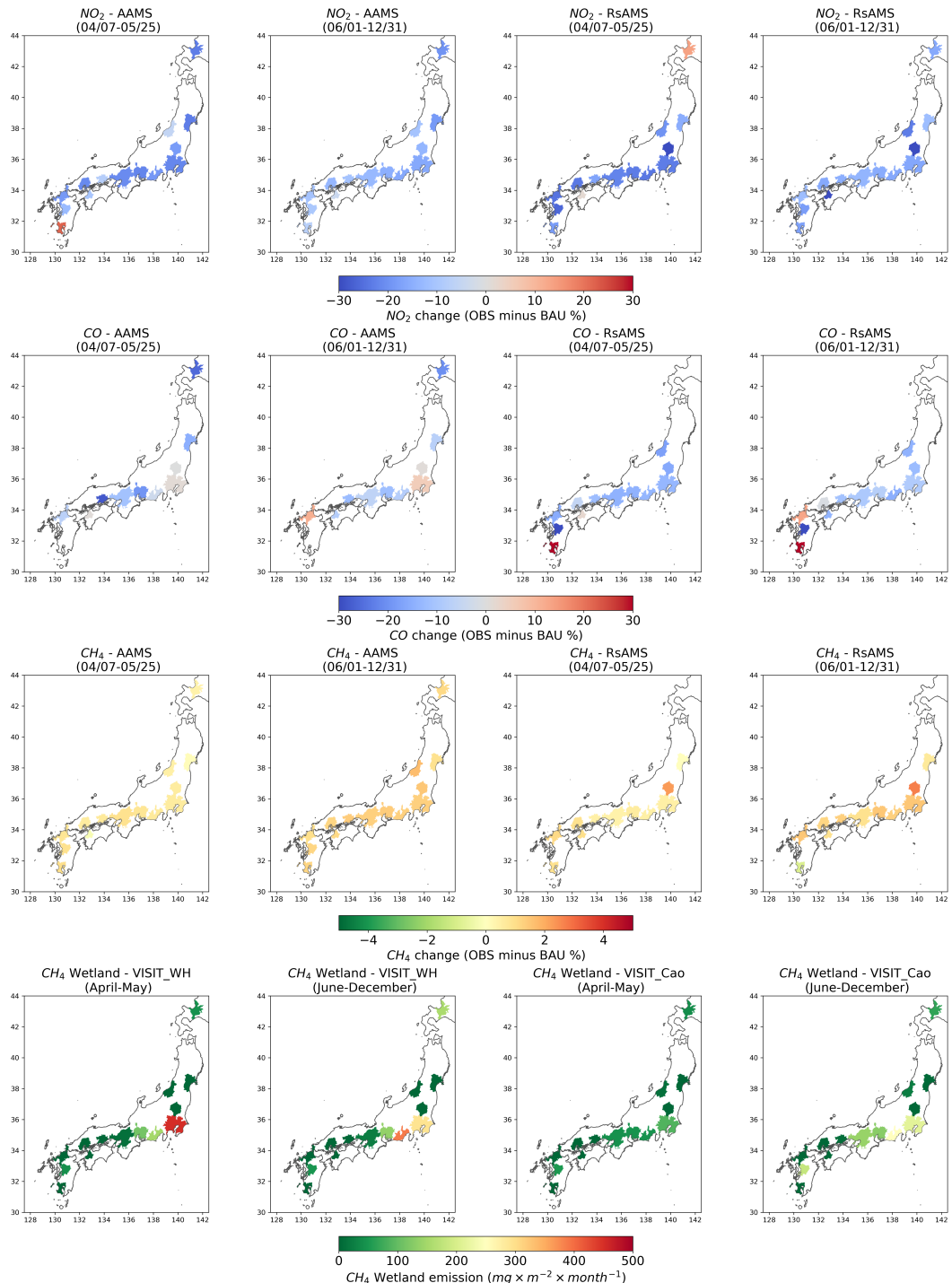


Figure 3.18. First and third columns show the plots for the lockdown (April to May). Second and last columns show the plots for the post-lockdown (June to December). First row: The “OBS-BAU” estimates of NO₂ for AAMS and RsAMS. Second row: The “OBS-BAU” estimates of CO for AAMS and RsAMS. Third row: The “OBS-BAU” estimate of CH₄ for AAMS and RsAMS. Last row: The CH₄ emission from wetland based on the simulation of VISIT model with Walter and Heimann scheme and Cao scheme.

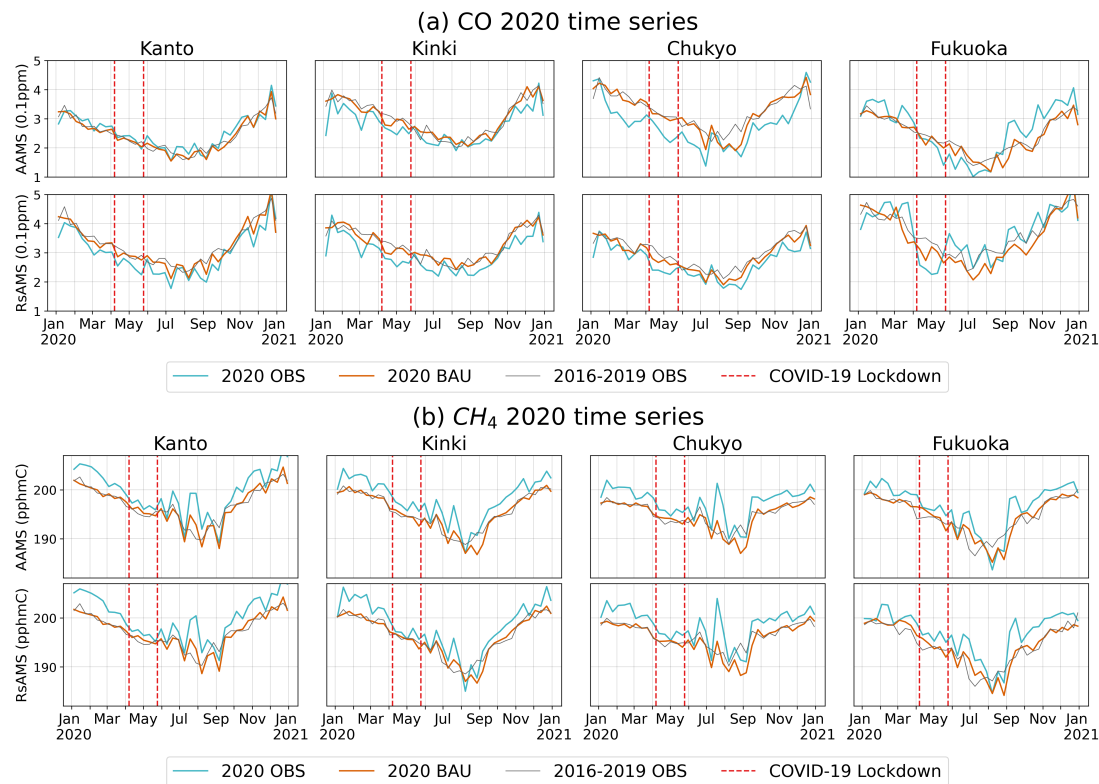


Figure 3.19. The seven-day rolling mean of 2020 observation (OBS), BAU prediction (BAU), and mean level of CO (a) and CH₄ (b) from 2016 to 2019 for 4 MAs (Kanto, Kinki, Chukyo, and Fukuoka)

1801 Fukuoka we also observed a steady rise of CO levels in both RsAMS (13%) and
 1802 AAMS (11.5%). In response to these changes in NO_x and CO, we observed a
 1803 greater increase in CH₄ levels during this period, with a rise of 1.3% for AAMS
 1804 and 1.1% for RsAMS.

1805 In general, we saw a slight increase in CH₄ levels both during the lockdown
 1806 and the post-lockdown periods, based on the OBS-BAU estimates. However, a
 1807 more pronounced increase in CH₄ was observed during the post-lockdown phase
 1808 in AAMS when compared to RsAMS, which can be attributed to the more sub-
 1809 stantial recovery of CO levels in AAMS relative to the lockdown period. Although
 1810 it has been reported that global CH₄ growth in 2020 is primarily attributed to
 1811 the atmospheric sink resulting from lower anthropogenic NO_x emissions (Stevens-
 1812 son et al., 2022; Peng et al., 2022), our findings regarding the contribution of

Table 3.9. OBS-BAU estimates for NO₂ and CO and CH₄ during the lockdown (April 7 to May 25) and the post-lockdown (June 1 to December 31). For CH₄ analysis we only consider timeseries estimate which include all days of the week. The values are represented as mean (standard deviation)

Pollutant	Station type	(April 7 –May 25)	(June 1 –December 31)
		(%)	(%)
NO ₂	AAMS	-14.5 (12.1)	-12.8 (4.3)
	RsAMS	-19.1 (13.5)	-18.3 (6.4)
CO	AAMS	-10.9 (11.0)	-5.7 (9.4)
	RsAMS	-8.8 (24.6)	-5.5 (25.2)
CH ₄	AAMS	0.6 (0.3)	1.3 (0.2)
	RsAMS	0.8 (0.6)	1.1 (0.9)

1813 NO_x reduction to the CH₄ growth in Japan in 2020 align with a previous study
1814 (Akimoto and Tanimoto, 2022; Qu et al., 2022; Feng et al., 2023), indicating that
1815 the impact of changes in NO_x and CO levels on the increase in CH₄ growth in
1816 Japan during the lockdown and post-lockdown period are not as significant as
1817 the impacts of the direct CH₄ emissions themselves.

1818 3.2.5 Discussion

1819 3.2.5.1 Variations in spatial resolution of multisource data

1820 Since we utilized multisource data for the analysis, we acknowledge that variations
1821 in spatial resolution among input data can influence the consistency and
1822 reliability of data analysis. In certain situations, the need for interpolation to
1823 achieve a uniform grid may arise, particularly when generating inputs for a Con-
1824 volutional Neural Network (CNN). This interpolation process inadvertently in-
1825 troduces uncertainty into the results. However, in this study, we refrained from
1826 any data interpolation and used it at its provided original resolution. The mul-
1827 tisource data was employed for two primary objectives: weather-normalization
1828 model development and visual examination.

1829 For weather-normalization model development, we used ERA5 data and ground

station data to construct the weather-normalization model. Certain variables, such as total cloud cover and boundary layer height, are exclusively available from ERA5. The ERA5 data we employed has a resolution of $0.25^\circ \times 0.25^\circ$, meaning that some stations might share identical ERA5 records. This can influence the model development, even though, ideally, local ERA5 values for each station should be distinct, albeit not significantly deviating from the $0.25^\circ \times 0.25^\circ$ spatial resolution value. To mitigate this effect on the model development, we have integrated spatial context values (latitude and longitude) and station types as additional inputs. Since these features are distinct for each station, we anticipate that they can help minimize the impact of the coarse spatial resolution from ERA5 on the model.

To visually inspect the sensitivity of tropospheric O₃ production utilizing S5P HCHO and NO₂, as well as CH₄ emission estimates from wetland, we rely exclusively on original data with consistent spatial resolution. It's important to note that our primary focus is to visually inspect the prevailing trends at the MA level, which has a spatial resolution coarser than that of any input data we utilized. Therefore, we believe that the dominant trends at the MA level remain unaffected by these spatial disparities in this particular MA-level context.

3.2.5.2 Limitations

In this research, we utilized the S5P FNR to examine the sensitivity of O₃ production. Although HCHO could be an alternative indicator for the presence of NMVOCs, the significant uncertainty in the FNR threshold from previous studies, along with the lack of NMVOCs observations and reliable satellite HCHO and NO₂ data, poses challenges in understanding O₃ level variations during and after the lockdown period. This issue is particularly crucial and warrants in-depth exploration in future studies.

Additionally, it's important to mention that the study did not include an analysis of long-range air pollution transportation from China to western MAs of Japan following the Chinese economic recovery from the pandemic (Itahashi et al., 2022). This aspect was beyond the scope of the current research but should be considered in future investigations.

3.2.6 Conclusion

This study presents an air quality analysis that examines the changes in four air pollutants, namely NO₂, O₃, CO, and CH₄, during the COVID-19 pandemic in 14 MAs of Japan from April 7 to December 31 in 2020. First, we developed a machine learning BAU model that incorporates meteorological, spatial, and temporal features to account for weather variability in air quality time series. Next, we utilized the BAU model predictions and observation data to estimate the actual reduction (OBS-BAU estimate) in NO₂ levels. We then integrated temperature and solar radiation anomalies from ERA5 reanalysis data and S5P TROPOMI data (FNR and HCHO) along with the OBS-BAU estimate to investigate the unique response of O₃ to reduced NO₂ levels during the lockdown and post-lockdown period (August 1 –31, 2020). Finally, we evaluated the impact of NO₂ and CO changes on the CH₄ levels using a combination of OBS-BAU estimate and wetland CH₄ emission simulations from the VISIT model. The main findings of the study can be summarized as follows:

Based on ground observations of NO₂, the reduction of NO₂ during the lockdown period in 2020 corresponds to a decrease equivalent to 3.4 years and 5 years of the 2010-2019 trend of NO₂ levels for roadside and ambient air monitoring stations respectively. After normalizing the meteorological effects based on BAU predictions, the NO₂ reduction was 14.5% for AAMS and 19.1% for RsAMS. The decrease in NO₂ levels is more pronounced during the weekend than on weekdays.

By analyzing ground observations of NO₂ and O₃, along with BAU simulations and meteorological data from ERA5, as well as FNR and HCHO data from S5P TROPOMI, we found that the reduction in NO₂ levels during the lockdown did not immediately result in an increase in O₃. Instead, we observed that an increase in O₃ occurred after the lockdown, specifically in August when sunny conditions were reinforced. This finding is significant for Japan, as it has not been previously reported in other studies.

Furthermore, when analyzing the ground observations of NO₂, CO, and CH₄ alongside BAU simulations and model-simulated CH₄ emissions from wetlands, we found that the changes in NO₂ and CO contributed marginally to the variations in CH₄ levels, ranging from 0.6% to 1.3%, across the study areas. This finding aligns with previous studies (Akimoto and Tanimoto, 2022; Qu et al.,

1894 2022; Feng et al., 2023), but also differs from others where the reduction in at-
1895 mospheric sink has been reported as a major contributor to increased CH₄ levels
1896 (Stevenson et al., 2022; Peng et al., 2022).

1897 Based on the findings of this study, we recommend simultaneous reduction of
1898 NO_x and NMVOCs (both anthropogenic and biogenic VOCs), to mitigate their
1899 adverse effects on future policies related to air pollution reduction and climate
1900 change mitigation at local level.

¹⁹⁰¹ 4 Terrestrial carbon fluxes ¹⁹⁰² estimation

¹⁹⁰³ This chapter is based on my paper (Phan et al., 2022), and a preprint (Phan and
¹⁹⁰⁴ Fukui, 2023b):

- ¹⁹⁰⁵ • A. Phan, K. Takejima, T. Hirakawa and H. Fukui (2022), "Forest-Related
¹⁹⁰⁶ SDG Issues Monitoring for Data-Scarce Regions Employing Machine Learn-
¹⁹⁰⁷ ing and Remote Sensing - A Case Study for Ena City, Japan," IGARSS
¹⁹⁰⁸ 2022 - 2022 IEEE International Geoscience and Remote Sensing Sympo-
¹⁹⁰⁹ sium, Kuala Lumpur, Malaysia, 2022, pp. 4343-4346, doi: <https://doi.org/10.1109/IGARSS46834.2022.9883037>.
- ¹⁹¹¹ • Anh Phan, Hiromichi Fukui (2023), FluxFormer: Upscaled Global Carbon
¹⁹¹² Fluxes from Eddy Covariance Data with Multivariate Timeseries Trans-
¹⁹¹³ former, Preprint, EarthArXiv, doi: <https://doi.org/10.31223/X5BQ2H>.

¹⁹¹⁴ 4.1 Local plant functional types mapping

¹⁹¹⁵ We proposed a combined machine learning approach with a deep convolutional
¹⁹¹⁶ neural network (CNN) to monitor forest utilization toward Sustainable Develop-
¹⁹¹⁷ ment Goals (SDGs) for data-scarce regions. First, we employed the Random For-
¹⁹¹⁸ est (RF) classifier using Google Earth Engine (GEE) for forest mapping. Then,
¹⁹¹⁹ we designed a deep CNN architecture that works for PFTs/age mapping from
¹⁹²⁰ coarse and polygonal ground-truth data. The proposed network has U-shape
¹⁹²¹ and comprises 3D Atrous Convolutions. The model was optimized by a weighted
¹⁹²² cross-entropy loss function. We trained the model with times-series Sentinel 1, 2,
¹⁹²³ and Digital Elevation Model (DEM) data with sparse annotations. Our proposed

models achieved 94.5% overall accuracy (OA) for forest mapping, 77.80% (OA) for PFTs, and 81.74% (OA) for forest age classification, respectively in Ena city, Japan. The outcome of our study indicates the potential of remote sensing and machine learning in monitoring forest development, conservation, and utilization toward SDGs from coarse ground-truth data. Our source code for the implementation is available at: https://github.com/anhp95/forest_attr_segment

4.1.1 Introduction

The pivotal role of forests in advancing Sustainable Development Goal 15 (SDG15) and addressing global climate change is widely recognized. Leveraging the capabilities of remote sensing technology and cutting-edge machine learning algorithms, the mapping of forested areas, along with the identification of PFTs and forest age, emerges as a valuable contribution to the monitoring of SDG-related issues, encompassing indicators such as 15.1.1, 15.2.1, and 15.4.2.

While forest mapping is a familiar task in land-cover/land-use classification, generating a detailed map specifying plant functional types (PFTs) and forest age introduces heightened complexity. Previous studies focusing on PFTs/age classification often relied on either high-resolution input data or ground-truth information at the point level, as evidenced in the works of (Schiefer et al., 2020; La Rosa et al., 2021; Lee et al., 2016). However, these resources are known to be expensive, time-consuming to collect, and infrequently available in specific regions, particularly in developing areas. In response to these challenges, this study introduces a methodology aimed at monitoring forest areas, PFTs, and forest age, utilizing coarse annotations and freely available remote sensing data.

The approach begins with the application of a Random Forest (RF) classifier to classify forested areas. Subsequently, a deep Convolutional Neural Network (CNN) architecture is designed for the segmentation of PFTs and forest age. Notably, our proposed methodology demonstrates its efficacy in regions where data scarcity is a significant concern.

The structure of this study unfolds as follows: Section 4.1.2 provides insights into the study area and the data utilized in the study. Section 4.1.3 delves into the overall methodology employed, and the experimental results within the study area are expounded upon in Section 4.1.4. Finally, Section 4.1.5 encapsulates the

1956 conclusion of the study, highlighting avenues for future research and development.

1957 4.1.2 Data

1958 4.1.2.1 Study area

1959 The focal point of our investigation is Ena city (see Figure 4.1), strategically
 1960 positioned in the southeastern expanse of Gifu prefecture, nestled within the
 1961 heart of Japan. Encompassing an expansive total area of approximately 504
 1962 square kilometers, the city boasts an elevation of 282 meters, contributing to its
 1963 diverse topography. The climate exhibits a noteworthy annual temperature range,
 1964 spanning from a minimum of 2 °C to a maximum of around 26.4 °C, showcasing
 1965 the dynamic climatic conditions that characterize the region.

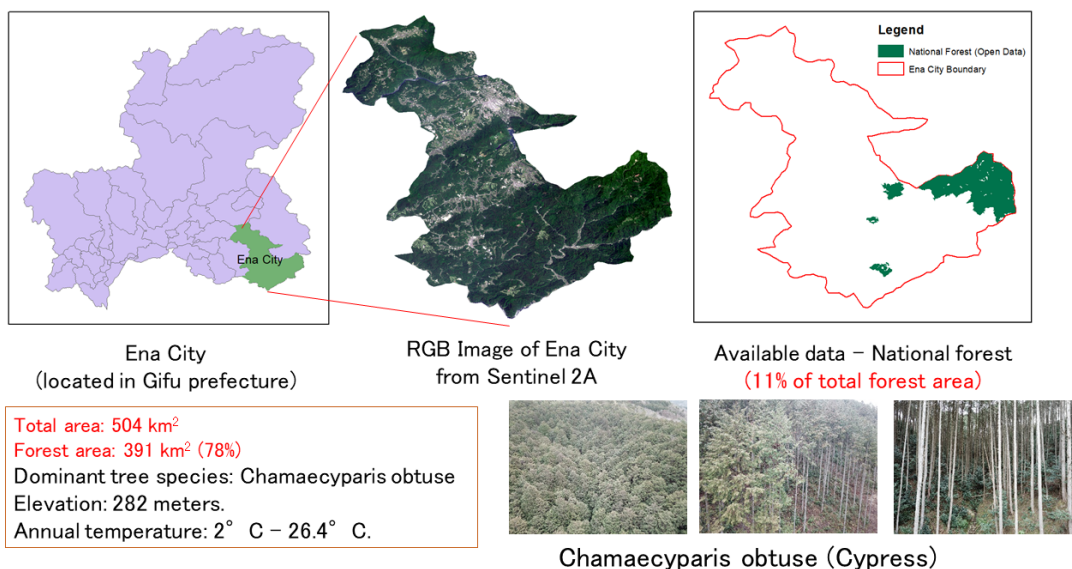


Figure 4.1. Ena city and national forest in Ena city.

1966 A compelling facet of Ena city lies in its rich forest cover, a significant portion
 1967 of which, as reported by local government statistics, comprises artificial forests,
 1968 constituting 60% of the total forested area. The dominant species within these
 1969 artificial forests is Chamaecyparis obtusa. This coniferous species plays a pivotal
 1970 role in the city's ecosystem, serving multifaceted purposes such as timber pro-

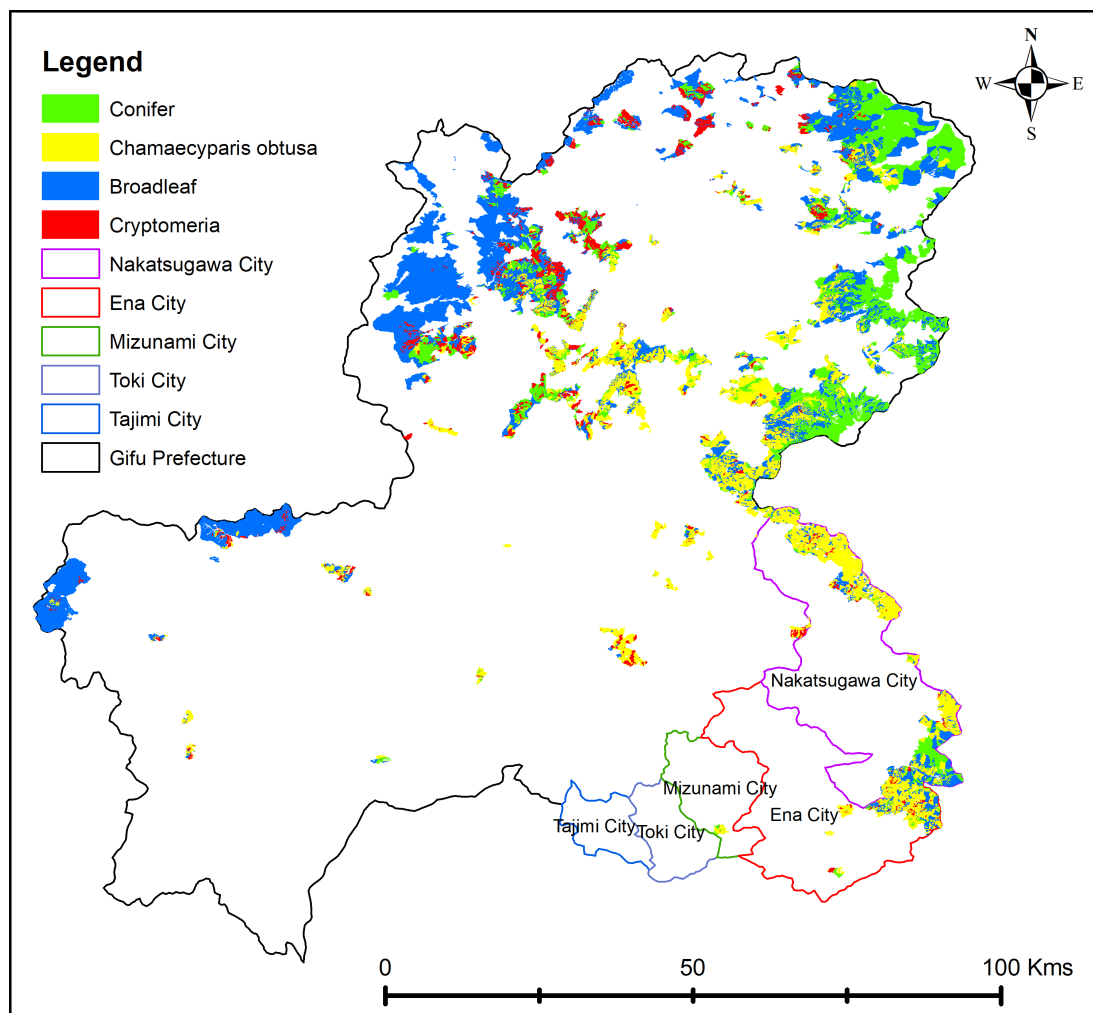
duction, prevention of water-related disasters, and the sequestration of carbon dioxide (CO_2). Notably, the artificial forest, largely populated by *Chamaecyparis obtusa*, underscores its significance as a valuable resource for sustainable timber harvesting, acting as a buffer against potential water-related calamities, and contributing to the mitigation of greenhouse gas emissions through effective CO_2 sequestration. This intricate interplay of environmental elements highlights the intricate web of ecological services provided by Ena city's forests, emphasizing their integral role in the broader context of regional sustainability and resilience.

4.1.2.2 Data collection

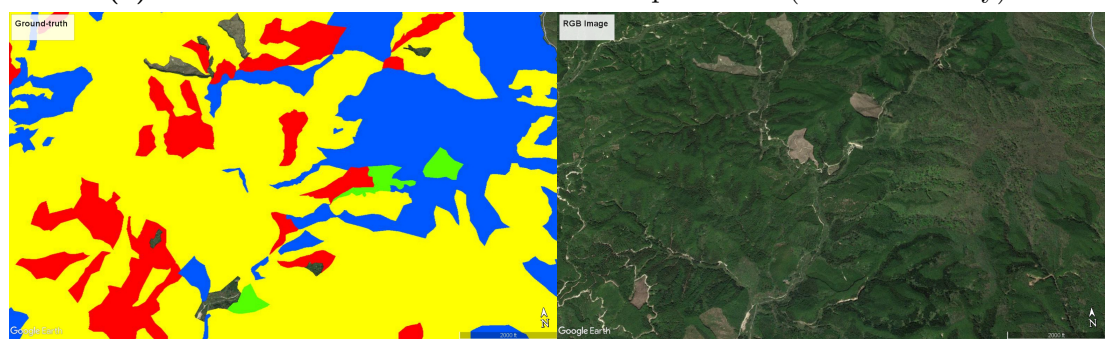
In our forest mapping approach, the creation of a training set involved a random selection of 750 forest and 250 non-forest points, alongside a validation set comprising 300 forest and 100 non-forest points. This selection was based on the 2016 land-use map provided by the National Land Information Portal. Transitioning to the task of mapping PFTs and forest age, our labeled data was sourced from the same repository. The ground-truth information, represented as coarse polygons, delineates mixed-species zones, with each polygon annotated according to the most dominant PFTs in that particular area. Notably, this ground-truth data is restricted to national forest areas, presenting a limitation in its coverage. To address this constraint, given the relatively small portion (11%) of national forest data available for Ena city, we supplemented our dataset with the annotations collected in 2018 from Gifu prefecture to enhance model training (Figure 4.2).

Our utilization of remote sensing resources encompassed Sentinel 1A, Sentinel 2 L1C, and a Digital Elevation Model (DEM), each featuring spatial resolutions of 10m, 10m, and 30m, respectively. The dataset comprises 11 spectral channels, encompassing the Red, Green, Blue, Red Edge, Near-infrared, Short-wave infrared, and Normalized Difference Vegetation Index (NDVI) from Sentinel 2, along with the VV and VH bands from Sentinel 1A. Additionally, the DEM data is derived from the NASA Shuttle Radar Topography Mission digital elevation model, providing crucial elevation information. This comprehensive dataset serves as the input features for our machine learning model.

In the subsequent sections, we describe the specifics of acquisition times for Sentinel 1 and Sentinel 2, pertaining to the segmentation of PFTs and forest age,



(a) Annotations of national forest in Gifu prefecture (black boundary)



(b) Example of annotated area

(c) The corresponding RGB image

Figure 4.2. (a) The designated study area outlined in red is Ena city, (b) demonstrates coarse annotations as an illustrative example, and (c) showcases the corresponding RGB image sourced from Google Earth.

as well as forest mapping. Recognizing the dynamic nature of forest ecosystems and evolving land-use patterns, the temporal dimension of data acquisition plays a crucial role in maintaining the relevance and accuracy of our models.

4.1.3 Methodology

The proposed workflow is depicted in Figure 4.3a. Initially, the Sentinel 1 data was obtained directly from Google Earth Engine (GEE). Each pixel represents the backscatter coefficient and undergoes a series of preprocessing steps, including the application of an orbit file, removal of GRD border noise, thermal noise elimination, radiometric calibration, and terrain correction. The Sentinel 2 data was mosaicked and monthly averaged to address clouds and missing values, also leveraging GEE. The training and validation sets for forest mapping, Plant Functional Types (PFTs), and forest age segmentation were extracted from the satellite images. Subsequent sections provide a detailed illustration of how these acquired sets are utilized to train the machine learning models.

4.1.3.1 Forest mapping

To expedite the forest mapping process, we implemented the Random Forest (RF) model, a widely recognized ensemble machine learning classifier for land-cover and land-use classification (Gislason et al., 2006). The utilization of RF is well-founded not only due to its popularity but also its demonstrated effectiveness in land-cover mapping, particularly when dealing with low-resolution ground-truth data (Robinson et al., 2021). This machine learning approach leverages the strength of ensemble techniques, combining multiple decision trees to enhance accuracy and robustness in the classification of forested areas. The choice of RF aligns with its established success in handling land-cover mapping challenges, making it an efficient solution for our specific context.

4.1.3.2 PFTs/forest age mapping

While Random Forest (RF) exhibits commendable performance with low-resolution labeled data, it falls short of achieving superior results compared to our proposed

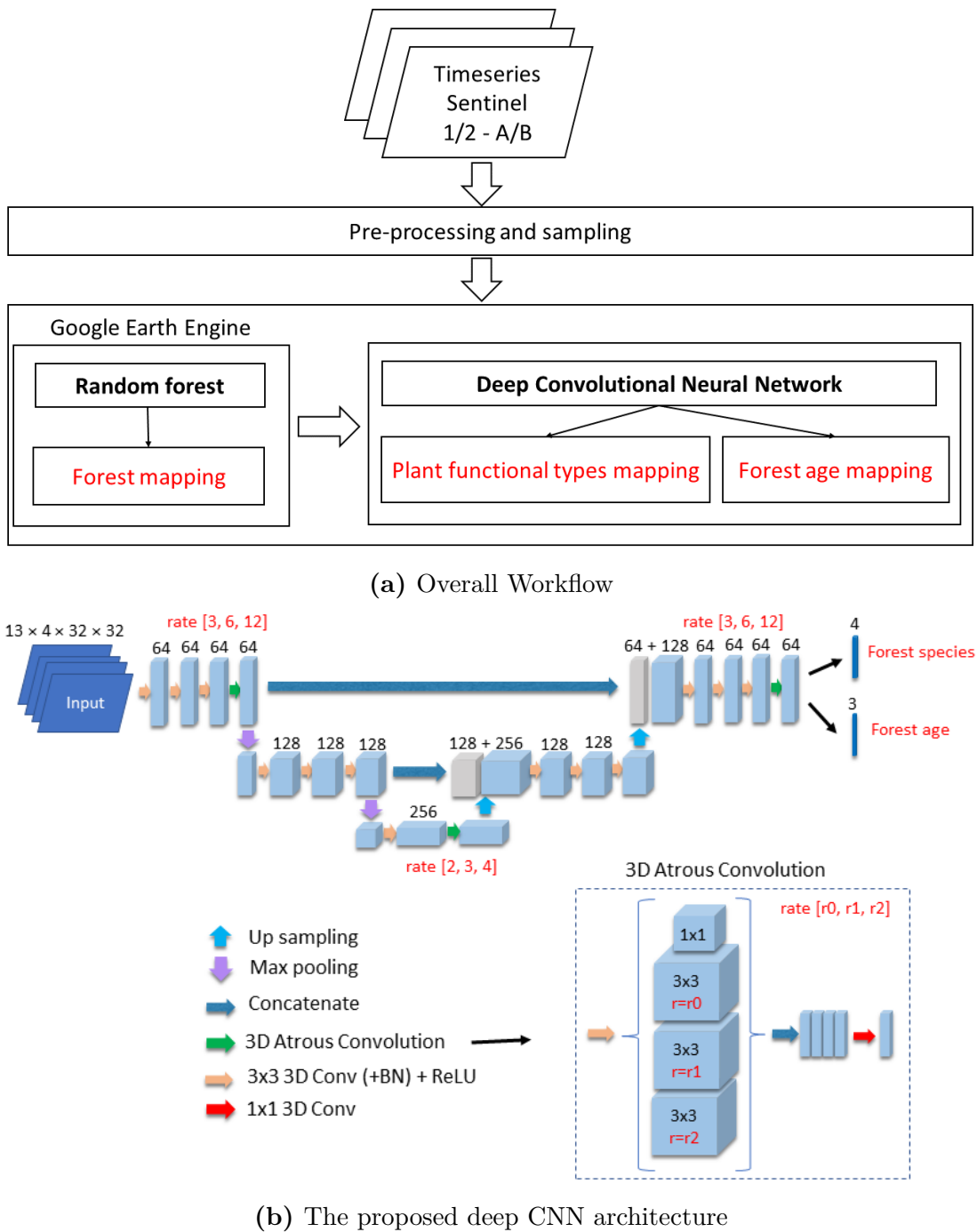


Figure 4.3. (a) Overall workflow and (b) The proposed deep CNN architecture.

2031 deep learning model, as indicated in Table 4.2. The architecture of our pro-
2032 posed network draws inspiration from the UNET architecture (Ronneberger et al.,
2033 2015) but is intentionally shallower, as depicted in Figure 4.3b. To enhance the
2034 model’s semantic segmentation capabilities, we incorporated 3D Atrous Convolution
2035 (3DACConv), a technique proven effective in handling semantic segmentation
2036 tasks with coarse annotations (Chen et al., 2017b). Atrous convolution, initially
2037 introduced in the DeepLab architecture (Chen et al., 2017a), involves convolution
2038 with upsampled filters.

2039 The model comprises an encoder and decoder path backbone. The encoder path
2040 encompasses three layers, with the first layer featuring three 3D convolutions
2041 (3DConv) followed by a 3DACConv. The second layer contains three 3DConvs,
2042 while the last layer consists of one 3DConv followed by a 3DACConv. A $2 \times 2 \times 2$
2043 max pooling layer with strides of two follows each encoder layer. Each 3DConv is
2044 followed by a rectified linear unit (ReLU), before each ReLU is a batch normal-
2045 ization (BN). Notably, we avoid doubling the number of channels immediately
2046 before the max pooling, a departure from the approach introduced in 3D UNET
2047 (Çiçek et al., 2016).

2048 Moving to the decoder path, ConvTranspose3D is employed for up-convolution
2049 to upsample the feature map. A 3DACConv is added at the end of the decoder
2050 path. The output dimensions are then reduced to the number of labels through
2051 a $1 \times 1 \times 1$ 3DConv following the last 3DACConv. In our specific case, the number
2052 of labels is 4 for Plant Functional Types : Broadleaf, Conifer, Cryptomeria,
2053 Chamaecyparis obtusa; and 3 for forest age: young forest (≤ 20 years), mature
2054 forest (21-50 years), and harvesting age (≥ 50 years).

2055 The input data is structured with dimensions $13 \times 4 \times 32 \times 32$, representing the
2056 number of channels, time-series periods, height, and width, respectively. Each
2057 input image consists of 32×32 pixels, encompassing a total of 13 channels dis-
2058 tributed across three time-series periods. The Digital Elevation Model (DEM)
2059 data was incorporated, contributing to the formation of the 4th dimension in the
2060 input. Further elaboration on these details is provided in the subsequent section
2061 for a more in-depth understanding.

2062 Given the imbalanced nature of the training set, as evident in Table 4.1, we
2063 fine-tuned the model by incorporating a weighted cross-entropy loss function.

Table 4.1. Training and validation samples and the corresponding weights for cross-entropy loss function.

Class	Training set	Validation set	Weight
PFTs (number of input images)			
Broadleaf	5017	264	0.153
Conifer	3048	160	0.252
Chamaecyparis obtusa	3191	168	0.241
Cryptomeria	768	40	1
Forest age (number of input images)			
Harvesting age	4000	205	0.05
Mature age	2095	110	0.1
Young age	186	10	1

2064 Specifically, distinct weights were assigned for PFTs and age categories, as outlined in Table 4.1.
2065

2066 4.1.3.3 Experiment design and settings

2067 To assess the performance of the proposed network against Random Forest (RF),
2068 2D UNET, and 3D UNET, we devised an experiment for Plant Functional Types
2069 (PFTs) and age mapping using time-series satellite data from Sentinel 1 and 2 in
2070 2018. This data was organized into three distinct periods: January-April (P1),
2071 May-August (P2), and October-December (P3). For each period, we conducted
2072 a mosaicking and compositing process to create a comprehensive satellite im-
2073 age. Our initial exploration aimed to understand the impact of seasonal changes
2074 on PFTs and age mapping performance using RF and 2D UNET. Due to the
2075 constraints imposed by the input shape, the assessment of 3D UNET and our
2076 proposed model was carried out with data spanning the entire year. To facilitate
2077 training with our network and 3D UNET, the input shape needed to be adjusted
2078 to $13 \times 4 \times 32 \times 32$. This adjustment involved stacking the Digital Elevation Model
2079 (DEM) band with the Sentinel 1/2 data in P1, P2, and P3, resulting in input
2080 dimensions of each $13 \times 32 \times 32$.

2081 The performance evaluation of segmentation models was conducted using the

2082 Overall Accuracy (OA) score on the validation set. Subsequently, results maps
2083 generated by each model underwent visual examination to provide a qualitative
2084 assessment.

2085 Our deep learning model, implemented in PyTorch, underwent training on an
2086 NVIDIA GeForce RTX 3080 Ti GPU. The training process involved 100 epochs,
2087 utilizing the Adam optimizer (Kingma and Ba, 2014) with an initial learning rate
2088 of 10^{-5} . The learning rate underwent halving after every 10 epochs.

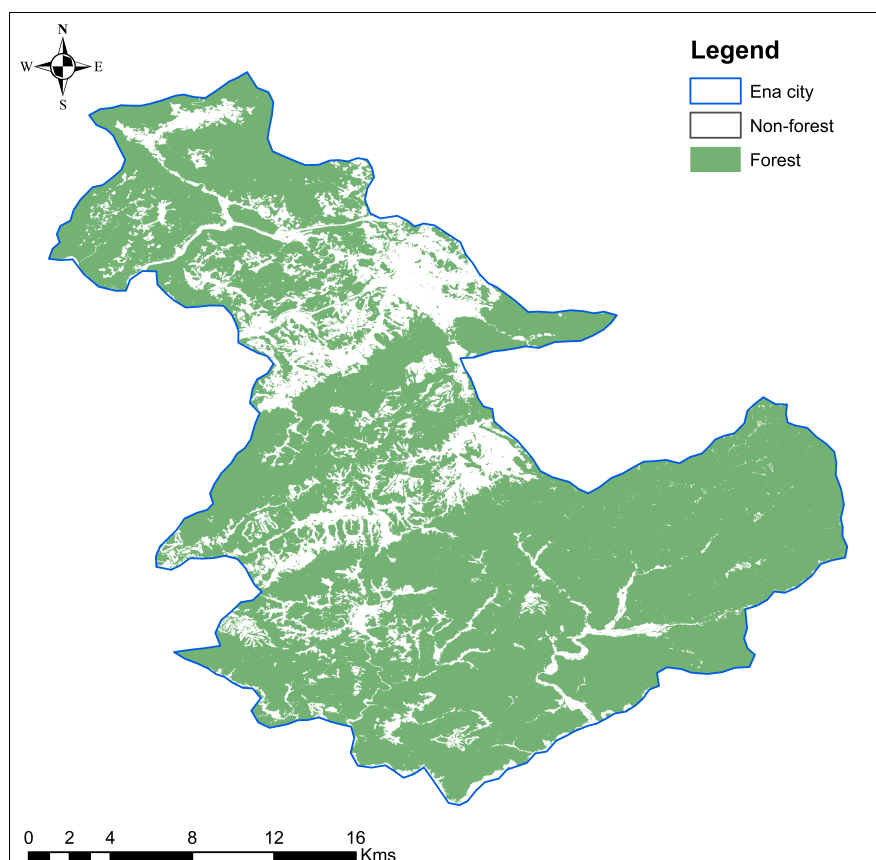
2089 In the context of forest mapping, our approach exclusively employed Sentinel 2
2090 data from June 2018, complemented by 10-meter-resampled DEM data retrieved
2091 from GEE. This choice was guided by our observation that June data exhibits
2092 minimal slope effects, particularly in regions characterized by higher elevations.
2093 The utilization of GEE’s API facilitated a seamless implementation, significantly
2094 boosting computational efficiency throughout the mapping stages.

2095 4.1.4 Experimental results

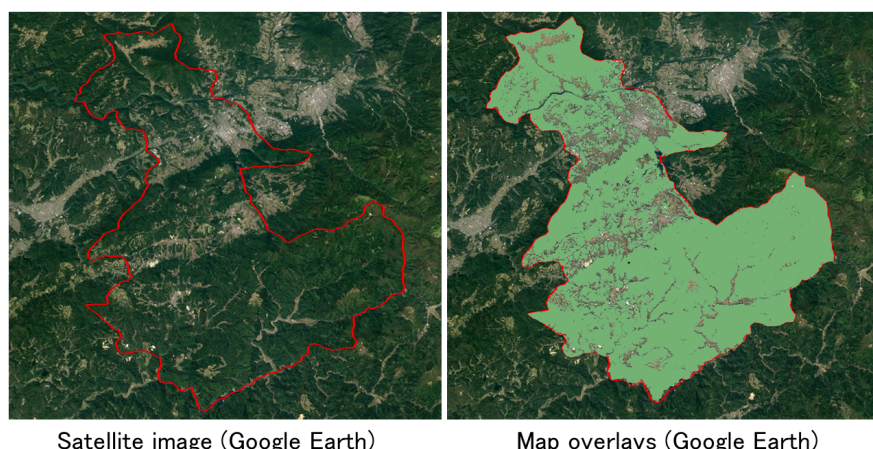
2096 For forest mapping, the model accomplished a 94.5% Overall Accuracy (OA)
2097 for the classification of forest and non-forest areas. The resulting forest map,
2098 generated by the model, is displayed in Figure 4.4. Upon scrutinizing the high-
2099 resolution satellite image from Google Earth alongside the overlaid inferred forest
2100 map, it becomes evident that the RF model has proficiently and accurately clas-
2101 sified the forest pixels using information derived from Sentinel 2 and DEM data.

2102 As evident from Table 4.2, RF consistently outperformed 2D UNET across
2103 all conducted tests. Notably, both the RF and 2D UNET experiments yielded
2104 suboptimal results when exclusively relying on data from the P2 period, result-
2105 ing in the lowest OA for both Plant Functional Types (PFTs) and forest age
2106 segmentation.

2107 Substantial improvements in OA were observed when extending the time-series
2108 scheme from P2 to encompass P1 + P2. However, the addition of P3 to the
2109 training set did not yield a significant enhancement in the performance of RF
2110 and 2D UNET when compared to the P1 + P2 configuration. This suggests that,
2111 for the effective utilization of time-series data in PFTs and forest age segmentation
2112 within the study area, the preferable approach involves employing data collected
2113 from the January to August period. This is best achieved through an ensemble

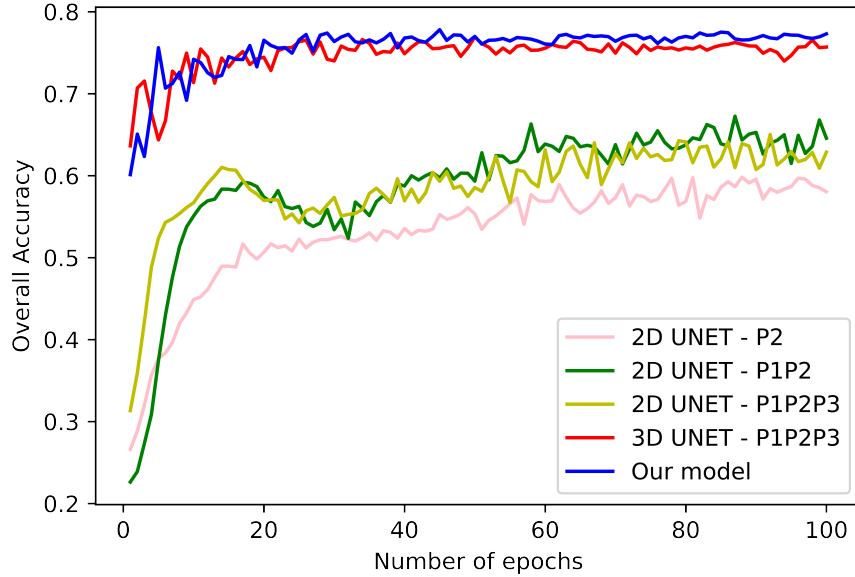


(a) Forest map in Ena City, Japan

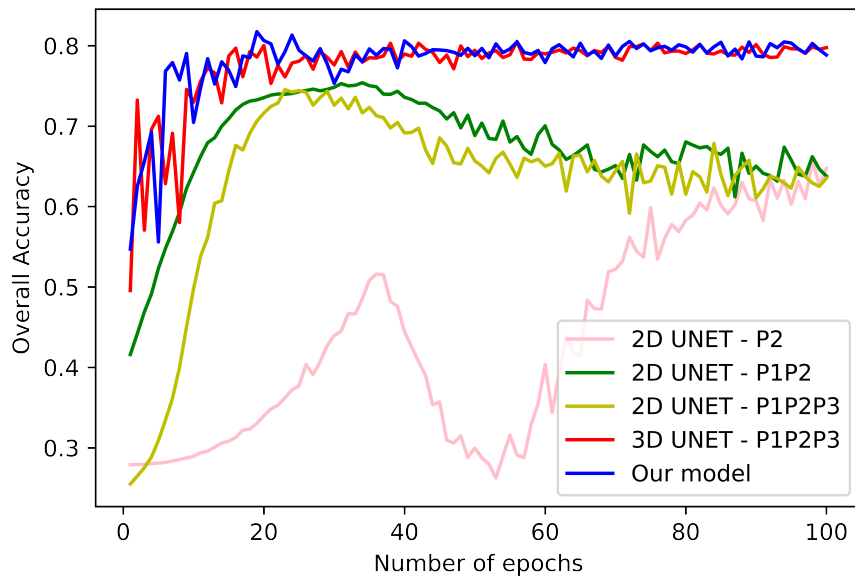


(b) Map overlays

Figure 4.4. Inferred forest map in Ena City, Japan –2018 (OA –94.5%)



(a) PFTs segmentation.



(b) Forest age segmentation.

Figure 4.5. OA profile of PFTs (a) and forest age (b) segmentation

Table 4.2. The experimental results of UNET and our model.

Model	Time-series period	Highest OA (%)	
		Species	Age
RF	P2	67.41	73.94
	P1 + P2	71.68	78.66
	P1 + P2 + P3	71.65	78.68
2D UNET	P2	59.81	65.67
	P1 + P2	67.25	75.4
	P1 + P2 + P3	65.02	74.55
3D UNET	P1 + P2 + P3	76.91	80.53
Our model	P1 + P2 + P3	77.80	81.74

2114 learning model like RF, or a CNN architecture based on 2D UNET.

2115 Despite the minimal impact of P3 data on the performance of RF and 2D
2116 UNET, with 3D CNN scheme in 3D UNET and our suggested model, the in-
2117 corporation of P3 data has significantly elevated the OA in discriminating Plant
2118 Functional Types (PFTs) and forest age. The performance comparison of our
2119 model, 2D/3D UNET, and RF over 100 epochs is presented in Table 3.3, and
2120 Figure 4.5. Notably, the OA has experienced a substantial improvement, in-
2121 creasing from 71.68% to 76.91% with 3D UNET, and reaching 77.80% with our
2122 proposed model for PFTs segmentation. Similarly, for forest age segmentation,
2123 the OA has risen from 78.66% to 80.53% with 3D UNET, and to 81.74% with
2124 our model.

2125 The OA profiles in Table 3.3, and Figure 4.5 underscore the superior perfor-
2126 mance of our model compared to RF, 2D UNET, and 3D UNET, exhibiting an
2127 approximate 6.12%, 10.55%, and 0.89% higher OA for PFTs, and 3.03%, 6.31%,
2128 and 1.18% higher OA for forest age segmentation, respectively.

2129 Figure 4.6 depicts the forest age map generated by our model, revealing that
2130 the primary harvesting-age areas are predominantly situated in the Northern,
2131 Southern, and central parts of the city. Mature-age forests are distributed exten-
2132 sively throughout the region, while smaller areas of young-age forests are scattered
2133 across the city from the west to the south.

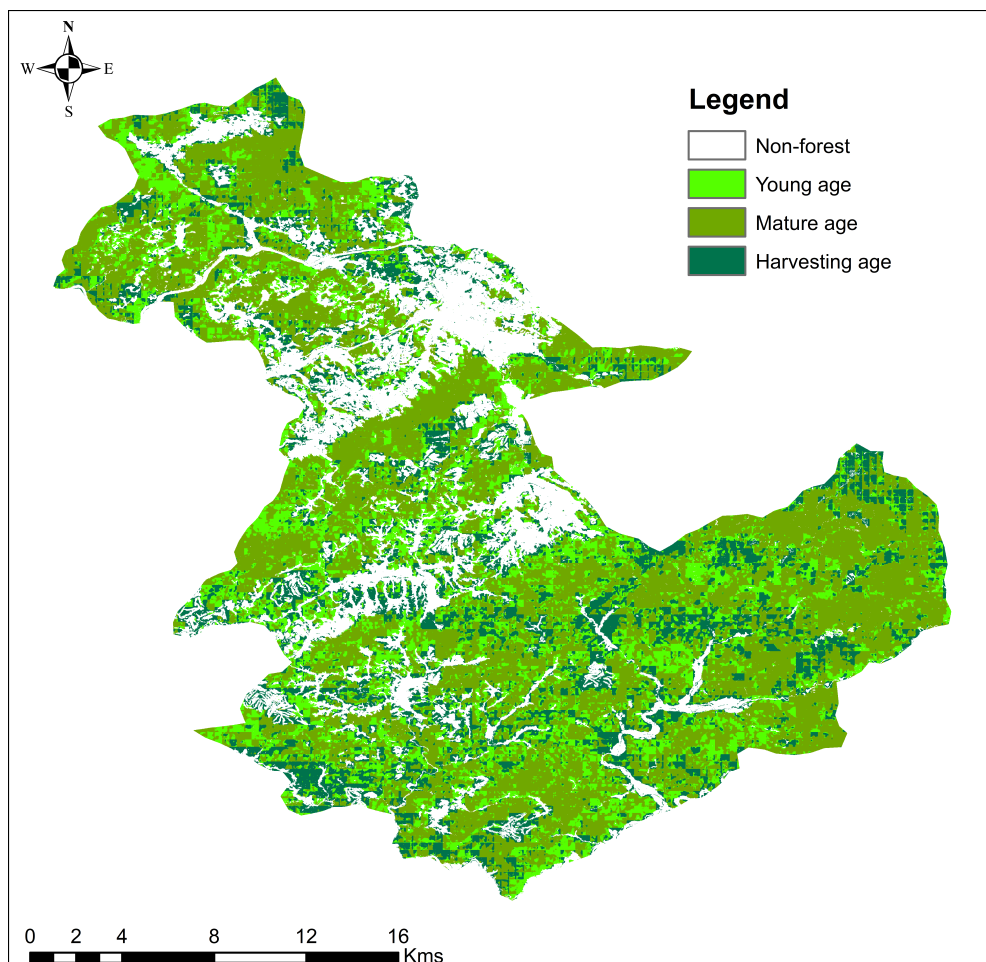


Figure 4.6. Inferred forest age map in Ena City, Japan –2018.

2134 The visual representation of the deduced PFTs map is presented in Figure
 2135 4.7. Notably, *Chamaecyparis obtusa* emerges as the prevailing PFTs, exhibiting
 2136 widespread distribution across the entire region. *Cryptomeria*, on the other
 2137 hand, dominates the central Southeast and Northwest sectors of the study area.
 2138 Broadleaf trees, in majority, are concentrated in the Northeast, Southern, and
 2139 Northwest segments of the region. The identified Conifer species, while dispersed
 2140 throughout the Northern and Southern regions, makes a minor contribution from
 2141 the Northwest portion of the city.

2142 Implementing the proposed methodology, we have expanded our mapping ef-
 2143 forts to encompass additional cities in Gifu prefecture, namely Nakatsugawa,

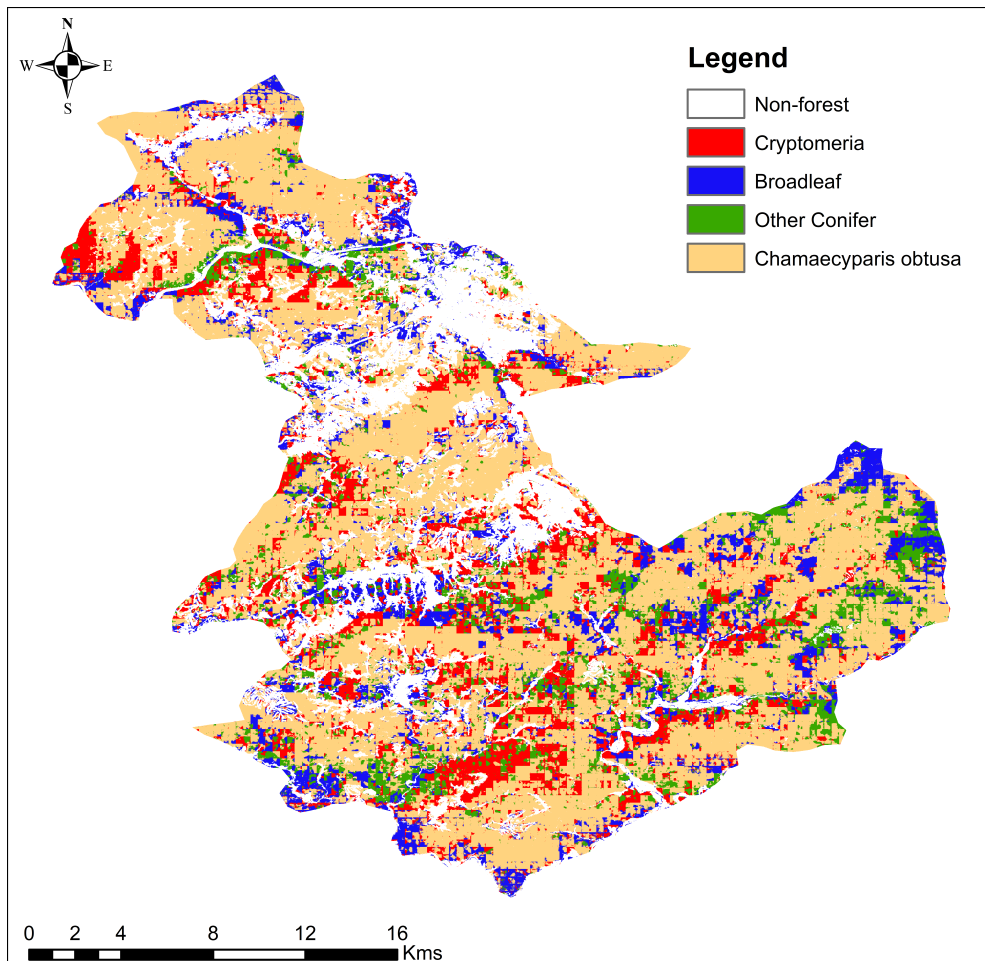


Figure 4.7. Inferred PFTs map in Ena City, Japan –2018.

2144 Mizunami, Toki, and Tajimi, as depicted in Figure 4.8. Our approach involved
 2145 the initial application of the proposed network, followed by the utilization of
 2146 a straightforward reclassification method. This process enabled the generation
 2147 of a high-resolution map of Plant Functional Types (PFTs), derived from the
 2148 pseudo-label output produced by the proposed model.

2149 4.1.5 Conclusion

2150 In this study, by utilizing remote sensing, RF classifier, and deep learning, the
 2151 approach for forest-related SDG issues monitoring in data-scarce regions has been

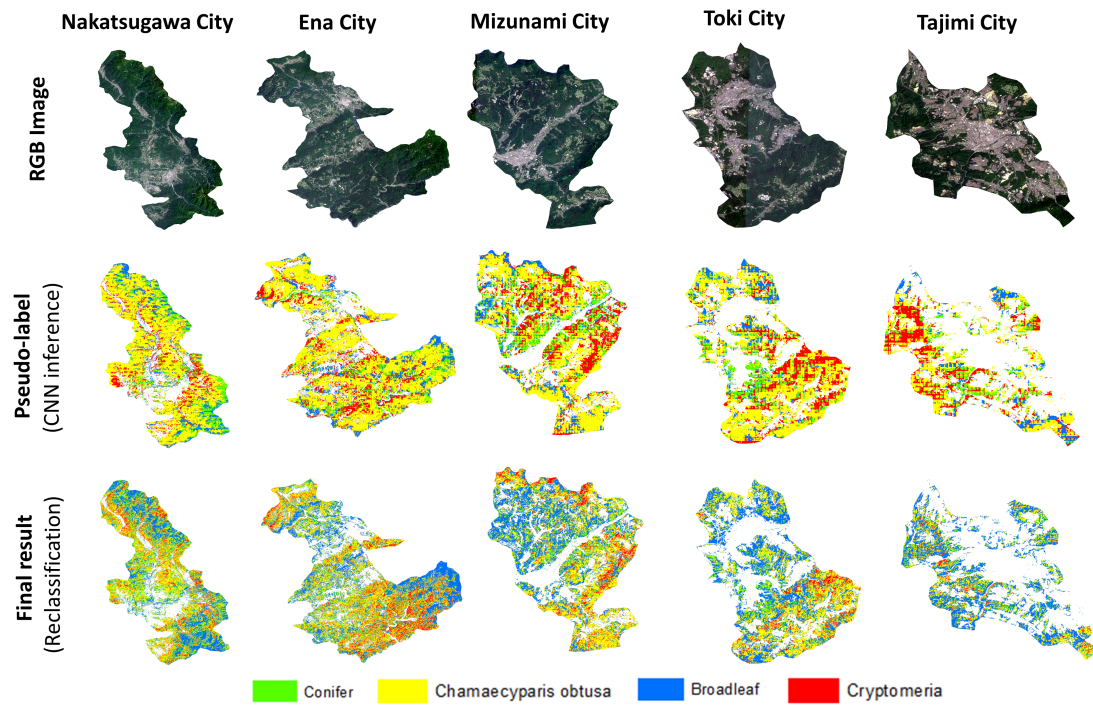


Figure 4.8. Performance of the proposed method in other regions.

proposed. We examined the approach in Ena City, Japan and achieved promising results in forest mapping, and PFTs and forest age mapping. Our proposed model outperforms the RF, 2D/3D UNET in PFTs and forest age segmentation with coarse-polygonal ground-truth data. The outcome of this study could be served as an input for further steps to produce high-resolution land cover map for the data-scarce regions. In the future, we will investigate the postprocessing method to improve the map quality from coarse annotations.

4.2 Global terrestrial carbon fluxes estimates

4.2.1 Introduction

Terrestrial ecosystems play a crucial role in mitigating global warming by serving as a persistent carbon sink, actively absorbing and storing excess carbon dioxide from the atmosphere (Pan et al., 2011). Over the period from 2010 to 2019,

the terrestrial CO₂ sink is estimated to offset fossil CO₂ emissions by 31%, surpassing the ocean, which is projected to remove 25% of fossil-fuel-derived CO₂ (Friedlingstein et al., 2023). The substantial global carbon flux, known as terrestrial gross primary production (GPP), significantly contributes to the reduction of anthropogenic CO₂ emissions (Beer et al., 2010).

Estimating GPP involves various methods, such as simulating dynamic global vegetation models (DGVMs) like those employed in the TRENDY project (Sitch et al., 2015; Le Quéré et al., 2018), upscaling from measurements obtained through eddy covariance (EC) flux tower and satellite observations (Jung et al., 2019; Zeng et al., 2020). However, all these approaches rely on plant functional types (PFTs) to estimate ecosystem productivity (Poulter et al., 2011, 2015; Lin et al., 2021; Guo et al., 2023; Yan et al., 2023). Inconsistencies in PFT maps can significantly contribute to uncertainties in GPP estimations, as well as other climate-relevant variables, at both regional and global scales (Poulter et al., 2011). Particularly in the tropical region, the sparse distribution of EC sites, the high species richness of trees, and the complex vertical structure of tropical rainforests pose challenges (Montgomery and Chazdon, 2001), making it difficult to accurately quantify the seasonality of carbon fluxes (Xu et al., 2015).

In recent times, there has been an increasing adoption of timeseries (TS) foundation models employing a transformer-inspired architecture for addressing time-series problems and representation learning. Notable examples include the MVTS Transformer (Zerveas et al., 2021), Informer (Zhou et al., 2021), Autoformer (Wu et al., 2021), and Fedformer (Zhou et al., 2022). The adoption of the Transformer architecture is anticipated to enhance the modeling of seasonality based on the timeseries representation. However, to the best of our knowledge, its application in the task of upscaling global carbon fluxes remains limited.

In this section, our goal is to evaluate the effectiveness of employing timeseries representation, specifically based on recently updated Plant Functional Types (PFTs) (Harper et al., 2022) and a Transformer-based architecture model (Zerveas et al., 2021), for predicting the trends and seasonality of carbon fluxes at a global scale. We present monthly global data at a spatial resolution of 0.25 degrees for GPP and Ecosystem Respiration (RECO). The evaluation of our dataset involves comparing it with other satellite-based carbon flux datasets, considering

correlations with FLUXNET 2015 and Solar-Induced Fluorescence (SIF) datasets, as well as assessing interannual trends and variations. The complete workflow of the study is illustrated in Figure 4.9, and we have named our dataset and framework FluxFormer.

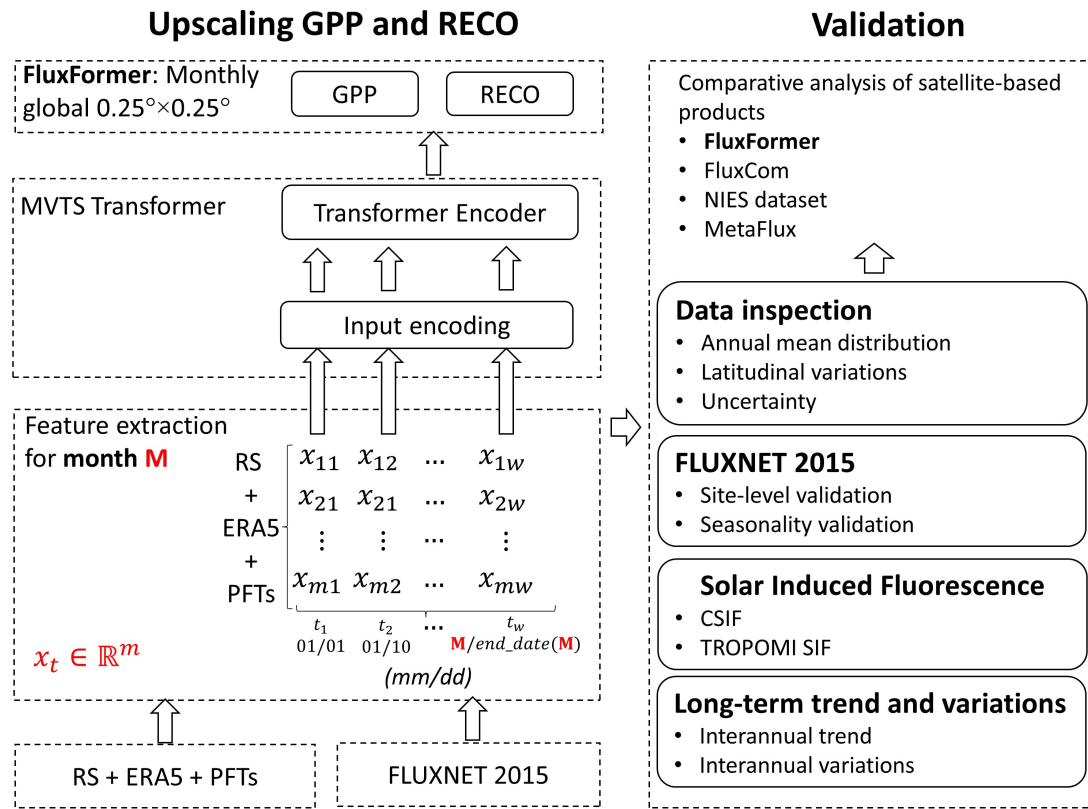


Figure 4.9. Schematic workflow of our FluxFormer methodology

4.2.2 Methods

4.2.2.1 Input data

FLUXNET 2015

The FLUXNET 2015 dataset (Pastorello et al., 2020) serves as the groundtruth for carbon fluxes in the transformer model in this study. Monthly GPP and RECO data were extracted from the dataset tier 1 of FLUXNET 2015, encompassing data from 206 sites. We filtered out records with a quality control value of less

than 80% for measured and good-quality gap-fill data. Relying solely on quality control values is reported to be insufficient for obtaining qualified data due to inconsistencies in the differences between GPP, RECO, and NEE (Zeng et al., 2020; Tramontana et al., 2016). Following the approach of (Zeng et al., 2020), we also excluded records with an absolute difference between GPP-RECO and NEE larger than $0.1 \text{ gC } m^{-2}d^{-1}$.

Remote sensing data

For the remote sensing data, we employed version 2 of the global leaf area index (LAI) and fraction of absorbed photosynthetically active radiation (FAPAR) datasets, generated using the algorithm proposed by (Verger et al., 2014). These datasets can be accessed through the Copernicus Global Land Service, providing a 1 km spatial resolution for every 10 days spanning from 1999 to 2019. The remote sensing data utilized in this study is in line with the approach presented in (Zeng et al., 2020). The latitude boundary of this dataset ranges from -60°S to 80°N.

Meteorological data

For meteorological data, we employed specific variables from the ERA5 reanalysis product (Hersbach et al., 2020), including 2-meter air temperature (T2M), surface short-wave (solar) radiation downwards (SSRD), vapor pressure deficit (VPD), total precipitation (TP), and evaporation (E). As VPD is not directly available in the original dataset, we estimated it using the relationship between saturated vapor pressure (SVP) and actual vapor pressure (AVP): $\text{VPD} = \text{SVP} - \text{AVP}$, based on 2-meter air and dewpoint temperature. The original spatial resolution of ERA5 data is $0.25^\circ \times 0.25^\circ$ and was obtained from the Copernicus Climate Change Service (C3S) Climate Data Store (CDS).

Plant function types

The PFTs dataset employed in this study, denoted as PFT v2.0.8 and obtained from (Harper et al., 2022), spans the period from 1992 to 2020. It provides the specific percentage cover of 14 PFTs for each pixel at a 300m resolution. The annual dataset comprises 14 layers, with pixel values at 300m resolution indicating the percentage cover (ranging from 0% to 100%) for each of the 14

PFTs. This updated PFTs dataset is considered a more accurate representation of PFT distributions as it relies on high-resolution, peer-reviewed mapping of specific vegetation classes to refine global assumptions about PFT fractions (Harper et al., 2022). Regional updates in PFT fractions are anticipated to enhance carbon fluxes estimation. The complete set of PFTs includes bare soil, built areas, water bodies, snow and ice, natural grasses, managed grasses (i.e., herbaceous cropland), broadleaved deciduous trees, broadleaved evergreen trees, needleleaved deciduous trees, needleleaved evergreen trees, broadleaved deciduous shrubs, broadleaved evergreen shrubs, needleleaved deciduous shrubs, and needle-leaved evergreen shrubs. The dataset can be accessed from the CEDA archive at <https://catalogue.ceda.ac.uk/uuid/26a0f46c95ee4c29b5c650b129aab788>.

4.2.2.2 Multivariate Time Series Transformer Framework

Figure 4.9 illustrates the overall workflow of our FluxFormer methodology to upscale GPP and RECO from remote sensing data, and PFTs data. We utilized the original Multivariate Time Series MVTS Transformer model which is transformer-based framework proposed by (Zerveas et al., 2021) which contains an input encoding layer with learnable positional encoding and a Transformer Encoder (Vaswani et al., 2017). MVTS Transformer achieved good performance on supervised and unsupervised regression task based on multivariate time series representation even with limited training samples.

In order to train the MVTS Transformer, first, we extracted the remote sensing data, meteorological data and PFTs for each monthly record from FLUXNET 2015 dataset. Then the extracted data is formed to feed to the deep learning model. In particular, for a specific month \mathbf{M} , each training sample $\mathbf{X} \in \mathbb{R}^{w \times n}$ where w is the lengths of timeseries for month \mathbf{M} ($w = 3 \times \mathbf{M}$ as we have three remote sensing products per month) and m is the number of different variables ($m = 21$ 2 remote sensing variables (LAI and FAPAR), 5 meteorological variables (T2M, SSRD, VPD, TP, E) and 14 PFTs variables), constitutes a sequence of w feature vectors $\mathbf{x}_t \in \mathbb{R}^m : \mathbf{X} \in \mathbb{R}^{w \times n} = [\mathbf{x}_1, \mathbf{x}_2, \dots, \mathbf{x}_w]$ is a multivariate timeseries of length w and m different variables.

2269 **4.2.2.3 Training setup**

2270 To train the model, approximately 80% of the monthly data was randomly chosen
 2271 for training, while the remaining 20% was allocated for validation. Twelve models
 2272 were trained over the course of 12 months.

Table 4.3. Number of samples for training and validation

Month	Number of samples	
	Training	Validation
January	295	68
February	305	72
March	315	77
April	310	75
May	320	88
June	306	66
July	313	66
August	298	67
September	319	68
October	335	71
November	310	75
December	295	62

2273 Notably, the distribution of FLUXNET 2015 sites is uneven across climate
 2274 zones, particularly in the tropics and semi-arid regions, despite the highest GPP
 2275 values being observed in tropical areas such as Amazonia, Central Africa, and
 2276 Southeast Asia (Chen et al., 2017c). Additionally, semi-arid regions play a crucial
 2277 role in influencing the global carbon cycle (Poulter et al., 2014). To reduce this
 2278 imbalance, we exclusively utilized the most recent data from the past three years
 2279 for each site as suggested by (Zeng et al., 2020). This choice aimed to guarantee
 2280 a fairer representation of each site during the training of the transformer model.
 2281 This approach yielded a total of 4576 samples over the 12-month period, derived
 2282 from the pool of 10655 qualified monthly samples. The distribution of samples
 2283 for training and validation is outlined in Table 4.3.

4.2.2.4 Validation

FluxFormer's quality was assessed through comprehensive comparisons. First, we examined the annual mean distribution as well as latitudinal variations of FluxFormer and other products. To evaluate uncertainties in our analysis, we employed bootstrapping. We generated 100 separate samples of the eddy covariance data, ensuring each sample contained a balanced representation of different PFTs through stratification. We then trained 100 model versions on these samples and used them to make predictions. The standard deviation of these predictions represents the associated uncertainty.

Subsequently, we analyzed site-level correlations, errors, and seasonal patterns across climate zones by comparing monthly GPP and RECO from FLUXNET 2015 with corresponding data from leading satellite-based upscaled products like FluxCom (Jung et al., 2019), NIES (Zeng et al., 2020), and MetaFlux (Nathaniel et al., 2023).

Next, we evaluated GPP seasonality against SIF due to its increasing use in GPP estimation (Norton et al., 2019; Liu et al., 2020; Bai et al., 2022). We incorporated independent products, namely CSIF (Zhang et al., 2018), and TROPOMI SIF (Köhler et al., 2018). We examined the pixel-level correlation distribution of FluxFormer and selected satellite-based products with the seasonal trend of CSIF from 2000 to 2019 and TROPOMI SIF from 2018 to 2019, as TROPOMI data is available only from 2018 onwards.

Finally, we examined the interannual trends and variations of our data FluxFormer in comparison with FluxCom, NIES, and MetaFlux. To evaluate interannual trends, we computed the annual global mean GPP and RECO, scaling the global average fluxes using the total global land area of 122.4 million square kilometers (Friedl et al., 2010), as recommended by (Jung et al., 2020) to ensure consistent global area representation across all products. The annual trends and their statistical significance in GPP and RECO were indicated by the slope of the linear regression line and the corresponding p-value. For the assessment of interannual variations, we determined the Interannual Variability (IAV) at the pixel level by calculating the standard deviation divided by the mean of annual fluxes.

4.2.3 Data records

We provided global monthly data of GPP and RECO available at 0.25-degree spatial resolution from 1999 to 2019. The latitude boundary extends from -60°S to 80°N which is same as the latitude boundary of the remote sensing used in this study. The longitude extends from -180°W to 180°S. The data is provided in Network Common Data Form (NetCDF) format. The data variables are defined by time, latitude, longitude coordinates. In the provided data, we purposely masked out the cold regions that consist of the Arctic circle and the desert region. The FluxFormer GPP and RECO products are available at <https://doi.org/10.5281/zenodo.10258644>.

Figure 4.10 illustrates the average GPP and RECO values for all products in 2017. As expected, both GPP and RECO are highest in tropical regions and lowest in semi-arid areas. Notably, the largest differences between product estimates occur in tropical regions, likely due to variations in input data and methodological approaches. Figure 4.11 depicts the latitudinal distribution of GPP and RECO. A consistent pattern emerges across all products, with both GPP and RECO values gradually increasing from colder climates towards warm and humid conditions in temperate and tropical regions. Figure 4.12 illustrates the uncertainty in predicted carbon fluxes for an example year (2017) through the standard deviation of predictions from 100 bootstrapped models. As expected, tropical regions exhibit notably higher uncertainty. This likely reflects the scarcity and uneven distribution of EC measurement sites in these areas, limiting the data available for model training and validation.

4.2.4 Technical validation

4.2.4.1 Validation with FLUXNET 2015

Site-level validation

We utilized the Pearson Correlation Coefficient (R) and Root Mean Square Error (RMSE) to assess the quality of our products in comparison to FLUXNET 2015 observations. As depicted in Figures 4.13a and 4.13b, our product demonstrates the highest correlation and the lowest RMSE with FLUXNET 2015 for both GPP and RECO data ($r = 0.89$, $RMSE = 1.74$ for GPP and $r = 0.86$, $RMSE = 1.26$

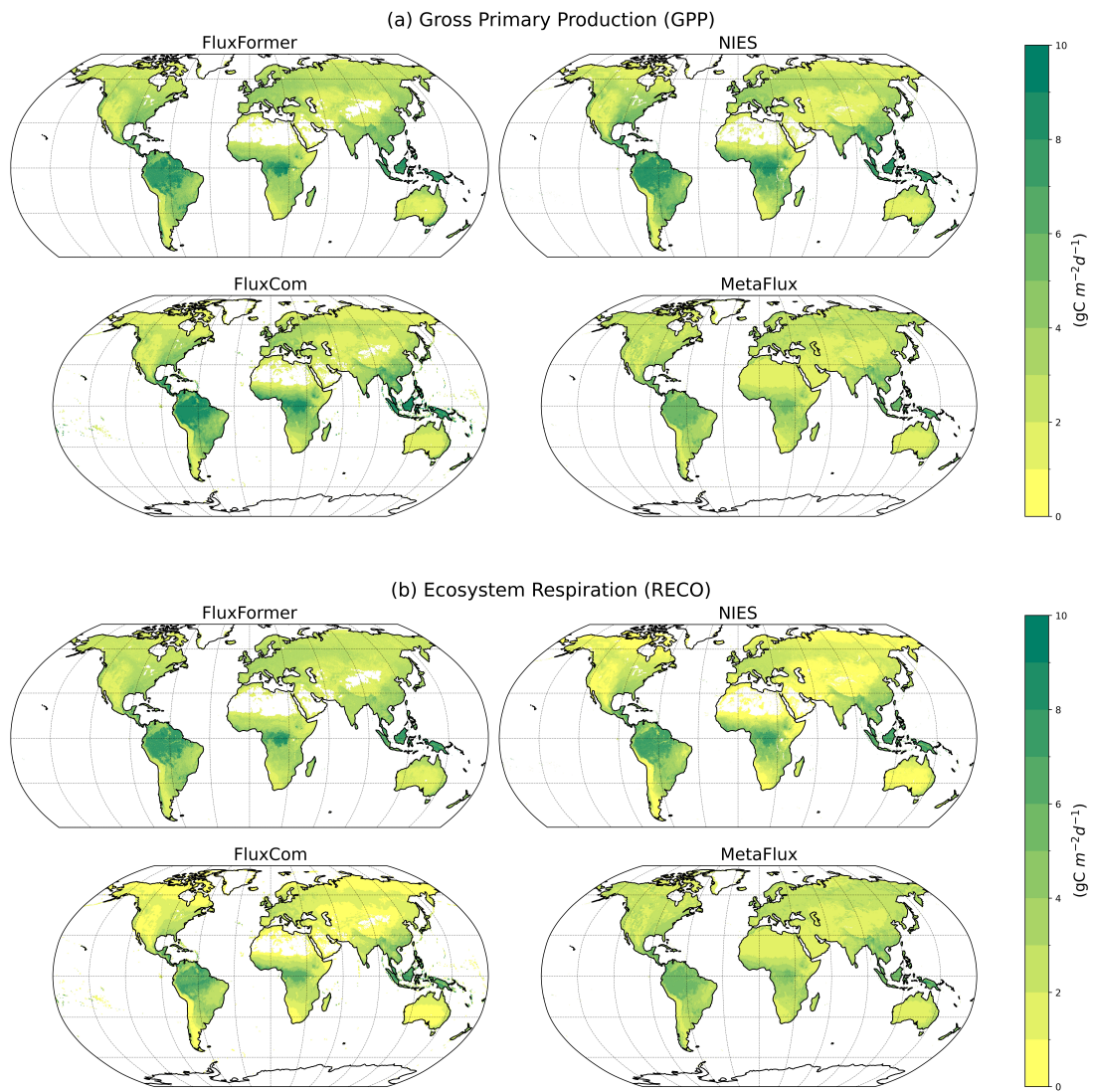


Figure 4.10. Mean estimate of (a) GPP and (b) RECO for the year 2017: GPP
 (a) RECO (b)

for RECO). In contrast, MetaFlux shows the lowest correlation with FLUXNET 2015 ($r = 0.6$, $RMSE = 3.16$ for GPP and $r = 0.56$, $RMSE = 2.08$ for RECO). NIES and FLUXCOM also exhibit strong correlations with the ground truth data, achieving $r/RMSE : 0.88/1.78$ (NIES), $0.81/2.31$ (FLUXCOM) for GPP and $r/RMSE : 0.84/1.35$ (NIES), $0.79/1.64$ (FLUXCOM) for RECO.

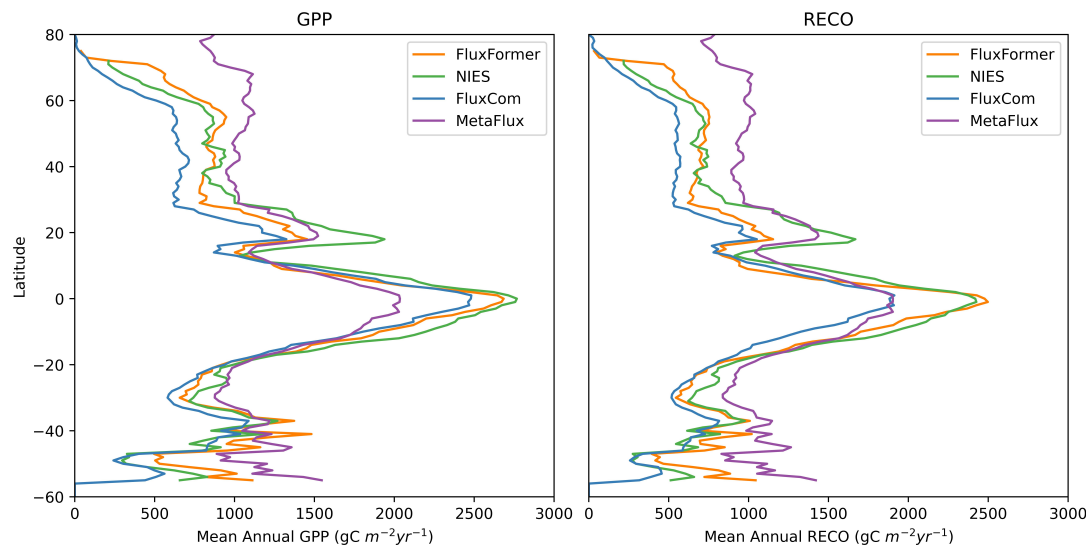


Figure 4.11. Latitudinal distribution of mean annual GPP and RECO from 2001 to 2019

2352 Seasonality validation

2353 We analyzed the seasonal trend using FLUXNET 2015 data, calculating monthly
 2354 mean values across climate zones, as depicted in Figure 4.14 and Table 4.4. In arid
 2355 regions, FluxFormer, FluxCom, and NIES exhibited high correlation ($r > 0.9$)
 2356 with FLUXNET for both GPP and RECO. However, MetaFlux showed lower cor-
 2357 relation with $r = 0.48$ for GPP and $r = 0.66$ for RECO in arid regions. For tem-
 2358 perate and cold regions, all satellite-based products (FluxFormer, FLUXCOM,
 2359 NIES, and MetaFlux) demonstrated high correlations ($r > 0.9$) with FLUXNET
 2360 2015 GPP and RECO.

2361 In the tropical region, we partitioned the area into tropical savanna (Trop.
 2362 SVN), tropical monsoon (Trop. MS), and tropical rainforest (Trop. RF). In Trop.
 2363 SVN, all satellite-based products displayed a high correlation with FLUXNET
 2364 2015 for both GPP and RECO. Conversely, for Trop. MS, our data exhibited
 2365 the highest correlation at $r = 0.84$, while NIES data showed a slightly lower
 2366 correlation ($r = 0.78$). FLUXCOM and MetaFlux demonstrated no correlation
 2367 with FLUXNET 2015 for GPP, with $r < 0.1$. Regarding RECO in Trop. MS,
 2368 our data maintained the highest correlation with the seasonal trend of the ground
 2369 truth, whereas other products showed lower correlation (FLUXCOM: $r = 0.51$,

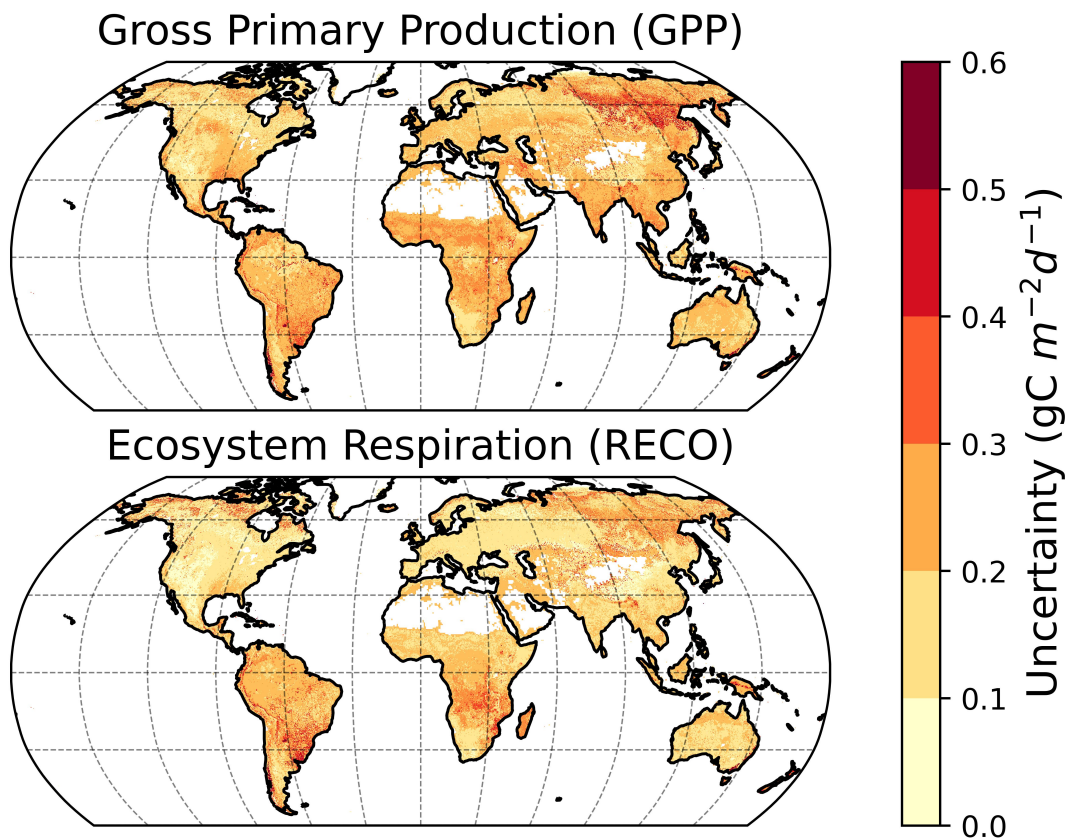


Figure 4.12. Estimated uncertainty for the year 2017 of GPP and RECO

2370 NIES: $r = 0.21$) or no correlation with the ground truth (MetaFlux: $r = 0$). In
 2371 the Trop. RF area, our data exhibited the second-highest correlation with GPP
 2372 seasonal trend ($r = 0.68$) and the highest correlation with RECO seasonal trend
 2373 ($r = 0.68$).

2374 Overall, our data demonstrates a robust correlation in arid, temperate, conti-
 2375 nental, and Trop. SVN regions, surpassing $r > 0.9$ for both GPP and RECO.
 2376 Specifically, in Trop. MS, our data exhibits the highest correlation, reaching
 2377 $r = 0.84$ for GPP and $r = 0.88$ for RECO. In the Trop. RF region, our data ex-
 2378 hibits the second-highest correlation with the ground truth GPP seasonal trend
 2379 ($r = 0.68$) and the highest correlation with the ground truth RECO seasonal
 2380 trend ($r = 0.68$) among the selected satellite-based products.

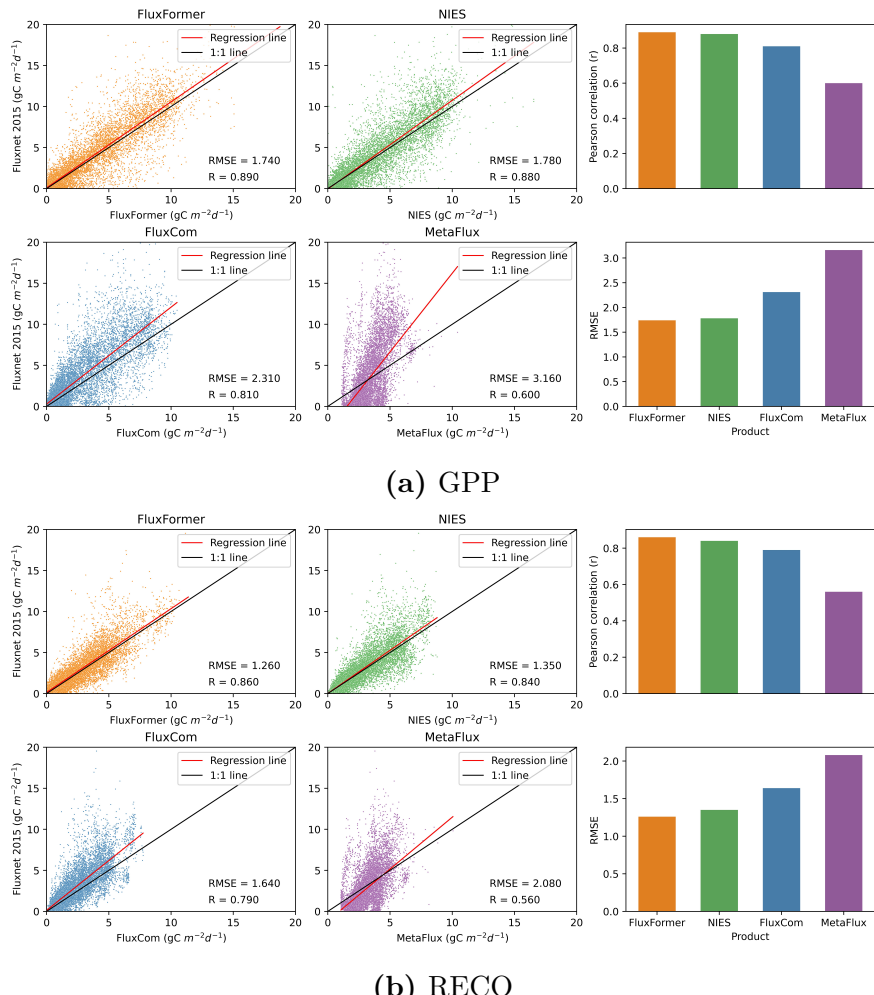


Figure 4.13. Validation with FLUXNET 2015: GPP (a) RECO (b)

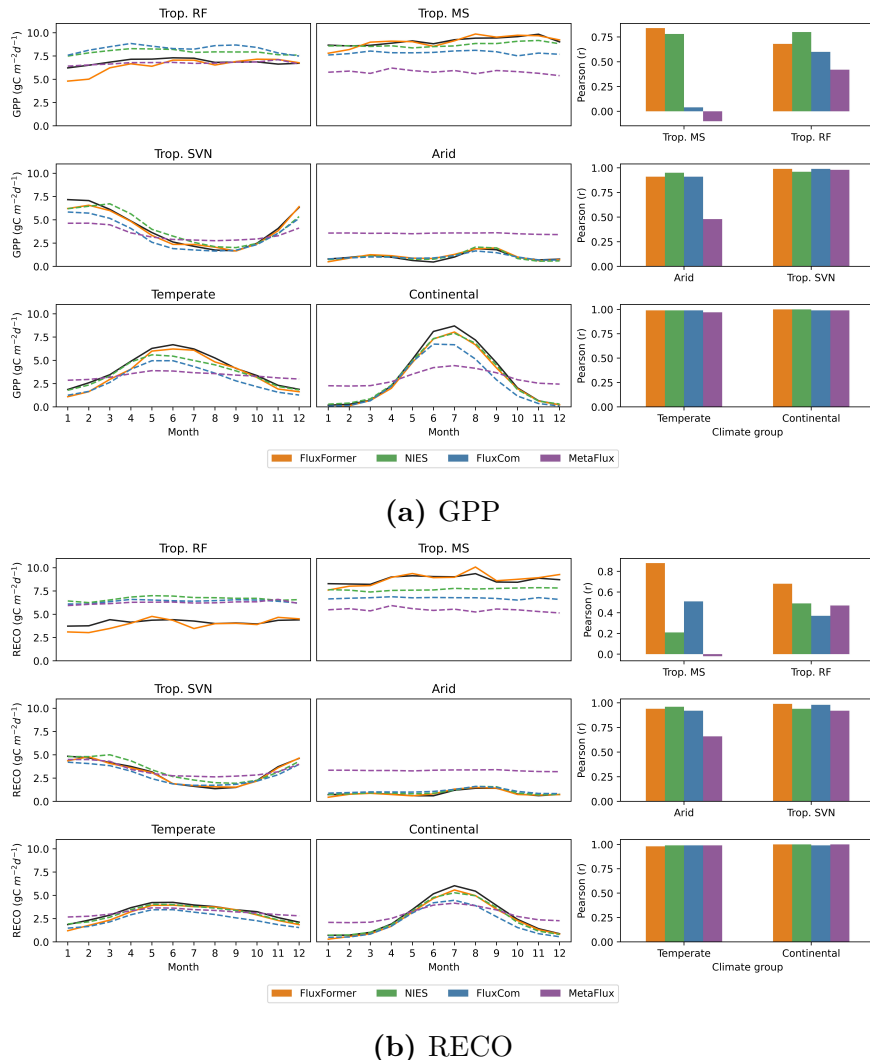


Figure 4.14. Seasonality validation with FLUXNET 2015: GPP (a) RECO (b)

Table 4.4. Pearson correlation of seasonal trend with FLUXNET 2015

Climate groups	FluxFormer	FluxCom	NIES	MetaFlux
GPP				
Arid	0.91	0.90	0.95	0.48
Temperate	0.99	0.99	0.99	0.97
Continental	1	0.99	1	0.99
Trop. SVN	0.99	0.99	0.96	0.98
Trop. MS	0.84	0.04	0.78	-0.1
Trop. RF	0.68	0.6	0.8	0.42
RECO				
Arid	0.94	0.92	0.96	0.66
Temperate	0.98	0.99	0.99	0.99
Continental	1	0.99	1	1
Trop. SVN	0.99	0.98	0.94	0.92
Trop. MS	0.88	0.51	0.21	0
Trop. RF	0.68	0.37	0.49	0.47

2381 4.2.4.2 Validation with SIF

2382 While a linear relationship between GPP and SIF has been widely assumed in
 2383 previous studies (Guanter et al., 2012; Yang et al., 2017), this assumption remains
 2384 uncertain across diverse climate regions and PFTs (Gu et al., 2019; Xiao et al.,
 2385 2019b; Zhang et al., 2016; Chen et al., 2021a). This uncertainty is particularly
 2386 pronounced in tropical regions, where weak seasonality in photosynthesis leads
 2387 to a less robust linear relationship between SIF and GPP (Doughty et al., 2021).
 2388 Regionally, tropical forests and savannahs are often water-limited rather than sun-
 2389 light-limited (Guan et al., 2015; Madani et al., 2017, 2020; Palmer et al., 2023).
 2390 Furthermore, tropical forests, dominated by evergreen broadleaf forests (EBFs),
 2391 exhibit complex vegetation structures that contribute to larger uncertainties in
 2392 both satellite observations and ground-based GPP estimates from eddy covariance
 2393 (EC) sites, further weakening the SIF-GPP correlation in these regions (Hayek
 2394 et al., 2018; Li et al., 2018; Zhang et al., 2020; Shekhar et al., 2022). Additionally,
 2395 frequent cloud cover in the tropics contaminates SIF signals from satellite

2396 observations, adding to the challenge of using SIF as a reliable proxy for GPP
 2397 (Doughty et al., 2021; Shekhar et al., 2022).

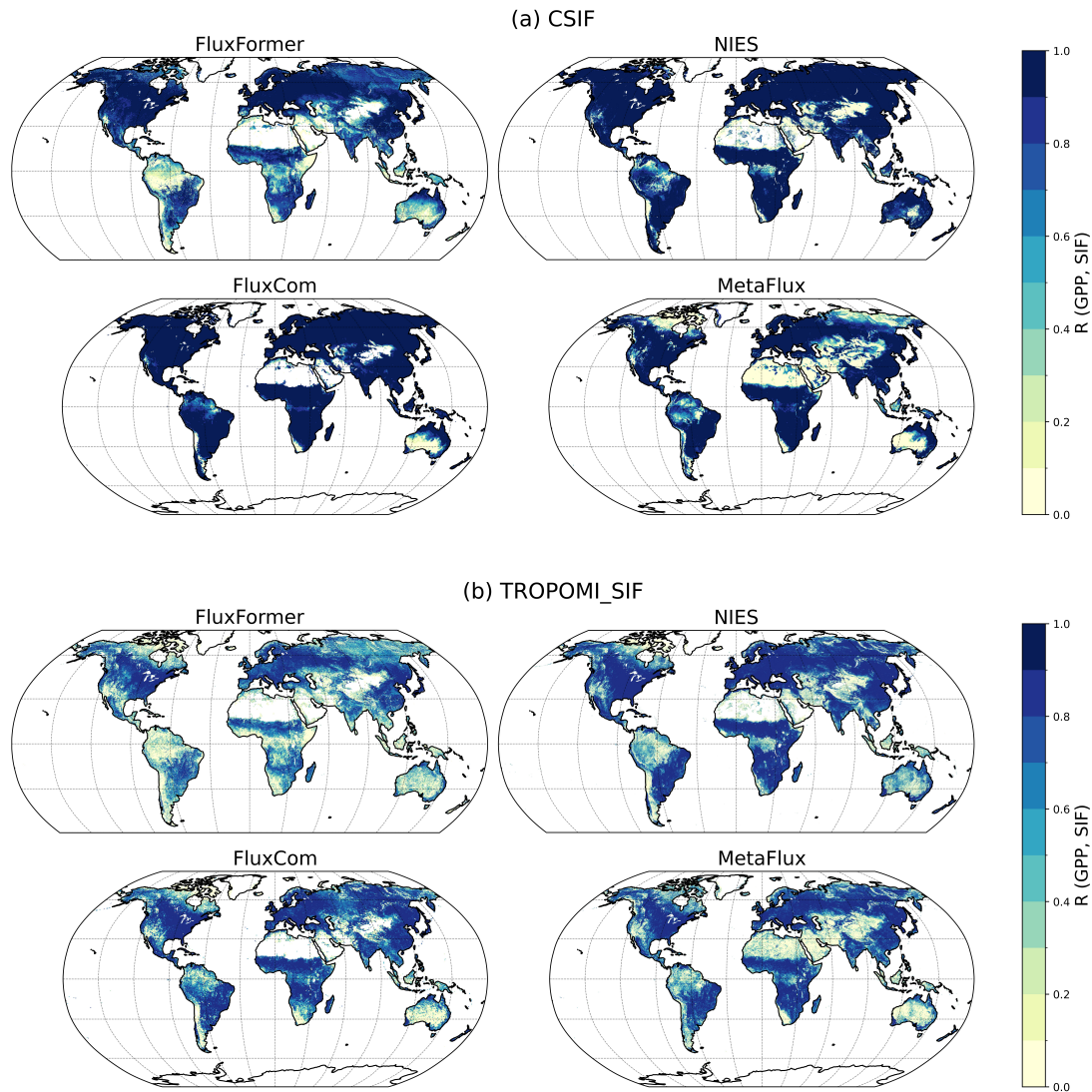


Figure 4.15. Validation with SIF products: CSIF (a) TROPOMI SIF (b)

2398 Figure 4.15 depicts the temporal correlations between monthly SIF and GPP.
 2399 In temperate and continental regions, most products show moderate to high GPP-
 2400 SIF correlations. CSIF (Figure 4.15a) exhibits slightly higher correlations than
 2401 TROPOMI SIF (Figure 4.15b), likely due to its longer observation period. How-
 2402 ever, in arid regions, FluxFormer show lower GPP-SIF correlations, especially in

the Horn of Africa deserts. This corresponds with the findings of (Palmer et al., 2023), highlighting the more substantial influence of rainfall on GPP than sunlight in this eastern desert region of Africa. In tropical regions, our data shows lower correlations with CSIF and TROPOMI SIF compared to FluxCom, NIES, and MetaFlux, particularly in Central/South America, West/Central Africa, and Southeast Asia and arid regions compared to FluxCom, NIES, and MetaFlux. This aligns with observations from previous studies (Sanders et al., 2016; Doughty et al., 2021; Shekhar et al., 2022), suggesting weak seasonality in tropical photosynthesis weakens the GPP-SIF correlation to background levels.

4.2.4.3 Interannual variations between products

Examining the global annual time series of GPP and RECO from 2001 to 2019 (Figure 4.16), we observe diverse patterns in carbon fluxes across different products. Estimated annual mean fluxes range from 120 to 150 PgC/year for GPP (Figure 4.16a) and 97 to 141 PgC/year for RECO (Figure 4.16b) in FluxFormer and other products. Among these, our FluxFormer dataset exhibits the most pronounced positive GPP trend, increasing at a rate of 0.45 PgC/year. NIES follows closely with a growth rate of 0.32 PgC/year. While MetaFlux suggests a subtle upward trend, its statistical significance remains uncertain (p -value = 0.08). Conversely, FluxCom shows a slight negative trend, indicating a decrease of 0.04 PgC/year in GPP. It is worth noting that the long-term GPP trends in our data and NIES align with the anticipated increase due to the CO₂ fertilization effect, which could potentially enhance the land carbon sink (Piao et al., 2020; Yang et al., 2022; Guo et al., 2023).

Focusing on interannual variations (Figure 4.17), we find that our GPP data exhibits lower variability compared to NIES in desert regions like Australia, West and Central Asia, Eastern and Southern Africa, and parts of North America (Figure 4.17a). This aligns with the expected low GPP in these areas (Hadley and Szarek, 1981), suggesting greater plausibility of our data in these regions. However, FluxFormer displays higher interannual variability compared to FluxCom and MetaFlux. This discrepancy can be attributed to the different remote sensing data sources used for upscaling carbon fluxes. We utilize same LAI and FAPAR from SPOT/VEGETATION and PROBA-V, similar to NIES (Zeng et al., 2020).

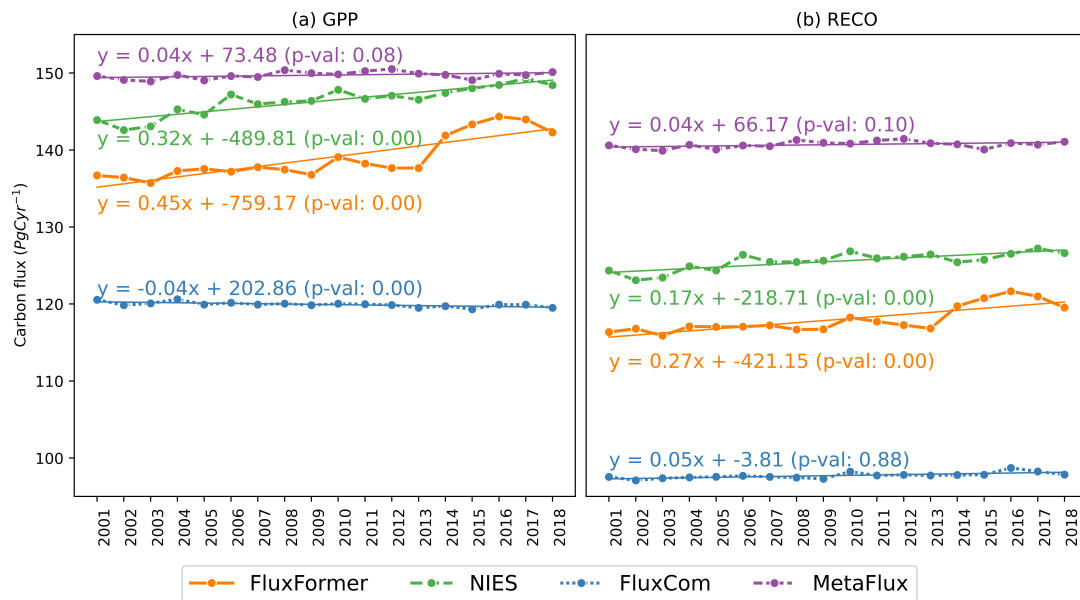


Figure 4.16. Long term trend of global annual mean GPP (a) and RECO (b) from 2001 to 2019 of the four products

2435 In contrast, FluxCom and MetaFlux rely on MODIS data (Jung et al., 2019;
 2436 Nathaniel et al., 2023). Understanding these data source differences and their
 2437 potential impact on interannual variability is crucial for interpreting and com-
 2438 paring carbon flux estimates.

2439 4.2.5 Conclusion

2440 In this study, we present our work in upscaling global gross primary production
 2441 and ecosystem respiration. This is achieved through the application of an MVT
 2442 Transformer model (Zerveas et al., 2021) in conjunction with the updated global
 2443 PFT data (Harper et al., 2022). We provide monthly global data for GPP and
 2444 RECO at a spatial resolution of $0.25^\circ \times 0.25^\circ$, covering the period from 1999 to
 2445 2019.

2446 Our data show improvement with increased correlation and reduced error when
 2447 compared to FLUXNET 2015 data at both the site level and seasonal trends.
 2448 Notably, our data mostly exhibits strong correlations with the seasonal trends of
 2449 GPP and RECO in tropical monsoon and rainforest regions.

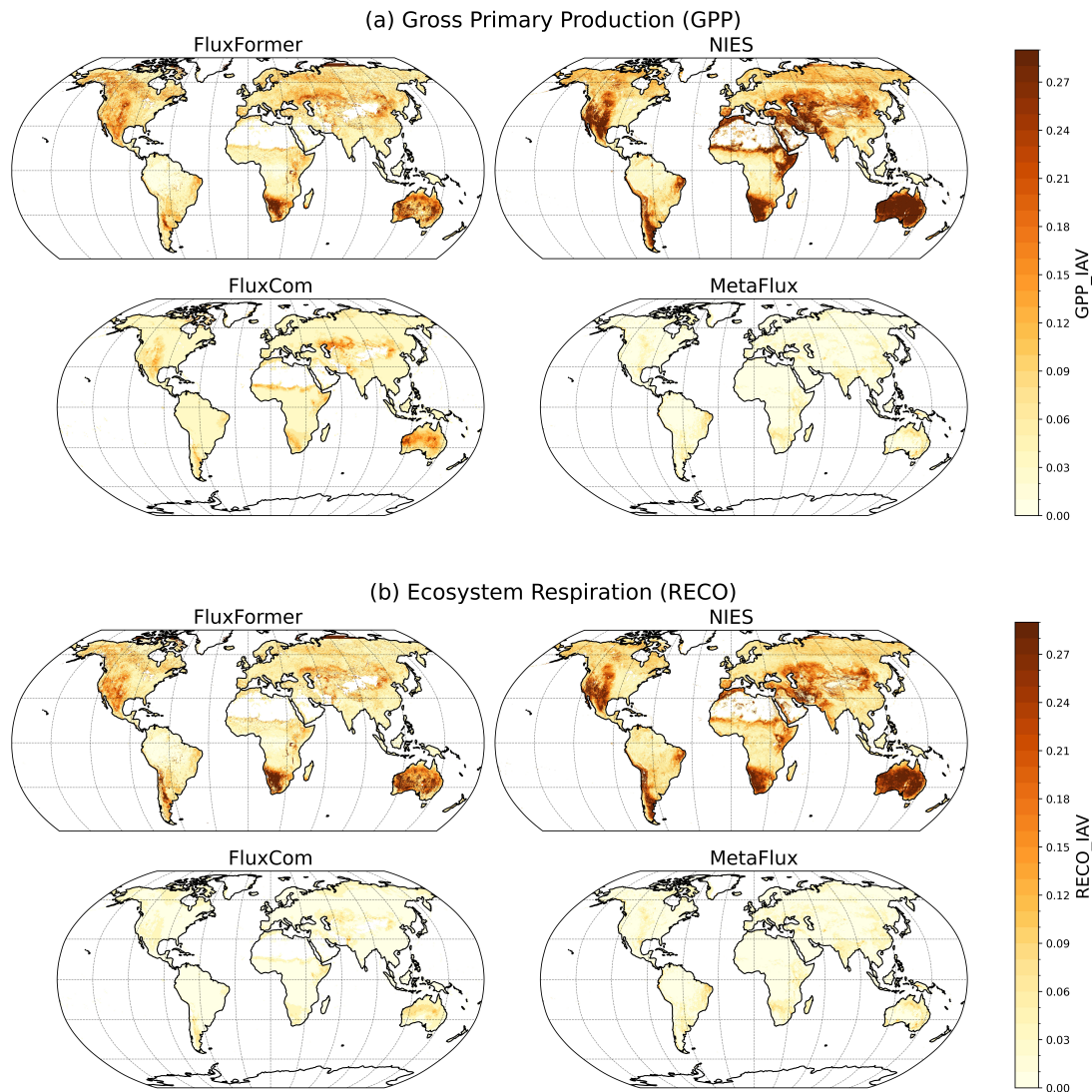


Figure 4.17. Interannual variations from 2001 to 2019 of GPP (a), and RECO (b)

We further assess the seasonal trend of our dataset using two SIF products, CSIF and TROPOMI SIF. Our dataset exhibits a strong GPP-SIF correlation in continental and temperate regions, consistent with other products. However, in tropical and semi-arid regions, our dataset shows lower GPP-SIF correlations compared to others, aligning with findings in (Sanders et al., 2016; Doughty et al., 2021; Shekhar et al., 2022). This lower correlation is attributed to the

2456 weak seasonality in tropical photosynthesis (Montgomery and Chazdon, 2001),
2457 making the linear GPP-SIF relationship less evident.

2458 We also investigated the long-term trends of GPP and RECO from 2001 to
2459 2019 and observed that our data exhibits the highest positive trend in GPP
2460 during this period, with a growth rate of 0.45 PgC per year. This finding aligns
2461 with previous studies (Piao et al., 2020; Yang et al., 2022; Guo et al., 2023),
2462 supporting the assumption that the CO₂ fertilization effect should increase GPP
2463 over time. In contrast, MetaFlux and FluxCom fail to replicate the long-term
2464 trend of GPP, contradicting the currently recognized significant greening observed
2465 from regional to global scales (Piao et al., 2020).

2466 Lastly, we examined the interannual variations of FluxFormer in comparison
2467 with other datasets. We observed that FluxFormer exhibits lower variations in
2468 extreme-low-GPP regions, such as deserts and semi-arid regions, when utilizing
2469 the same source of remote sensing data as NIES. However, FluxFormer shows
2470 higher variations than FluxCom and MetaFlux, possibly due to the utilization of
2471 different remote sensing resources.

5 Carbon neutrality roadmaps

platform

²⁴⁷⁴ This chapter is partially based on the paper (Fukui et al., 2021):

- ²⁴⁷⁵ • Hiromichi Fukui, Duc Chuc Man, Anh Phan (2021), Digital Earth: A
²⁴⁷⁶ platform for the SDGs and green transformation at the global and local
²⁴⁷⁷ level, employing essential SDGs variables, Big Earth Data, 5:4, 476-496,
²⁴⁷⁸ doi: <https://doi.org/10.1080/20964471.2021.1948677>.

5.1 Introduction

²⁴⁸⁰ The widely acknowledged importance of climate change across various aspects
²⁴⁸¹ (Primack et al., 2009; Watanabe and Kume, 2009; Ogawa-Onishi and Berry, 2013;
²⁴⁸² Shibuya and Croxford, 2016) is driving an accelerated momentum toward achiev-
²⁴⁸³ ing Carbon Neutrality (CN) in local Japanese governments (Nakazawa et al.,
²⁴⁸⁴ 2023). In both major corporations and small businesses, there is a rising demand
²⁴⁸⁵ for the measurement of greenhouse gas (GHG) emissions (Kauffmann et al., 2012).
²⁴⁸⁶ Companies are mandated to visualize their CO₂ emissions and implement mea-
²⁴⁸⁷ sures to reduce them. As of September 2023, 991 local governments, including
²⁴⁸⁸ Tokyo, Kyoto, and Yokohama, have demonstrated increased enthusiasm for this
²⁴⁸⁹ initiative by declaring their commitment to achieving net-zero carbon emissions
²⁴⁹⁰ by 2050 (Ministry of the Environment, 2023). However, to specifically implement
²⁴⁹¹ mitigation and adaptation measures, it is necessary to perform comprehensive
²⁴⁹² risk analysis and calculate detailed emissions for each sector. Furthermore, it is
²⁴⁹³ required to visualize this information in an easy-to-understand manner in time
²⁴⁹⁴ and space, and to explain and disclose it to various stakeholders. On the other
²⁴⁹⁵ hand, in recent years, local governments have been accelerating the integration

of map information that had previously been prepared separately for each department, such as taxation, urban planning, and the environment. Integrated geographic information systems (GIS) enable cross-sectional analysis of various elements, have become one of the cornerstones of administrative digital transformation (DX), and have been introduced in 60% of all 1,741 municipalities (Nikkei, 2023).

By using WebGIS functions, local CN-related policy makers can monitor energy consumption and CO₂ emissions by sector such as industry, electricity, transportation, buildings and housing. By integrating it into the Geo-portal site, it will be possible to better understand the actual situation and make appropriate plans to introduce renewable energy and reduce emissions. However, for example, although national energy consumption and power generation can be determined from the regional energy supply and demand database (Tohoku University, 2023) and the electric power database (Asanobu, 2023; Planning and Regional Policy Bureau, 2023), the visualization systems for these databases have been developed separately, therefore it is difficult for policy makers to analyze comprehensibly and make integrated planning.

In this chapter, we presented a case study illustrating the development of a comprehensive tool for developing a "Supporting and Visualizing Carbon Neutrality (CN) Roadmap". This tool serves as a Digital Earth application designed to aid Japanese local governments in their pursuit of CN goals. To achieve CN, it is necessary to create cost-effective roadmaps (scenarios) based on the characteristics of each region and local government. Drafting such scenarios requires a comprehensive understanding of energy use and CO₂ emission patterns in each sector. The Project Drawdown (Brennan et al., 2020), a prominent initiative in this realm, represents a collaborative effort among multidisciplinary scientists, researchers, and practitioners. Its primary objective is to identify and advocate for the most impactful solutions to mitigate and potentially reverse global warming. A research group composed of researchers and policymakers has formulated and recommended various solutions for reducing greenhouse gas emissions. Despite these proposals, none of the tools have been fully integrated into the GIS platform. The integration of greenhouse gas (GHG) monitoring and zero carbon roadmap simulation into GIS platforms is currently under exploration within the

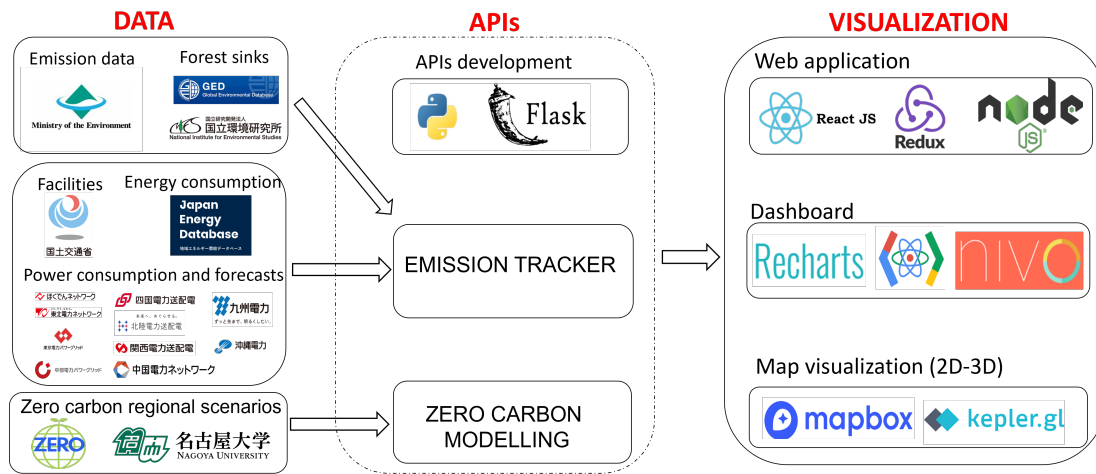


Figure 5.1. Platform Architecture and the technology used to develop the GIS platform

2529 Digital Earth platform (Fukui et al., 2021). Consequently, we are engaged in re-
 2530 search and development efforts aimed at creating a Digital Earth-based platform.
 2531 This platform is designed to furnish policymakers with comprehensive roadmaps,
 2532 progress tracking toward goals, and other pertinent information, all within a uni-
 2533 fied GIS platform (Figure 5.1).

5.2 Method

2534 Figure 5.1 depicts the components of the GIS platform established in this study
 2535 and the core technologies utilized in its development. Initially, the process in-
 2536 volves collecting, preprocessing, and archiving CO₂ emissions and related data
 2537 from various sources. This data is then made available to end-users for visualiza-
 2538 tion and other purposes through the development of Application Programming
 2539 Interfaces (APIs). The API is designed to encompass two main functionalities:
 2540 the CO₂ Emissions Tracker and Zero Carbon Modeling (also referred to as Draw-
 2541 down). In the CO₂ Emissions section, users can analyze trends and patterns in
 2542 CO₂ emissions. In the Zero Carbon Modeling (Drawdown) section, roadmaps are
 2543 presented for 1,741 municipalities, each delineating effective reduction strategies
 2544 for achieving carbon neutrality by 2050.

2546 **5.2.1 Data collection**

2547 Table 5.1 compiles information on datasets integrated into the GIS platform,
 2548 along with their respective data sources. All data utilized underwent collection
 2549 or preprocessing to maintain original resolution and municipality granularity.

Table 5.1. The dataset used for the GIS platform development

Dataset	Data source
CO ₂ emissions by sector	(Ministry of the Environment, 2022)
Energy consumption statistics	(Tohoku University, 2023)
Power generation facility	(Planning and Regional Policy Bureau, 2023)
Power consumption and forecasts	(Hokkaido Electric Power, 2023) (Tohoku Electric Power, 2023) (Tokyo Electric Power, 2023) (Chubu Electric Power, 2023) (Hokuriku Electric Power, 2023) (Kansai Electric Power, 2023) (Chugoku Electric Power, 2023) (Shikoku Electric Power, 2023) (Kyushu Electric Power, 2023) (Okinawa Electric Power, 2023)
Gross Primary Production	
Net Ecosystem Production	(Ito, 2019)
Ecosystem respiration	
Zero carbon regional scenario	(Tsuneo et al., 2023)

2550 Initially, for monitoring current greenhouse gas emissions and energy-related
 2551 issues, we employed diverse data sources. Specifically, we utilized CO₂ emission
 2552 estimates by sectors from (Ministry of the Environment, 2022) to visualize the
 2553 overall emission landscape. Additionally, we delved into industrial emissions de-
 2554 tails, using data from the Ministry of the Environment spanning 2009 to 2017.
 2555 To depict forest sink capabilities, we incorporated three terrestrial carbon flux
 2556 variables—gross primary production, net ecosystem production, and ecosystem
 2557 respiration—from (Ito, 2019). For presenting energy-related information, energy

consumption data from (Tohoku University, 2023) showcased the contrast between 2013 and 2019. The distribution of power plants across the country was illustrated using data from (Planning and Regional Policy Bureau, 2023). To offer near-real-time power consumption, we utilized data from 10 electric power companies, as outlined in Table 5.1, showcasing power consumption and forecasts.

Subsequently, we integrated data from the Zero Carbon Region Scenario Analysis Tool (Tsuneo et al., 2023), specifically designed to assist municipal staff in identifying and achieving CO₂ reduction targets for 2030, 2040, and 2050 to attain net-zero carbon by 2050. This information was utilized to generate corresponding maps and charts for visualization.

5.2.2 API development

In the development of the API for handling this data, we employed Flask (Grinberg, 2018), a lightweight web framework coded in Python, and conformed to the JSON API specification for data formatting. The API within this system is responsible for rendering dashboards related to Emission Tracker and Zero Emission Modeling (Drawdown). JSON functions as the predominant data format for the API, with all responses aligning with the specifications outlined in Table 5.2. The APIs are deployed on the cloud-based platform Heroku, and the interfaces are depicted in Figure 5.2.

Table 5.2. APIs specifications

End point	Parameters	Description
Base URL: https://emissionjp.herokuapp.com/ems_tracker/		
GET /overall_ems/country	year: year of the emission data	Emissions at national level
GET /overall_ems/municipality	adm_code: municipality code year: year of the emission data	Emissions at municipality level in a specific year
GET /overall_ems/municipality_ts	adm_code: municipality code	Time-series emissions at municipality level.
GET /overall_ems/sector	sector_type: sector type	Emissions categorized by sectors.
GET /ee_stats/5mins	None	Near real time power usage, forecast
GET /ee_stats/energy_consumption	adm_code: municipality code	Energy consumption at municipality level.
GET /forest_sink/municipality	adm_code: municipality code	Forest variable at municipality level.
GET /industry/annual_ems	adm_code: municipality code year: year of the emission data	Industrial emission at municipality level
Base URL: https://emissionjp.herokuapp.com/zero_ems/		
GET /zero_ems/municipality	adm_code: municipality code	Roadmap to reduce GHG at municipality level

We present examples of two API responses, achieved through the execution of

2578 a GET request directed to two distinct endpoints: /overall_ems/municipality for
 2579 generating a map visualization and /overall_ems/municipality_ts for generating
 2580 a line chart visualization specific to a municipality. This demonstration offers a
 2581 clear and practical example of the API's functionality. Users can initiate these
 2582 requests without the need for authentication.

Listing 5.1. A response from GET /overall_ems/municipality

```

2583 {
2584   "features": [
2585     {
2586       "geometry": {
2587         "coordinates": [[[...]],
2588         "type": "Polygon"
2589       },
2590       "id": "26",
2591       "properties": {
2592         "adm_code": 23100,
2593         "agriculture": 30,
2594         "building": 3435,
2595         "business": 5034,
2596         "city": "Nagoya Shi",
2597         "construction_mining": 235,
2598         "consumer_total": 8469,
2599         "freight_car": 1222,
2600         "industry_total": 3900,
2601         "manufacture": 3635,
2602         "passenger_car": 2134,
2603         "pref": "Aichi Ken",
2604         "railway": 126,
2605         "ship": 46,
2606         "total": 16017,
2607         "transportation_total": 3528,
2608         "waste": 121
2609       },
2610     }
2611   }
2612 }
```

Listing 5.2. A response from GET /overall_ems/municipality_ts

```
2613 {  
2614     "result": [  
2615         {  
2616             "agriculture": 39,  
2617             "building": 2473,  
2618             "business": 3032,  
2619             "construction_mining": 311,  
2620             "freight_car": 1478,  
2621             "manufacture": 6910,  
2622             "passenger_car": 1840,  
2623             "railway": 133,  
2624             "ship": 36,  
2625             "waste": 144,  
2626             "year": 1990  
2627         },  
2628         ...  
2629         {  
2630             "agriculture": 30,  
2631             "building": 3435,  
2632             "business": 5034,  
2633             "construction_mining": 235,  
2634             "freight_car": 1222,  
2635             "manufacture": 3635,  
2636             "passenger_car": 2134,  
2637             "railway": 126,  
2638             "ship": 46,  
2639             "waste": 121,  
2640             "year": 2005  
2641         },  
2642     ]  
2643 }  
2644 }
```

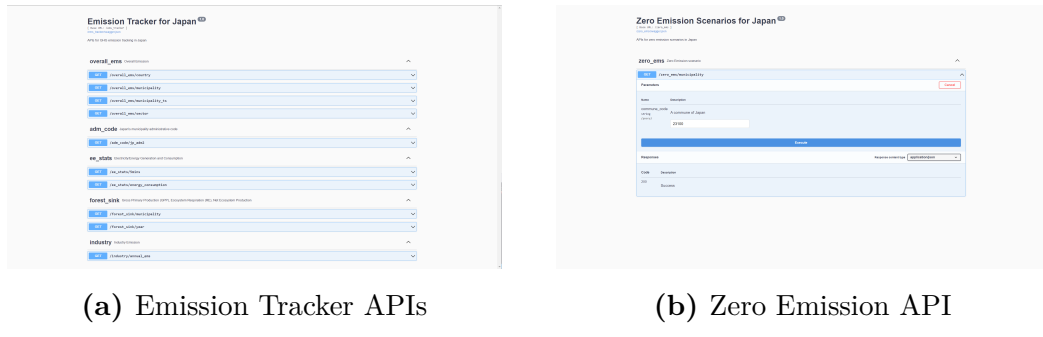


Figure 5.2. APIs interfaces Emission Tracker APIs (a) Zero Emission APIs (b)

5.2.3 Web application

The web application comprises two primary functionalities: (1) tracking greenhouse gas (GHG) emissions, referred to as the Emissions Tracker, and (2) modeling scenarios for achieving zero-carbon emissions, known as Drawdown. The objective of the GHG emission tracker is to offer a comprehensive overview of emissions and forest sinks at the municipality level. Additionally, we provide data on energy consumption to enhance end-users' understanding of the current situation. To achieve this, we have organized the GHG emission tracker into five specific tabs: Emission Overview, Forest Sinks, Energy Consumption, Electricity Statistics, and Industrial Emission. In the context of Drawdown modeling, we present simulation results that serve as a roadmap for maximizing emission reduction by 2050. To construct the interactive and informative GIS dashboard, we utilized the following technologies for platform development.

- Web Application: Node.js, ReactJS, Redux
- Interactive Charts: Rechart, React Google Charts, NIVO
- Interactive Maps: Mapbox and Kepler.gl

5.3 Result and discussion

5.3.1 Result

The summary of usage scenarios for the created GIS platform is presented below. Initially, we delve into the interface of Emission Tracker-related pages (see Figure 5.3) and the Drawdown page see Figure 5.4. Subsequently, we elaborate on other functionalities of the platform (see Figure 5.5).

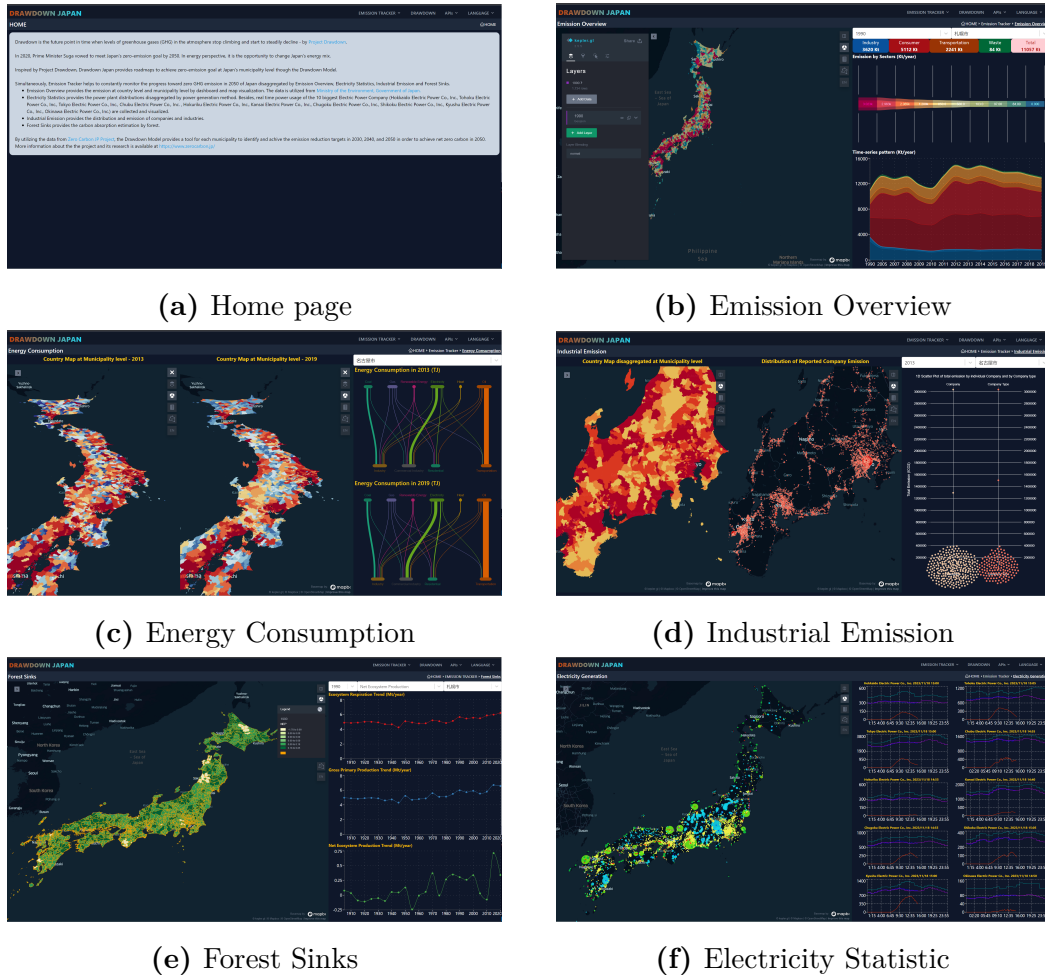


Figure 5.3. Emission Tracker interfaces

The Emission Tracker, depicted in Figure 5.3, furnishes details about emissions and energy consumption at the municipal level. The visualized data is categorized

2670 into tabs, encompassing an overview of emissions, energy consumption, electricity
2671 statistics, industrial emissions, and forest sinks. Users can conveniently access
2672 pertinent information by choosing a municipality of interest through a dropdown
2673 selection box or a map.

2674 [Emission Overview]: The content of this webpage, illustrated in Figure 5.3b,
2675 presents emission data categorized by sector (Industry, Consumer, Transportation,
2676 Waste) spanning from 1990 to 2019. This section offers insights into the
2677 current status and temporal fluctuations in emissions.

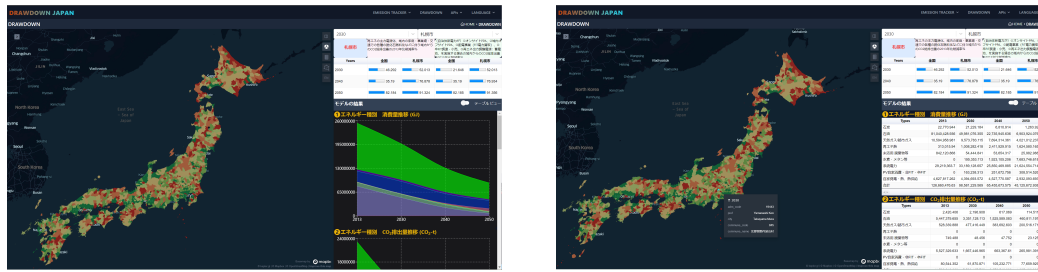
2678 [Energy Consumption]: The contents of this webpage, depicted in Figure 5.3c,
2679 provide in-depth details regarding energy consumption at the municipal level in
2680 Japan spanning from 2013 to 2019. The data is compiled based on energy type
2681 and sector, aiding in decision-making processes related to efficient energy use and
2682 savings.

2683 [Electricity Statistics]: The content on this webpage, illustrated in Figure 5.3f,
2684 presents details on the spatial distribution of power plants in Japan, categorized
2685 by plant type. The information encompasses data from major domestic power
2686 companies, covering electricity usage, usage forecasts, and supply forecasts. This
2687 data is sourced through the provided APIs from 10 major electric power compa-
2688 nies, each representing a region in Japan (Table 5.1 contains the API endpoints
2689 for the data utilized in the platform, sourced from 10 electric companies).

2690 [Industrial Emissions]: The content on this webpage, depicted in Figure 5.3d,
2691 provides a thorough perspective on industrial sector emissions. It displays emis-
2692 sion profiles for each company (specific operators under the Energy Saving Act
2693 with a total energy usage of 1500kl/year or more) from 2009 to 2017. The web-
2694 page utilizes reporting information in accordance with the Energy Saving Act to
2695 consolidate municipal-level emissions, offering insights into the nationwide distri-
2696 bution of industrial emissions. Additionally, it ranks companies based on annual
2697 emissions within municipalities, serving as reference information for monitoring
2698 industrial sector emissions.

2699 [Forest Sinks]: The content on this webpage, illustrated in Figure 5.3e, exhibits
2700 three crucial variables associated with forest absorption: Gross Primary Produc-
2701 tion (GPP), Net Ecosystem Production (NEP), and ecosystem respiration. These
2702 variables, obtained from simulations conducted by the global model Vegetation

2703 Integrative Simulator for Trace Gas (VISIT), depict a long-term trend spanning
 2704 from 1901 to 2020. The data is presented at the municipal level, offering a rolling
 2705 display of 5 years of data.



(a) Map and charts

(b) Map and tables

Figure 5.4. Drawdown tab interfaces

2706 The "Drawdown" page (refer to Figure 5.4) outlines a comprehensive roadmap
 2707 for achieving a reduction in CO₂ emissions by 2050 at the municipal level in
 2708 Japan. Specifically, it provides a roadmap with diverse parameters, including
 2709 trends in energy consumption, trends in CO₂ emissions by energy type, trends in
 2710 CO₂ emissions by sector/industry, regional renewable energy electricity, regional
 2711 production-consumption planning, and the ratio of total regional production-
 2712 consumption to total energy usage. Additionally, it visually represents the total
 2713 CO₂ emissions reduction by 2030, 2040, and 2050. This enables municipal officials
 2714 not only to scrutinize their municipality's data intricately but also to enhance
 2715 their understanding through personalized data comparisons with other similar
 2716 municipalities.



(a) 3D buildings visualization

(b) Japanese text

Figure 5.5. Additional platform interfaces

In addition to the functionalities outlined earlier, as we incorporated Kepler.gl for map visualization, which enables end-users to customize the map personally with options such as 2D/3D views, color schemes, tooltips, and various settings (refer to Figure 5.5). Users also have the capability to upload their own data for visualization and comparison with the provided data. Furthermore, we offer content in both English and Japanese to facilitate easy comprehension of information on our GIS platform.

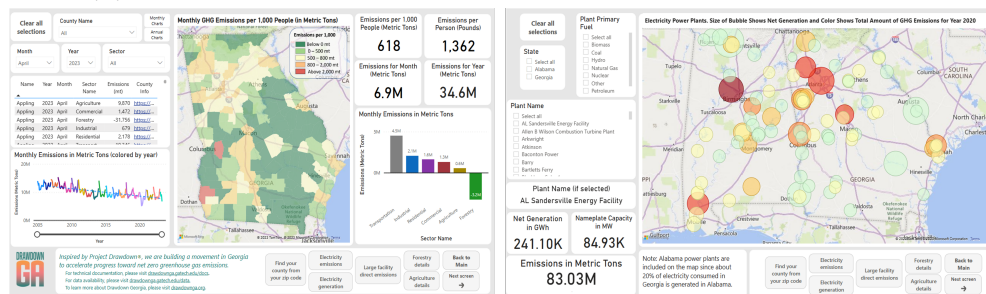
The GIS platform is accessible at <http://de14.digitalasia.chubu.ac.jp/>.

5.3.2 Discussion

When comparing this GIS platform to existing platforms like Project Drawdown (refer to Figure 5.6a) and Drawdown Georgia (Brown et al., 2022, 2021) (refer to Figure 5.6b), the interface design may differ slightly, but the commonality lies in charts and maps being fundamental components.



(a) The Drawdown modelling interface of the Project Drawdown



(b) The GHG Tracker interface of the Drawdown Georgia project

Figure 5.6. The interfaces of the Project Drawdown (a) and the GHG Tracker (Drawdown Georgia) (b)

The key distinction between this GIS platform and these existing platforms

2731 is that this platform has become an integrated Geo-portal, utilizing GIS for all
2732 components from emission tracking to drawdown modelling. This integration
2733 allows for a comprehensive representation of emission data and simultaneously
2734 provides a simulated roadmap, setting it apart from other platforms.

2735 In the future, we plan to enhance the user interface based on user experience
2736 feedback and incorporate a global perspective into the system development.

6 Conclusions and future prospects

6.1 Key finding and contributions

In this study, my initial focus was on researching air pollution at the local level. I investigated the impact of intervention events on regional air pollution changes, aiming to provide evidence and recommendations for future local policies. Subsequently, my attention shifted to GHGs monitoring. Specifically, I worked on estimating global terrestrial carbon fluxes using updated PFTs data and Transformer-based models which have been limitedly adopted in previous studies. Finally, I developed a digital earth platform to monitor fossil fuel GHGs as well as the capacity of terrestrial forest carbon fluxes, enabling the development of efficient carbon neutrality roadmaps at the local level. In this section of the study, I address the five research questions raised in Chapter 1, with references to the chapters and their relevant contributions.

1. What was the influence of the COVID-19 lockdown and the armed conflict on air quality in Ukraine, and how can this information offer evidence and recommendations for future policies?

I analyzed tropospheric NO₂ levels in Ukraine during two significant periods and found that meteorological variations were the primary contributors to the reduction in NO₂ in populous cities during the lockdown period in 2020. After normalizing for meteorological effects, I observed a moderation in the increase of NO₂ levels during the lockdown compared to pre-lockdown levels. Examining the same months during the conflict in 2022, we identified even more substantial reductions in NO₂ levels in these cities. Additionally, beyond our investigation of major urban areas, we noticed decreases in NO₂ levels in areas surrounding

2762 coal power plants that were damaged or destroyed during the conflict. Regarding
2763 major urban areas in Ukraine, we conclude that changes in daily anthropogenic
2764 activities due to conflict-related events had a more significant impact on NO₂
2765 levels than the COVID-19 lockdown.

2766 In Europe, road transport is identified as the primary contributor to NO₂
2767 emissions (González Ortiz et al., 2020). Conversely, in Ukraine, the major source
2768 of NO₂ emissions is traced back to Coal Power Plants (CPPs) (Lauri and Rosa,
2769 2021). The imposition of COVID-19 lockdown measures in 2020 resulted in a
2770 substantial decrease in NO₂ emissions in European cities due to reduced mobility
2771 (Barré et al., 2021; Grange et al., 2021). In contrast, such reduction was not
2772 observable in Ukraine after accounting for weather effects, likely due to limited
2773 reductions in the operation of CPPs, as detailed in Chapter 3, section 3.1 of our
2774 study. However, during the armed conflict with Russia in 2022, numerous CPPs
2775 in Ukraine incurred damage, leading to a noticeable decline in NO₂ emissions in
2776 densely populated cities. Our findings and evidence suggest that future policies
2777 targeting NO₂ reduction from road transportation may not yield comparable
2778 effectiveness in Ukraine's populous cities. Comprehensive results for this analysis
2779 are presented in Chapter 3, section 3.1.

2780 *2. In what ways did the COVID-19 lockdown influence air quality in Japan,
2781 and how can this information serve as evidence and provide suggestions for future
2782 policies?*

2783 I investigated the influence of NO₂ reduction on O₃ and CH₄ variations in
2784 14 metropolitan areas (MAs) of Japan in 2020, utilizing air quality time series
2785 generated by machine learning models under business-as-usual conditions. Addi-
2786 tionally, I employed satellite observations and biogeochemical model simulations
2787 to analyze changes in air quality. During the lockdown period from April 7 to
2788 May 25, 2020, I observed a NO₂ reduction equivalent to a decrease representing
2789 3.4 years and 5 years of the corresponding trends in roadside and ambient air
2790 quality recorded from 2010 to 2019. After meteorological normalization, NO₂
2791 decreased by 14.5% at ambient air stations and 19.1% at roadside stations. Sur-
2792 prisingly, the NO₂ reduction did not immediately lead to increased O₃, contrary
2793 to what has been widely observed in European cities during the lockdown in 2020
2794 (Grange et al., 2021; Shi et al., 2021). Instead, O₃ levels rose after the lockdown,

2795 specifically in August due to favourable sunny conditions. This finding is impor-
2796 tant for Japan and has not been reported in previous studies. We also found that
2797 changes in NO₂ and CO marginally contributed to variations in CH₄ levels across
2798 the study areas.

2799 We present evidence indicating an increase in O₃ after the lockdown in most
2800 of the MAs from Okayama northwards. This occurrence could potentially be at-
2801 tributed to these MAs being VOC-limited areas, implying that future reductions
2802 in NO₂ could pose a risk of increased O₃ levels under favorable sunny condi-
2803 tions. However, in MAs from Hiroshima southwards, instances of NO_x limitation
2804 were observed, implying that future reductions in anthropogenic non-methane
2805 volatile organic compounds (NMVOCs) may have minimal effectiveness in low-
2806 ering O₃ levels (Akimoto and Tanimoto, 2022). Therefore, based on our findings
2807 and evidence, to effectively mitigate the adverse effects on O₃ as well as CH₄, it
2808 is recommended to simultaneously reduce air pollutants, as well as anthropogenic
2809 and biogenic volatile organic compounds, in future policies. Detailed results for
2810 this analysis are presented in Chapter 3, section 3.2.

2811 *3. What methodologies can be employed to improve PFTs mapping performance
2812 in data-sparse regions?*

2813 We proposed a combined machine learning approach with a deep convolutional
2814 neural network (CNN) which improves the accuracy of PFTs mapping and tree
2815 age estimation in Ena city, Japan. First, we employed the Random Forest (RF)
2816 classifier using Google Earth Engine (GEE) for forest mapping. Then, we de-
2817 signed a deep CNN architecture that works for PFTs and forest age mapping
2818 from coarse and polygonal ground-truth data. The proposed network has U-shape
2819 and comprises 3D Atrous Convolutions. The model was optimized by a weighted
2820 cross-entropy loss function. We trained the model with times-series Sentinel 1, 2,
2821 and Digital Elevation Model data with sparse annotations. Our proposed mod-
2822 els achieved 94.5% overall accuracy (OA) for forest mapping, 77.80% (OA) for
2823 PFTs, and 81.74% (OA) for forest age classification, respectively which outper-
2824 formed the 2D and 3D UNET performance. Detailed results for this analysis are
2825 presented in Chapter 4, section 4.1.

2826 *4. Can the utilization of updated PFT maps and Transformer-based models
2827 enhance the accuracy of global terrestrial carbon flux estimates?*

Yes, by utilizing the new PFTs dataset (Harper et al., 2022) in combination with multivariate timeseries Transformer-based model (Zerveas et al., 2021) we provided a monthly global gross primary production (GPP) and ecosystem respiration (RECO) dataset from 1990 to 2019 at $0.25^\circ \times 0.25^\circ$ spatial resolution named FluxFormer which outperforms FLUXCOM (Jung et al., 2019), NIES (Zeng et al., 2020), and MetaFlux (Nathaniel et al., 2023) datasets when comparing the correlation at site-level and seasonal pattern with FLUXNET 2015, especially in tropical regions. Additionally, our dataset shows the highest positive trend in GPP from 2001 to 2019, aligning with studies like (Piao et al., 2020; Guo et al., 2023; Yang et al., 2022). Notably, it captures long-term trends that FLUXCOM and MetaFlux fail to replicate, contradicting the observed significant greening reported by (Piao et al., 2020). Finally, we compare the interannual variations in our dataset with those in other datasets, noting reduced variations in deserts and semi-arid regions compared to the NIES data, given the same remote sensing resources. We find this observation more reasonable due to the extremely low GPP in these areas, which should not lead to high interannual variations. The FluxFormer GPP and RECO products are available at <https://doi.org/10.5281/zenodo.10258644>. Detailed results for this analysis are presented in Chapter 4, section 4.2.

5. How can we efficiently monitor fossil fuels GHGs emissions as well as the capacity of terrestrial forest carbon fluxes, enabling the development of efficient carbon neutrality roadmaps as well as tracking progress at the local level?

We have developed a digital earth platform with a specific focus on providing roadmaps for attaining carbon neutrality at the municipal level in Japan. This platform not only monitors greenhouse gas emissions from fossil fuels and assesses the capacity of local terrestrial forest carbon fluxes but also integrates energy-related data. This encompasses information on energy consumption, electricity statistics, and facilities from major domestic power companies, including data on electricity usage, forecasts, supply, and the distribution of electricity power plants across the country. By consolidating this information, the platform offers a comprehensive overview of the current progress toward achieving a zero-carbon status at the municipal level in Japan. You can access the platform at the following URL: <http://de14.digitalasia.chubu.ac.jp/>. Detailed results for this

2861 analysis are presented in Chapter 5.

2862 6.2 Future prospects

2863 CO₂ is a critical greenhouse gas, but real-time monitoring of fossil fuel CO₂ emis-
2864 sions faces challenges, resulting in high uncertainties in estimated results (Mar-
2865 land, 2008). Traditional bottom-up inventories are time-consuming (Marland,
2866 2008). A recent top-down method uses advancements in satellite observations
2867 and data assimilation frameworks. However, current satellites like GOSAT and
2868 OCO-2 focus on natural carbon fluxes at regional scales, limiting their ability
2869 to quantify anthropogenic emissions (Nassar et al., 2017; Yang et al., 2023). In
2870 contrast, satellite-derived NO₂ observations, such as OMI or TROPOMI, offer
2871 advanced capabilities and higher resolutions. They can potentially constrain fos-
2872 sil fuel CO₂ emissions at city levels. An indirect top-down method leverages NO₂
2873 observations as proxies for fossil fuel CO₂ combustion, beneficial for constraining
2874 emissions and monitoring fluctuations (Ciais et al., 2014; Goldberg et al., 2019).
2875 These approaches, applied in national scales in countries such as the US, Eu-
2876 rope, China, and India (Konovalov et al., 2016; Zheng et al., 2020; Miyazaki and
2877 Bowman, 2023) and in cities like Wuhan (Zhang et al., 2023a), Buenos Aires,
2878 Melbourne, and Mexico City (Yang et al., 2023), have not been extensively stud-
2879 ied in Japan at national or municipal levels. Conducting such studies in Japan
2880 could provide supplementary datasets to refine "bottom-up" inventories and eval-
2881 uate climate change mitigation strategies. These investigations are necessary for
2882 refining our understanding of CO₂ emissions and mitigation strategies, offering
2883 valuable insights from local to global scales.

2884 Additionally, leveraging the high-frequency temporal data from satellite-derived
2885 NO₂ observations for predicting fossil fuel CO₂, along with the global upscaled
2886 terrestrial carbon fluxes detailed in Chapter 4, section 4.2, is anticipated to pro-
2887 vide the most current assessment of achieving zero carbon emissions on both
2888 regional and global scales when integrated into a Digital Earth platform as de-
2889 scribed in Chapter 5. Recent publications in this field within the current year,
2890 such as (Zhang et al., 2023a; Yang et al., 2023; Miyazaki and Bowman, 2023),
2891 reflect active research in these areas. This presents a room for my future works.

²⁸⁹² Bibliography

- ²⁸⁹³ Hajime Akimoto and Hiroshi Tanimoto. Rethinking of the adverse effects of nox-
²⁸⁹⁴ control on the reduction of methane and tropospheric ozone—challenges toward
²⁸⁹⁵ a denitrified society. *Atmospheric Environment*, 277:119033, 2022.
- ²⁸⁹⁶ Robert J Andres, Thomas A Boden, and David M Higdon. Gridded uncertainty
²⁸⁹⁷ in fossil fuel carbon dioxide emission maps, a cdiac example. *Atmospheric
Chemistry and Physics*, 16(23):14979–14995, 2016.
- ²⁸⁹⁹ Robert Joseph Andres, Thomas A Boden, F-M Bréon, Philippe Ciais, Steve
²⁹⁰⁰ Davis, D Erickson, J Sterling Gregg, Andrew Jacobson, Gregg Marland,
²⁹⁰¹ J Miller, et al. A synthesis of carbon dioxide emissions from fossil-fuel com-
²⁹⁰² bustion. *Biogeosciences*, 9(5):1845–1871, 2012.
- ²⁹⁰³ Robbie M Andrew. A comparison of estimates of global carbon dioxide emissions
²⁹⁰⁴ from fossil carbon sources. *Earth System Science Data*, 12(2):1437–1465, 2020.
- ²⁹⁰⁵ Kitamoto Asanobu. Electrical japan, 2023. URL <http://agora.ex.nii.ac.jp/earthquake/201103-eastjapan/energy/electrical-japan/>.
- ²⁹⁰⁷ Salvi Asefi-Najafabady, PJ Rayner, KR Gurney, A McRobert, Y Song, K Coltin,
²⁹⁰⁸ J Huang, C Elvidge, and K Baugh. A multiyear, global gridded fossil fuel
²⁹⁰⁹ co₂ emission data product: Evaluation and analysis of results. *Journal of
Geophysical Research: Atmospheres*, 119(17):10–213, 2014.
- ²⁹¹¹ Shiri Avnery, Denise L Mauzerall, Junfeng Liu, and Larry W Horowitz. Global
²⁹¹² crop yield reductions due to surface ozone exposure: 1. year 2000 crop pro-
²⁹¹³ duction losses and economic damage. *Atmospheric Environment*, 45(13):2284–
²⁹¹⁴ 2296, 2011a.

- 2915 Shiri Avnery, Denise L Mauzerall, Junfeng Liu, and Larry W Horowitz. Global
2916 crop yield reductions due to surface ozone exposure: 2. year 2030 potential crop
2917 production losses and economic damage under two scenarios of O_3 pollution.
2918 *Atmospheric Environment*, 45(13):2297–2309, 2011b.
- 2919 Jia Bai, Helin Zhang, Rui Sun, Xing Li, Jingfeng Xiao, and Yan Wang. Estimation
2920 of global gpp from gome-2 and oco-2 sif by considering the dynamic variations
2921 of gpp-sif relationship. *Agricultural and Forest Meteorology*, 326:109180, 2022.
- 2922 Jérôme Barré, Hervé Petetin, Augustin Colette, Marc Guevara, Vincent-Henri
2923 Peuch, Laurence Rouil, Richard Engelen, Antje Inness, Johannes Flemming,
2924 Carlos Pérez García-Pando, et al. Estimating lockdown-induced european NO_2
2925 changes using satellite and surface observations and air quality
2926 models. *Atmospheric chemistry and physics*, 21(9):7373–7394, 2021.
- 2927 M Bauwens, S Compernolle, T Stavrakou, J-F Müller, J Van Gent, H Eskes,
2928 Pieter Nel Felicitas Levelt, R Van Der A, JP Veefkind, J Vlietinck, et al. Impact
2929 of coronavirus outbreak on NO_2 pollution assessed using tropomi and omi
2930 observations. *Geophysical Research Letters*, 47(11):e2020GL087978, 2020.
- 2931 Christian Beer, Markus Reichstein, Enrico Tomelleri, Philippe Ciais, Martin
2932 Jung, Nuno Carvalhais, Christian Rödenbeck, M Altaf Arain, Dennis Baldocchi,
2933 Gordon B Bonan, et al. Terrestrial gross carbon dioxide uptake: global
2934 distribution and covariation with climate. *Science*, 329(5993):834–838, 2010.
- 2935 Roland Bobbink, Kevin Hicks, James Galloway, T Spranger, Rob Alkemade,
2936 M Ashmore, Mercedes Bustamante, S Cinderby, E Davidson, Franciscus Den-
2937 tener, et al. Global assessment of nitrogen deposition effects on terrestrial plant
2938 diversity: a synthesis. *Ecological applications*, 20(1):30–59, 2010.
- 2939 Roberto Bono, Valeria Romanazzi, Valeria Bellisario, Roberta Tassinari, Giulia
2940 Trucco, Antonio Urbino, Claudio Cassardo, Consolata Siniscalco, Pierpaolo
2941 Marchetti, and Alessandro Marcon. Air pollution, aeroallergens and admissions
2942 to pediatric emergency room for respiratory reasons in turin, northwestern italy.
2943 *BMC public health*, 16:1–11, 2016.

- 2944 Rachel A Brennan, Julio Urbina, Jose F Oliden, and Juan Martín Rodríguez.
2945 Project drawdown. In *2020 ASEE Virtual Annual Conference Content Access*,
2946 2020.
- 2947 Marilyn A Brown, Blair Beasley, Fikret Atalay, Kim M Cobb, Puneet Dwivedi,
2948 Jeffrey Hubbs, David M Iwaniek, Sudhagar Mani, Daniel Matisoff, Jacqueline E
2949 Mohan, et al. Translating a global emission-reduction framework for subna-
2950 tional climate action: A case study from the state of georgia. *Environmental*
2951 *Management*, 67(2):205–227, 2021.
- 2952 Marilyn A Brown, Ranal Tudawe, and Hamilton Steimer. Carbon drawdown
2953 potential of utility-scale solar in the united states: Evidence from the state of
2954 georgia. *Renewable and Sustainable Energy Reviews*, 161:112318, 2022.
- 2955 Mingkui Cao, Stewart Marshall, and Keith Gregson. Global carbon exchange
2956 and methane emissions from natural wetlands: Application of a process-based
2957 model. *Journal of Geophysical Research: Atmospheres*, 101(D9):14399–14414,
2958 1996.
- 2959 Anping Chen, Jiafu Mao, Daniel Ricciuto, Dan Lu, Jingfeng Xiao, Xing Li, Pe-
2960 ter E Thornton, and Alan K Knapp. Seasonal changes in gpp/sif ratios and
2961 their climatic determinants across the northern hemisphere. *Global Change*
2962 *Biology*, 27(20):5186–5197, 2021a.
- 2963 D. Chen, M. Rojas, B.H. Samset, K. Cobb, A. Diongue Niang, P. Edwards,
2964 S. Emori, S.H. Faria, E. Hawkins, P. Hope, P. Huybrechts, M. Meinshausen,
2965 S.K. Mustafa, G.-K. Plattner, and A.-M. Tréguier. *Framing, Context, and*
2966 *Methods*, page 147–286. Cambridge University Press, Cambridge, United King-
2967 dom and New York, NY, USA, 2021b. doi: 10.1017/9781009157896.003.
- 2968 Liang-Chieh Chen, George Papandreou, Iasonas Kokkinos, Kevin Murphy, and
2969 Alan L Yuille. Deeplab: Semantic image segmentation with deep convolutional
2970 nets, atrous convolution, and fully connected crfs. *IEEE transactions on pattern*
2971 *analysis and machine intelligence*, 40(4):834–848, 2017a.

- 2972 Liang-Chieh Chen, George Papandreou, Florian Schroff, and Hartwig Adam. Re-
2973 thinking atrous convolution for semantic image segmentation. *arXiv preprint
2974 arXiv:1706.05587*, 2017b.
- 2975 Min Chen, Rashid Rafique, Ghassem R Asrar, Ben Bond-Lamberty, Philippe
2976 Ciais, Fang Zhao, Christopher PO Reyer, Sebastian Ostberg, Jinfeng Chang,
2977 Akihiko Ito, et al. Regional contribution to variability and trends of global
2978 gross primary productivity. *Environmental Research Letters*, 12(10):105005,
2979 2017c.
- 2980 Inc Chubu Electric Power. Electricity forecast for chubu area, 2023. URL <https://powergrid.chuden.co.jp/>.
- 2981 Inc Chugoku Electric Power. Electricity forecast for chugoku area, 2023. URL
2982 <https://www.energia.co.jp/nw/>.
- 2983 Clifford Chuwah, Twan van Noije, Detlef P van Vuuren, Elke Stehfest, and Wilco
2984 Hazeleger. Global impacts of surface ozone changes on crop yields and land
2985 use. *Atmospheric Environment*, 106:11–23, 2015.
- 2986 Philippe Ciais, A Johannes Dolman, Antonio Bombelli, R Duren, A Peregon,
2987 Peter J Rayner, C Miller, Nadine Gobron, G Kinderman, Gregg Marland, et al.
2988 Current systematic carbon-cycle observations and the need for implementing
2989 a policy-relevant carbon observing system. *Biogeosciences*, 11(13):3547–3602,
2990 2014.
- 2991 Özgün Çiçek, Ahmed Abdulkadir, Soeren S Lienkamp, Thomas Brox, and Olaf
2992 Ronneberger. 3d u-net: learning dense volumetric segmentation from sparse
2993 annotation. In *Medical Image Computing and Computer-Assisted Intervention–
2994 MICCAI 2016: 19th International Conference, Athens, Greece, October 17–21,
2995 2016, Proceedings, Part II 19*, pages 424–432. Springer, 2016.
- 2996 Matthew J Cooper, Randall V Martin, Melanie S Hammer, Pieter Nel F Levelt,
2997 Pepijn Veefkind, Lok N Lamsal, Nickolay A Krotkov, Jeffrey R Brook, and
2998 Chris A McLinden. Global fine-scale changes in ambient no₂ during covid-19
2999 lockdowns. *Nature*, 601(7893):380–387, 2022.

- 3001 Monica Crippa, Efisio Solazzo, Ganlin Huang, Diego Guizzardi, Ernest Koffi,
3002 Marilena Muntean, Christian Schieberle, Rainer Friedrich, and Greet Janssens-
3003 Maenhout. High resolution temporal profiles in the emissions database for
3004 global atmospheric research. *Scientific data*, 7(1):121, 2020.
- 3005 Ivan Csizsar, Wilfrid Schroeder, Louis Giglio, Evan Ellicott, Krishna P Vadrevu,
3006 Christopher O Justice, and Brad Wind. Active fires from the suomi npp visible
3007 infrared imaging radiometer suite: Product status and first evaluation results.
3008 *Journal of Geophysical Research: Atmospheres*, 119(2):803–816, 2014.
- 3009 Alessandro Damiani, Hitoshi Irie, Dmitry A Belikov, Shuei Kaizuka, Hossain
3010 Mohammed Syedul Hoque, and Raul R Cordero. Peculiar covid-19 effects in
3011 the greater tokyo area revealed by spatiotemporal variabilities of tropospheric
3012 gases and light-absorbing aerosols. *Atmospheric Chemistry and Physics*, 22
3013 (18):12705–12726, 2022.
- 3014 Bohdan Danylyshyn. The peculiarities of economic crisis due to covid-19 pan-
3015 demic in a developing country: case of ukraine. *Problems and Perspectives in
3016 Management*, 18(2):13–22, 2020.
- 3017 André de Palma, Shaghayegh Vosough, and Feixiong Liao. An overview of effects
3018 of covid-19 on mobility and lifestyle: 18 months since the outbreak. *Trans-
3019 portation Research Part A: Policy and Practice*, 159:372–397, 2022.
- 3020 S. Dhakal, J.C. Minx, F.L. Toth, A. Abdel-Aziz, M.J. Figueroa Meza,
3021 K. Hubacek, I.G.C. Jonckheere, Yong-Gun Kim, G.F. Nemet, S. Pachauri,
3022 X.C. Tan, and T. Wiedmann. Emissions trends and drivers. in ipcc, 2022:
3023 Climate change 2022: Mitigation of climate change. contribution of working
3024 group iii to the sixth assessment report of the intergovernmental panel on cli-
3025 mate change [p.r. shukla, j. skea, r. slade, a. al khourdajie, r. van diemen, d.
3026 mccollum, m. pathak, s. some, p. vyas, r. fradera, m. belkacemi, a. hasija, g.
3027 lisboa, s. luz, j. malley, (eds.)]. 2022. doi: 10.1017/9781009157926.004.
- 3028 Russell Doughty, Xiangming Xiao, Philipp Köhler, Christian Frankenberg, Yuan-
3029 wei Qin, Xiaocui Wu, Shuang Ma, and Berrien Moore III. Global-scale
3030 consistency of spaceborne vegetation indices, chlorophyll fluorescence, and

- 3031 photosynthesis. *Journal of Geophysical Research: Biogeosciences*, 126(6):
3032 e2020JG006136, 2021.
- 3033 Carmelia Mariana Dragomir, Daniel-Eduard Constantin, Mirela Voiculescu, Lu-
3034 cian Puiu Georgescu, Alexis Merlaud, and Michel Van Roozendael. Modeling
3035 results of atmospheric dispersion of no₂ in an urban area using meti-lis and
3036 comparison with coincident mobile doas measurements. *Atmospheric Pollution
3037 Research*, 6(3):503–510, 2015.
- 3038 V. Dumitru, P. Inga, M. Danu, S. Andreas, K. Ievgen, and Y Vik-
3039 toriiia. Covid-19 impact on air quality in ukraine and the republic
3040 of moldova, 2020. URL [https://www.undp.org/ukraine/publications/
3041 covid-19-impact-air-quality-ukraine-and-republic-moldova](https://www.undp.org/ukraine/publications/covid-19-impact-air-quality-ukraine-and-republic-moldova).
- 3042 Bryan N Duncan, Yasuko Yoshida, Jennifer R Olson, Sanford Sillman, Randall V
3043 Martin, Lok Lamsal, Yongtao Hu, Kenneth E Pickering, Christian Retscher,
3044 Dale J Allen, et al. Application of omi observations to a space-based indicator
3045 of nox and voc controls on surface ozone formation. *Atmospheric Environment*,
3046 44(18):2213–2223, 2010.
- 3047 Mark Elder. Strengthening the linkages between air pollution and the sustainable
3048 development goals. *JSTOR Sustainability Collection*, 2016.
- 3049 Liang Feng, Paul I Palmer, Robert J Parker, Mark F Lunt, and Hartmut Bösch.
3050 Methane emissions are predominantly responsible for record-breaking atmo-
3051 spheric methane growth rates in 2020 and 2021. *Atmospheric Chemistry and
3052 Physics*, 23(8):4863–4880, 2023.
- 3053 Mark A Friedl, Damien Sulla-Menashe, Bin Tan, Annemarie Schneider, Navin
3054 Ramankutty, Adam Sibley, and Xiaoman Huang. Modis collection 5 global land
3055 cover: Algorithm refinements and characterization of new datasets. *Remote
3056 sensing of Environment*, 114(1):168–182, 2010.
- 3057 P. Friedlingstein, M. W. Jones, M. O’Sullivan, R. M. Andrew, J. Hauck, G. P.
3058 Peters, W. Peters, J. Pongratz, S. Sitch, C. Le Quéré, D. C. E. Bakker, J. G.
3059 Canadell, P. Ciais, R. B. Jackson, P. Anthoni, L. Barbero, A. Bastos, V. Bas-
3060 trikov, M. Becker, L. Bopp, E. Buitenhuis, N. Chandra, F. Chevallier, L. P.

- 3061 Chini, K. I. Currie, R. A. Feely, M. Gehlen, D. Gilfillan, T. Gkritzalis, D. S.
3062 Goll, N. Gruber, S. Gutekunst, I. Harris, V. Haverd, R. A. Houghton, G. Hurttt,
3063 T. Ilyina, A. K. Jain, E. Joetzjer, J. O. Kaplan, E. Kato, K. Klein Goldewijk,
3064 J. I. Korsbakken, P. Landschützer, S. K. Lauvset, N. Lefèvre, A. Lenton,
3065 S. Lienert, D. Lombardozzi, G. Marland, P. C. McGuire, J. R. Melton,
3066 N. Metzl, D. R. Munro, J. E. M. S. Nabel, S.-I. Nakaoka, C. Neill, A. M.
3067 Omar, T. Ono, A. Peregón, D. Pierrot, B. Poulter, G. Rehder, L. Resplandy,
3068 E. Robertson, C. Rödenbeck, R. Séférian, J. Schwinger, N. Smith,
3069 P. P. Tans, H. Tian, B. Tilbrook, F. N. Tubiello, G. R. van der Werf, A. J.
3070 Wiltshire, and S. Zaehle. Global carbon budget 2019. *Earth System Science Data*, 11(4):1783–1838, 2019. doi: 10.5194/essd-11-1783-2019. URL
3071 <https://essd.copernicus.org/articles/11/1783/2019/>.
- 3072
- 3073 P. Friedlingstein, M. O’Sullivan, M. W. Jones, R. M. Andrew, L. Gregor,
3074 J. Hauck, C. Le Quéré, I. T. Luijkx, A. Olsen, G. P. Peters, W. Peters, J. Pon-
3075 gratz, C. Schwingshackl, S. Sitch, J. G. Canadell, P. Ciais, R. B. Jackson, S. R.
3076 Alin, R. Alkama, A. Arneth, V. K. Arora, N. R. Bates, M. Becker, N. Bel-
3077 louin, H. C. Bittig, L. Bopp, F. Chevallier, L. P. Chini, M. Cronin, W. Evans,
3078 S. Falk, R. A. Feely, T. Gasser, M. Gehlen, T. Gkritzalis, L. Gloege, G. Grassi,
3079 N. Gruber, Ö. Gürses, I. Harris, M. Hefner, R. A. Houghton, G. C. Hurttt,
3080 Y. Iida, T. Ilyina, A. K. Jain, A. Jersild, K. Kadono, E. Kato, D. Kennedy,
3081 K. Klein Goldewijk, J. Knauer, J. I. Korsbakken, P. Landschützer, N. Lefèvre,
3082 K. Lindsay, J. Liu, Z. Liu, G. Marland, N. Mayot, M. J. McGrath, N. Metzl,
3083 N. M. Monacci, D. R. Munro, S.-I. Nakaoka, Y. Niwa, K. O’Brien, T. Ono, P. I.
3084 Palmer, N. Pan, D. Pierrot, K. Pocock, B. Poulter, L. Resplandy, E. Robert-
3085 son, C. Rödenbeck, C. Rodriguez, T. M. Rosan, J. Schwinger, R. Séférian,
3086 J. D. Shutler, I. Skjelvan, T. Steinhoff, Q. Sun, A. J. Sutton, C. Sweeney,
3087 S. Takao, T. Tanhua, P. P. Tans, X. Tian, H. Tian, B. Tilbrook, H. Tsujino,
3088 F. Tubiello, G. R. van der Werf, A. P. Walker, R. Wanninkhof, C. White-
3089 head, A. Willstrand Wranne, R. Wright, W. Yuan, C. Yue, X. Yue, S. Za-
3090 ehle, J. Zeng, and B. Zheng. Global carbon budget 2022. *Earth System Sci-
3091 ence Data*, 14(11):4811–4900, 2022. doi: 10.5194/essd-14-4811-2022. URL
3092 <https://essd.copernicus.org/articles/14/4811/2022/>.

- 3093 P. Friedlingstein, M. O’Sullivan, M. W. Jones, R. M. Andrew, D. C. E. Bakker,
3094 J. Hauck, P. Landschützer, C. Le Quéré, I. T. Luijckx, G. P. Peters, W. Pe-
3095 ters, J. Pongratz, C. Schwingshackl, S. Sitch, J. G. Canadell, P. Ciais, R. B.
3096 Jackson, S. R. Alin, P. Anthoni, L. Barbero, N. R. Bates, M. Becker, N. Bel-
3097 louin, B. Decharme, L. Bopp, I. B. M. Brasika, P. Cadule, M. A. Chamberlain,
3098 N. Chandra, T.-T.-T. Chau, F. Chevallier, L. P. Chini, M. Cronin, X. Dou,
3099 K. Enyo, W. Evans, S. Falk, R. A. Feely, L. Feng, D. J. Ford, T. Gasser,
3100 J. Ghattas, T. Gkritzalis, G. Grassi, L. Gregor, N. Gruber, Ö. Gürses, I. Har-
3101 ris, M. Hefner, J. Heinke, R. A. Houghton, G. C. Hurt, Y. Iida, T. Ilyina,
3102 A. R. Jacobson, A. Jain, T. Jarníková, A. Jersild, F. Jiang, Z. Jin, F. Joos,
3103 E. Kato, R. F. Keeling, D. Kennedy, K. Klein Goldewijk, J. Knauer, J. I. Ko-
3104 rsbakken, A. Kötzinger, X. Lan, N. Lefèvre, H. Li, J. Liu, Z. Liu, L. Ma,
3105 G. Marland, N. Mayot, P. C. McGuire, G. A. McKinley, G. Meyer, E. J.
3106 Morgan, D. R. Munro, S.-I. Nakaoka, Y. Niwa, K. M. O’Brien, A. Olsen,
3107 A. M. Omar, T. Ono, M. Paulsen, D. Pierrot, K. Pocock, B. Poulter, C. M.
3108 Powis, G. Rehder, L. Resplandy, E. Robertson, C. Rödenbeck, T. M. Rosan,
3109 J. Schwinger, R. Séférian, T. L. Smallman, S. M. Smith, R. Sospedra-Alfonso,
3110 Q. Sun, A. J. Sutton, C. Sweeney, S. Takao, P. P. Tans, H. Tian, B. Tilbrook,
3111 H. Tsujino, F. Tubiello, G. R. van der Werf, E. van Ooijen, R. Wanninkhof,
3112 M. Watanabe, C. Wimart-Rousseau, D. Yang, X. Yang, W. Yuan, X. Yue,
3113 S. Zaehle, J. Zeng, and B. Zheng. Global carbon budget 2023. *Earth System
3114 Science Data*, 15(12):5301–5369, 2023. doi: 10.5194/essd-15-5301-2023. URL
3115 <https://essd.copernicus.org/articles/15/5301/2023/>.
- 3116 Pierre Friedlingstein, Michael O’sullivan, Matthew W Jones, Robbie M An-
3117 drew, Judith Hauck, Are Olsen, Glen P Peters, Wouter Peters, Julia Pongratz,
3118 Stephen Sitch, et al. Global carbon budget 2020. *Earth System Science Data
3119 Discussions*, 2020:1–3, 2020.
- 3120 Jerome H Friedman. Greedy function approximation: a gradient boosting ma-
3121 chine. *Annals of statistics*, pages 1189–1232, 2001.
- 3122 Hiromichi Fukui, Duc Chuc Man, and Anh Phan. Digital earth: A platform
3123 for the sdgs and green transformation at the global and local level, employing
3124 essential sdgs variables. *Big Earth Data*, 5(4):476–496, 2021.

- 3125 Akinori Fukunaga, Takaharu Sato, Kazuki Fujita, Daisuke Yamada, Shinya
3126 Ishida, and Shinji Wakamatsu. Relationship between changes over time in
3127 factors, including the impact of meteorology on photochemical oxidant concen-
3128 tration and causative atmospheric pollutants in kawasaki. *Atmosphere*, 12(4):
3129 446, 2021.
- 3130 Francesco Fuso Nerini, Benjamin Sovacool, Nick Hughes, Laura Cozzi, Ellie Cos-
3131 grave, Mark Howells, Massimo Tavoni, Julia Tomei, Hisham Zerriffi, and Ben
3132 Milligan. Connecting climate action with other sustainable development goals.
3133 *Nature Sustainability*, 2(8):674–680, 2019.
- 3134 Pall Oskar Gislason, Jon Atli Benediktsson, and Johannes R Sveinsson. Random
3135 forests for land cover classification. *Pattern recognition letters*, 27(4):294–300,
3136 2006.
- 3137 Daniel L Goldberg, Zifeng Lu, Tomohiro Oda, Lok N Lamsal, Fei Liu, Debora
3138 Griffin, Chris A McLinden, Nickolay A Krotkov, Bryan N Duncan, and David G
3139 Streets. Exploiting omi no2 satellite observations to infer fossil-fuel co2 emis-
3140 sions from us megacities. *Science of The Total Environment*, 695:133805, 2019.
- 3141 A González Ortiz, C Guerreiro, and J Soares. *Air quality in Europe – 2020 report*,
3142 European Environment Agency. Publications Office, 2020. doi: doi/10.2800/
3143 786656.
- 3144 Noel Gorelick, Matt Hancher, Mike Dixon, Simon Ilyushchenko, David Thau, and
3145 Rebecca Moore. Google earth engine: Planetary-scale geospatial analysis for
3146 everyone. *Remote sensing of Environment*, 202:18–27, 2017.
- 3147 Stuart K Grange and David C Carslaw. Using meteorological normalisation to
3148 detect interventions in air quality time series. *Science of the Total Environment*,
3149 653:578–588, 2019.
- 3150 Stuart K Grange, David C Carslaw, Alastair C Lewis, Eirini Boleti, and Christoph
3151 Hueglin. Random forest meteorological normalisation models for swiss pm 10
3152 trend analysis. *Atmospheric Chemistry and Physics*, 18(9):6223–6239, 2018.

- 3153 Stuart K Grange, James D Lee, Will S Drysdale, Alastair C Lewis, Christoph
3154 Hueglin, Lukas Emmenegger, and David C Carslaw. Covid-19 lockdowns high-
3155 light a risk of increasing ozone pollution in european urban areas. *Atmospheric*
3156 *Chemistry and Physics*, 21(5):4169–4185, 2021.
- 3157 Miguel Grinberg. *Flask web development: developing web applications with*
3158 *python*. " O'Reilly Media, Inc.", 2018.
- 3159 Lianhong Gu, Jimei Han, Jeffrey D Wood, Christine Y-Y Chang, and Ying Sun.
3160 Sun-induced chl fluorescence and its importance for biophysical modeling of
3161 photosynthesis based on light reactions. *New Phytologist*, 223(3):1179–1191,
3162 2019.
- 3163 Kaiyu Guan, Ming Pan, Haibin Li, Adam Wolf, Jin Wu, David Medvigy, Kelly K
3164 Caylor, Justin Sheffield, Eric F Wood, Yadavinder Malhi, et al. Photosynthetic
3165 seasonality of global tropical forests constrained by hydroclimate. *Nature Geo-
3166 science*, 8(4):284–289, 2015.
- 3167 Luis Guanter, Christian Frankenberg, Anu Dudhia, Philip E Lewis, José Gómez-
3168 Dans, Akihiko Kuze, Hiroshi Suto, and Roy G Grainger. Retrieval and global
3169 assessment of terrestrial chlorophyll fluorescence from gosat space measure-
3170 ments. *Remote Sensing of Environment*, 121:236–251, 2012.
- 3171 Renjie Guo, Tiexi Chen, Xin Chen, Wenping Yuan, Shuci Liu, Bin He, Lin Li,
3172 Shengzhen Wang, Ting Hu, Qingyun Yan, et al. Estimating global gpp from the
3173 plant functional type perspective using a machine learning approach. *Journal*
3174 *of Geophysical Research: Biogeosciences*, page e2022JG007100, 2023.
- 3175 Neil F Hadley and Stan R Szarek. Productivity of desert ecosystems. *BioScience*,
3176 31(10):747–753, 1981.
- 3177 Andy Haines, R Sari Kovats, Diarmid Campbell-Lendrum, and Carlos Corvalán.
3178 Climate change and human health: impacts, vulnerability, and mitigation. *The*
3179 *Lancet*, 367(9528):2101–2109, 2006.
- 3180 Ghassan B Hamra, Francine Laden, Aaron J Cohen, Ole Raaschou-Nielsen,
3181 Michael Brauer, and Dana Loomis. Lung cancer and exposure to nitrogen

- 3182 dioxide and traffic: a systematic review and meta-analysis. *Environmental*
3183 *health perspectives*, 123(11):1107–1112, 2015.
- 3184 Pengfei Han, Ning Zeng, Tom Oda, Xiaohui Lin, Monica Crippa, Dabo Guan,
3185 Greet Janssens-Maenhout, Xiaolin Ma, Zhu Liu, Yuli Shan, et al. Evaluating
3186 China's fossil-fuel CO₂ emissions from a comprehensive dataset of nine inventories.
3187 *Atmospheric Chemistry and Physics*, 20(19):11371–11385, 2020.
- 3188 Kandice L Harper, Céline Lamarche, Andrew Hartley, Philippe Peylin, Catherine
3189 Ottlé, Vladislav Bastrikov, Rodrigo San Martín, Sylvia I Bohnenstengel, Grit
3190 Kirches, Martin Boettcher, et al. A 29-year time series of annual 300-metre
3191 resolution plant functional type maps for climate models. *Earth System Science
3192 Data Discussions*, 2022:1–37, 2022.
- 3193 Matthew N. Hayek, Richard Wehr, Marcos Longo, Lucy R. Hutyra, Kenia
3194 Wiedemann, J. William Munger, Damien Bonal, Scott R. Saleska, David R.
3195 Fitzjarrald, and Steven C. Wofsy. A novel correction for biases in for-
3196 est eddy covariance carbon balance. *Agricultural and Forest Meteorol-
3197 ogy*, 250–251:90–101, 2018. ISSN 0168-1923. doi: <https://doi.org/10.1016/j.agrformet.2017.12.186>. URL <https://www.sciencedirect.com/science/article/pii/S0168192317306007>.
- 3200 Hans Hersbach, Bill Bell, Paul Berrisford, Gionata Biavati, András Horányi,
3201 Joaquín Muñoz Sabater, Julien Nicolas, Carole Peubey, Raluca Radu, Iryna
3202 Rozum, et al. Era5 hourly data on single levels from 1979 to present. *Coperni-
3203 cus climate change service (c3s) climate data store (cds)*, 10(10.24381), 2018.
- 3204 Hans Hersbach, Bill Bell, Paul Berrisford, Shoji Hirahara, András Horányi,
3205 Joaquín Muñoz-Sabater, Julien Nicolas, Carole Peubey, Raluca Radu, Dinand
3206 Schepers, et al. The era5 global reanalysis. *Quarterly Journal of the Royal
3207 Meteorological Society*, 146(730):1999–2049, 2020.
- 3208 Rachel M Hoesly, Steven J Smith, Leyang Feng, Zbigniew Klimont, Greet
3209 Janssens-Maenhout, Tyler Pitkanen, Jonathan J Seibert, Linh Vu, Robert J
3210 Andres, Ryan M Bolt, et al. Historical (1750–2014) anthropogenic emissions of
3211 reactive gases and aerosols from the community emissions data system (ceds).
3212 *Geoscientific Model Development*, 11(1):369–408, 2018.

- 3213 Inc Hokkaido Electric Power. Electricity forecast for hokkaido area, 2023. URL
3214 <https://denkiyoho.hepco.co.jp/>.
- 3215 Inc Hokuriku Electric Power. Electricity forecast for hokuriku area, 2023. URL
3216 <https://www.rikuden.co.jp/nw/denki-yoho/>.
- 3217 Maya G Hutchins, Jeffrey D Colby, Gregg Marland, and Eric Marland. A compar-
3218 ision of five high-resolution spatially-explicit, fossil-fuel, carbon dioxide emis-
3219 sion inventories for the united states. *Mitigation and Adaptation Strategies for*
3220 *Global Change*, 22:947–972, 2017.
- 3221 IPCC. Ipcc, sr15, faq chapter 5, 2018. URL <https://www.ipcc.ch/sr15/faq/>
3222 [faq-chapter-5/](#).
- 3223 Hitoshi Irie, Daichi Yonekawa, Alessandro Damiani, Hossain Mohammed Syedul
3224 Hoque, Kengo Sudo, and Syuichi Itahashi. Continuous multi-component max-
3225 doas observations for the planetary boundary layer ozone variation analysis at
3226 chiba and tsukuba, japan, from 2013 to 2019. *Progress in Earth and Planetary*
3227 *Science*, 8(1):31, 2021.
- 3228 Syuichi Itahashi, Yuki Yamamura, Zhe Wang, and Itsushi Uno. Returning long-
3229 range pm2. 5 transport into the leeward of east asia in 2021 after chinese
3230 economic recovery from the covid-19 pandemic. *Scientific Reports*, 12(1):5539,
3231 2022.
- 3232 Akihiko Ito. Disequilibrium of terrestrial ecosystem co 2 budget caused by
3233 disturbance-induced emissions and non-co 2 carbon export flows: a global
3234 model assessment. *Earth System Dynamics*, 10(4):685–709, 2019.
- 3235 Akihiko Ito. Output data of greenhouse gas budget and carbon cycle simulated
3236 by the visit terrestrial ecosystem model, ver.2021.1_ch4wetl_cao, 2021a. URL
3237 [10.17595/20210521.001](https://doi.org/10.17595/20210521.001).
- 3238 Akihiko Ito. Output data of greenhouse gas budget and carbon cycle simulated
3239 by the visit terrestrial ecosystem model, ver.2021.1_ch4wetl_wh, 2021b. URL
3240 [10.17595/20210521.001](https://doi.org/10.17595/20210521.001).

- 3241 Akihiko Ito and Kazuhito Ichii. Terrestrial ecosystem model studies and their
3242 contributions to asiaflux. *Journal of Agricultural Meteorology*, 77(1):81–95,
3243 2021.
- 3244 Akihiko Ito, Yasunori Tohjima, Takuya Saito, Taku Umezawa, Tomohiro Hajima,
3245 Ryuichi Hirata, Makoto Saito, and Yukio Terao. Methane budget of east asia,
3246 1990–2015: A bottom-up evaluation. *Science of the total environment*, 676:
3247 40–52, 2019.
- 3248 Akiyoshi Ito, Shinji Wakamatsu, Tazuko Morikawa, and Shinji Kobayashi. 30
3249 years of air quality trends in japan. *Atmosphere*, 12(8):1072, 2021.
- 3250 Xiaomeng Jin, Arlene Fiore, K Folkert Boersma, Isabelle De Smedt, and Lukas
3251 Valin. Inferring changes in summertime surface ozone–no x–voc chemistry over
3252 us urban areas from two decades of satellite and ground-based observations.
3253 *Environmental science & technology*, 54(11):6518–6529, 2020.
- 3254 Martin Jung, Sujan Koirala, Ulrich Weber, Kazuhito Ichii, Fabian Gans, Gustau
3255 Camps-Valls, Dario Papale, Christopher Schwalm, Gianluca Tramontana, and
3256 Markus Reichstein. The fluxcom ensemble of global land-atmosphere energy
3257 fluxes. *Scientific data*, 6(1):74, 2019.
- 3258 Martin Jung, Christopher Schwalm, Mirco Migliavacca, Sophia Walther, Gustau
3259 Camps-Valls, Sujan Koirala, Peter Anthoni, Simon Besnard, Paul Bodesheim,
3260 Nuno Carvalhais, et al. Scaling carbon fluxes from eddy covariance sites to
3261 globe: synthesis and evaluation of the fluxcom approach. 2020.
- 3262 L. Júlia, M. Dylan, R. Danielle, and B Adrian. Nearly 3 million
3263 people have left ukraine, foreshadowing a massive humanitarian cri-
3264 sis, 2022. URL <https://www.washingtonpost.com/world/2022/02/27/ukraine-refugees-photos-videos/>.
- 3266 Marilena Kampa and Elias Castanas. Human health effects of air pollution.
3267 *Environmental pollution*, 151(2):362–367, 2008.
- 3268 Akiyoshi Kannari and Kazuo Kokuryo. Thirty-year histories of atmospheric emis-
3269 sions from road vehicles in japan. *J. Jpn. Soc. Atmos. Environ*, 48(1):20–34,
3270 2013.

- 3271 Inc Kansai Electric Power. Electricity forecast for kansai area, 2023. URL <https://www.kansai-td.co.jp/>.
- 3273 Céline Kauffmann, Cristina Tébar Less, and Dorothee Teichmann. Corporate
3274 greenhouse gas emission reporting: A stocktaking of government schemes. 2012.
- 3275 Guolin Ke, Qi Meng, Thomas Finley, Taifeng Wang, Wei Chen, Weidong Ma,
3276 Qiwei Ye, and Tie-Yan Liu. Lightgbm: A highly efficient gradient boosting
3277 decision tree. *Advances in neural information processing systems*, 30, 2017.
- 3278 FJ Kelly and JC Fussell. Air pollution and airway disease. *Clinical & Experi-
3279 mental Allergy*, 41(8):1059–1071, 2011.
- 3280 Christine M Kendrick, Peter Koonce, and Linda A George. Diurnal and seasonal
3281 variations of no, no₂ and pm_{2.5} mass as a function of traffic volumes alongside
3282 an urban arterial. *Atmospheric Environment*, 122:133–141, 2015.
- 3283 Robert O Keohane and David G Victor. The regime complex for climate change.
3284 *Perspectives on politics*, 9(1):7–23, 2011.
- 3285 Diederik P Kingma and Jimmy Ba. Adam: A method for stochastic optimization.
3286 *arXiv preprint arXiv:1412.6980*, 2014.
- 3287 Philipp Köhler, Christian Frankenberg, Troy S Magney, Luis Guanter, Joanna
3288 Joiner, and Jochen Landgraf. Global retrievals of solar-induced chlorophyll
3289 fluorescence with tropomi: First results and intersensor comparison to oco-2.
3290 *Geophysical Research Letters*, 45(19):10–456, 2018.
- 3291 Igor B Konovalov, Evgeny V Berezin, Philippe Ciais, Grégoire Broquet, Ruslan V
3292 Zhuravlev, and Greet Janssens-Maenhout. Estimation of fossil-fuel co₂ emis-
3293 sions using satellite measurements of "proxy" species. *Atmospheric Chemistry
3294 and Physics*, 16(21):13509–13540, 2016.
- 3295 J Kurokawa, T Ohara, I Uno, M Hayasaki, and H Tanimoto. Influence of me-
3296 teorological variability on interannual variations of springtime boundary layer
3297 ozone over japan during 1981–2005. *Atmospheric Chemistry and Physics*, 9
3298 (17):6287–6304, 2009.

- 3299 Inc Kyushu Electric Power. Electricity forecast for kyushu area, 2023. URL
3300 https://www.kyuden.co.jp/td_power_usages/pc.html.
- 3301 Laura Elena Cué La Rosa, Camile Sothe, Raul Queiroz Feitosa, Cláudia Maria
3302 de Almeida, Marcos Benedito Schimalski, and Dário Augusto Borges Oliveira.
3303 Multi-task fully convolutional network for tree species mapping in dense forests
3304 using small training hyperspectral data. *ISPRS Journal of Photogrammetry*
3305 and *Remote Sensing*, 179:35–49, 2021.
- 3306 M. Lauri and G. Rosa. Health impacts of coal power plant emissions
3307 in ukraine, 2021. URL [https://energyandcleanair.org/publication/](https://energyandcleanair.org/publication/health-impacts-of-coal-power-plant-emissions-in-ukraine/)
3308 [health-impacts-of-coal-power-plant-emissions-in-ukraine/](https://energyandcleanair.org/publication/health-impacts-of-coal-power-plant-emissions-in-ukraine/).
- 3309 Corinne Le Quéré, Robbie M Andrew, Pierre Friedlingstein, Stephen Sitch, Judith
3310 Hauck, Julia Pongratz, Penelope Pickers, Jan Ivar Korsbakken, Glen P Peters,
3311 Josep G Canadell, et al. Global carbon budget 2018. *Earth System Science*
3312 *Data Discussions*, 2018:1–3, 2018.
- 3313 Hoesung Lee, Katherine Calvin, Dipak Dasgupta, Gerhard Krinner, Aditi
3314 Mukherji, Peter Thorne, Christopher Trisos, José Romero, Paulina Aldunce,
3315 Ko Barrett, et al. Climate change 2023: synthesis report. contribution of work-
3316 ing groups i, ii and iii to the sixth assessment report of the intergovernmental
3317 panel on climate change. 2023.
- 3318 Juheon Lee, Xiaohao Cai, Jan Lellmann, Michele Dalponte, Yadvinder Malhi,
3319 Nathalie Butt, Mike Morecroft, Carola-Bibiane Schönlieb, and David A
3320 Coomes. Individual tree species classification from airborne multisensor im-
3321 agery using robust pca. *IEEE Journal of Selected Topics in Applied Earth*
3322 *Observations and Remote Sensing*, 9(6):2554–2567, 2016.
- 3323 Xing Li, Jingfeng Xiao, Binbin He, M. Altaf Arain, Jason Beringer, Ankur R.
3324 Desai, Carmen Emmel, David Y. Hollinger, Alisa Krasnova, Ivan Mammarella,
3325 Steffen M. Noe, Penélope Serrano Ortiz, A. Camilo Rey-Sánchez, Adrian V.
3326 Rocha, and Andrej Varlagin. Solar-induced chlorophyll fluorescence is strongly
3327 correlated with terrestrial photosynthesis for a wide variety of biomes: First
3328 global analysis based on oco-2 and flux tower observations. *Global Change*

- 3329 *Biology*, 24(9):3990–4008, 2018. doi: <https://doi.org/10.1111/gcb.14297>. URL
3330 <https://onlinelibrary.wiley.com/doi/abs/10.1111/gcb.14297>.
- 3331 Shangrong Lin, Jing Li, Qinhuo Liu, Beniamino Gioli, Eugenie Paul-Limoges,
3332 Nina Buchmann, Mana Gharun, Lukas Hörtnagl, Lenka Foltynová, Jiří Dušek,
3333 et al. Improved global estimations of gross primary productivity of natural
3334 vegetation types by incorporating plant functional type. *International Journal
3335 of Applied Earth Observation and Geoinformation*, 100:102328, 2021.
- 3336 Shuguang Liu, Ben Bond-Lamberty, Jeffrey A Hicke, Rodrigo Vargas, Shuqing
3337 Zhao, Jing Chen, Steven L Edburg, Yueming Hu, Jinxun Liu, A David
3338 McGuire, et al. Simulating the impacts of disturbances on forest carbon cy-
3339 cling in north america: Processes, data, models, and challenges. *Journal of
3340 Geophysical Research: Biogeosciences*, 116(G4), 2011.
- 3341 Xinjie Liu, Liangyun Liu, Jiaochan Hu, Jian Guo, and Shanshan Du. Improving
3342 the potential of red sif for estimating gpp by downscaling from the canopy level
3343 to the photosystem level. *Agricultural and Forest Meteorology*, 281:107846,
3344 2020.
- 3345 Yiming Liu, Tao Wang, Trissevgeni Stavrakou, Nellie Elguindi, Thierno Doumbia,
3346 Claire Granier, Idir Bouarar, Benjamin Gaubert, and Guy P Brasseur. Diverse
3347 response of surface ozone to covid-19 lockdown in china. *Science of the Total
3348 Environment*, 789:147739, 2021.
- 3349 Zhu Liu, Dabo Guan, Wei Wei, Steven J Davis, Philippe Ciais, Jin Bai, Shushi
3350 Peng, Qiang Zhang, Klaus Hubacek, Gregg Marland, et al. Reduced carbon
3351 emission estimates from fossil fuel combustion and cement production in china.
3352 *Nature*, 524(7565):335–338, 2015.
- 3353 Nima Madani, John S. Kimball, Lucas A. Jones, Nicholas C. Parazoo, and Kaiyu
3354 Guan. Global analysis of bioclimatic controls on ecosystem productivity using
3355 satellite observations of solar-induced chlorophyll fluorescence. *Remote Sensing*,
3356 9(6), 2017. ISSN 2072-4292. doi: 10.3390/rs9060530. URL <https://www.mdpi.com/2072-4292/9/6/530>.

- 3358 Nima Madani, John S Kimball, Nicholas C Parazoo, Ashley P Ballantyne,
3359 Torben Tagesson, Lucas A Jones, Rolf H Reichle, Paul I Palmer, Isabella
3360 Velicogna, A Anthony Bloom, Sassan Saatchi, Zhihua Liu, and A Geruo. Below-
3361 surface water mediates the response of african forests to reduced rainfall. *Envi-
3362 ronmental Research Letters*, 15(3):034063, mar 2020. doi: 10.1088/1748-9326/
3363 ab724a. URL <https://dx.doi.org/10.1088/1748-9326/ab724a>.
- 3364 Virginie Marécal, V-H Peuch, Camilla Andersson, Stefan Andersson, Joaquim
3365 Arteta, Matthias Beekmann, Anna Benedictow, Robert Bergström, Bertrand
3366 Bessagnet, Alberto Cansado, et al. A regional air quality forecasting system
3367 over europe: the macc-ii daily ensemble production. *Geoscientific Model De-
3368 velopment*, 8(9):2777–2813, 2015.
- 3369 Gregg Marland. Uncertainties in accounting for co2 from fossil fuels. *Journal of
3370 Industrial Ecology*, 12(2):136–139, 2008.
- 3371 Randall V Martin, Arlene M Fiore, and Aaron Van Donkelaar. Space-based
3372 diagnosis of surface ozone sensitivity to anthropogenic emissions. *Geophysical
3373 Research Letters*, 31(6), 2004.
- 3374 Erin E McDuffie, Steven J Smith, Patrick O'Rourke, Kushal Tibrewal, Chandra
3375 Venkataraman, Eloise A Marais, Bo Zheng, Monica Crippa, Michael Brauer,
3376 and Randall V Martin. A global anthropogenic emission inventory of atmo-
3377 spheric pollutants from sector-and fuel-specific sources (1970–2017): an appli-
3378 cation of the community emissions data system (ceds). *Earth System Science
3379 Data*, 12(4):3413–3442, 2020.
- 3380 Japan Ministry of the Environment. Current estimation of co2 emissions by
3381 sector, 2022. URL https://www.env.go.jp/policy/local_keikaku/tools/suikei2.html.
- 3383 Japan Ministry of the Environment. 2050 zero carbon cities in japan,
3384 2023. URL https://www.env.go.jp/en/earth/cc/2050_zero_carbon_cities_in_japan.html.
- 3386 Kazuyuki Miyazaki and Kevin Bowman. Predictability of fossil fuel co2 from air
3387 quality emissions. *Nature communications*, 14(1):1604, 2023.

- 3388 Kazuyuki Miyazaki, Kevin Bowman, Takashi Sekiya, Masayuki Takigawa, Jes-
3389 sica L Neu, Kengo Sudo, Greg Osterman, and Henk Eskes. Global tropospheric
3390 ozone responses to reduced no x emissions linked to the covid-19 worldwide
3391 lockdowns. *Science Advances*, 7(24):eabf7460, 2021.
- 3392 Rebecca A Montgomery and Robin L Chazdon. Forest structure, canopy ar-
3393 chitecture, and light transmittance in tropical wet forests. *Ecology*, 82(10):
3394 2707–2718, 2001.
- 3395 Takashi Nakazawa, Keiichi Satoh, Gregory Trencher, Tomoyuki Tatsumi, and
3396 Koichi Hasegawa. Net-zero carbon declarations by japanese local governments:
3397 What caused the domino-like diffusion? *Review of Policy Research*, 2023.
- 3398 Ray Nassar, Timothy G Hill, Chris A McLinden, Debra Wunch, Dylan BA Jones,
3399 and David Crisp. Quantifying co2 emissions from individual power plants from
3400 space. *Geophysical Research Letters*, 44(19):10–045, 2017.
- 3401 Juan Nathaniel, Jiangong Liu, and Pierre Gentine. Metaflux: Meta-learning
3402 global carbon fluxes from sparse spatiotemporal observations. *Scientific Data*,
3403 10(1):440, 2023.
- 3404 G. Nichita and M Ana. War in ukraine one year on, nowhere
3405 safe, 2023. URL [https://acleddata.com/2023/03/01/
3406 war-in-ukraine-one-year-on-nowhere-safe/](https://acleddata.com/2023/03/01/war-in-ukraine-one-year-on-nowhere-safe/).
- 3407 Nikkei. Map information, the cornerstone of administrative dx: Introduction of
3408 “integrated” 1099 local governments, 2023. URL [https://www.nikkei.com/
article/DGXZQ0CC314EI0R30C23A1000000/](https://www.nikkei.com/
3409 article/DGXZQ0CC314EI0R30C23A1000000/).
- 3410 Alexander J Norton, Peter J Rayner, Ernest N Koffi, Marko Scholze, Jeremy D
3411 Silver, and Ying-Ping Wang. Estimating global gross primary productivity
3412 using chlorophyll fluorescence and a data assimilation system with the bethy-
3413 scope model. *Biogeosciences*, 16(15):3069–3093, 2019.
- 3414 Tomohiro Oda and Shamil Maksyutov. A very high-resolution (1 km × 1 km)
3415 global fossil fuel co 2 emission inventory derived using a point source database
3416 and satellite observations of nighttime lights. *Atmospheric Chemistry and
3417 Physics*, 11(2):543–556, 2011.

- 3418 Tomohiro Oda, Shamil Maksyutov, and Robert J Andres. The open-source data
3419 inventory for anthropogenic co₂, version 2016 (odiac2016): a global monthly
3420 fossil fuel co₂ gridded emissions data product for tracer transport simulations
3421 and surface flux inversions. *Earth System Science Data*, 10(1):87–107, 2018.
- 3422 Tomohiro Oda, Rostyslav Bun, Vitaliy Kinakh, Petro Topylko, Mariia
3423 Halushchak, Gregg Marland, Thomas Lauvaux, Matthias Jonas, Shamil
3424 Maksyutov, Zbigniew Nahorski, et al. Errors and uncertainties in a gridded
3425 carbon dioxide emissions inventory. *Mitigation and Adaptation Strategies for
3426 Global Change*, 24:1007–1050, 2019.
- 3427 Yuko Ogawa-Onishi and Pam M Berry. Ecological impacts of climate change
3428 in japan: The importance of integrating local and international publications.
3429 *Biological Conservation*, 157:361–371, 2013.
- 3430 Inc Okinawa Electric Power. Electricity forecast for okinawa area, 2023. URL
3431 <https://www.okiden.co.jp/denki2/>.
- 3432 Carlos Ordóñez, Jose M Garrido-Perez, and Ricardo García-Herrera. Early spring
3433 near-surface ozone in europe during the covid-19 shutdown: Meteorological ef-
3434 fects outweigh emission changes. *Science of the total environment*, 747:141322,
3435 2020.
- 3436 A. Ortiz, Cristina Guerreiro, Frank de Leeuw, and Jan Horálek. Air quality in eu-
3437 rope - 2017 report, 2017. URL <https://www.eea.europa.eu/publications/air-quality-in-europe-2017>.
- 3439 Paul I Palmer, Caroline M Wainwright, Bo Dong, Ross I Maidment, Kevin G
3440 Wheeler, Nicola Gedney, Jonathan E Hickman, Nima Madani, Sonja S Folwell,
3441 Gamal Abdo, et al. Drivers and impacts of eastern african rainfall variability.
3442 *Nature Reviews Earth & Environment*, 4(4):254–270, 2023.
- 3443 Yude Pan, Richard A Birdsey, Jingyun Fang, Richard Houghton, Pekka E
3444 Kauppi, Werner A Kurz, Oliver L Phillips, Anatoly Shvidenko, Simon L Lewis,
3445 Josep G Canadell, et al. A large and persistent carbon sink in the world’s
3446 forests. *Science*, 333(6045):988–993, 2011.

- 3447 Gilberto Pastorello, Carlo Trotta, Eleonora Canfora, Housen Chu, Danielle Chris-
3448 tianson, You-Wei Cheah, Cristina Poindexter, Jiquan Chen, Abdelrahman El-
3449 bashandy, Marty Humphrey, et al. The fluxnet2015 dataset and the oneflux
3450 processing pipeline for eddy covariance data. *Scientific data*, 7(1):225, 2020.
- 3451 Shushi Peng, Xin Lin, Rona L Thompson, Yi Xi, Gang Liu, Didier Hauglustaine,
3452 Xin Lan, Benjamin Poulter, Michel Ramonet, Marielle Saunois, et al. Wet-
3453 land emission and atmospheric sink changes explain methane growth in 2020.
3454 *Nature*, 612(7940):477–482, 2022.
- 3455 Paulo Pereira, Wenwu Zhao, Lyudmyla Symochko, Miguel Inacio, Igor Bo-
3456 gunovic, and Damia Barcelo. The russia-ukrainian armed conflict impact
3457 will push back the sustainable development goals, 2022.
- 3458 Hervé Petetin, Dene Bowdalo, Albert Soret, Marc Guevara, Oriol Jorba, Kim
3459 Serradell, and Carlos Pérez García-Pando. Meteorology-normalized impact of
3460 the covid-19 lockdown upon no₂ pollution in spain. *Atmospheric Chemistry
3461 and Physics*, 20(18):11119–11141, 2020.
- 3462 Anh Phan and Hiromichi Fukui. Quantifying the impacts of the covid-19 pan-
3463 demic lockdown and the armed conflict with russia on sentinel 5p tropomi no₂
3464 changes in ukraine. *Big Earth Data*, 0(0):1–24, 2023a. doi: 10.1080/20964471.
3465 2023.2265105.
- 3466 Anh Phan and Hiromichi Fukui. Fluxformer: Upscaled global carbon fluxes from
3467 eddy covariance data with multivariate timeseries transformer, 2023b.
- 3468 Anh Phan and Hiromichi Fukui. Unusual response of o₃ and ch₄ to no₂ emissions
3469 reduction in japan during the covid-19 pandemic. *International Journal of
3470 Digital Earth*, 17(1):2297844, 2024. doi: 10.1080/17538947.2023.2297844.
- 3471 Anh Phan, Kiyoshi Takejima, Tsubasa Hirakawa, and Hiromichi Fukui. Forest-
3472 related sdg issues monitoring for data-scarce regions employing machine learn-
3473 ing and remote sensing-a case study for ena city, japan. In *IGARSS 2022-2022
3474 IEEE International Geoscience and Remote Sensing Symposium*, pages 4343–
3475 4346. IEEE, 2022.

- 3476 Shilong Piao, Xuhui Wang, Taejin Park, Chi Chen, XU Lian, Yue He, Jarle W
3477 Bjerke, Anping Chen, Philippe Ciais, Hans Tømmervik, et al. Characteristics,
3478 drivers and feedbacks of global greening. *Nature Reviews Earth & Environment*,
3479 1(1):14–27, 2020.
- 3480 National Land Information Division National Spatial Planning and MLIT
3481 of Japan Regional Policy Bureau. Power generation facility, 2023. URL
3482 <https://nlftp.mlit.go.jp/ksj/gml/datalist/KsjTmplt-P03.html>.
- 3483 B Poulter, P Ciais, E Hodson, H Lischke, F Maignan, S Plummer, and NE Zim-
3484 mermann. Plant functional type mapping for earth system models. *Geoscientific-
3485 Model Development*, 4(4):993–1010, 2011.
- 3486 Ben Poulter, Natasha MacBean, Andrew Hartley, Iryna Khlystova, Olivier Arino,
3487 Richard Betts, Sophie Bontemps, Martin Boettcher, Carsten Brockmann,
3488 Pierre Defourny, et al. Plant functional type classification for earth system
3489 models: results from the european space agency’s land cover climate change
3490 initiative. *Geoscientific Model Development*, 8(7):2315–2328, 2015.
- 3491 Benjamin Poulter, David Frank, Philippe Ciais, Ranga B Myneni, Niels Andela,
3492 Jian Bi, Gregoire Broquet, Josep G Canadell, Frederic Chevallier, Yi Y Liu,
3493 et al. Contribution of semi-arid ecosystems to interannual variability of the
3494 global carbon cycle. *Nature*, 509(7502):600–603, 2014.
- 3495 Richard B Primack, Hiroyoshi Higuchi, and Abraham J Miller-Rushing. The
3496 impact of climate change on cherry trees and other species in japan. *Biological
3497 Conservation*, 142(9):1943–1949, 2009.
- 3498 Kyoto Protocol. United nations framework convention on climate change. *Kyoto
3499 Protocol, Kyoto*, 19(8):1–21, 1997.
- 3500 Zhen Qu, Daniel J Jacob, Yuzhong Zhang, Lu Shen, Daniel J Varon, Xiao Lu,
3501 Tia Scarpelli, Anthony Bloom, John Worden, and Robert J Parker. Attribu-
3502 tion of the 2020 surge in atmospheric methane by inverse analysis of gosat
3503 observations. *Environmental Research Letters*, 17(9):094003, 2022.

- 3504 Clonadh Raleigh, rew Linke, Håvard Hegre, and Joakim Karlsen. Introducing
3505 acled: An armed conflict location and event dataset. *Journal of peace research*,
3506 47(5):651–660, 2010.
- 3507 Jie Ren, Fangfang Guo, and Shaodong Xie. Diagnosing ozone–no x–voc sensitivity
3508 and revealing causes of ozone increases in china based on 2013–2021 satellite
3509 retrievals. *Atmospheric Chemistry and Physics*, 22(22):15035–15047, 2022.
- 3510 Caleb Robinson, Kolya Malkin, Nebojsa Jojic, Huijun Chen, Rongjun Qin,
3511 Changlin Xiao, Michael Schmitt, Pedram Ghamisi, Ronny Hänsch, and Naoto
3512 Yokoya. Global land-cover mapping with weak supervision: Outcome of the
3513 2020 ieee grss data fusion contest. *IEEE Journal of Selected Topics in Applied
3514 Earth Observations and Remote Sensing*, 14:3185–3199, 2021.
- 3515 Olaf Ronneberger, Philipp Fischer, and Thomas Brox. U-net: Convolutional
3516 networks for biomedical image segmentation. In *Medical Image Computing
3517 and Computer-Assisted Intervention–MICCAI 2015: 18th International Con-
ference, Munich, Germany, October 5–9, 2015, Proceedings, Part III 18*, pages
3518 234–241. Springer, 2015.
- 3520 Abram FJ Sanders, Willem W Verstraeten, Maurits L Kooreman, Thomas C
3521 Van Leth, Jason Beringer, and Joanna Joiner. Spaceborne sun-induced vegeta-
3522 tion fluorescence time series from 2007 to 2015 evaluated with australian flux
3523 tower measurements. *Remote Sensing*, 8(11):895, 2016.
- 3524 Mykhailo Savenets. Air pollution in ukraine: a view from the sentinel-5p satellite.
3525 *JOURNAL OF THE HUNGARIAN METEOROLOGICAL SERVICE*, 125(2):
3526 271–290, 2021.
- 3527 Felix Schiefer, Teja Kattenborn, Annett Frick, Julian Frey, Peter Schall, Barbara
3528 Koch, and Sebastian Schmidlein. Mapping forest tree species in high resolution
3529 uav-based rgb-imagery by means of convolutional neural networks. *ISPRS
3530 Journal of Photogrammetry and Remote Sensing*, 170:205–215, 2020.
- 3531 Quirin Schiermeier. Why pollution is falling in some cities—but not others. *Na-
3532 ture*, 580(7803):313, 2020.

- 3533 Jason R Schroeder, James H Crawford, Alan Fried, James Walega, Andrew Wein-
3534 heimer, Armin Wisthaler, Markus Müller, Tomas Mikoviny, Gao Chen, Michael
3535 Shook, et al. New insights into the column ch₂o/no₂ ratio as an indicator of
3536 near-surface ozone sensitivity. *Journal of Geophysical Research: Atmospheres*,
3537 122(16):8885–8907, 2017.
- 3538 Wilfrid Schroeder, Patricia Oliva, Louis Giglio, and Ivan A Csiszar. The new
3539 viirs 375 m active fire detection data product: Algorithm description and initial
3540 assessment. *Remote Sensing of Environment*, 143:85–96, 2014.
- 3541 Ankit Shekhar, Nina Buchmann, and Mana Gharun. How well do recently
3542 reconstructed solar-induced fluorescence datasets model gross primary pro-
3543 ductivity? *Remote Sensing of Environment*, 283:113282, 2022. ISSN 0034-
3544 4257. doi: <https://doi.org/10.1016/j.rse.2022.113282>. URL <https://www.sciencedirect.com/science/article/pii/S0034425722003881>.
- 3546 Andrii Shelestov, Hanna Yailymova, Bohdan Yailymov, and Nataliia Kussul. Air
3547 quality estimation in ukraine using sdg 11.6. 2 indicator assessment. *Remote
3548 Sensing*, 13(23):4769, 2021.
- 3549 Zongbo Shi, Congbo Song, Bowen Liu, Gongda Lu, Jingsha Xu, Tuan Van Vu,
3550 Robert JR Elliott, Weijun Li, William J Bloss, and Roy M Harrison. Abrupt
3551 but smaller than expected changes in surface air quality attributable to covid-
3552 19 lockdowns. *Science advances*, 7(3):eabd6696, 2021.
- 3553 Toshihiko Shibuya and Ben Croxford. The effect of climate change on office
3554 building energy consumption in japan. *Energy and Buildings*, 117:149–159,
3555 2016.
- 3556 Inc Shikoku Electric Power. Electricity forecast for shikoku area, 2023. URL
3557 <https://www.yonden.co.jp/nw/denkiyoho/>.
- 3558 Stephen Sitch, Pierre Friedlingstein, Nicolas Gruber, Steve D Jones, Guillermo
3559 Murray-Tortarolo, Anders Ahlström, Scott C Doney, H Graven, Christoph
3560 Heinze, Chris Huntingford, et al. Recent trends and drivers of regional sources
3561 and sinks of carbon dioxide. *Biogeosciences*, 12(3):653–679, 2015.

- 3562 Amir H Souri, Matthew S Johnson, Glenn M Wolfe, James H Crawford, Alan
3563 Fried, Armin Wisthaler, William H Brune, Donald R Blake, Andrew J Wein-
3564heimer, Tijl Verhoelst, et al. Characterization of errors in satellite-based hcho/
3565 no 2 tropospheric column ratios with respect to chemistry, column-to-pbl trans-
3566lation, spatial representation, and retrieval uncertainties. *Atmospheric Chem-
3567istry and Physics*, 23(3):1963–1986, 2023.
- 3568 David S Stevenson, Richard G Derwent, Oliver Wild, and William J Collins.
3569 Covid-19 lockdown emission reductions have the potential to explain over half of
3570 the coincident increase in global atmospheric methane. *Atmospheric Chemistry
3571 and Physics*, 22(21):14243–14252, 2022.
- 3572 T.F. Stocker, G.-K. Plattner D. Qin, M. Tignor, S.K. Allen, J. Boschung,
3573 A. Nauels, Y. Xia, V. Bex, and P.M. Midgley. Ipcc, 2013: Climate change
3574 2013: The physical science basis. contribution of working group i to the fifth
3575 assessment report of the intergovernmental panel on climate changes. Technical
3576 report, Cambridge University Press, Cambridge, United Kingdom and New
3577 York, NY, USA, 2013.
- 3578 Amos PK Tai and Maria Val Martin. Impacts of ozone air pollution and temper-
3579 ature extremes on crop yields: Spatial variability, adaptation and implications
3580 for future food security. *Atmospheric Environment*, 169:11–21, 2017.
- 3581 Akira Tani and Tomoki Mochizuki. Exchanges of volatile organic compounds
3582 between terrestrial ecosystems and the atmosphere. *Journal of Agricultural
3583 Meteorology*, 77(1):66–80, 2021.
- 3584 Inc Tohoku Electric Power. Electricity forecast for tohoku area, 2023. URL
3585 <https://setsuden.nw.tohoku-epco.co.jp/>.
- 3586 Toshihiko Nakata Laboratory Tohoku University. Regional energy supply and de-
3587 mand database (version 2.6), 2023. URL <https://energy-sustainability.jp>.
- 3588 Inc Tokyo Electric Power. Electricity forecast for tokyo area, 2023. URL <https://www.tepco.co.jp/forecast/>.

- 3591 Gianluca Tramontana, Martin Jung, Christopher R Schwalm, Kazuhito Ichii,
3592 Gustau Camps-Valls, Botond Ráduly, Markus Reichstein, M Altaf Arain,
3593 Alessandro Cescatti, Gerard Kiely, et al. Predicting carbon dioxide and energy
3594 fluxes across global fluxnet sites with regression algorithms. *Biogeosciences*, 13
3595 (14):4291–4313, 2016.
- 3596 Takeuchi Tsuneo, Takano Masao, Tanikawa Hiroki, and Sugiyama Noriko. Zero
3597 carbon regional scenario analysis tool provided in excel file format, 2023. URL
3598 <https://zerocarbon.jp/>.
- 3599 Alexander J Turner, Christian Frankenberg, and Eric A Kort. Interpreting
3600 contemporary trends in atmospheric methane. *Proceedings of the National
3601 Academy of Sciences*, 116(8):2805–2813, 2019.
- 3602 Jos Van Geffen, Henk Eskes, Steven Compernolle, Gaia Pinardi, Tijl Verhoelst,
3603 Jean-Christopher Lambert, Maarten Sneep, Mark Ter Linden, Antje Ludewig,
3604 K Folkert Boersma, et al. Sentinel-5p tropomi no 2 retrieval: impact of ver-
3605 sion v2. 2 improvements and comparisons with omi and ground-based data.
3606 *Atmospheric Measurement Techniques*, 15(7):2037–2060, 2022.
- 3607 Ashish Vaswani, Noam Shazeer, Niki Parmar, Jakob Uszkoreit, Llion Jones,
3608 Aidan N Gomez, Łukasz Kaiser, and Illia Polosukhin. Attention is all you
3609 need. *Advances in neural information processing systems*, 30, 2017.
- 3610 Aleixandre Verger, Frédéric Baret, and Marie Weiss. Near real-time vegetation
3611 monitoring at global scale. *IEEE Journal of Selected Topics in Applied Earth
3612 Observations and Remote Sensing*, 7(8):3473–3481, 2014.
- 3613 Shinji Wakamatsu, Tazuko Morikawa, and Akiyoshi Ito. Air pollution trends in
3614 japan between 1970 and 2012 and impact of urban air pollution countermea-
3615 sures. *Asian Journal of Atmospheric Environment*, 7(4):177–190, 2013.
- 3616 Julie Wallace and Pavlos Kanaroglou. The effect of temperature inversions on
3617 ground-level nitrogen dioxide (no2) and fine particulate matter (pm2. 5) using
3618 temperature profiles from the atmospheric infrared sounder (airs). *Science of
3619 the Total Environment*, 407(18):5085–5095, 2009.

- 3620 Bernadette P Walter and Martin Heimann. A process-based, climate-sensitive
3621 model to derive methane emissions from natural wetlands: Application to five
3622 wetland sites, sensitivity to model parameters, and climate. *Global Biogeochemical Cycles*, 14(3):745–765, 2000.
- 3624 Chi Wang, Qingyun Wu, Markus Weimer, and Erkang Zhu. Flaml: A fast and
3625 lightweight automl library. *Proceedings of Machine Learning and Systems*, 3:
3626 434–447, 2021.
- 3627 You-Ren Wang, Nina Buchmann, Dag O Hessen, Frode Stordal, Jan Willem Eris-
3628 man, Ane Victoria Vollsnæs, Tom Andersen, and Han Dolman. Disentangling
3629 effects of natural and anthropogenic drivers on forest net ecosystem production.
3630 *Science of the Total Environment*, 839:156326, 2022.
- 3631 Tsugihiro Watanabe and Takashi Kume. A general adaptation strategy for cli-
3632 mate change impacts on paddy cultivation: special reference to the japanese
3633 context. *Paddy and Water Environment*, 7:313–320, 2009.
- 3634 A WHO. World health statistics 2020: monitoring health for the sdgs sustainable
3635 development goals. *World Health Organization*, 2020.
- 3636 Haixu Wu, Jiehui Xu, Jianmin Wang, and Mingsheng Long. Autoformer: De-
3637 composition transformers with auto-correlation for long-term series forecasting.
3638 *Advances in Neural Information Processing Systems*, 34:22419–22430, 2021.
- 3639 Jingfeng Xiao, Frederic Chevallier, Cecile Gomez, Luis Guanter, Jeffrey A Hicke,
3640 Alfredo R Huete, Kazuhito Ichii, Wenjian Ni, Yong Pang, Abdullah F Rahman,
3641 et al. Remote sensing of the terrestrial carbon cycle: A review of advances over
3642 50 years. *Remote Sensing of Environment*, 233:111383, 2019a.
- 3643 Jingfeng Xiao, Xing Li, Binbin He, M Altaf Arain, Jason Beringer, Ankur R
3644 Desai, Carmen Emmel, David Y Hollinger, Alisa Krasnova, Ivan Mammarella,
3645 et al. Solar-induced chlorophyll fluorescence exhibits a universal relationship
3646 with gross primary productivity across a wide variety of biomes. *Global change
3647 biology*, 25(4):e4–e6, 2019b.

- 3648 Liang Xu, Sassan S Saatchi, Yan Yang, Ranga B Myneni, Christian Frankenberg,
3649 Diya Chowdhury, and Jian Bi. Satellite observation of tropical forest seasonal-
3650 ity: spatial patterns of carbon exchange in amazonia. *Environmental Research
Letters*, 10(8):084005, 2015.
- 3652 Pu Yan, Nianpeng He, Kailiang Yu, Li Xu, and Koenraad Van Meerbeek. In-
3653 tegrating multiple plant functional traits to predict ecosystem productivity.
3654 *Communications Biology*, 6(1):239, 2023.
- 3655 Emily G Yang, Eric A Kort, Lesley E Ott, Tomohiro Oda, and John C Lin. Using
3656 space-based co2 and no2 observations to estimate urban co2 emissions. *Journal
3657 of Geophysical Research: Atmospheres*, 128(6):e2022JD037736, 2023.
- 3658 Hualei Yang, Xi Yang, Yongguang Zhang, Mary A Heskel, Xiaoliang Lu,
3659 J William Munger, Shucun Sun, and Jianwu Tang. Chlorophyll fluorescence
3660 tracks seasonal variations of photosynthesis from leaf to canopy in a temperate
3661 forest. *Global Change Biology*, 23(7):2874–2886, 2017.
- 3662 Jianbo Yang, Jingle Liu, Suqin Han, Qing Yao, and Ziying Cai. Study of the
3663 meteorological influence on ozone in urban areas and their use in assessing
3664 ozone trends in all seasons from 2009 to 2015 in tianjin, china. *Meteorology
3665 and Atmospheric Physics*, 131:1661–1675, 2019.
- 3666 Ruqi Yang, Jun Wang, Ning Zeng, Stephen Sitch, Wenhan Tang, Matthew Joseph
3667 McGrath, Qixiang Cai, Di Liu, Danica Lombardozzi, Hanqin Tian, et al. Di-
3668 vergent historical gpp trends among state-of-the-art multi-model simulations
3669 and satellite-based products. *Earth System Dynamics*, 13(2):833–849, 2022.
- 3670 Ruilian Yu, Yiling Lin, Jiahui Zou, Yangbin Dan, and Chen Cheng. Review on
3671 atmospheric ozone pollution in china: Formation, spatiotemporal distribution,
3672 precursors and affecting factors. *Atmosphere*, 12(12):1675, 2021.
- 3673 Rasa Zalakeviciute, Danilo Mejia, Hermel Alvarez, Xavier Bermeo, Santiago
3674 Bonilla-Bedoya, Yves Rybarczyk, and Brian Lamb. War impact on air quality
3675 in ukraine. *Sustainability*, 14(21):13832, 2022.

- 3676 Jiye Zeng, Tsuneo Matsunaga, Zheng-Hong Tan, Nobuko Saigusa, Tomoko Shirai,
3677 Yanhong Tang, Shushi Peng, and Yoko Fukuda. Global terrestrial carbon fluxes
3678 of 1999–2019 estimated by upscaling eddy covariance data with a random forest.
3679 *Scientific data*, 7(1):313, 2020.
- 3680 George Zerveas, Srideepika Jayaraman, Dhaval Patel, Anuradha Bhamidipaty,
3681 and Carsten Eickhoff. A transformer-based framework for multivariate time
3682 series representation learning. In *Proceedings of the 27th ACM SIGKDD conference on knowledge discovery & data mining*, pages 2114–2124, 2021.
- 3684 Qianqian Zhang, K Folkert Boersma, Bin Zhao, Henk Eskes, Cuihong Chen,
3685 Haotian Zheng, and Xingying Zhang. Quantifying daily no x and co2 emissions
3686 from wuhan using satellite observations from tropomi and oco-2. *Atmospheric
3687 Chemistry and Physics*, 23(1):551–563, 2023a.
- 3688 Yao Zhang, Joanna Joiner, Seyed Hamed Alemohammad, Sha Zhou, and Pierre
3689 Gentine. A global spatially contiguous solar-induced fluorescence (csif) dataset
3690 using neural networks. *Biogeosciences*, 15(19):5779–5800, 2018.
- 3691 Yongguang Zhang, Luis Guanter, Joseph A Berry, Christiaan van der Tol,
3692 Xi Yang, Jianwu Tang, and Fangmin Zhang. Model-based analysis of the
3693 relationship between sun-induced chlorophyll fluorescence and gross primary
3694 production for remote sensing applications. *Remote Sensing of Environment*,
3695 187:145–155, 2016.
- 3696 Zhaoying Zhang, Yongguang Zhang, Albert Porcar-Castell, Joanna Joiner, Luis
3697 Guanter, Xi Yang, Mirco Migliavacca, Weimin Ju, Zhigang Sun, Shiping Chen,
3698 David Martini, Qian Zhang, Zhaohui Li, James Cleverly, Hezhou Wang, and
3699 Yves Goulas. Reduction of structural impacts and distinction of photosynthetic
3700 pathways in a global estimation of gpp from space-borne solar-induced
3701 chlorophyll fluorescence. *Remote Sensing of Environment*, 240:111722, 2020.
3702 ISSN 0034-4257. doi: <https://doi.org/10.1016/j.rse.2020.111722>. URL <https://www.sciencedirect.com/science/article/pii/S0034425720300912>.
- 3704 Zhen Zhang, Benjamin Poulter, Andrew F Feldman, Qing Ying, Philippe Ciais,
3705 Shushi Peng, and Xin Li. Recent intensification of wetland methane feedback.
3706 *Nature Climate Change*, 13(5):430–433, 2023b.

- 3707 Bo Zheng, Dan Tong, Meng Li, Fei Liu, Chaopeng Hong, Guannan Geng, Haiyan
3708 Li, Xin Li, Liqun Peng, Ji Qi, et al. Trends in china's anthropogenic emissions
3709 since 2010 as the consequence of clean air actions. *Atmospheric Chemistry and*
3710 *Physics*, 18(19):14095–14111, 2018.
- 3711 Bo Zheng, Guannan Geng, Philippe Ciais, Steven J Davis, Randall V Martin,
3712 Jun Meng, Nana Wu, Frederic Chevallier, Gregoire Broquet, Folkert Boersma,
3713 et al. Satellite-based estimates of decline and rebound in china's co2 emissions
3714 during covid-19 pandemic. *Science Advances*, 6(49):eabd4998, 2020.
- 3715 Haoyi Zhou, Shanghang Zhang, Jieqi Peng, Shuai Zhang, Jianxin Li, Hui Xiong,
3716 and Wancai Zhang. Informer: Beyond efficient transformer for long sequence
3717 time-series forecasting. In *Proceedings of the AAAI conference on artificial*
3718 *intelligence*, volume 35, pages 11106–11115, 2021.
- 3719 Tian Zhou, Ziqing Ma, Qingsong Wen, Xue Wang, Liang Sun, and Rong Jin.
3720 Fedformer: Frequency enhanced decomposed transformer for long-term series
3721 forecasting. In *International Conference on Machine Learning*, pages 27268–
3722 27286. PMLR, 2022.
- 3723 Maria A Zoran, Roxana S Savastru, Dan M Savastru, and Marina N Tautan.
3724 Peculiar weather patterns effects on air pollution and covid-19 spread in tokyo
3725 metropolis. *Environmental Research*, 228:115907, 2023.